



**BERGISCHE  
UNIVERSITÄT  
WUPPERTAL**

**Kinetic energy measurements for  
ion dynamics studies in API-MS  
and  
Modeling of an FT-QIT**

**Dissertation**

zur Erlangung des akademischen Grades  
Doktor der Naturwissenschaften (Dr. rer. nat.)

vorgelegt von  
Marco Thinius  
geboren in Haan, Deutschland

Bergische Universität Wuppertal  
Fakultät für Mathematik und Naturwissenschaften  
Physikalische und Theoretische Chemie  
unter Leitung von  
Prof. Dr. Thorsten Benter

Wuppertal, Juli 2021

The PhD thesis can be quoted as follows:

urn:nbn:de:hbz:468-urn:nbn:de:hbz:468-20211125-104825-8

[<http://nbn-resolving.de/urn/resolver.pl?urn=urn%3Anbn%3Ade%3Ahbz%3A468-20211125-104825-8>]

DOI: 10.25926/0y06-7727

[<https://doi.org/10.25926/0y06-7727>]

## Danksagung

Obwohl auf dem Deckblatt nur ein Name steht, haben sehr viele Menschen auf unterschiedlichste Art und Weise dazu beigetragen, dass diese Arbeit nun fertiggestellt wurde.

Ich danke Prof. Dr. Thorsten Benter für die Möglichkeit diese Arbeit durchführen zu können und die stetige Unterstützung und Motivation.

Dem gesamten Team der PTC und allen Kolleg\*innen und Freund\*innen, die ich über die Jahre an der BUW und darüber hinaus kennengelernt habe, danke ich für die Unterstützung, die gute Zusammenarbeit und die familiäre Atmosphäre. Insbesondere an Kai, Christine, Alex, Stefan und Walter möchte ich an dieser Stelle meinen Dank für die vielen unvergesslichen Momente aussprechen. Mit euch war jede Arbeit ein Privileg.

Ein ganz besonderer Dank geht an die Menschen, die einfach immer da waren – Sven, Luke und Svenja, sowie meine Familie. Ihr hattet immer ein offenes Ohr und habt mir immer Mut gemacht.



## **Erklärung**

„Ich versichere, die Arbeit selbständig verfasst zu haben, nur die in der Dissertation angegebenen Hilfsmittel benutzt und alle wörtlich oder inhaltlich übernommenen Stellen als solche gekennzeichnet zu haben, und dass die Dissertation in der gegenwärtigen oder einer anderen Fassung noch keiner anderen Fakultät, keiner Gesamthochschule und keiner anderen wissenschaftlichen Hochschule vorgelegen hat.“

Wuppertal, den 19.07.2021

Marco Thinius



## Abstract

This work consists of two parts that are concerned with different aspects of the ion dynamics in quadrupole ion trap (QIT) mass spectrometers.

The first part describes the development and application of a method for detecting changes of ion kinetic energy distributions (KED), based on the interaction of ions with a variable potential barrier in the ion transfer stage. The potential barrier is introduced by applying a deceleration potential at the transfer stage exit. Deceleration potential response (DPR) curves are measured with a Faraday cup electrode and an ion trap. The Faraday cup measurements allow direct evaluation of the KED, because the data reflect the direct interaction of the ion charge with the potential barrier. In contrast, the DPR curves measured with the ion trap exhibit complex shapes. Modeling of the ion injection process confirmed that this is the result of the energy-dependent ion acceptance function of the ion trap which is superimposed on the DPR. The fringe field between the transfer stage exit and ion trap entrance electrodes introduces an RF-phase-dependent modulation of the ion kinetic energy. As conclusion, the absolute KED cannot be precisely determined from the ion trap data; however, the method is sensitive to changes of the KED. Further characterization of the method demonstrated that changes of the transfer voltages are conserved in the kinetic energy distribution only downstream of the second vacuum stage in Bruker HCT and amaZon mass spectrometers. Collisional re-equilibration of the kinetic energy occurs in the first and second vacuum stages. The RF voltage, or more generally, the stability parameter  $q_z$ , was found to have a systematic impact on the shape of the DPR curves. The effect of different incident KEDs was studied in simulations to support interpretation of experimentally observed shifts of the DPR. It was demonstrated that the method supports the investigation of the ion evolution with electrospray ionization (ESI). The combination with survival yield experiments revealed that ion activation in the ion transfer stage impacts on the observed ion distribution due to changes of the KED. Finally, the method was applied to study the impact of experimental parameters on the KED of ions generated with ESI. It was found that the ESI tip voltage as well as the addition of chemical modifiers to the background gas strongly impacts on the ion formation process, likely due to a change of the droplet formation and evolution dynamics. The results support the hypothesis that gas phase ion formation with ESI is not completed within the ion source but occurs downstream within the ion transfer stage.

In the second part, the formation and storage of ions in a Fourier transform (FT) QIT with in-trap electron ionization (EI) is described. Ionization is carried out

## Abstract

in a transient gas pulse within the quadrupolar field, which introduces nonlinear dependencies of the ionization rate on controllable ionization parameters. Modeling of the gas pulse suggests that chemical ionization (CI) conditions can easily be attained during ionization, i.e., ion-molecule chemistry is invoked. In combination with the RF-modulated electron beam energy, this renders the interpretation of mass spectra difficult and thus compromises compound identification with EI databases. Ionization rates, as determined from electron beam simulations, suggest that the trap is easily overloaded with ions. The controlled ejection of matrix ions, e.g., by instability ejection or selective excitation techniques, is thus a prerequisite for detection of compounds present at low mixing ratios. Collisions of ions with the background gas during the sample gas pulse adversely affect the ion lifetime in the ion trap. Collision-induced ion loss was found to significantly contribute to suppression of low-mass ions. This effect distorts the observed ion population significantly and leads to pronounced loss of spectral information.

The simulation framework IDSimF, concurrently developed in a separate major research effort, was successfully applied in this work. The simulation results were in very good agreement with literature data. The capability of simulating realistic ion numbers, i.e., on the order of several ten thousand ions, in ion trap applications with consideration of space charge effects renders IDSimF a valuable tool for future complex ion dynamics studies.

# Contents

<b>1</b>	<b>Scope of this work .....</b>	<b>1</b>
<b>2</b>	<b>Software packages .....</b>	<b>3</b>
2.1	IDSImF .....	3
2.2	SIMION .....	4
2.3	SPARTA .....	4
2.4	Data processing .....	6
<b>3</b>	<b>Kinetic energy measurements for ion dynamics studies in API-MS 7</b>	
3.1	Introduction .....	7
3.1.1	Ion kinetic energy in mass spectrometry.....	8
3.1.2	Internal energy deposition and ion transformation processes	9
3.1.3	Fragmentation response as a diagnostic tool.....	14
3.1.4	Kinetic energy response as a diagnostic tool .....	15
3.1.5	Ion dynamics in a quadrupole ion trap.....	16
3.2	Experimental and instrumentation .....	20
3.2.1	Bruker mass spectrometers .....	20
3.2.2	Chemicals .....	25
3.3	Kinetic measurement methods.....	25
3.3.1	Potential barrier method .....	26
3.3.2	Survival yield method .....	27
3.4	Numerical models.....	29
3.4.1	Gas simulations.....	29
3.4.2	Ion trajectory simulations.....	32
3.5	KEDs in the Bruker HCTplus.....	34
3.6	Characterization of the DPS method .....	37
3.6.1	Axial acceleration voltages in the ion transfer stage.....	38
3.6.2	Comparison of ion trap instruments.....	41
3.6.3	Extended DPS range.....	42
3.7	Modeling of the DPR .....	47
3.7.1	Gas dynamics in the transfer stage.....	47
3.7.2	Collisional broadening in the transfer stage.....	51
3.7.3	Ion focusing and the observed KED .....	58
3.7.4	KED modulation by fringe fields.....	60
3.7.5	Ion acceptance of the QIT .....	64
3.7.6	DPR data and the actual ion KED.....	67
3.8	Application: DPS experiments as a diagnostic tool.....	72

## Contents

3.8.1	Combined survival yield and DPS experiments.....	72
3.8.2	Sensing changes of the ion evolution during ESI .....	77
3.9	Summary and outlook.....	85
3.10	Appendix.....	87
3.10.1	Fitting functions and optimized parameters used in 3.7.1 .....	87
<b>4</b>	<b>Modeling of an FT ion trap.....</b>	<b>89</b>
4.1	Introduction.....	89
4.1.1	iTrap: principle of operation .....	91
4.1.2	Perturbations in ion trap mass spectrometry.....	93
4.1.3	Electron ionization .....	96
4.2	Gas sampling.....	97
4.2.1	SPARTA DSMC model .....	98
4.2.2	Equilibrium pressure distribution.....	99
4.2.3	Transient pressure evolution.....	102
4.3	Electron beam simulations .....	107
4.3.1	SIMION model.....	108
4.3.2	Electron beam density and energy .....	109
4.3.3	In-trap ionization rates.....	111
4.3.4	Ion definition files for trajectory simulations .....	115
4.4	Ion storage.....	116
4.4.1	SIMION and IDSimF model.....	116
4.4.2	Ion acceptance of the QIT .....	116
4.4.3	Stored ion ensemble and storage capacity.....	124
4.4.4	Collisions and ion loss .....	126
4.4.5	Ion suppression.....	136
4.5	Implications for operation of an FT-QIT with in-trap ionization – summary and conclusion .....	139
4.5.1	Comment on mass resolution and space charge.....	142
4.5.2	Space charge simulations with IDSimF .....	143
	<b>List of abbreviations.....</b>	<b>145</b>
	<b>List of tables .....</b>	<b>147</b>
	<b>List of figures .....</b>	<b>149</b>
	<b>References.....</b>	<b>155</b>

# 1 Scope of this work

The scope of the present work is - in the widest sense - the investigation of the ion dynamics in two quadrupole ion trap (QIT) mass spectrometers, namely an atmospheric pressure ionization (API) scanning ion trap and an electron ionization (EI) Fourier transform (FT) ion trap. The term ion dynamics refers to the motion of ions in electric fields in combination with ion-neutral and ion-ion interactions, respectively.

One challenge in API mass spectrometry (MS) is the comprehensive understanding of the ion transfer process from the ion source into the high vacuum region of the mass analyzer. During this transfer, ions experience often rapidly changing conditions and can undergo chemical reactions and fragmentation. In combination with electrospray ionization (ESI), another level of complexity is introduced because ions are initially transported within charged droplets from which they are eventually released at some point in the instrument. This process is still not entirely understood. The first part of this work describes the development, characterization, and application of a method for detecting changes in the ion formation pathway based on changes of the ion kinetic energy distribution (KED) in an API ion trap equipped with an ESI source. The experimental procedure relies on the interactions of ions with a potential barrier and can in principle be implemented in every type of mass spectrometer. Interpretation of experimental results is supported by comprehensive modeling of the ion transfer stage and ion trap injection process, leading to a deeper understanding of the fundamental processes that impact the kinetic energy response. The development of the method aims at providing an additional tool for studying aspects of the droplet evolution and ion formation pathway occurring with ESI.

The second part addresses the investigation of ion formation and storage in an FT-QIT. Ions are generated in a transient gas pulse with electron ionization in a quadrupolar field. This results in varying ionization conditions that impact on ionization rates and storage of ions in the QIT. The different stages of a measurement cycle are studied with numerical models, which are successively combined to obtain a comprehensive description of the entire process. Thus, underlying fundamental processes that impact the stored ion population can be studied individually. The results are put into context with experimental observations, which exhibit

## Scope of this work

only the final outcome of the convoluted effects. Furthermore, the application of the simulation program IDSimF (Ion Dynamics Simulation Framework) for ion trajectory simulations with consideration of space charge with realistic particle numbers is demonstrated.

## 2 Software packages

This chapter gives a brief overview of the simulation programs used in this work.

### 2.1 IDSimF

Development of the Ion Dynamics Simulation Framework (IDSimF) was started by Walter Wissdorf in the department for physical and theoretical chemistry (PTC) and the Institute for Pure and Applied Mass Spectrometry (ipaMS) at the University of Wuppertal. The code was published in 2020 under the GNU General Public License v3.0 and is available on [GitHub](#) [1]. The main motivation for this development was the necessity for a tool that allows ion trajectory simulations in electric fields *with* consideration of ion-ion interactions within large particle ensembles.

Numerical trajectory integration is done with the Verlet algorithm [2]. The electric particle-particle interactions are calculated with the Barnes-Hut algorithm [3]. With this approach, long range inter-particle forces are not calculated separately but are approximated by the summed force of a pseudo particle representing a group of individual particles. In addition, the charge of each particle can be scaled with a space charge factor (scf), which can be used for artificially increasing the total charge density without adding additional particles. IDSimF includes a hard-sphere collision model, a chemistry model, and an image-current-induction model based on the Shockley-Ramo theorem [4, 5]. The different program parts are developed as individual modules, which can be combined as required for different simulation applications. Currently, IDSimF does not contain an electric field solver. Fields can either be defined with analytical functions or imported from other programs, e.g., [SIMION](#) (Scientific Instrument Services, Inc., Ringoes, NJ) or [COMSOL Multiphysics](#) (COMSOL AB, Stockholm, Sweden).

IDSimF has already been used in different projects for the study of MS-related topics, e.g., cluster dynamics in ion mobility devices [6–8], and space charge effects in quadrupoles [9] and ion traps [10, 11].

IDSimPy is a Python [12] library for pre- and post-processing of IDSimF simulation results and was developed by PTC/ipaMS in parallel with IDSimF; it is also available on [GitHub](#) [1].

## 2.2 SIMION

SIMION 8.1 (Scientific Instrument Services, Inc., Ringoes, NJ, [www.simion.com](http://www.simion.com)) is one of the most commonly used electromagnetic field solvers and ion trajectory simulation packages in the MS community. The field solver uses the finite differences method. Electrode geometries and potentials are defined in a potential array. The solution for each electrode is calculated and stored separately. The total field in the simulation is the linear combination of all electrode solutions. The potentials applied to the individual electrodes are scaling factors in the linear combination, which allows for rescaling of electrode potentials “on the fly”, without the necessity for recalculating the entire field. This allows the implementation of dynamic fields with a static field solver, by applying time-dependent scaling factors. Electrode geometries can be imported from computer-aided design (CAD) models or created with geometry files, in which geometries are defined with a scripting language. The latter allows for automated geometry modifications during a simulation.

Trajectory integration is done in SIMION with a Runge-Kutta method [13]. The accuracy of the integrator can be adjusted with the quality parameter T.Qual, which adapts the timestep length relative to the grid resolution of potential array. Generally, larger positive or negative values for T.Qual increase the accuracy. For  $T.Qual > 0$  the time step size is additionally adapted dynamically in certain cases to improve accuracy, e.g., when particles approach electrode surfaces. For  $T.Qual \leq 0$  the timestep size is static. [13]

SIMION provides a programming interface based on Lua [14] that allows users to control simulation parameters and create customized simulation procedures. External libraries written in Lua can be easily imported and are used also for extensions that are already provided by SIMION, e.g., the hard sphere collision model HS1 and the reaction simulation model RS [15]. The latter was also developed by Walter Wissdorf and has become a part of the SIMION program package.

## 2.3 SPARTA

The Stochastic Parallel Rarefied-gas Time-accurate Analyzer (SPARTA) [16, 17] is a program for the simulation of rarefied gas flows based on the Direct Simulation Monte Carlo (DSMC) [18] method. DSMC was initially developed by Graeme Bird [18] and is nowadays widely applied for the study of large scale rarefied gas flows, e.g., the gas flow around spacecraft during atmospheric reentry [19], as well as in microstructures [20]. Modeling of gas flows in the transition regime between continuum and free-molecular flow conditions requires the treatment of individual

particles because the continuum assumption of fluid dynamics is no longer valid and inter-particle interactions cannot be neglected as in the case of free-molecular flows. The particles in a DSMC simulation are characterized by their spatial coordinates, velocity, and potentially internal energy. The latter is important for proper modeling of energy transfer and chemical reactions. The translational motion of particles is determined by their velocity in a given timestep. Particle-particle collisions and reactions are modeled statistically with appropriate distribution functions. The simulation domain is overlaid with a grid to accelerate the calculation of particle collisions. Collisions are calculated per cell, i.e., only for particles in the same cell, so that only particles are considered that can potentially interact with each other during a timestep. Typically used collision models are the variable hard sphere (VHS) [21] and variable soft sphere (VSS) models [22], which consider energy-dependent collision cross sections and are significantly more accurate than simple hard sphere models. The VSS model also accounts for variable diffusion cross sections and is thus more accurate than the VHS model [23]. For accurate modeling of gas flows, a proper statistic representation of collisions is necessary. This requires careful settings of the timesteps and grid cell sizes in relation to the particle density as well as a sufficiently large number of simulated particles.

SPARTA is optimized for performance and parallel computation and targets topics that require simulation of large particle numbers. Simulations can be performed in two and three dimensions and geometries can be manually created by defining the coordinates of the geometry boundaries in a text file or can be imported from CAD models. The grid in the simulation domain can be static or dynamically adjusted during the simulation based on local grid cell properties, which allows optimization of accuracy and computation time. The boundaries of the simulation can be set to different interaction models for different boundary conditions, e.g., in- and outflow of particles, or reflective or periodic behavior. Surfaces allow the application of different surface collision and reaction models for particle-surface interactions. The VHS and VSS collision models are both available in SPARTA. Time-averaged cell data can be selected as simulation output when time resolution of the time step length is not required, which reduces the total size of the result files. The result files contain selected parameters for each grid cell, e.g., particle density or temperature. A comprehensive manual for SPARTA is available online and as a PDF file [24]. The SPARTA developers also provide a set of Python scripts called [Pizza.py](#) for pre- and postprocessing, e.g., conversion of STL files into SPARTA-readable format for geometry definition or conversion of SPARTA result files into different formats for further analysis.

## 2.4 Data processing

The simulation results presented in this work are processed with custom Python scripts, depending mainly on NumPy [25] for data handling, SciPy [26] for processing, e.g., data fitting, and Matplotlib [27] for plotting. Functions that are used for specific tasks are referenced in the corresponding sections. The handling of raw output is different for the three programs:

**IDSimF** stores the trajectory results in the HDF5 [28] format. IDSimPy provides functions for parsing the data and converting them into basic Python objects or NumPy arrays.

**SIMION** results are stored as delimited text files. These are easily readable with Python/NumPy.

**SPARTA** result files are converted into the PVD file format of Paraview [29] with the Pizza.py toolkit. The PyVista [30] library is used for reading of PVD files in Python.

## 3 Kinetic energy measurements for ion dynamics studies in API-MS

In this chapter, a complementary approach to the established survival yield method for characterizing ion dynamics and formation pathways in API-MS is presented, which is based on the determination of *kinetic energy distributions* (KED) in the analyzer region of API instruments. A direct evaluation of the kinetic energy response can potentially reveal similar dependencies as the fragmentation response, since changes of the internal energy of ions in a mass spectrometer are mostly induced by changes of their kinetic energy. In contrast to the survival yield method, the KED approach does not require additional information, such as the fragmentation energy, and is applicable to every single observed ion species, and not only to a set of ions with characteristic properties. The experimental procedure is implemented and characterized in Bruker ion trap mass spectrometers. The interpretation of the experimental data is supported by computational modeling of the ion transfer stage and the ion trap injection process. Finally, the application of this method for studying ion dynamics during ESI is demonstrated.

### 3.1 Introduction

Mass spectrometry dates back to the experiments on 'rays of positive electricity' by J. J. Thomson in the early 20<sup>th</sup> century [31]. After more than 100 years, the understanding of fundamental processes in mass spectrometry is yet incomplete. This is on the one hand caused by the complexity of some processes occurring during a mass spectrometric experiment, but also the sheer amount of available mass spectrometric methods and combinations thereof. One of the main challenges in API-MS is to understand ion transformation processes occurring during a measurement, as they determine the observed ion population. Chemical reactions, e.g., radical chemistry and oxidation of the analyte in the discharge region of plasma-based ion sources [32], can lead to more complex mass spectra (additional peaks, e.g.,  $M^+$ ,  $[M+16]^+$ ,  $[M+32]^+$ ) and, thus, masking of the identity of molecular ions. Corona discharges can also readily occur at the liquid surface of the Taylor cone in ESI sources, even when moderate spray voltages are applied, resulting in comparable chemical transformations [33]. In thermodynamically controlled ion sources, charge transfer between different analyte ions can lead to complete depletion of

ion signals. In this case, the observed ion population does not reflect the neutral composition of the sample anymore [34]. Additional ion transformations can occur within the ion transfer stage. Strong electric fields, that are usually applied for ion sampling and focusing, can not only induce fragmentation (*collision induced dissociation*, CID) [35] but can also shift reactivities of reagent cluster ions [36]. These processes depend on the physical and chemical interactions during the lifetime of an ion, which are in turn depending on the instrument geometry (e.g., ion source and vacuum interface design, mass analyzer type) as well as operational parameters (e.g., ionization parameters, acceleration voltages) during a measurement.

### 3.1.1 Ion kinetic energy in mass spectrometry

The ion kinetic energy is a critical parameter for the operation of all mass spectrometers, as it affects the performance of ion optics, RF-driven ion guides, and mass analyzers. For example, the axial ion energy determines the residence time in a quadrupole mass filter and, thus, the number of secular oscillations, which impacts on the mass resolution of the filter [37, 38]. Ions with a large radial kinetic energy are more likely to be lost from multipole ion guides. Ions that are injected into RF multipoles with insufficient axial kinetic energy have a longer interaction time with the fringe field at the entrance, which adversely affects the acceptance of the multipole [39, 40]. In TOF analyzers the kinetic energy spread before acceleration into the flight tube greatly affects the attainable mass resolution. The success of TOF instruments was enabled by development of space and energy focusing techniques [41, 42].

Under collision-free conditions, the change of ion kinetic energy  $\Delta E_{\text{kin}}$  is directly controllable by electric fields, as it scales linearly with the change of the electric potential  $\Delta U$  that ions experience [43]:

$$\Delta E_{\text{kin}} = ze\Delta U, \quad (3-1)$$

where  $e$  is the elementary charge in atomic units and  $z$  is the charge number of the considered ion. With the introduction of API, ions need to be guided through collision-dominated regions, i.e., the ion source and vacuum interface, before entering the mass analyzer. DC voltages are thus applied for axial transport, while radial confinement is usually achieved with RF-voltage-driven multipole ion guides or ion funnels. A fraction of the kinetic energy gained upon acceleration in an electric field is lost due to collisions with the background gas. When the electric acceleration is constant over a time period exceeding the ion velocity relaxation time  $\tau$ , i.e., the time it takes for the accelerating and damping forces to equilibrate, the motion of ions is characterized by their drift velocity  $v_d$ . It is determined by the ion mobility  $K$  and the electric field strength  $E$  [44]:

$$v_d = \frac{K}{E}. \quad (3-2)$$

The ion mobility scales inversely with the gas number density  $N$  and the collision cross section  $\Omega$ , according to the Mason-Schamp equation [44]:

$$K = \frac{3}{16} \left( \frac{2\pi}{\mu k_B T} \right)^{1/2} \frac{e}{N\Omega}, \quad (3-3)$$

where  $\mu$  is the reduced mass of the ion and gas,  $k_B$  is the Boltzmann constant,  $T$  is the absolute gas temperature and  $e$  is the ion charge. As a result, ions may exhibit different velocities not only due to their  $m/z$  but also their size.

Axial acceleration voltages are scaled according to the respective pressure ranges in different compartments of the MS, e.g., higher pressures require higher voltages to compensate for the collisional damping of the ion motion. RF voltages are usually set to fit the  $m/z$  range of interest, as the transmission properties of ion guides are  $m/z$ -dependent [45]. It becomes apparent that the ion velocity or kinetic energy may change significantly in an ion transfer stage, as both the pressure and electric field strength are variable. Therefore, the kinetic energy of ions arriving at the mass analyzer is not easily inferred from the total potential gradient in the transfer stage and can also not be considered as a drift motion along the total length of the ion optics. Ultimately, the ion *kinetic energy* defines directly the *physical* interactions inside a mass spectrometer under collision-free conditions and, hence, its physical characteristics, e.g., ion transmission or mass resolution, and thus needs to be carefully controlled.

### 3.1.2 Internal energy deposition and ion transformation processes

Vacuum ionization techniques were utilized at large until the development of atmospheric pressure ionization and corresponding vacuum interfaces in the 1960s [35, 46]. The internal energy uptake of ions during the ionization process is characteristic for different ionization techniques, which has led to categorizing into *soft* (no or little fragmentation, e.g., field ionization (FI)) and *hard* ionization (strong fragmentation, e.g., electron ionization (EI)) [47]. With vacuum ionization techniques, the energy transfer onto the ionized molecule does manifest itself directly (excluding the kinetic shift<sup>1</sup>) in the degree of fragmentation observed in a mass spectrum. The *internal energy* dictates the *chemical* transformations an ion can potentially undergo.

---

<sup>1</sup> A kinetic shift is observed when the dissociation rate of an activated ion is small compared to the temporal delay between the activation event and detection. This leads to a lower observed fragmentation yield or a higher apparent activation energy [48, 49].

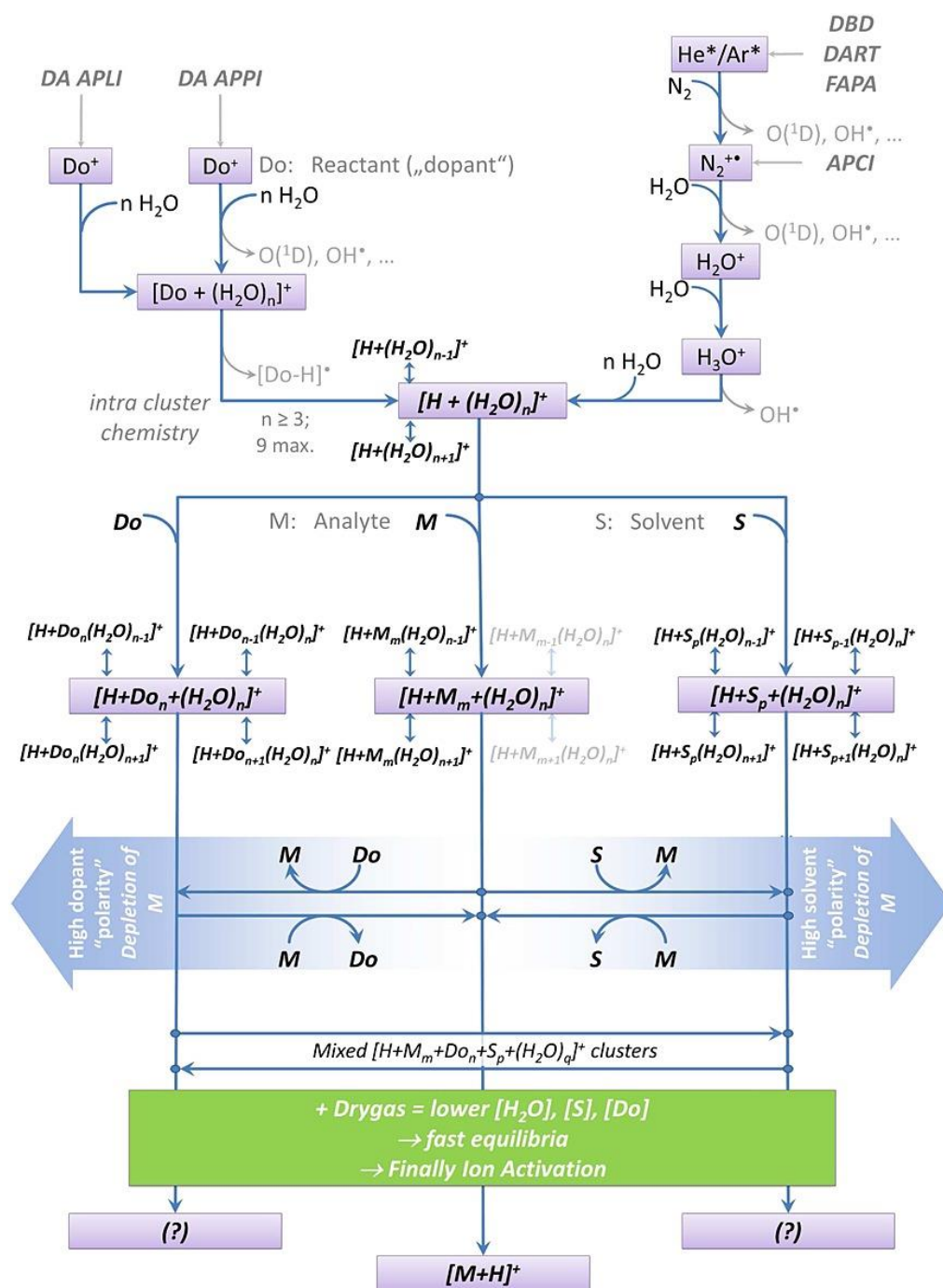


**Figure 1:** Comprehensive API cluster chemistry mechanism. Reprinted with permission from [36]. Copyright 2014 John Wiley & Sons, Ltd.

Under atmospheric pressure conditions, excess internal energy transferred to a molecule during the ionization process is quickly dissipated into the background gas, due to the high collision frequency. Also, the primary ionization event produces predominantly matrix ions, which are normally present in great excess, and

analyte ions are subsequently generated via secondary ion-molecule reactions. [34] Because of that, the ionization processes that yield the typically observed protonated molecules  $[M+H]^+$  with API methods, is *per se* “soft”<sup>2</sup>. Figure 1 summarizes the processes that lead to formation of observed analyte ions for different API methods operating in the gas phase. The displayed mechanism focusses on the formation of protonated water clusters as the common reagent ion population of different primary ionization techniques. Neutral analyte molecules interact with these clusters, e.g., leading to ligand-switch or association reactions. Subsequent CID in the transfer stage can then yield the protonated analyte [50].

The harshness of the interaction of ions with electric fields can be characterized by the *reduced field strength*  $E_0$ , which is defined as the ratio of the electric field strength  $E$  and the particle density  $N$ :

$$E_0 = \frac{E}{N}. \quad (3-4)$$

$E_0$  provides a measure of the deviation of the ion kinetic energy from thermal energy, induced by electric acceleration [51]. Ion-neutral collisions will not result in a significant increase of the ion internal energy (*low-field* conditions), when the acceleration distance between collisions is too short at the prevailing electric field strength for ions to attain sufficiently large kinetic energies. This is generally the case in atmospheric pressure ion sources. Ion activation thus occurs mostly in intermediate pressure regions, where a significant increase of the mean collision energy is attained via electric acceleration (*high-field* conditions), due to the increased mean free path. High-field conditions are easily obtained in API transfer stages. It is noted that for ion activation to take place, a high reduced field strength is only one prerequisite; of course, collisions still need to occur.

The water cluster system is highly dynamic and responds almost instantaneously to changes of the reduced field strength. Under thermal conditions and typical ambient water mixing ratios in the range of 1%, the most abundant cluster sizes of the type  $[H+(H_2O)_n]^+$  are  $n = 4 \dots 8$  [52]. In regions of high reduced field strengths, the mean cluster size decreases. The proton affinity also decreases with the cluster size [53] and as small clusters ( $[H+(H_2O)_n]^+$ ,  $n < 3$ ) are generated direct proton transfer reactions can occur [32, 54]. This is utilized in proton transfer reaction mass spectrometry (PTR-MS), where  $[H_3O]^+$  is predominantly produced for direct

---

<sup>2</sup> It should be noted that ionization of an analyte molecule may not only occur in the ion source but also in the vacuum interface region, where the collision rate is significantly reduced and ions are experiencing strong electric fields. Dissociative ionization processes may become more prominent under such conditions, resulting in overall *harder* ionization [36].

protonation of analytes [54]. With protonated water clusters as the dominant ionization reagent, the typical occurrence of protonated molecules in API is readily rationalized, even when the primary ionization process produces radical cations as primary reagent ions, which is the case for virtually every API method operating in the gas phase [34]. Since API sources are usually not sealed against the environment, water from the surrounding air can easily penetrate into the system and thus becomes one of the most abundant matrix components inside the ion source. Additionally, analytes are often introduced into the ion source in aqueous solutions, which elevates the water content in the ion source background gas. Naturally, all compounds present in the ion source can participate in the ionization mechanism, which may open additional reaction pathways and explains, e.g., the occurrence of adduct ions [55]. In collision-dominated regions, ions will always be solvated by polar molecules present in the matrix gas [56]. It is thus highly unlikely that bare gas phase ions but rather solvated ions (clusters) are entering the mass spectrometer inlet. The adiabatic expansion of the ion source effluent into the vacuum system may even promote cluster growth.<sup>3</sup> Therefore, gas-phase-based API is generally characterized by cluster chemistry. “Desolvation” of these clusters is supported by heating and auxiliary gas streams (“drying gas”) in the ion source region, but is often only achieved by CID in the ion transfer stage [35]. The products of the desolvation process, i.e., the observed ion population, are eventually determined by the proton affinities or gas phase basicities/acidities of the cluster constituents. It is generally assumed that accumulation of internal energy in analyte ions occurs only after complete desolvation [57]. This implies, that the occurrence of fragment ions requires desolvation of precursor ions and subsequent activation via energetic collisions, i.e., CID.

While the cluster-chemistry nature of API is generally acknowledged, cluster-chemistry itself is often left out in the discussions of the ESI process. This is due to the fact that the primary ionization of analyte ions with ESI occurs within the liquid phase, within charged droplets or at droplet-gas interfaces, which is also the only feasible explanation for the occurrence of multiply charged ions [58]. The ions are at some point transferred into the gas phase, depending on the droplet composition, analyte properties, and instrument operational parameters. However, when ions have already been transferred into the gas phase in a collision-dominated

---

<sup>3</sup> This is a well-known issue of API interfaces and is counteracted by applying suitable acceleration voltages in the first differential vacuum stage, resulting in CID of solvent clusters [35].

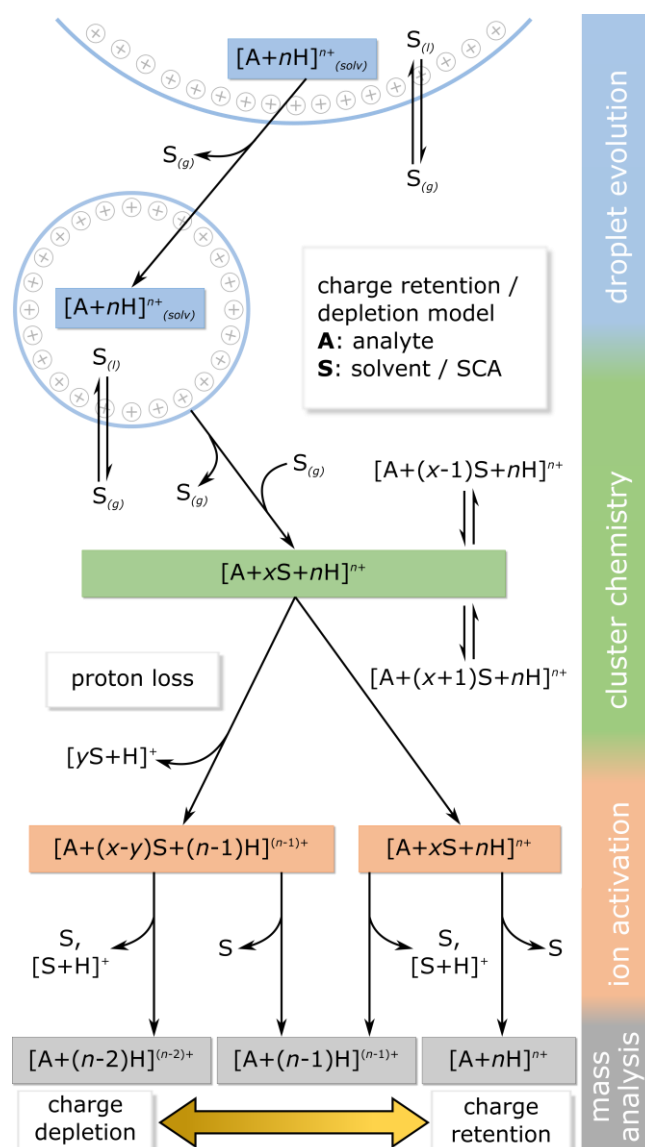


**Figure 2:** Charge retention/charge depletion mechanism scheme. SCA stands for super-charging reagent. Reprinted with permission from [59]. Copyright 2020 American Chemical Society.

environment, they cannot evade cluster chemistry. It was demonstrated that the gas composition can significantly affect the observed ion population in ESI experiments [57, 59–61]. Figure 2 depicts a mechanism that combines the ion release from charged droplets with subsequent cluster chemistry. As shown in the API cluster chemistry mechanism (Figure 1), it is proposed that bare gas phase ions will be only produced after desolvation in the ion transfer stage. Observing fragments, i.e. CID of ions generated with ESI in any part of the ion transfer stage, implies that the ion release from charged droplets and complete desolvation occurred before CID processes operated on the ion.

Both gas-phase-based API and ESI yield solvated ions and the desolvation process requires activation of these ion-solvent aggregates. This is the step in which significant internal energy deposition does occur in API-MS. Inattentive settings of “declustering potentials”, which are applied to dissociate ion-solvent clusters, can promote CID of ions. Modern mass spectrometers are usually tuned for sensitivity, which also requires strong electric fields for ion transport and focusing in collision-dominated regions, such as the ion source and the vacuum interface. This does in turn promote energetic collisions with neutrals and the extent of fragmentation scales with the collision energy [62]. The internal energy uptake of ions is thus directly coupled to their transport in the ion transfer stage and therefore not characteristic for different ionization techniques, but rather for entire instrumental setups, i.e., combinations of ion source, vacuum interface, ion optics, mass analyzer, and applied voltages.

### 3.1.3 Fragmentation response as a diagnostic tool

Even though fragmentation of analyte ions in API is usually no direct result of the primary ionization step, subsequent fragmentation can be utilized for studying the internal energy deposition in different API systems. The extent of fragmentation is linked to the ion evolution from its point of creation to the point of activation. Therefore, differences in the fragmentation response between instrument settings can give insights into this process. The *survival yield* method is widely applied for determination of internal energy distributions under various experimental conditions. The method relies on the fragmentation of so-called *thermometer ions* with known fragmentation energies [63]. From the survival yield of multiple ions with different fragmentation energies, the internal energy distribution can be inferred. The relative dependence of the internal energy deposition during ionization on ionization parameters is observable as shifts of the fragmentation response in regions *downstream* of the ion source. Since the kinetic shift is difficult to assess within API mass spectrometers, the absolute position of the energy distribution can usually not be evaluated from a survival yield experiment [64], but relative shifts of the energy distribution are still observable. The impact of different ionization methods [65–68] and ion source parameters [64, 69–72] on the observed energy deposition in the ion transfer stage was extensively studied and linked to ion formation and desolvation pathways.

Prior to fragmentation of covalent bonds, dissociation of loosely bound clusters is frequently induced by activation. This was very clearly demonstrated in experiments in which polar solvent vapor was abundantly added to the matrix gas in nano-electrospray experiments, which completely suppressed fragmentation of

molecular ions [59] or even labile noncovalent complexes [57]. Ion solvation depends also on ion source parameters, such as gas flows, which was observed in survival yield experiments [73]. Thus, the fragmentation response, i.e., the internal energy deposition, is predominantly linked to the mechanism that leads to desolvated gas phase ions, rather than to the primary ionization step. While the latter is well understood, e.g. protonation, the formation of bare gas phase ions with ESI is still under discussion. Especially the release of ions from charged droplets remains unresolved and is subject of recent research [74, 75].

#### 3.1.4 Kinetic energy response as a diagnostic tool

The kinetic energy of ions can reveal fundamental insights into their formation process. In 1928, Condon and Smyth [76] predicted the formation of  $H^+$  ions with excess kinetic energies from different excited states of molecular ions during electron ionization of  $H_2$ , based on quantum mechanics regarding the hydrogen atom. The  $H^+$  ions should exhibit different kinetic energies, depending on the state from which they are formed. The abundance of these ions should depend on the energy of the incident electron beam, as the formation of the states requires different energies. This effect is termed *kinetic energy release* (KER) [77] and was experimentally confirmed by Bleakney [78] and Lozier [79] in 1930, who determined ion velocity distributions of the  $H^+$  ions in dependence of the incident electron energy by utilizing a retarding potential between the point of ion creation and the detector. The method was used for further studies on dissociation of diatomic molecules and determination of their heats of dissociation, see for example [80, 81]. In 1941, Hagstrum and Tate proposed an alternative experiment for studying the dissociation of diatomic molecules with a magnetic sector field mass spectrometer, which allows simultaneous ion kinetic energy and mass analysis. The analysis was based on the distortion of peaks of ions that are formed with different kinetic energies in the ion source and are, thus, focused non-uniformly in the instrument.[82] Similar observations were later linked to *metastable ions* that fragment in field-free regions in the mass spectrometer [83], which extended the applicability of the method to polyatomic ions and became known as *ion kinetic energy spectrometry* (IKES) [84]. The development of double-focusing sector field instruments enabled *mass-analyzed ion kinetic energy spectrometry* (MIKES) [85], which allows for the analysis of isolated ions.<sup>4</sup> These techniques are used to study the KER in unimolecular fragmentations of ions in the field-free region of sector field instruments. The

---

<sup>4</sup> McLafferty and coworkers identified isomers by analyzing metastable ions and the respective fragments [86]. Cooks and coworkers used a MIKE spectrometer specifically for

electric sector downstream of the fragmentation region is used for the kinetic energy analysis. MIKES experiments were utilized to gather information on ionic structures, e.g., protonation sites in peptides [89], reaction energetics, e.g., gas phase basicities [89] and proton affinities [90], and reaction dynamics, e.g., transition states in fragmentation [91] and ion-molecule reactions [92]. The evaluation of such fundamental atomic or molecular properties requires a well-prepared ion ensemble, i.e., the availability of precise control of ionization and fragmentation parameters. When ions are formed in an environment where they cannot be analyzed undisturbedly, the sensitivity of a kinetic energy analysis is shifted from the ionization process itself towards the ion evolution after the ion has been created, which is determined by collisions and chemical transformations under the given conditions. Analysis of the “bulk” kinetic energy distribution of ion ensembles is commonly done with retarding potential analyzers (RPA) [93] and is of interest for characterizing plasmas [94, 95]. RPAs were also coupled with mass spectrometers for evaluation of mass-resolved energy distributions [96]. The principle of applying a retarding potential for measuring the kinetic energy dependent integral ion current was also used inside the ion optics of mass spectrometers. Instead of grids, neighboring ion optical elements were utilized to implement a potential barrier. This was done, e.g., for characterizing kinetic energy distributions of ions formed in an inductively coupled plasma (ICP) mass spectrometer [97] and for selectively blocking secondarily formed ions inside the ion optics, depending on their kinetic energy [98]. In principle, this method can be implemented in every mass spectrometer. Since ion optics voltages do also impact strongly on the transfer properties, the change of the transfer *efficiency* has to be evaluated and included in the interpretation of the kinetic energy analysis.

### 3.1.5 Ion dynamics in a quadrupole ion trap

A quadrupole ion trap consists of three electrodes with hyperbolically shaped surfaces. The central ring electrode is positioned between the two cap electrodes. Storage of ions in a QIT is based on their interactions with a dynamic electric field that is applied between the ring and cap electrodes. During an acquisition cycle in a QIT mass spectrometer, ions are injected and stored inside the trap and are subsequently mass-selectively ejected. In addition, ion isolation and excitation steps

---

selecting precursor ions in the magnetic sector, subsequent fragmentation and mass analysis of the fragment ions in the electric sector [87], laying the foundation for tandem mass spectrometry [88].

can be performed prior to mass analysis. Therefore, ions can undergo various levels of kinetic and internal excitation during a QIT experiment.

The mass-selective operation of a QIT depends on the characteristic ion motion in a quadrupolar field, which is described by solutions to the Mathieu equation [99]. A brief overview of the fundamentals is given in the following. For a detailed treatment of the theory the reader is referred to [100]. The stability of an ion is expressed in terms of two *stability parameters*  $a_u$  and  $q_u$ , where  $u$  represents the spatial coordinates  $x$ ,  $y$  and  $z$ . Due to the symmetry of the quadrupolar field the stability parameters for the  $x$  and  $y$  coordinate are identical and the ion motion can thus be separated into a radial and axial component. Stability parameters for the radial ( $a_r$  and  $q_r$ ) and axial coordinate ( $a_z$  and  $q_z$ ) are given:

$$a_z = -2a_r = -\frac{16eU}{m(r_0^2 + 2z_0^2)\Omega^2} \quad (3-5)$$

and

$$q_z = -2q_r = \frac{8eV}{m(r_0^2 + 2z_0^2)\Omega^2}, \quad (3-6)$$

where  $e$  is the elementary charge,  $U$  is a DC voltage,  $V$  is an RF voltage,  $m$  is the ion mass,  $r_0$  and  $z_0$  are the trap electrode dimensions in radial and axial direction, respectively, and  $\Omega$  is the radial frequency of the RF voltage. In the context of QIT-MS, the axial ion motion is usually of predominant importance, because the ion trajectory manipulation inside a QIT is achieved by dipolar excitation between the cap electrodes, i.e., along the axial coordinate. Therefore, in the following section all expressions are written with regard to the axial coordinate (index  $z$ ), if not

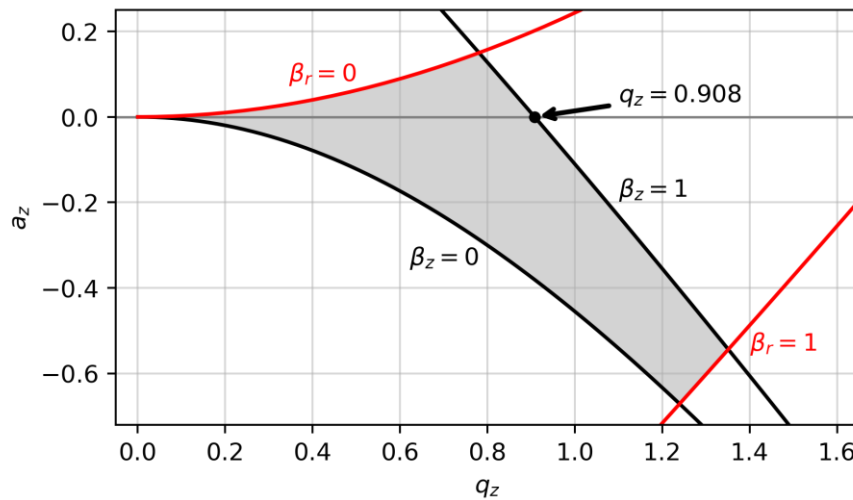


**Figure 3:** Excerpt of the stability diagram in  $(a_z, q_z)$  phase space. The space between the red ( $\beta_r$ ) and black lines ( $\beta_z$ ) are  $r$ - and  $z$ -stable regions, respectively. QITs are usually operated in the space of overlapping  $r$  and  $z$  stability (grey area).

stated otherwise. Conversion between the axial and radial terms is possible via eqs. (3-5) and (3-6). The stability diagram in  $(a_z, q_z)$  phase space reveals regions of ion stability in both  $r$  and  $z$  direction. QIT mass spectrometers are operated in the region of overlapping  $r$  and  $z$  stability which extends around the  $q_z$  axis of the stability diagram, as shown in Figure 3.

QIT mass analyzers are usually operated without a DC voltage, so that  $a_z$  is zero and the ion stability can be characterized by only one parameter  $q_z$ . The stability region intersects the  $q_z$  axis at 0 and 0.908, which defines the mass range that can be stored in a QIT at given dimensions and field parameters. A  $q_z$  value of 0.908 defines the *low mass cut-off* (LMCO), i.e., the lowest  $m/z$  ratio<sup>5</sup> that is stable in the quadrupolar field:

$$\text{LMCO} = \left(\frac{m}{e}\right)_{\min} = \frac{8V}{0.908(r_0^2 + 2z_0^2)\Omega^2}. \quad (3-7)$$

There is no fundamental high mass limit for the stability of ions, as  $q_z = 0$  corresponds to an ion with infinite  $m/z$  (cf. eq. (3-6)).<sup>6</sup>

The motion of a charged particle in a quadrupolar field is periodic and is characterized by two fundamental secular oscillations with the axial and radial frequencies  $\omega_z$  and  $\omega_r$ , respectively:

$$\omega_z = -2\omega_r = \frac{\beta_z \Omega}{2}. \quad (3-8)$$

The dimensionless parameter  $\beta_z$  is a function of  $a_z$  and  $q_z$ . An approximation for  $\beta_z \ll 1$  was found by Major and Dehmelt [101]:

$$\beta_z \approx \sqrt{a_z + \frac{q_z^2}{2}}. \quad (3-9)$$

The exact value of  $\beta_z$  is defined by a continued fraction expression. Integer values of  $\beta_z$  describe the boundaries of regions of stability in the stability diagram, as depicted in Figure 3. The region of operation for QITs is between  $\beta_z = 0$  and  $\beta_z = 1$ . According to eq. (3-8), the axial secular frequency of an ion at the stability limit  $\beta_z = 1$  is half the RF frequency. From eqs. (3-6), (3-8) and (3-9) the axial secular frequency in an ion trap ( $a_z = 0$ ) can be calculated for any  $q_z$ :

$$\omega_z = \frac{2\sqrt{2}eV}{m(r_0^2 + 2z_0^2)\Omega}. \quad (3-10)$$

---

<sup>5</sup> It is noted that eq. (3-7) yields the LMCO in [kg/C], while in mass spectrometry  $m/z$  is usually given in [Da/e], where  $e$  is the elementary charge in atomic units.

<sup>6</sup> The required voltages for mass selective ejection limit the upper mass limit of QIT mass spectrometers.

A second oscillating motion, the so-called *micromotion*, is superimposed on the secular oscillation. Its frequency equals the RF frequency.

An important parameter that impacts on ion dynamics in a QIT is the pseudopotential  $\bar{D}_z$  which determines the effective focusing force acting on ions. The pseudopotential is also called Dehmelt potential, after Hans Georg Dehmelt, who found a simple equation for calculating  $\bar{D}_z$ , which is valid for  $q_z < 0.4$  [102]:

$$\bar{D}_z \approx \frac{q_z V}{8}. \quad (3-11)$$

With knowledge of  $\bar{D}_z$  the maximum kinetic energy of the secular oscillation can be calculated:

$$e\bar{D}_z \approx \frac{eq_z V}{8}. \quad (3-12)$$

Trapping ions that are generated in an external ion source requires that the ions lose a fraction of their kinetic energy after entering the ion trap, so that their maximum kinetic energy decreases below the pseudopotential<sup>7</sup>. This is achieved by increasing the pressure inside the QIT with a buffer gas, typically in the range of  $10^{-3}$  mbar [106, 107]. Helium is commonly used as buffer gas, as its low mass facilitates energy transfer from ions to the gas (*collisional cooling*). As the ion energy decreases, the maximum oscillation amplitude declines as well, resulting in an ion ensemble which is eventually centered in the ion trap. In addition to enabling effective storage of injected ions, collisional cooling of stored ions also improves mass resolution, as it reduces the spatial ion spread along the ejection axis [106, 108].

Resonant dipolar excitation is utilized in modern QIT mass spectrometers for manipulation of the stored ion ensemble, i.e., ion isolation, excitation and ejection<sup>8</sup>. An auxiliary RF voltage is applied between the cap electrodes for either single-frequency<sup>9</sup>, narrow- or broadband excitation. Multiple-frequency excitation can be achieved with the SWIFT (stored waveform inverse Fourier transform) excitation technique [111, 112], that was adapted from Fourier transform ion cyclotron resonance (FTICR) MS and nuclear magnetic resonance (NMR) spectroscopy. The excitation voltage is in resonance with the axial secular oscillation frequencies of ions

---

<sup>7</sup> Different approaches for storing externally generated ions in a QIT were studied (e.g., [103–105]), most of which were theoretical considerations, but none was successfully applied in a commercial instrument.

<sup>8</sup> Initially, mass selective ejection was achieved by an instability scan, i.e., ejection at the LMCO by ramping the RF amplitude [106].

<sup>9</sup> The actual secular frequencies may differ from the values obtained with eq. (3-10), e.g., due to field imperfections or space charge. Different techniques were developed to compensate for these adverse effects [109, 110].

inside the trap, resulting in swift energy transfer into the axial motion, leading to an increase of its amplitude. From eq. (3-12) it follows that the attainable kinetic energy of stored ions in a QIT is proportional to the RF voltage. The attainable internal energy is therefore also proportional to the RF voltage, since it depends on the energy of inelastic collisions with the buffer gas and thus the ion kinetic energy [113]; increasing the RF voltage during resonant excitation allows for larger excitation amplitudes, resulting in stronger activation. This in turn also increases the LMCO (eq. (3-7)), which may result in instability and ejection of fragment ions and has to be considered in the layout and interpretation of fragmentation experiments.

## 3.2 Experimental and instrumentation

The kinetic energy distribution of ions can be measured by applying a potential barrier between consecutive ion optical elements. Ions with a sufficiently low axial kinetic energy cannot overcome this barrier and are removed from the detected ion signal. When the barrier height is gradually incremented, the KED of the ions can be calculated from the ion intensity progression. The implementation of this method in Bruker ion trap mass spectrometers and associated experiments are described in this section.

### 3.2.1 Bruker mass spectrometers

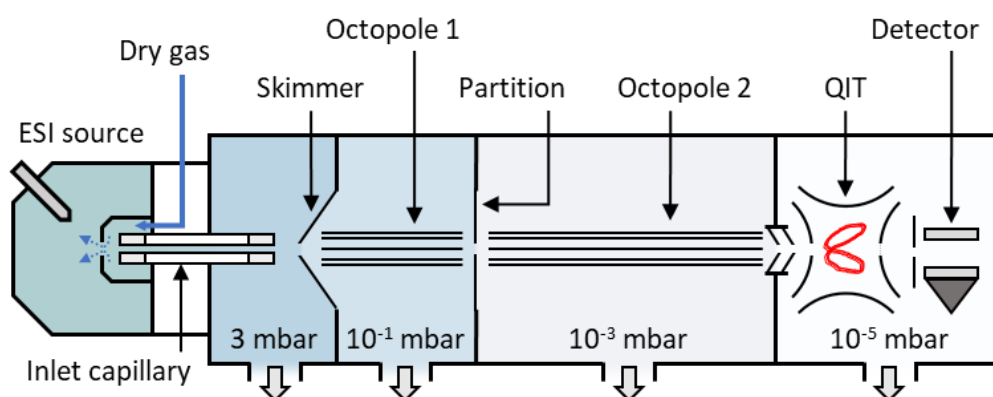
The experiments are performed with Bruker HCTplus and amaZon ion trap mass spectrometers, equipped with the Bruker Apollo ESI source, and a Bruker micrO-TOF time-of-flight mass spectrometer equipped with a custom-built nano-electrospray ionization (nESI) source. The Bruker DataAnalysis 4.1 software is used for qualitative evaluation and export of selected data. Further analysis and visualization are performed with Python scripts.

#### *Bruker HCTplus ion trap*

The HCTplus is based on a four-stage differentially pumped vacuum system. A schematic overview of the instrument layout is given in Figure 4. The gas intake through the glass inlet capillary (18 cm length, 0.5 mm i.d.) is 0.9 L/min. The first vacuum stage is pumped by a rotary vane pump and the resulting background pressure is about 3.6 mbar. A skimmer is positioned coaxially with the inlet capillary for ion sampling into the second vacuum stage. Ions are further transported via two consecutive octopole ion guides, operating in the range of  $10^{-2}$ - $10^{-1}$  mbar and  $10^{-2}$ - $10^{-3}$  mbar [114], respectively. Ions are focused into the ion trap via an

**Table 1:** HCTplus standard ion source and transfer stage settings

Ion source	Capillary high voltage	-4500 V
	Spray shield offset	-500 V
	Dry gas flow	1.5 L/min
	Dry gas temperature	180 °C
	Nebulizer pressure	500 mbar
Transfer stage	Capillary exit	111.9 V
	Skimmer	40.0 V
	Octopole 1 DC	12.0 V
	Octopole partition	6.8 V
	Octopole 2 DC	1.7 V
	Lens 1	-5.0 V
	Lens 2	-60.0 V

**Figure 4:** Schematic of the Bruker HCTplus instrument with attached Apollo ESI source.

electrostatic lens array at the transfer stage exit. The background pressure in the analyzer recipient is around  $10^{-5}$  mbar. The standard settings for the ion source and ion transfer stage (smart parameter setting, SPS) used in most experiments, unless stated otherwise, are listed in Table 1.

#### *Ion current measurements*

For measuring absolute ion currents, the complete ion trap assembly of the HCTplus instrument is replaced by an aluminum Faraday cup electrode. The cup is mounted onto an electrically insulated fixture and positioned directly in front of the ion transfer exit lens at a distance of 3 mm. The diameter of the cup electrode (18 mm) is significantly larger than the exit lens diameter (1.5 mm), ensuring that all ions are efficiently collected. Ion currents are recorded with a 610C Solid State

Electrometer (Keithley Instruments, Inc., Ohio, USA). The analog output of the electrometer is connected to the input of a Voltcraft VC870 digital multimeter (Conrad Electronic SE, Hirschau, Germany). Data from the multimeter are transferred to a computer with a USB interface. The Voltcraft VC870 Interface Program 4.2.1 is used for data logging.

In normal ion trap operation, the potentials of the capillary exit, skimmer, lens 1 and lens 2 are switched during mass analysis to prevent ions from entering the ion trap. This potential change is picked up by the Faraday cup and periodically disturbs the ion current signal. Setting the ion accumulation time of the instrument, i.e., the time between these potential jumps, to the largest possible value of 50 s, allowed the ion current to stabilize within this time. The actual ion current is determined in the data post-processing stage, where the recorded signal is cut into segments, which are then assigned to the respective ion transfer stage settings during an experiment. The spikes in the recorded signal are used for automated segment recognition. A threshold value is manually defined for detecting the spikes in the differential ion current  $\Delta I$  (cf. Figure 5, bottom left). The mean ion current is calculated from the last 15 values preceding the positive spike in each segment (cf. Figure 5, right).

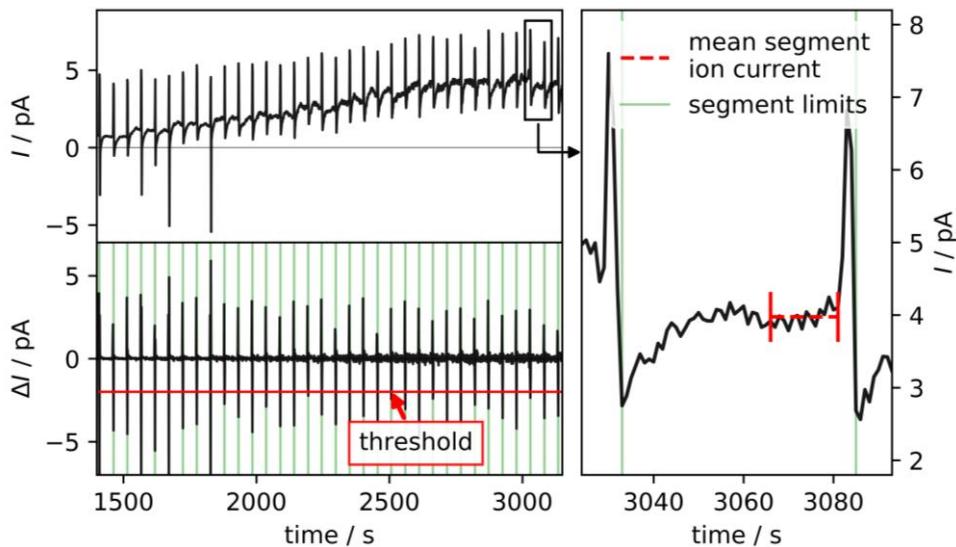


**Figure 5:** Exemplary excerpt of a temporal evolution of the ion current  $I$  during a DPS experiment (top left) and the differential ion current  $\Delta I$  used for segment recognition (bottom left).

*Bruker amaZon ion traps*

The amaZon ETD and amaZon Speed ETD instruments utilize a dual ion funnel inlet stage replacing the skimmer used in the HCT instrument for ion sampling. A schematic overview of the instruments' layout is given in Figure 6 and the standard ion source and transfer stage DC potentials are listed in Table 2. The inlet capillary (18 cm length, 0.6 mm i.d.) is aligned off-axis to the ion transfer stage to reduce transport of larger neutral aggregates into the downstream part of the instrument. The gas inflow is 1.3 L/min. The first ion funnel is operated at 3.6 mbar and has a large entrance diameter of 3.5 cm for efficient sampling from a large volume. The RF voltage applied to the funnel electrodes establishes a radial trapping field. A DC gradient accelerates ions towards the funnel exit and into the second funnel, which is smaller in diameter and length and operates at about 0.1 mbar. Downstream of the second funnel, ions are further transported via an octopole, which is split in the center for applying an additional axial acceleration voltage. The background pressure in this region is at  $10^{-4}$  mbar. The ion beam is focused by an electrostatic lens array into the analyzer chamber, where the pressure drops to  $10^{-5}$  mbar. A short multipole and a further subsequent lens array are used for transferring the ion beam into the ion trap.

**Table 2:** amaZon ETD/amazon speed ETD standard ion source and transfer stage settings

Ion source	Capillary high voltage	-4500 V
	Spray shield offset	-500 V
	Dry gas flow	4 L/min
	Dry gas temperature	180 °C
	Nebulizer pressure	500 mbar
Transfer stage	Capillary exit	140.0 V
	Funnel 1 in/out/lens	100.0/35.0/25.0 V
	Funnel 2 in/out/lens	12.0/10.0/3.3 V
	Octopole 1/partition/2	2.3/1.7/1.1 V
	Focus 1 lens 1/2/3	0.5/-20.0/-6.0 V
	Multipole lens/DC	-6.0/-4.0 V
	Focus 4 lens 1/2/3	-4.0/-5.0/-75.0 V

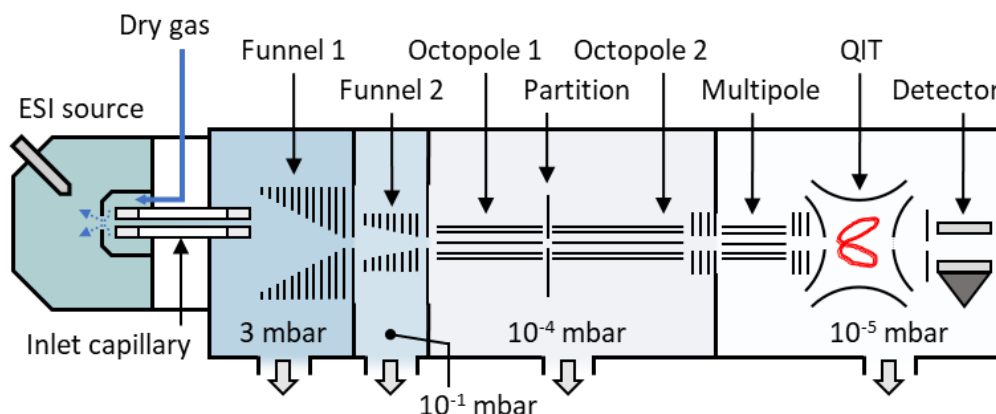


**Figure 6:** Schematic of the Bruker amaZon instrument with attached Apollo ESI source.

### *Bruker micrOTOF*

In the experiments with the Bruker micrOTOF time-of-flight (TOF) mass spectrometer a custom nano-electrospray ionization (nESI) source is used in positive mode. Variable mixing ratios of solvent vapor can be added to the matrix gas of the ion source. A schematic overview of the instrument layout is given in Figure 7. The experimental setup is described in [59]. The ion source is connected to the differentially pumped vacuum system of the mass spectrometer with a glass capillary (18 cm length, 0.5 mm i.d.). A skimmer is positioned on-axis downstream of the capillary exit for ion sampling into the second vacuum chamber, comparable to the HCTplus ion trap setup (cf. Figure 4). The ions are transported further by two hexa-

**Table 3:** micrOTOF standard ion source and transfer stage settings

Ion source	Gas flow	800 mL/min
	Liquid flow	300 nL/min
	nESI voltage	1200-1800 V
Transfer stage	Capillary exit	50.0 V
	Skimmer 1	35.0 V
	Hexapole 1	28.5 V
	Skimmer 2	23.9 V
	Hexapole 2	22.2 V
	Hexapole RF	600.0 V
	Lens transfer time	50.0 $\mu$ s
	Lens pre-pulse storage	4.0 $\mu$ s
	Lens 1 storage/extraction	30.0/21.3 V
	Lens 2/3/4/5	9.0/-20.0/0.0/-27.5 V

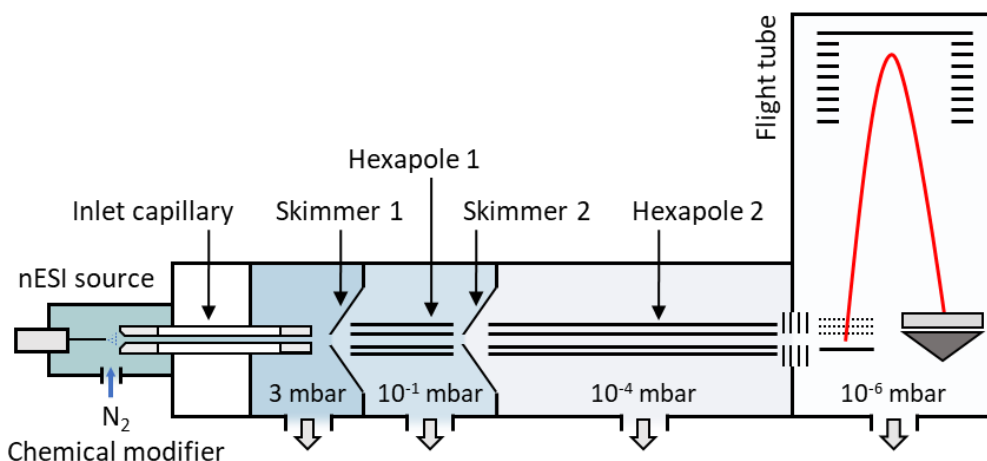


**Figure 7:** Schematic of the Bruker micrOTOF instrument with attached custom nESI source.

pole ion guides, which are separated by another skimmer. Downstream of the second hexapole, ions are focused by an electrostatic lens into the orthogonal acceleration stage. The ion transfer voltages are summarized in Table 3.

### 3.2.2 Chemicals

All chemicals were purchased from Sigma-Aldrich Chemie GmbH (Munich, Germany) and were used without further purification. HPLC grade solvents and Millipore water were used for preparation of analyte solutions, all other substances were purchased with the highest available purity. For analysis all analytes were diluted in a blank solution of acetonitrile/water (1/1) with 0.1% formic acid added, unless stated otherwise.

#### *Synthesis of benzylpyridinium salts*

Different benzylpyridinium salts were prepared by stirring the respective benzyl bromide derivative with an equimolar amount of pyridine in acetonitrile (HPLC grade) for 15-30 minutes at room temperature. After filtration, the obtained white powder was washed with diethyl ether, dried and then stored at -26 °C until use.

## 3.3 Kinetic measurement methods

The response of the ion population to changes of instrument parameters in the ion transfer stage is studied in this work. Changes of transfer voltages have a direct impact on the electric acceleration and thus the kinetic energy of ions in the considered region. Therefore, the corresponding methods are bundled under the term *kinetic measurement methods*.

### 3.3.1 Potential barrier method

The KED of the ion beam exiting the ion transfer stage of an API ion trap mass spectrometer is determined by applying a variable deceleration potential  $U_d$  between the transfer stage exit and the ion trap entrance electrode. Essentially collision-free conditions are assumed in this region, so that the applied potential directly corresponds to a change of the ion kinetic energy, according to eq. (3-1). The change of the ion signal intensity  $I$  with increasing  $U_d$  is proportional to the number of ions with a kinetic energy that is insufficient to overcome the potential barrier. Thus, a deceleration potential scan (DPS) yields the integral signal intensity  $I(U_d)$  of all ions with a sufficiently high kinetic energy in dependence of the applied deceleration potential  $U_d$ , and is referred to as *deceleration potential response* (DPR) in this work. The derivative of the DPR corresponds to the probability distribution function  $P(E_{\text{kin}})$  of the ions, which is referred to as KED in the following:

$$\text{KED} \equiv P(E_{\text{kin}}) = \frac{dI(U_d)}{dU_d}. \quad (3-1)$$

The diagram shown in Figure 8 depicts the workflow for obtaining the KED from experimental data.

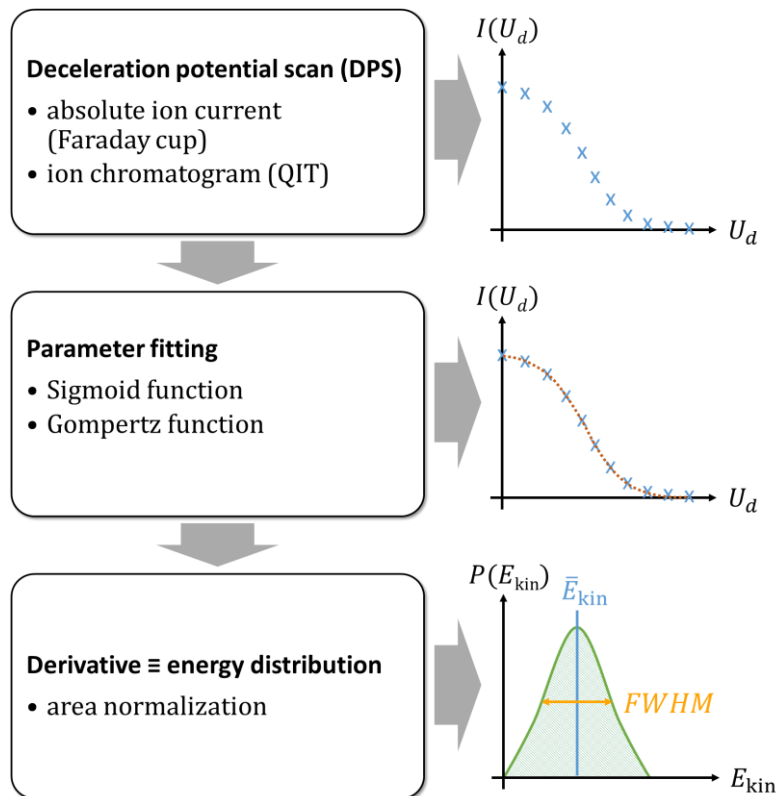


**Figure 8:** Workflow for obtaining KEDs from experimental data.

The DPR can be obtained as the ion current measured with a Faraday cup and electrometer or the ion intensity obtained from mass spectra recorded with the ion trap. The latter allows evaluation of mass-resolved KEDs. The normalized DPR curve is fitted with an appropriate fitting function. Data fitting is performed with the `scipy.optimize.curve_fit` method from the SciPy package [26]. The sigmoid function  $S(x)$  (3-2) is symmetric around the inflection point, whereas the Gompertz function [115]  $G(x)$  (3-4) is asymmetric, resulting in symmetric or asymmetric KED curves ( $S'(x)$  (3-3) or  $G'(x)$  (3-5)), respectively.

$$S(x) = \frac{1}{1 + e^{\frac{x-a}{b}}} \quad (3-2)$$

$$S'(x) = -\frac{e^{\frac{x+a}{b}}}{b \left( e^{\left(\frac{a}{b}\right)} + e^{\left(\frac{x}{b}\right)} \right)^2} \quad (3-3)$$

$$G(x) = 1 - e^{-a \cdot e^{-b \cdot (x-c)}} \quad (3-4)$$

$$G'(x) = -a \cdot b \cdot e^{-a \cdot e^{-b \cdot (x-c)} - (b \cdot (x-c))} \quad (3-5)$$

The deceleration potential is applied between the ion transfer stage exit and the ion trap entrance. To accomplish that, the potential of the entire transfer stage is decreased relative to the standard setting, i.e., the potential of each ion optical element is changed by the same value. In this way, the DC gradient and thus the ion transmission through the transfer stage remains unaffected. The entrance cap electrode of the ion trap and the Faraday cup are always held at ground potential.

The DPS is automated via acquisition segments in the Bruker ion trap control software. In the first segment the standard settings are applied. In the following segments, the deceleration potential is ramped from the highest value to the standard settings again. By comparison of the first and last segment the data can be checked for intensity drifts. Segments are usually 1 min in duration. The data of each segment are averaged and assigned to the deceleration potentials in the post-processing routine.

### 3.3.2 Survival yield method

The survival yield method is used for determination of internal energy distributions of ions in a mass spectrometer (cf. section 3.1.3). This is done by exciting a series of ions with known critical energies of fragmentation, e.g., by collisional activation in the ion transfer stage or in collision cells. From the signal intensities of the precursor ( $I_M$ ) and fragment ions ( $I_{F,i}$ ) the survival yield  $SY$  is calculated:

$$SY = \frac{I_M}{I_M + \sum_i I_{F,i}}. \quad (3-6)$$

An exemplary survival yield analysis is shown in Figure 9. The SY for each ion is calculated from the intensities at different activation levels, e.g., acceleration voltages in a collision cell. The values at a selected activation level, preferably where the SY values are evenly distributed between zero and one, are then plotted against the ions' respective fragmentation energies  $E_0$ . Two additional points are added to this set of data, based on the following assumptions:

- 1) A fragmentation energy of the molecules of zero will always lead to complete dissociation ( $SY(E_0=0) = 0$ ).
- 2) No dissociation will occur when the fragmentation energy is significantly larger than that of the most stable ion used in the experiment ( $SY(E_0 \gg E_{0,max}) = 1$ ).

The resulting curve corresponds to the integral of the internal energy distribution. The internal energy distribution  $P(E_0)$  is obtained by per-interval differentiation or data fitting with a sigmoid function and subsequent differentiation.

The compounds used in survival yield experiments must have different fragmentation energies, but also the same internal energy distribution and thus the same molecular structure, which are two contradicting requirements. As an approximation, compounds with similar molecular structures, such as derivatives of

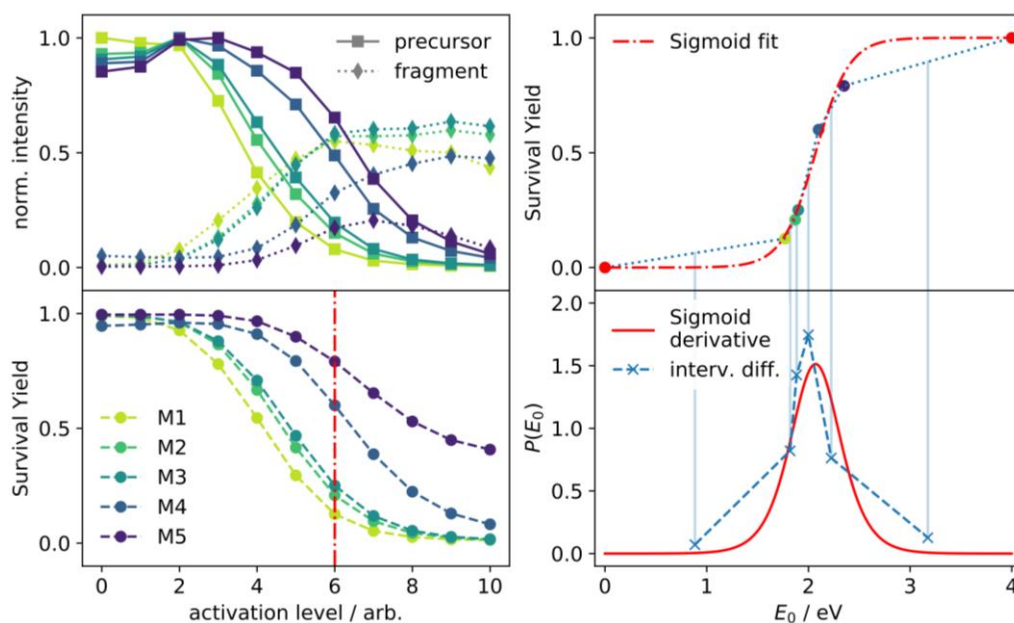


**Figure 9:** Survival yield analysis example; left: precursor and fragment ion intensities (top) and respective SY (bottom) in dependence of the activation level for five substances M1-M5 with different fragmentation energies  $E_0$ ; right: SY in dependence of  $E_0$  with sigmoid fit (top); energy distribution obtained from the data fit and from interval-wise differentiation (bottom).

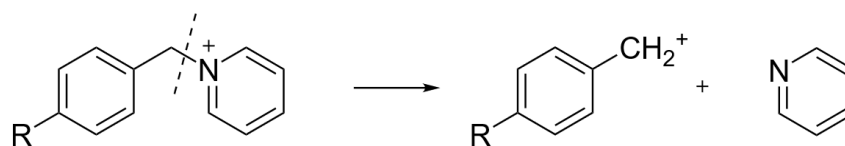


**Figure 10:** Fragmentation scheme for benzylpyridinium ions.

the same compound class, are used. An example for such a class are benzylpyridinium (BP) salts, which are well characterized with regards to their fragmentation energy [116–118] and were already widely used in survival yield studies [65, 119, 120]. The typical fragmentation reaction of these compounds is depicted in Figure 10. The fragment ion carries the variable substituent R, so that multiple benzylpyridinium derivatives can be analyzed simultaneously in a mass spectrometric analysis. Benzylpyridinium salts used in this work were synthesized in-house, the procedure is described in section 3.2.2. Table 4 summarizes the ion properties.

**Table 4:** Precursor and fragment  $m/z$  and critical energies of benzylpyridinium ions

Substance	ID	Precursor $m/z$	Fragment $m/z$	$E_0$ (eV)[64]
<i>p</i> -Cl BP	BP1	204	125	1.90
<i>p</i> -CN BP	BP2	195	116	2.10
<i>p</i> -F BP	BP3	188	109	1.87
<i>p</i> -CH <sub>3</sub> BP	BP4	184	105	1.77
<i>p</i> -NO <sub>2</sub> BP	BP5	215	136	2.35

## 3.4 Numerical models

The gas dynamics in the transfer stage is evaluated with DSMC simulations with the open-source simulation program SPARTA. Ion trajectory simulations for modeling of kinetic energy distributions are conducted with SIMION 8.1 (cf. section 2.2).

### 3.4.1 Gas simulations

The pressure distribution within the ion transfer stage of an API mass spectrometer has a strong impact on the ion kinetic energy evolution. Collisions with the background gas damp the ion motion, which is compensated for by accelerating ions electrically. Prior to entering the mass analyzer, ions have to transition from

the collision-dominated ion source region into the high vacuum compartment of the instrument, where collision-free conditions prevail. The pressure and electric field distribution in the transition regime determines the shape of the ions' KED. As soon as collision-free conditions are reached, the change of the ion kinetic energy can be directly inferred from the change of the electric potential.

The SPARTA DSMC program (cf. section 2.3) is used for modeling the pressure inside the second octopole of the HCTplus instrument (cf. section 3.2.1, *Bruker HCTplus ion trap*). Three-dimensional simulations have very high computational demand due to the size of the entire geometry. Therefore, two-dimensional axisymmetric simulations are performed to reduce computation time. For this purpose, the 3D model of the stage was converted to an equivalent 2D structure with appropriate dimensions. A comparison of the real and the adapted geometry is shown in Figure 11. The octopole ion guides do not exhibit rotational symmetry and were replaced by a set of stacked rings. The width of the rings equals the width of the octopole rods and the distance between two neighboring rings equals the inter-rod-distance in the octopoles. With these dimensions, the ratio of open to closed surfaces and the critical length of the real octopole structure are mimicked and thus the gas conductance of the structure is retained. The real geometry includes both octopoles, the octopole mounts, the octopole partition orifice, and the exit lenses. In the simulation model, the exit lenses are represented by a single orifice which separates octopole 2 from the analyzer recipient. The size of the octopole 2 chamber is 164.65×65.00 mm in the simulation, which resembles the actual vacuum recipient dimensions. The boundary conditions for the simulation box are given in Table 5. The lower and upper boundaries of the simulation box are named *xlo* and *xhi* for the *x* axis and *ylo* and *yhi* for the *y* axis, respectively.

**Table 5:** Boundary parameters for the octopole DSMC simulations

<i>xlo</i>	surface boundary, surface collision model: <code>vanish</code> , particle emission: <code>emit/face/file</code> (inlet: 0.36 mbar, 298 K, turbo pump 2 (in): 0.019 mbar, 298 K)
<i>xhi</i>	outflow boundary, particle emission: <code>emit/face subsonic</code> (outlet: 10 <sup>-5</sup> mbar, 298 K)
<i>ylo</i>	axis of symmetry
<i>yhi</i>	outflow boundary, particle emission: <code>emit/face subsonic</code> (turbo pump 1 (out): 10 <sup>-5</sup> mbar, 298 K)

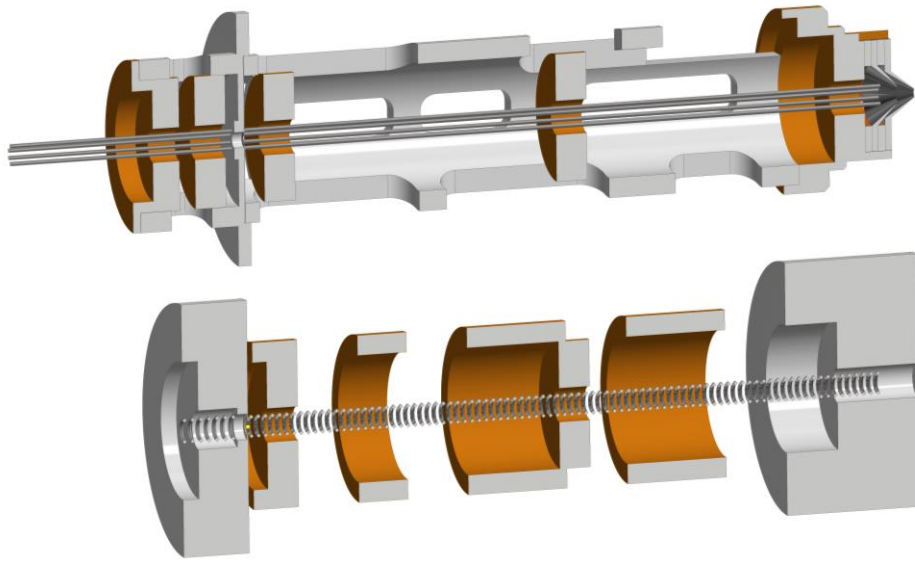


**Figure 11:** Half section views of the real octopole 3D model (top) and the 3D representation of the axisymmetric geometry used for SPARTA simulations (bottom).

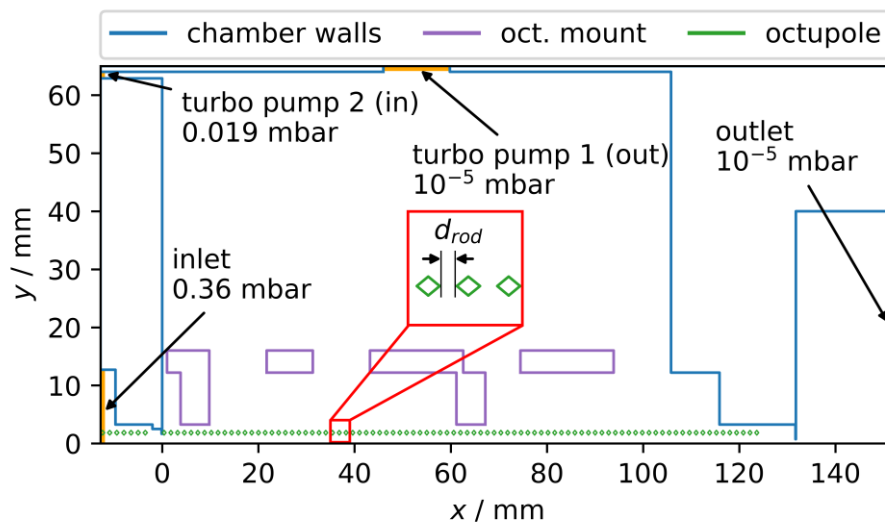


**Figure 12:** Octopole SPARTA model. Blue, purple and green lines represent the geometry surfaces. The orange lines indicate outflow boundaries with subsonic conditions at the stated pressures.

Four different particle emission regions are defined in the simulation as highlighted in Figure 12. The *inlet* represents the region in the vacuum chamber containing octopole 1. The pressures in the two octopole chambers of 0.36 mbar and 0.019 mbar, respectively, were determined in the real instrument with a TPR 280 Pirani gauge (Pfeiffer Vacuum GmbH, Asslar, Germany). The octopoles are separated by an aperture with a diameter of 2.3 mm. The octopole 2 chamber is con-

ected to the ion trap chamber by an orifice with 1.5 mm diameter, which represents the exit lens of the transfer stage. The *outlet* region at the right boundary is set to a pressure of  $10^{-5}$  mbar, which is the approximate pressure in the real ion trap recipient. Additional particle emission regions represent the turbo pump attached to the octopole 2 chamber (*turbo pump 1 (out)*) and the exhaust of the second turbo pump (*turbo pump 2 (in)*), which is connected to the octopole 2 chamber. The pressure for *turbo pump 1 (out)* is estimated to  $10^{-5}$  mbar and the pressure for *turbo pump 2 (in)* is set to the measured value of 0.019 mbar in this region. The simulation geometry consists of three groups (cf. Figure 12). The chamber walls (blue lines) give the rough outline of the vacuum chamber. The octopole mount (purple lines) consists of several parts, whose dimensions are chosen so that the opening areas resemble the real geometry. The octopole itself (green lines) cannot be represented properly in a 2D axisymmetric model. Instead, the rods are approximated by rings with a square profile. The ring dimensions resemble the rod dimensions. The inner diameter is 2.9 mm, the width is 0.8 mm and the distance between two rings  $d_{rod}$  is 0.6 mm. For all surfaces the *specular* collision model is used. All temperatures are set to 298 K. Nitrogen is used as gas species, since the mass spectrometer inlet is constantly flushed with an excess flow of nitrogen during the experiments.

### 3.4.2 Ion trajectory simulations

The trajectory simulations are conducted with SIMION 8.1. Individual models are used for the ion transfer stage and the ion trap simulations.

#### *Ion transfer stage model*

Ion trajectory simulations for the ion transfer stage of the HCTplus instrument are performed to model the collisional broadening of the KED. The simulation geometry (cf. Figure 13) is adapted from the 3D CAD model of the ion transfer stage and

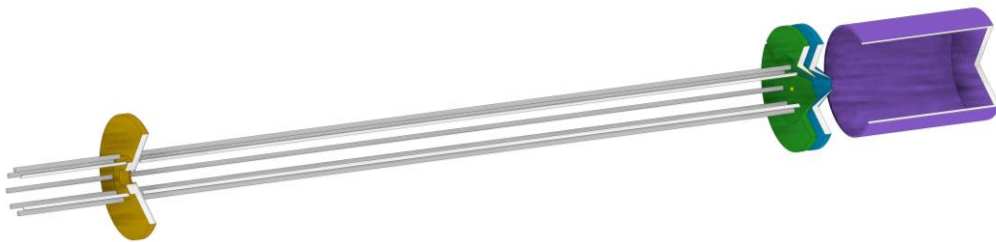


**Figure 13:** Three-quarter section view of the transfer-stage model used for SIMION simulations; electrodes (from left to right): octopole 1 rods, octopole partition (orange), octopole 2 rods, two focusing lenses (green and blue) and cup electrode (purple).

**Table 6:** Electrode potentials in the transfer stage ion trajectory simulations

Octopole 1 DC	12 V
Octopole partition	6.8 V
Octopole 2 DC	1.7 V
Focusing lens 1	-5.0 V
Focusing lens 2	-60.0 V
Cup electrode	0.0 V

contains the octopole 1 and octopole 2 rods, the octopole partition orifice, the focusing lenses and the cup electrode. The electrode potentials are defined according to the values used in the experiments and are listed in Table 6.

The RF voltage applied to the octopole rods has a frequency of 3 MHz and an amplitude of 75 V. Variable electrode potentials are set in the `fast_adjust` segment in the SIMION user program. The RF voltages of neighboring rods are phase-shifted by 180°. Ions are started in a circular area ( $r = 0.5$  mm) in the center of the first octopole. The initial kinetic energy is set according to a Maxwell-Boltzmann distribution (MBD) ( $T = 298$  K) with random direction. Additional parameters for individual simulations are given in the results section. Interactions of ions with the neutral background gas are modeled as hard sphere collisions with the HS1 collision model. The background gas mass is set to 28 Da ( $N_2$ ) and the collision cross section is set according to the ion  $m/z$  (cf. section 3.7.2). The position-dependent pressures and gas velocities are evaluated from DSMC simulations and are calculated in the `other_actions` segment of the SIMION user program, prior to execution of the HS1 code.

#### *Quadrupole ion trap model*

The ion trap geometry is adapted from the SIMION *pseudopotential* example. The ring electrode radius is 10.0 mm and the cap electrode distance is 14.2 mm. Holes in the cap electrodes with a diameter of 1.6 mm and a conic injection electrode with a tip diameter of 1.6 mm are added. The distance between the injection electrode tip and the cap electrode entrance hole is 1.1 mm. The geometry is shown in Figure 14.

For modeling of a DPS experiment multiple simulations with different injection electrode potentials are performed. The cap electrode potentials are set to 0 V. The RF voltage with a frequency 1 MHz at the ring electrode is realized via the `fast_adjust` segment in the SIMION user program. The respective RF amplitudes of individual simulations are given in the results section. The HS1 collision model

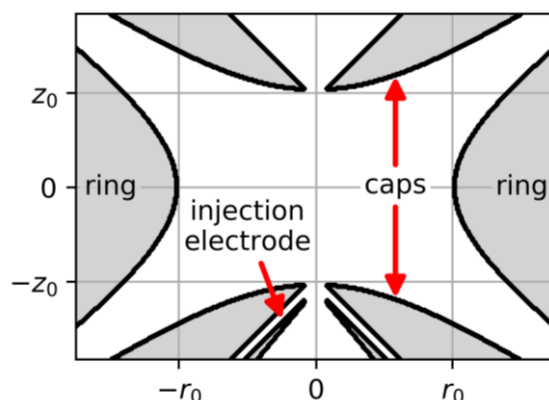


**Figure 14:** Half section view of the ion trap geometry used for modeling of the DPS experiments in SIMION.

is used, with a pressure of  $3 \cdot 10^{-3}$  mbar and a gas mass of 4 Da (helium), resembling the conditions inside the real ion trap. Ions are started evenly distributed in a circular area ( $r = 0.2$  mm) at the lower boundary of the simulation box, in the center of the injection electrode. The initial kinetic energy in  $z$  direction is set according to a Gaussian distribution with a mean of 2.5 eV and a FWHM of 1 eV. The time of birth (TOB) is uniformly distributed over a full RF cycle, i.e., from 0 to 1  $\mu$ s. The number of trapped ions after 1 ms is evaluated as ion intensity for the DPR curve.

### 3.5 KEDs in the Bruker HCTplus

Kinetic energy distributions are experimentally determined from absolute ion current and ion trap measurements with the HCTplus ion trap mass spectrometer. Initial experiments are carried out with a solution of sodium formate (1.5  $\mu$ mol/L) in acetonitrile/water (1/1) with 0.1% formic acid. A representative mass spectrum, recorded prior to KED runs with the ion trap at otherwise identical settings and conditions, is shown in Figure 15. The spectrum exhibits signals of sodium formate clusters ( $[(\text{HCOONa})_n + \text{Na}]^+$ ,  $n = 2, 3, 5, 6^{10}$ ), background phthalate species, and other, unidentified background ions, which may have formed by ion-neutral reactions in the ion source or transfer stage.

For the DPS experiments the relative potential shift  $\Delta U$  of the transfer stage is changed in steps of -0.5 V to a final value of -10 V. The negative value of  $\Delta U$  corresponds to the deceleration potential  $U_d$ . Consequently, the deceleration potential range is 0 – 10 V. The acceleration voltage between the transfer stage and the cup

---

<sup>10</sup> The absence of the cluster with  $n = 4$  is attributed to fragmentation during the trap injection process [121].

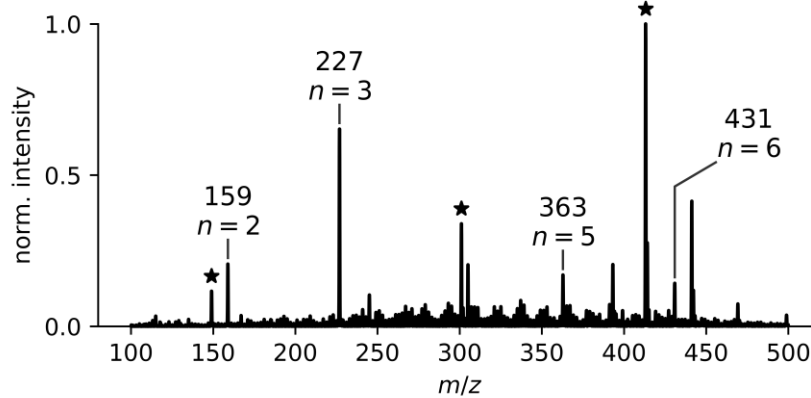


**Figure 15:** Ion trap mass spectrum of the sodium formate solution showing  $[(\text{HCOONa})_n + \text{Na}]^+$  clusters ( $n = 2, 3, 5, 6$ ) and background ions. The peaks labeled with a star can be assigned to phthalate background ions ( $m/z$  149: protonated phthalic anhydride,  $m/z$  301: dibutyl phthalate ( $\text{Na}^+$  adduct),  $m/z$  413: diisooctyl phthalate ( $\text{Na}^+$  adduct)).

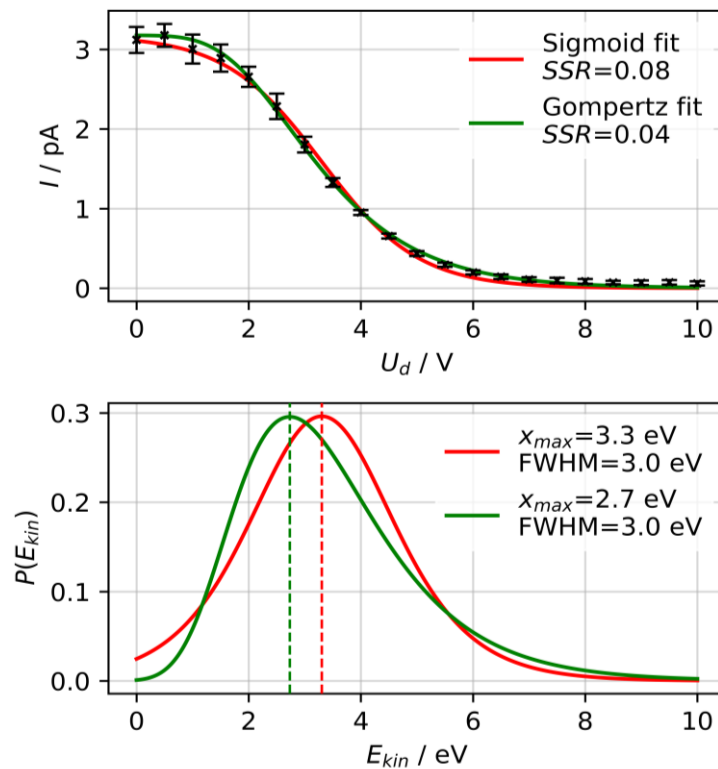


**Figure 16:** Acceleration-voltage-dependent ion current from a DPS experiment with two fitting models (top) and the resulting energy distributions (bottom).

electrode is thereby effectively decreased from 1.7 V to -8.3 V. The results of the experiment are shown in Figure 16. The maximum ion current is in the range of 3 pA and is obtained, as expected, when no deceleration potential is applied. Since the standard acceleration voltage is 1.7 V, ions arriving at the detector electrode

have at least 1.7 eV kinetic energy, assuming collision-free conditions. That is reflected in the detected ion current progression, which starts decreasing at a deceleration potential in the range between 1 and 2 V. This trend is also well reproduced using the Gompertz fit, which gives overall slightly better results than the sigmoid fit, when inspecting the sum of squared residuals (*SSR*, cf. Figure 16 top). The corresponding KED has a maximum at 2.7 eV and a full width at half maximum (FWHM) of 2.9 eV. The shape of the KED has some implications: The total change of electric potential that the ions experience between entering the mass spectrometer and arriving at cup electrode is 111.9 V. The ions reaching the cup electrode have a significantly lower kinetic energy, between approximately 1 and 8 eV. Kinetic energy is lost within the ion transfer stage due to collisions with neutrals. The acceleration voltage between the two octopoles is 10.3 V. Hence, most ions still undergo several collisions inside the second octopole.

The experiment is repeated with the ion trap installed. The total ion chromatogram (TIC) yields the DPR for the complete ion population. Mass-resolved curves can be obtained from extracted ion chromatograms (EICs). Figure 17 shows the DPR of sodium formate clusters present in the mass spectrum in Figure 15. The curve obtained from the TIC is shifted by approximately 0.4 V compared to the cup electrode measurement. This may be a result of the electric potential distribution along the ion pathway. The field is weaker in the center of the holes in the electrodes than at the electrode surface. As a result, the effective potential barrier height is lower than the potential difference between the electrodes leading to a higher mean kinetic energy observed with the ion trap. With the cup electrode, the potential barrier is directly applied at the sensing electrode, therefore the ions experience the actual barrier voltage.

The DPR traces from extracted ion chromatograms show different shifts relative to the TIC. The EIC traces of sodium formate clusters are shifted to larger deceleration potentials. Since the TIC is comprised of all present ions, the DPR of other ions must be shifted to lower potentials and this is the case for the detected phthalate background ions present in the spectra (cf. Figure 15). The DPR curves of different compound classes, e.g., sodium formate clusters and phthalate ions, are grouped in different regions. This may be a hint for the DPR being linked to the *ion formation process*, which is potentially different for sodium formate clusters and phthalate ions. Even though the curves of individual ions of one compound group are slightly shifted, there are no systematic correlations between the curve shift and properties of the corresponding ions, e.g., mass-to-charge ratio or size. A shared feature of the traces from ion chromatograms that differs from the ion

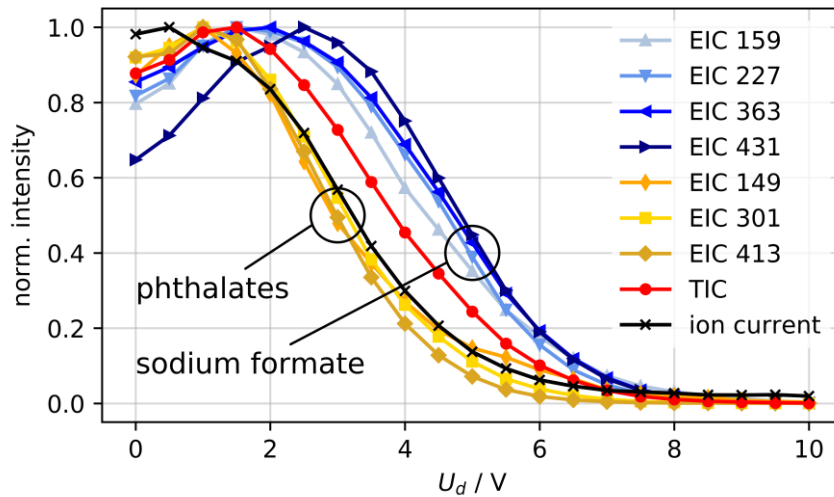


**Figure 17:** Normalized DPS results from the TIC, EICs of sodium formate clusters and phthalate ions, and the ion current measured with the cup electrode. Error bars are not shown for clarity.

current measurement is the decreasing intensity towards 0 V. Instead of reaching a plateau at low deceleration potentials, the traces have maxima around  $U_d = 2$  V and decrease towards 0 V. This progression cannot be explained solely with the potential barrier interaction. When the potential barrier is lowered, the signal intensity can only increase or remain constant since the integral ion current is measured. Decreasing intensity must be a result of ion losses downstream of the potential barrier and, i.e., in the ion trap. The ion injection and storage in the trap does apparently introduce another, kinetic-energy-dependent effect in the experiments, because the ion kinetic energy is the only varied parameter during the DPS. This suggests that the actual KED cannot be directly obtained from the ion trap data. However, *changes* of the KED should be clearly discernible with the method.

### 3.6 Characterization of the DPS method

The initial ion trap experiments indicate that the shape of the DPR depends on the ion type. The decreasing intensity towards  $U_d = 0$  V suggests that the ion trap parameters, particularly the *trap drive*<sup>11</sup>, which determines the operating point of the ion trap, impact on the DPR. For a better understanding of the DPR traces obtained from ion trap data, the dependency on different experimental parameters is evaluated.

<sup>11</sup> The trap drive is the LMCO of the ion trap and is thus proportional to the RF amplitude (cf. eq. (3-7)).

### 3.6.1 Axial acceleration voltages in the ion transfer stage

When acceleration voltages in an upstream part of the ion transfer stage are changed, the DPR should shift accordingly. To systematically investigate this behavior, the acceleration voltages at the entrance of the first, second, and third differential vacuum stage, respectively, are varied. These correspond to the potential differences between the capillary exit and skimmer (1<sup>st</sup> stage), skimmer and octopole 1 (2<sup>nd</sup> stage) and octopole 1 and octopole 2 (3<sup>rd</sup> stage) in the HCTplus (cf. section 3.2.1, *Bruker HCTplus ion trap*), and capillary exit and funnel 1 in (1<sup>st</sup> stage), funnel 1 lens and funnel 2 in (2<sup>nd</sup> stage), and funnel 2 lens and octopole 1 (3<sup>rd</sup> stage) in the amaZon ETD instrument (cf. section 3.2.1, *Bruker amaZon ion traps*). A solution of sodium formate (0.1 mg/L) is used for the HCTplus experiments. The amaZon experiments are performed with a solution of five benzylpyridinium salts (*p*-CH<sub>3</sub>, *p*-F, *p*-CN, *p*-Cl and *p*-NO<sub>2</sub> BP, each in the range of 1 mg/L). The standard acceleration voltages are listed in Table 7.

The potentials of all upstream transfer elements are shifted by the same value to change the respective voltage without changing the DC gradient in the rest of the transfer stage. For example, the capillary exit and skimmer potential are both raised by 5 V to increase the acceleration voltage between the skimmer and octopole 1 by 5 V without affecting the DC gradient in the other region. Exemplary DPS results for the HCTplus ion trap are shown in Figure 18. The experimental results clearly show that the acceleration voltages in the first two vacuum stages have *no* effect on the DPR, regardless of the ion species investigated. This observation has an important consequence: Up to the second vacuum stage, the collision number is high enough for the ion kinetic energy to become completely re-equilibrated with the background gas, i.e., no net energy change is achieved. The re-equilibration must still take place inside octopole 1, since acceleration before octopole 1 does not impact the KED. Since the acceleration voltages are applied only between two consecutive ion transfer elements there is no axial DC gradient inside the octopole. Partial conservation of the gained kinetic energy is only observed downstream of the first octopole, which indicates the transition into collision-free conditions.

**Table 7:** Standard values for entrance voltages in the first three vacuum stages

Instrument	1 <sup>st</sup> stage	2 <sup>nd</sup> stage	3 <sup>rd</sup> stage
HCTplus	71.9 V	28.0 V	10.3 V
amaZon ETD	40.0 V	13.0 V	1.0 V

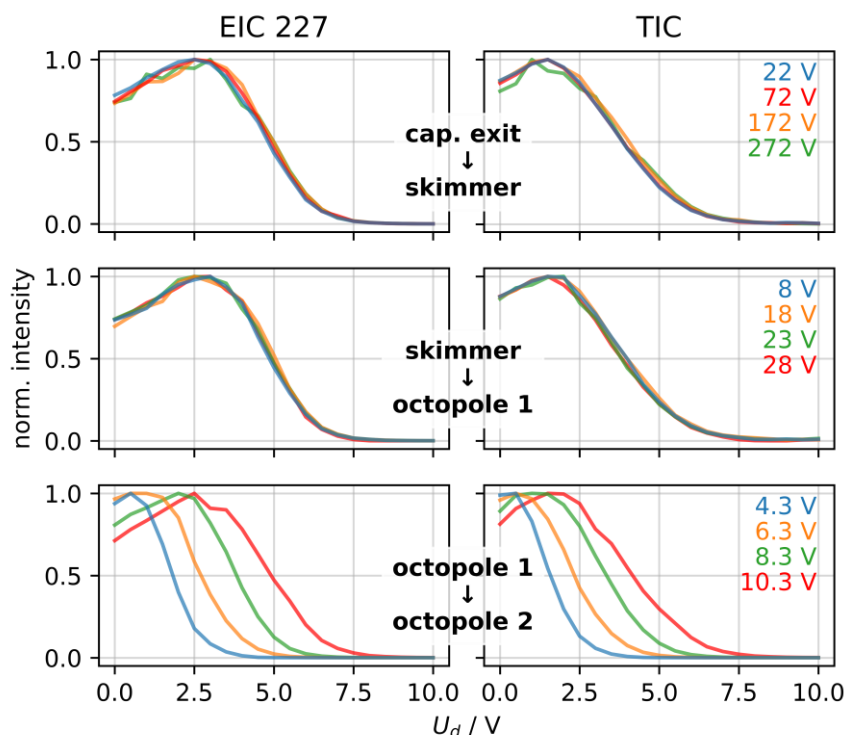


**Figure 18:** Exemplary DPR traces from the EIC of  $[(\text{HCOONa})_3+\text{Na}]^+$  (left) and the TIC (right) recorded with the HCTplus instrument (cf. Figure 4) for different acceleration voltages between the inlet capillary exit and skimmer (top), skimmer and octopole 1 (center) and octopole 1 and octopole 2 (bottom). The red traces are obtained with the standard settings. Each trace is normalized to its maximum value.

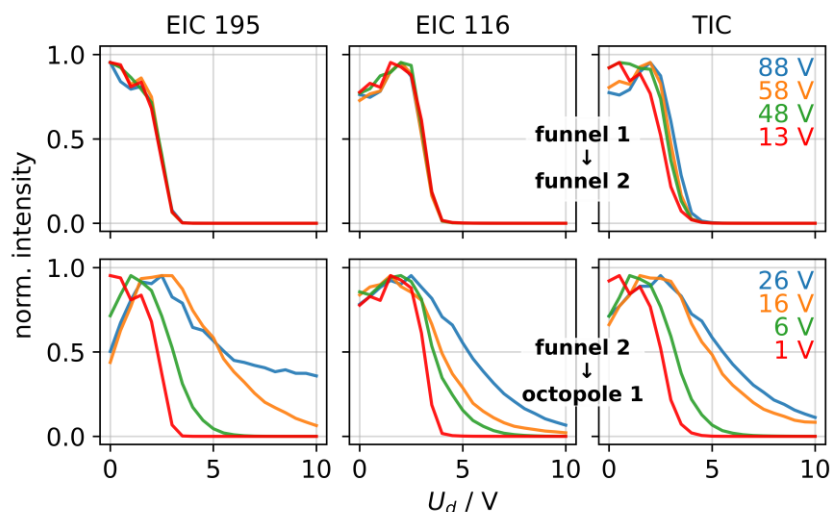


**Figure 19:** DPR traces from EICs of *p*-CN BP ( $m/z$  195) and its fragment ion ( $m/z$  116) and the TIC, recorded with the amaZon ETD instrument (cf. Figure 6) for different acceleration voltages between funnel 1 lens and funnel 2 in (top) and funnel 2 lens and octopole 1 (bottom). The red traces are obtained with the standard settings. Each trace is normalized to its maximum value. Data with variation of the acceleration voltage in the first vacuum stage (between capillary exit and funnel 1) are not available.

The results of the experiments with the amaZon ETD ion trap are shown in Figure 19. In contrast to the HCT experiments, the TIC DPR traces of the amaZon experiments exhibit a shift to higher  $U_d$ , when the acceleration voltage in the second vacuum stage is increased, while the EIC DPR traces remain unchanged regarding shape and position (cf. Figure 19 top). However, the relative intensities of the detected ions change significantly. This is due to fragmentation of BP precursor ions, which sets in as the acceleration voltage is increased. The fragment ions are also detected but contribute to the TIC DPR traces differently than the precursor ions, which changes the shape of the TIC trace. The constant shape of the EIC traces indicate that the kinetic energy is completely re-equilibrated inside the second funnel. The DPR from EICs shift when the acceleration voltage between funnel 2 out and the octopole is increased (cf. Figure 19 bottom). This is a combined result of relative intensity changes due to fragmentation of BP precursor ions and kinetic energy gain, which is partially conserved due to the sufficiently low collision number in the transfer stage downstream of funnel 2.

The HCTplus experiments are repeated with the cup electrode installed to determine energy distributions. The results are shown in Figure 20. The DPR obtained from the absolute ion current measurements are shifted towards lower deceleration potentials compared to the ion trap data (Figure 18 right), but show the same dependencies, i.e., the traces are shifted to lower deceleration potentials when the acceleration voltage between octopole 1 and 2 is decreased. The corresponding KEDs become narrower as the acceleration voltage is lowered. Changing the acceleration voltage from 10.3 to 4.3 V leads to a change of the FWHM from

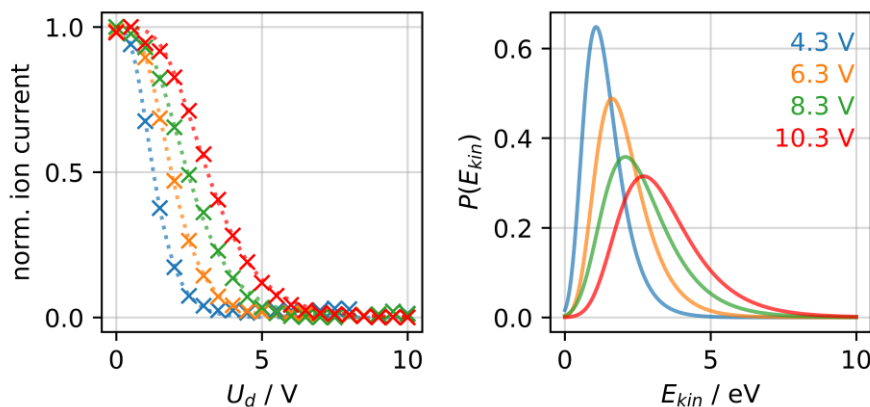


**Figure 20:** DPR with Gompertz fit (dotted lines) from ion current measurements with different acceleration voltages between octopole 1 and octopole 2 (left) and corresponding KEDs (right). The red traces are obtained with the standard settings. Sodium formate is used as analyte in the experiments.

2.9 to 1.3 eV and a shift of the KED's maximum from 2.7 to 1.1 eV. The latter is especially notable, since ions are accelerated with 1.7 V between the transfer stage and the detector with the standard settings ( $U_d = 0$ ). When the deceleration potential is below 1.7 V, ions are still accelerated between octopole 2 and the detector and no ions should be excluded from the ion beam based on their kinetic energy. However, a significant decrease of the signal intensity is observed within this deceleration potential range when the upstream acceleration voltage is lowered (Figure 20, blue and orange traces). This implies that either not all ions are transported through octopole 2 anymore at the decreased acceleration voltage, which would also lead to a reduced ion intensity, or that the assumption of collision-free conditions in the ion transfer exit region does not hold. The latter would result in underestimated ion energies for the ion current measurements. However, changes of the KED are still detectable. Changing the acceleration voltages upstream of octopole 1 has no effect on the KED, as was observed in the ion trap experiments.

### 3.6.2 Comparison of ion trap instruments

The ion trap instruments used for the experiments differ significantly regarding their transfer stage design (cf. section 3.2.1). A comparison of the experimental results clearly shows that this directly impacts on the KED of the exiting ion beam (Figure 21). The ions in the HCTplus exhibit significantly larger kinetic energies, and the KED is broader. The position of the inflection point of the HCTplus TIC curve, which was found to be slightly larger than in the ion current measurements (which portray the actual KED), is shifted more than 2 V compared to the amaZon

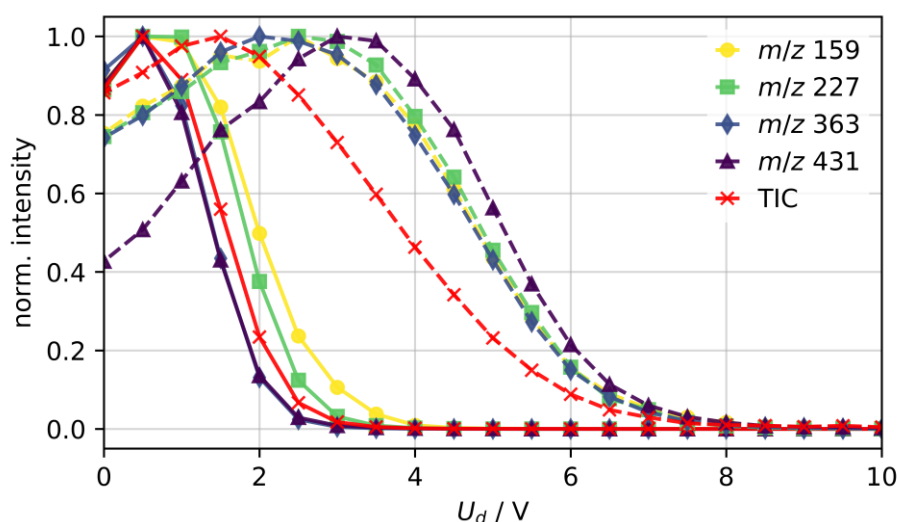


**Figure 21:** DPR of sodium formate clusters and the TIC obtained with the HCTplus (dashed lines) and amaZon Speed ETD ion trap (solid lines).

TIC curve. With the assumption that the energy-dependent ion acceptances of both ion traps are comparable, this translates to a shift of the KED by more than 2 eV. The position and width of the KED is determined by the acceleration voltages applied in (near) collision-free regions of the transfer stage. The experiments with variable acceleration voltages in the first and second vacuum stages of both instruments have shown that here no net changes of the KED can be achieved. Therefore, the difference in the DPR must originate in the third vacuum stage. The acceleration voltage at the entrance of the third vacuum stage is 10.3 V in the HCTplus (between octopole 1 and octopole 2) and 7.7 V in the amaZon (between funnel 2 out and octopole 1). The difference between these voltages matches nicely with the shift of the DPR curves and is a feasible explanation for this observation. The difference in width may result from different pressure gradients in this region in the two instruments. Another explanation could be the different extent of desolvation in the vacuum interfaces. The ion funnels promote stronger desolvation as compared to the skimmer inlet, caused by the higher reduced field strengths in the former. Thus, ions are desolvated to a higher degree when entering the third vacuum stage in the amaZon instrument as compared to the HCTplus instrument. This could yield a narrower KED, because the ion distribution is better defined (e.g., bare analyte ions vs. a broad distribution of clustered analyte ions).

### 3.6.3 Extended DPS range

The DPR traces from ion trap measurements do not saturate when approaching 0 V, but often exhibit a maximum at a deceleration potential of a few Volts (depending on the experimental conditions) and decrease towards lower deceleration potentials. The DPS range is extended into negative deceleration potentials to further map out the behavior. The position and shape of the curves are determined by the collisions and electric fields ions experience in the transfer stage. Consequently, differences in the ions' pathways through the ion transfer stage should be discernible in the DPR. This may include collision properties, desolvation and cluster equilibria, among other. The extended DPS are performed for several analytes, as listed in Table 8.

The extended DPR curves from extracted ion chromatograms of different analyte ions are depicted in Figure 22. The individual traces have strongly differing shapes in the range of negative deceleration potentials, either decreasing monotonically or exhibiting a second maximum. Not all recorded curves are completely mapped in the covered voltage range, e.g., for NaF1, TM1, and Bet. Each ion's or ion group's DPR is recorded with instrument settings adapted for the relevant  $m/z$  range, respectively. The axial potential gradient along the ion transfer stage is the

**Table 8:** Overview of analytes used in the experiments

Name	Shortcut	Formula	Ion	$m/z$	CCS ( $\text{\AA}^2$ )
Betaine	Bet	$\text{C}_5\text{H}_{11}\text{NO}_2$	$[\text{M}+\text{H}]^+$	118	121.1 <sup>b)</sup>
Caffeine	Caf	$\text{C}_8\text{H}_{10}\text{N}_4\text{O}_2$	$[\text{M}+\text{H}]^+$	195	140.2 <sup>b)</sup>
Cysteine	Cys	$\text{C}_3\text{H}_7\text{NO}_2\text{S}$	$[\text{M}+\text{H}]^+$	122	148.6 <sup>b)</sup>
DMSO	DMSO1	$\text{C}_2\text{H}_6\text{OS}$	$[\text{M}+\text{H}]^+$	79	
	DMSO2		$[\text{2M}+\text{H}]^+$	157	
ESI Tuning Mix	TM1	$\text{C}_6\text{H}_{18}\text{N}_3\text{O}_6\text{P}_3$	$[\text{M}+\text{H}]^+$	322	153.7 <sup>c)</sup>
	TM2	$\text{C}_{12}\text{H}_{18}\text{F}_{12}\text{N}_3\text{O}_6\text{P}_3$	$[\text{M}+\text{H}]^+$	622	203.0 <sup>c)</sup>
	TM3	$\text{C}_{18}\text{H}_{18}\text{F}_{24}\text{N}_3\text{O}_6\text{P}_3$	$[\text{M}+\text{H}]^+$	922	243.6 <sup>c)</sup>
	TM4	$\text{C}_{30}\text{H}_{18}\text{F}_{48}\text{N}_3\text{O}_6\text{P}_3$	$[\text{M}+\text{H}]^+$	1522	317.0 <sup>c)</sup>
	TM5	$\text{C}_{42}\text{H}_{18}\text{F}_{72}\text{N}_3\text{O}_6\text{P}_3$	$[\text{M}+\text{H}]^+$	2122	383.0 <sup>c)</sup>
<i>p</i> -chloro BP	BP1	$\text{C}_{12}\text{H}_{11}\text{ClN}$	$[\text{M}]^+$	204	139.3 <sup>d)</sup>
<i>p</i> -cyano BP	BP2	$\text{C}_{13}\text{H}_{11}\text{N}_2$	$[\text{M}]^+$	195	140.5 <sup>d)</sup>
<i>p</i> -fluoro BP	BP3	$\text{C}_{12}\text{H}_{11}\text{FN}$	$[\text{M}]^+$	188	142.5 <sup>d)</sup>
<i>p</i> -methyl BP	BP4	$\text{C}_{13}\text{H}_{14}\text{N}$	$[\text{M}]^+$	184	145.1 <sup>d)</sup>
<i>p</i> -nitro BP	BP5	$\text{C}_{12}\text{H}_{11}\text{N}_2\text{O}_2$	$[\text{M}]^+$	215	
Pyridine	Pyr	$\text{C}_5\text{H}_5\text{N}$	$[\text{M}+\text{H}]^+$	80	
Reserpine	Res	$\text{C}_{33}\text{H}_{40}\text{N}_2\text{O}_9$	$[\text{M}-\text{H}]^{+\text{a)}}$	607	254.3 <sup>e)</sup>
Sodium formate	NaF1	$\text{CHO}_2\text{Na}$	$[\text{2M}+\text{Na}]^+$	159	
	NaF2		$[\text{3M}+\text{Na}]^+$	227	
	NaF3		$[\text{4M}+\text{Na}]^+$	295	
	NaF4		$[\text{5M}+\text{Na}]^+$	363	
	NaF5		$[\text{6M}+\text{Na}]^+$	431	
	NaF6		$[\text{7M}+\text{Na}]^+$	499	
	NaF7		$[\text{8M}+\text{Na}]^+$	567	
Substance P	SP1	$\text{C}_{63}\text{H}_{98}\text{N}_{18}\text{O}_{13}\text{S}$	$[\text{M}+\text{2H}]^{2+}$	674	
	SP2		$[\text{M}+\text{3H}]^{3+}$	450	

a) The observed mass peak corresponds to 3,4-dihydroreserpine, an oxidation product of reserpine, which is formed upon aging of the sample [122]; protonated reserpine was not observed.

b) Taken from [123]; the data set (status as of 25.11.2019) was downloaded from [124].

c) Taken from [125].

d) Taken from [126].

e) Taken from [66].

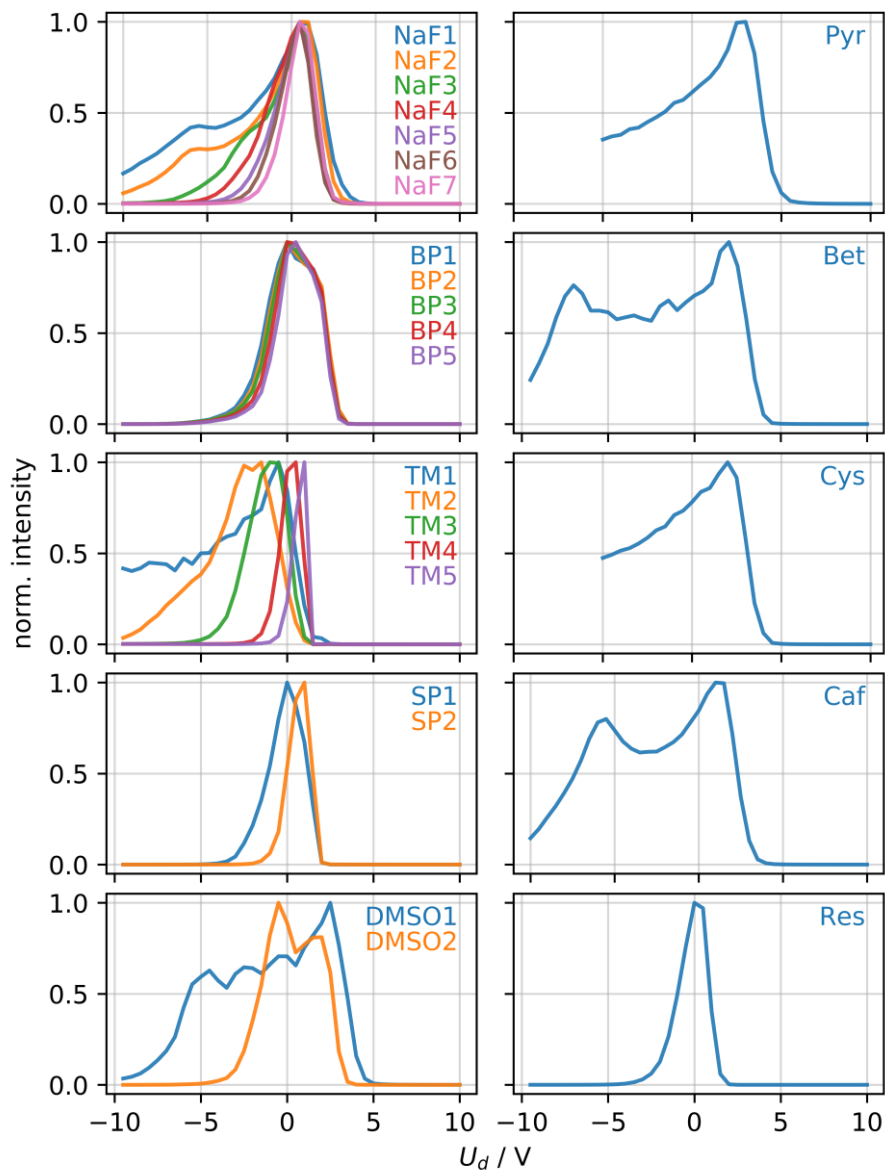


**Figure 22:** Normalized DPR from experiments with extended  $U_d$  range with multiple (left) and single ion signals (right). The left-hand legends are sorted by ascending  $m/z$  from top to bottom.

same for all experiments but the RF voltages applied to the multipole ion guides and funnels, and the trap drive are not. The ion guide RF voltages should not impact the axial ion velocity, since they lead to a *radial* ion confinement. The trap drive, however, defines the operation point, i.e., the ion acceptance, of the ion trap.

The DPR traces reveal certain systematic features. Low  $m/z$  ions exhibit broadened curves, often with a second maximum in the negative  $U_d$  range. At higher  $m/z$ , the traces become narrower and the second maximum eventually merges with the main maximum. The dependence of the position of the main maximum on the ion

$m/z$  is not consistent throughout all experiments. With sodium formate the main maximum position is the same for all observed ion signals and the second maximum is only visible for NaF1 and NaF2. For the NaF3 trace the second maximum is recognizable as a shoulder of the main peak. The benzylpyridinium ions all have a similar  $m/z$ . The traces of these ions overlap fully in the positive  $U_d$  range and approach zero around -4 V, with a systematic shift to slightly more negative values with decreasing  $m/z$ . The tune mix traces exhibit the same behavior, i.e., the DPR peaks become broader with decreasing  $m/z$ . However, the position of the maximum shifts to more negative values from TM1 to TM3 and then to more positive values as the  $m/z$  increases further. For Substance P and DMSO the peak widths scale in the same way with the  $m/z$  as in the sodium formate, benzylpyridinium, and tune mix experiments, but the positions of the maxima behave inversely. It is noticeable that the peak position changes non-systematically throughout all experiments and not only within a compound class.

Since the width of the DPR maxima exhibit a systematic dependency on the ion  $m/z$ , this behavior is further analyzed. To minimize superimposed effects, DPR curves are considered individually for sodium formate, benzylpyridinium, tuning mix, and caffeine ions, i.e., with individual trap drive settings. The widths of the DPS maxima are evaluated as the range that covers 90% of the respective total peak areas, beginning from the point where the intensity reaches 5% of the maximum. The FWHM is not a suitable parameter due to the varying shape of the DPR. The curve shape results from the combination of the kinetic energy shift of the incident ions with the applied voltage between the transfer stage and the ion trap, and the ion acceptance of the ion trap. The interaction of ions with the quadrupolar field depends on the ion  $m/z$  and the trap drive; as the trap drive is not uniform in the experiments, it is adjusted to the relevant  $m/z$  range in each experiment. Thus, the ratio of RF amplitude and  $m/z$  needs to be considered in this discussion. This ratio is comprised in the stability parameter  $q_z$  (eq. (3-6)). The peak width is plotted against  $q_z$  in Figure 23.

In general, the data of individual  $m/z$  values exhibit slightly disproportionate increases to  $q_z$ . Outliers with peak widths that are too low result from incompletely mapped traces. The data of each compound class show a pronounced systematic trend of the peak width, which strongly suggests a fundamental relationship resulting from the actual kinetic energy distribution that is defined in the transfer stage and the acceptance of the ion trap. It is reasonable to assume that both these properties are characteristic for ions within one compound class: The ion formation pathway should be comparable for such ions, as it is directly linked to their

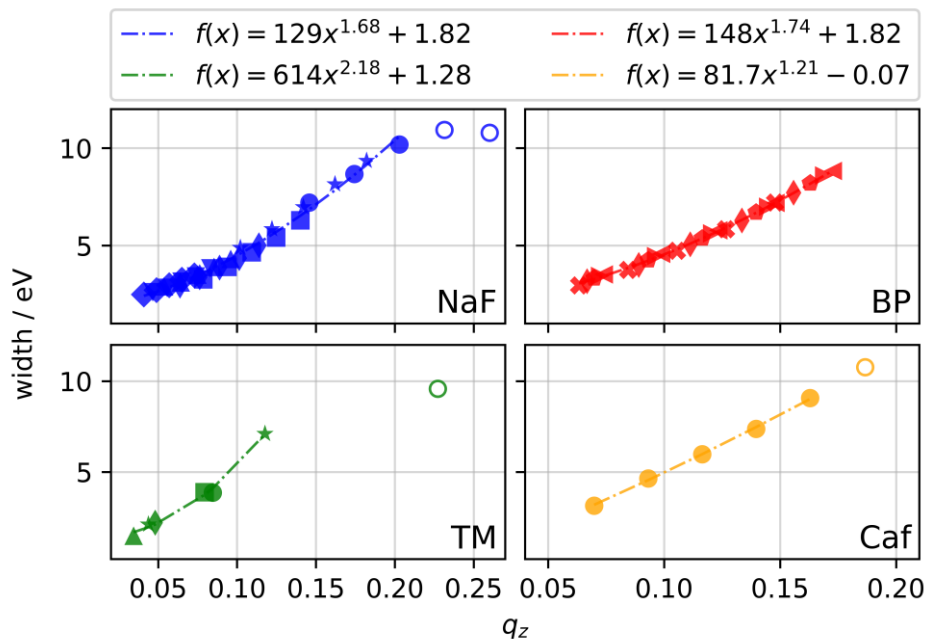


**Figure 23:** Width of the extended DPR peaks for different substance classes in dependence of the stability parameter  $q_z$ . Different markers represent different ions in each plot. Unfilled markers represent data from incomplete DPR curves, which result in underestimated peak widths. The dashed lines are data fits for each substance class, excluding unfilled markers.

physical and chemical properties. It is generally acknowledged that ions are formed via different mechanisms with ESI (e.g., ion evaporation [127, 128] or charged residue [129, 130]) depending on their properties. The ion acceptance depends on the ion  $m/z$  and the RF voltage, which are both connected by  $q_z$ . Different ions being injected into the ion trap with the same kinetic energy at constant  $q_z$  should therefore be stored with comparable efficiency. The consistency of data series of different ions within one compound class, as shown in Figure 23, is in accordance with this hypothesis. At higher trap drive values, the resetting force acting on ions increases and this enables trapping of ions with higher kinetic energies. The mean kinetic energy of the ion population arriving at the trap entrance is proportional to the injection voltage. Thus, the broadening of DPR maxima observed at higher trap drives is expected. As will be shown in section 3.7.5, the kinetic energy acceptance range of a QIT regarding injected ions scales with approximately  $q_z^2$ , as expected from the dependency of the pseudopotential on  $q_z$  (eq. (3-11)). The deviation from the quadratic trend of the data shown in Figure 23 can be explained with the actual kinetic energy range not covering the full energy range of the QIT acceptance.

### 3.7 Modeling of the DPR

The experimental results presented in sections 3.5 and 3.6 suggest a complex dependency of the KED of ions on both experimental parameters and molecular properties. Knowledge of one of these dependencies enables investigation of the other. For a detailed view on the parameters responsible for the shape of the DPR, simulations are carried out. There are three key objectives:

- 1) Collisions within the transfer stage lead to loss of kinetic energy, which impacts on the shape and position of the DPR curves. As a result, acceleration voltages cannot be directly translated into kinetic energy changes. Therefore, the gas dynamics inside the transfer stage needs to be investigated.
- 2) The electric field between the ion transfer stage exit and the ion trap entrance hole is not static but changes periodically due to the oscillating trapping field inside the ion trap. The kinetic energy of the ions is thus modulated accordingly. This is investigated with ion trajectory simulations.
- 3) The kinetic-energy-dependent ion acceptance of the ion trap itself determines the detected ion intensity and ultimately impacts on the shape of DPR curves. The ion acceptance is evaluated with ion trajectory simulations.

#### 3.7.1 Gas dynamics in the transfer stage

The pressure and gas velocity profile inside the second octopole (cf. Figure 4) is estimated from DSMC simulations. For the simulation initialization, the volume is filled uniformly with particles according to a pressure of  $10^{-4}$  mbar. The simulation box has a size of  $164.65 \times 65.00$  mm<sup>2</sup>. A grid of  $300 \times 150$  cells is chosen, yielding cell sizes of 0.55 mm in  $x$  and 0.43 mm in  $y$  direction. Each simulation is run for  $10^5$  timesteps, with a timestep length of  $10^{-7}$  s. Figure 24 shows three timeframes from such a simulation. A net inflow of particles is maintained through the particle emission surfaces *inlet* and *turbo pump 2 (in)*, while at the *outlet* and *turbo pump 1 (out)* particles are removed from the simulation box.

With the parameters given in section 3.4.1 the simulation reaches a steady state after 30000 timesteps (3 ms) and the steady state data were averaged (timesteps 30000 to 100000, total of 7 ms). The obtained spatial pressure profile inside the simulation box and along the center of the octopole, as well as the gas velocity along the octopole center axis, are depicted in Figure 25. The pressure in the volume outside of the octopole is in the range of  $10^{-3}$  to  $10^{-2}$  mbar, which is in good agreement with the value given by the manufacturer for a comparable transfer system [114]. The pressure is about 0.2 mbar at the interfacing orifice between

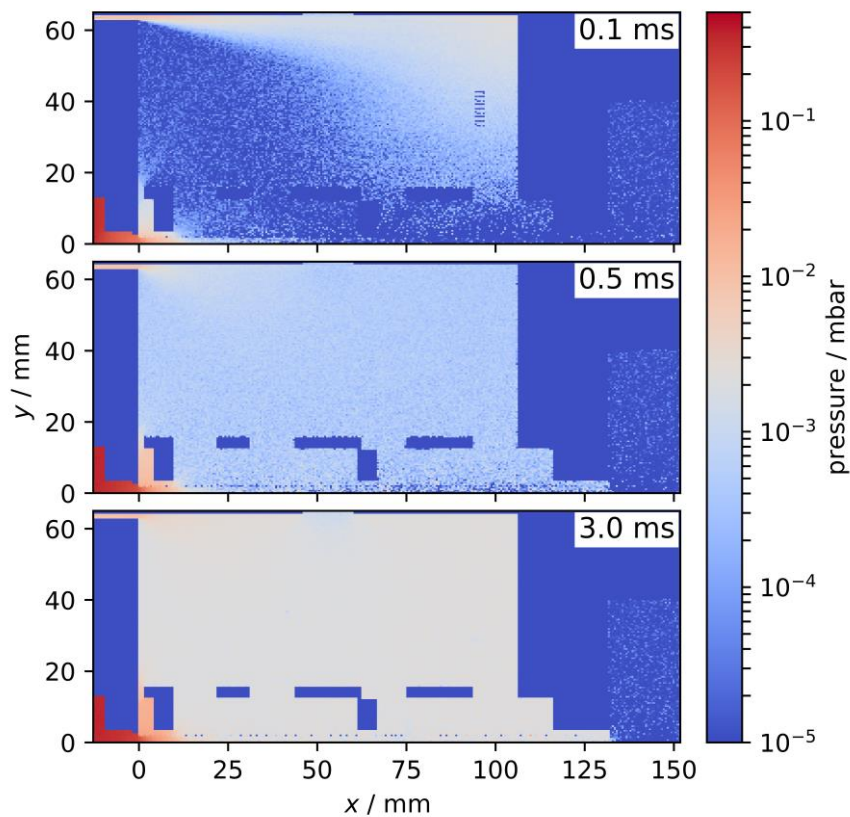


**Figure 24:** Frames from a DSMC simulation showing the pressure distribution inside the simulation box. A steady state is reached after 3 ms.

the two octopoles ( $x = 0$ ) and the gas is strongly accelerated in the forward ( $x$ ) direction, up to 220 m/s. In the first 20 mm of the second octopole the pressure decreases by two orders of magnitude, from  $2 \cdot 10^{-1}$  to  $2 \cdot 10^{-3}$  mbar. In this region, the transition to near collision-free conditions occurs. The mean free path for  $N_2$  at  $2 \cdot 10^{-3}$  mbar is around 3 cm. Thus, on average only a few collisions occur inside octopole 2. This matches well with the experimental observation that the acceleration voltage between octopole 1 and 2 does affect the kinetic energy of ions, since the gained energy is partly maintained due to the low collision number inside octopole 2. The octopole mount geometry creates a rather confined volume in the inlet region and the pressure curve changes its shape around 8 mm, where the geometry widens. The gas velocity increases again in this region to 140 m/s and decreases downstream of the octopole. The pressure remains constant at about  $3 \cdot 10^{-3}$  mbar in this section. In close proximity to the outlet orifice and within the ion trap chamber, the pressure drops fast, over a few millimeters, to  $10^{-5}$  mbar. This is the set background pressure in this region, defined by the boundary condition of the *xhi* boundary. At the exit orifice the gas is strongly accelerated again, to almost 500 m/s, due to the expansion into the next vacuum stage.

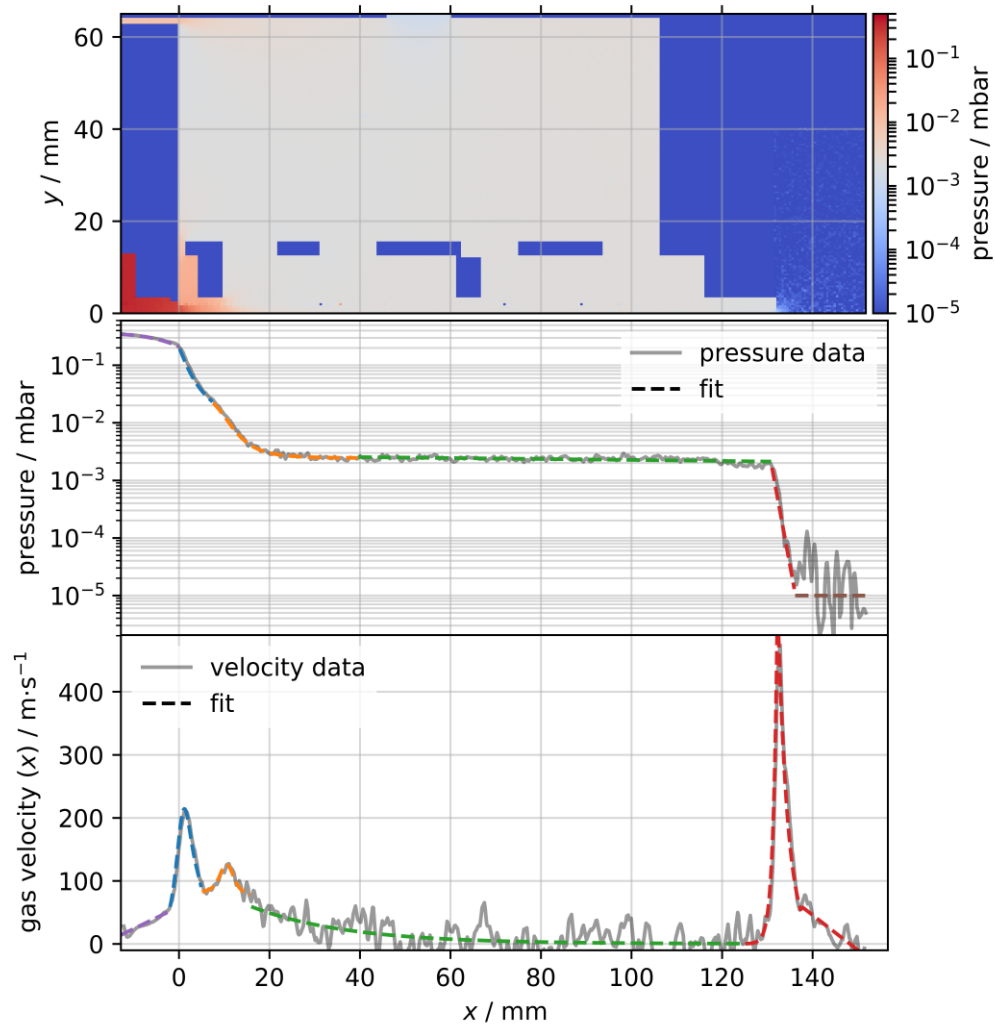


**Figure 25:** Results from simulation 1. Steady state pressure profile in the octopole chamber, averaged over 7 ms (top), pressure curve (center) and axial gas velocity curve along the center of octopole 2 from a SPARTA simulation (bottom). Different data segments are fitted with appropriate functions (cf. Appendix 3.10.1).

Additional simulations were carried out with different pressures at the *inlet* and *turbo pump 2 (in)* regions. The gauged octopole 2 chamber pressure of 0.019 mbar was determined directly at the turbo pump 2 exhaust flange. This pressure value is thus selected as the standard pressure for *turbo pump 2 (in)* in the simulations. In some simulations, *turbo pump 2 (in)* was set as a reflective boundary. The simulation parameters are summarized in Table 9.

Figure 26 shows the pressure and velocity data of all DSMC simulations. For clarity, the data were smoothed with the moving average algorithm. With the subsonic boundary condition at *turbo pump 2 (in)* (simulations 1 – 4, dashed lines) the

**Table 9:** SPARTA simulations, *inlet* and *turbo pump 2 (in)* pressures

sim.	<i>inlet</i> pressure (mbar)	<i>turbo pump 2 (in)</i> pressure (mbar)
1	0.36	0.019
2	0.30	0.019
3	0.20	0.019
4	0.20	0.010
5	0.36	No particle emission
6	0.30	(reflective boundary)
7	0.20	

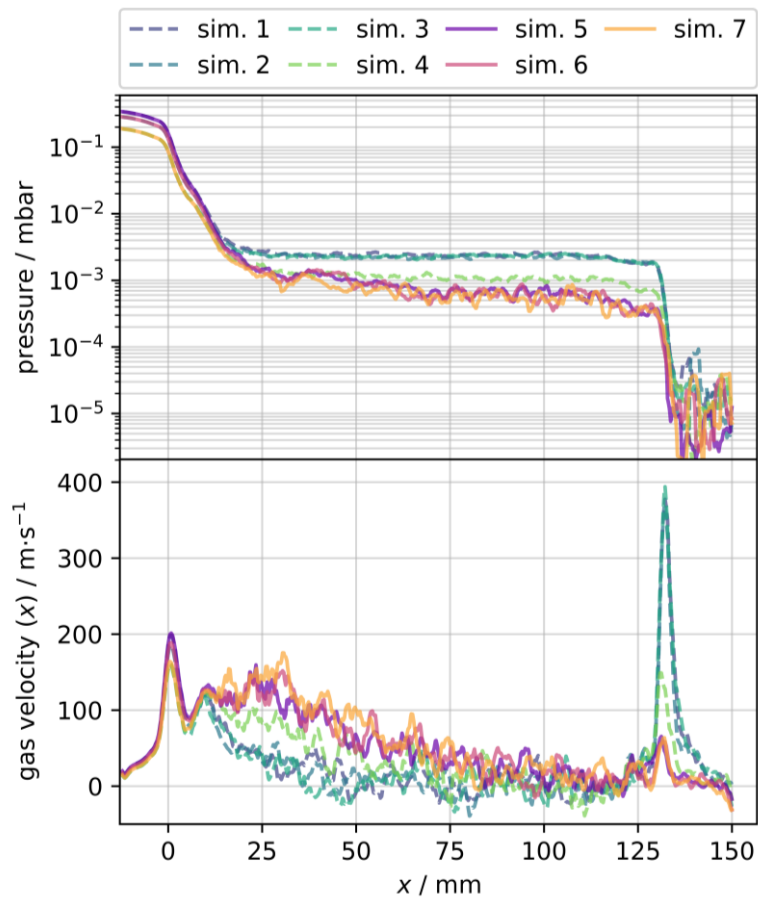


**Figure 26:** Pressure (top) and velocity curves (bottom) from SPARTA simulations (cf. Table 9); the data are smoothed with a moving average for clarity.

pressure inside octopole 2 remains nearly constant and only decreases slightly in the last 20 mm of the octopole. When the *turbo pump 2 (in)* region is set up as a

reflective boundary (simulations 5 – 7, solid lines) the pressure decreases gradually along octopole 2 and is independent of the inlet pressure. The inlet pressure impacts on the pressure curve only in the first 20 mm of the simulation box. The axial velocity curves show peaks in the interface regions between two vacuum chambers. Between the two octopoles the gas is accelerated to 200 m/s at the highest inlet pressure (0.36 mbar) and to 160 m/s at the lowest inlet pressure (0.2 mbar). It is noted that these values are slightly underestimated, due to the data smoothing. Between the octopole 2 exit and the downstream vacuum chamber the gas is also accelerated. Again, the maximum gas velocities are observed in the simulations with the largest pressure differences, i.e., simulations 1-3. In this region the collision number approaches zero, which explains the very high velocities of a few hundred meters per second. Other distinct velocity peaks can be seen in the simulations 1-3 in the region where the octopole mount geometry widens. In the other simulations the pressure is too low at this point, so that the gas is not decelerated sufficiently. The velocities remain around 100 m/s and decrease only slowly in these cases.

The radial pressure and velocity gradients are negligible inside the octopole. Therefore, only the data along the octopole center axis are used for subsequent ion trajectory simulations. The data array is cut into segments and appropriate functions are used for fitting the data. The functions and optimized parameters are given in the appendix (Table 11 and Table 12). The obtained fits are used for calculating the  $x$ -dependent gas pressure and velocity for the HS1 collision model in SIMION.

### 3.7.2 Collisional broadening in the transfer stage

The experiments with variable acceleration voltages in the region between the capillary exit and octopole 1 revealed that the ions' axial motion is completely re-equilibrated with the background gas inside octopole 1 (cf. section 3.6.1). The ions' axial kinetic energies are therefore significantly lower than the energies attained by electrical acceleration in near-collision-free regions.<sup>12</sup> Under collision-free conditions, the ions' KED after acceleration in an electric field should resemble the initial KED, shifted according to the experienced potential change. When collisions occur, kinetic energy is transferred to the background gas and this leads to a shift of the KED to lower energies and to a change of the shape of the distribution.

---

<sup>12</sup>The mean thermal kinetic energy of an ion with  $m/z$  100 is in the range of 26 meV at 298 K.

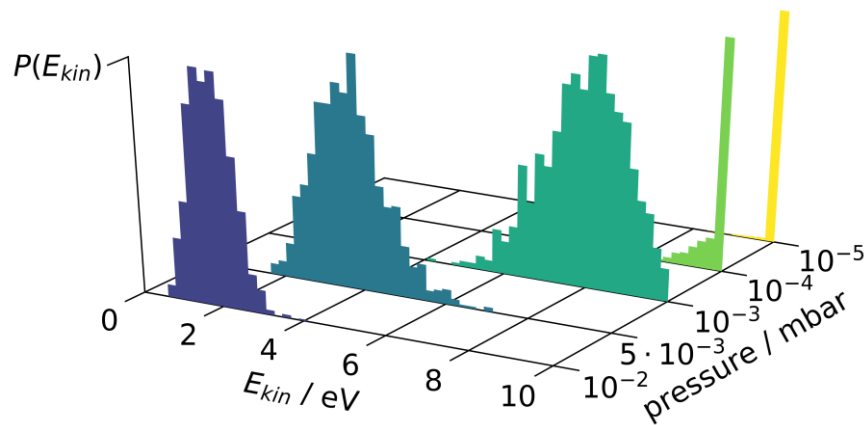


**Figure 27:** Ion energy histograms after passage through a plate capacitor at different pressures.

This effect is qualitatively modeled in preliminary SIMION simulations with a simplified geometry. The simulation model contains two parallel plates at a distance of 10 cm. The potentials of the plates are 10 V and 0 V. 1000 ions with  $m/z$  100 are started at the surface of the 10 V electrode, moving towards the 0 V electrode with an initial kinetic energy of 0.1 eV. Simulations are carried out with different gas pressures between  $10^{-5}$  and  $10^{-2}$  mbar, using the HS1 collision model.

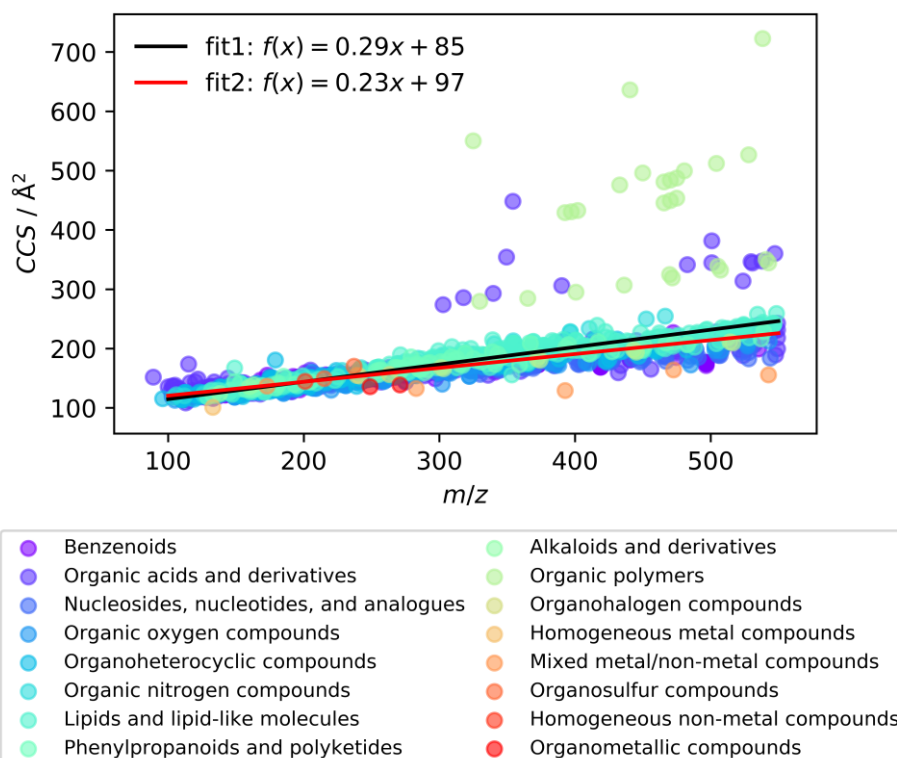
After the ions have arrived at the 0 V electrode, their KEDs have changed depending on the pressure. At  $10^{-5}$  mbar the ions travel essentially undisturbed between the electrodes and virtually all arriving ions have a kinetic energy of 10 eV. At pressures  $>10^{-5}$  mbar the KED at the 0 V electrode begins to shift towards lower ion energies, caused by gas collisions. At  $10^{-4}$  mbar only a small fraction of the ions experiences collisions and the final KED develops a low energy tail. At  $10^{-3}$  mbar the KED changes significantly and exhibits a distinct left-skewed shape. At  $5 \cdot 10^{-3}$  mbar the KED becomes slightly right-skewed and at  $10^{-2}$  mbar the KED is symmetric. The position of the KED shifts to lower energies as the pressure is increased. These results demonstrate the collisional broadening of kinetic energy distributions at intermediate pressure conditions in a highly simplified approach. In the ion transfer stage of a mass spectrometer, additional effects occur due to changing electrical fields, gas dynamics, more complex ion motion in RF-driven ion guides, and potentially also chemical processes.

The collisional broadening within the transfer stage of the HCTplus instrument is modeled in SIMION; the ion trajectory model was described in section 3.4.2. Ions are started in a circular area ( $r = 0.4$  mm) inside the first octopole. The kinetic energy is set according to an MBD at 298 K. A set of simulation runs is performed to recreate a DPS experiment. The potential offset between the transfer stage and the

cup electrode is increased stepwise, in accordance to the corresponding experiments. The number of ions hitting the cup electrode represents the measured ion current. The pressure and gas velocity distributions derived from SPARTA simulations (cf. section 3.7.1) are used as input for the collision model in SIMION.

The ion ensemble for the simulations is adapted from the mass spectrum depicted in Figure 15, containing sodium formate clusters and phthalate background species. The ions'  $m/z$ , relative intensities and estimated CCS are summarized in Table 10. CCS reference data [123] are fitted with a linear model (cf. Figure 28, fit1) and the values for the simulations are interpolated from that model. As can be seen in the reference data, ions of  $m/z$  100-500 typically exhibit CCS values in the range of 115-250 Å<sup>2</sup>. There are only few compounds with CCS values above 250 Å<sup>2</sup>. Another linear fit (Figure 28, fit2), which does ignore these values, is thus used for comparison.

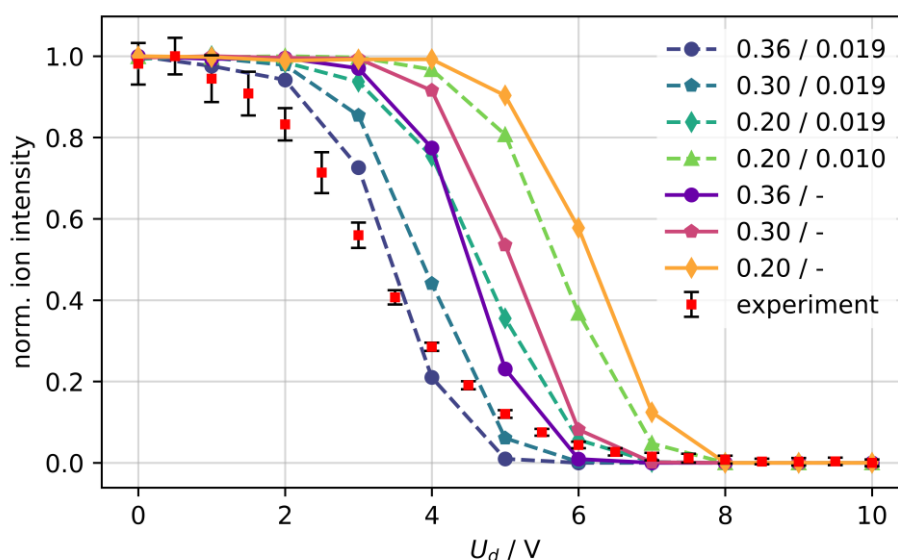
The simulations yield the DPR curves shown in Figure 29. Results are shown for different gas dynamics solutions, as described in section 3.7.1. When comparing the data without the *turbo pump 2 (in)* particle emission (solid lines) it becomes apparent that the *inlet* pressure strongly impacts on the offset potential, at which the ion intensity decreases. The intensity decrease sets in at lower offset potentials



**Figure 28:** CCS reference data [123] were fitted with a linear model for estimating mass-dependent CCS values. Fit1 considers all values, fit2 ignores values above 250 Å<sup>2</sup>.

**Table 10:** Ion species in SIMION simulations for modeling of the DPR, adapted from experiments in section 3.5. CCS values are estimated from reference data

represented ion	$m/z$	rel. intensity	CCS ( $\text{\AA}^2$ )
$[\text{C}_{16}\text{H}_{22}\text{O}_4+\text{H}]^+$	149	15	129
$[(\text{CHO}_2\text{Na})_2+\text{Na}]^+$	159	25	132
$[(\text{CHO}_2\text{Na})_3+\text{Na}]^+$	227	70	152
$[\text{C}_{16}\text{H}_{22}\text{O}_4+\text{Na}]^+$	301	40	173
$[(\text{CHO}_2\text{Na})_5+\text{Na}]^+$	363	20	192
$[\text{C}_{24}\text{H}_{38}\text{O}_4+\text{Na}]^+$	413	100	206
$[(\text{CHO}_2\text{Na})_6+\text{Na}]^+$	431	15	212

**Figure 29:** DPR curves from simulations with different *inlet* and *turbo pump 2 (in)* pressures and experimental data. The values in the legend are the respective pressures in millibars.

and the higher the *inlet* pressure, the faster the decrease. Such behavior is as expected, since the average ion kinetic energy scales with the collision number and thus with pressure. Ions exhibit higher axial kinetic energies the lower the pressure becomes, and can overcome higher potential barriers. It is noticeable that all DPR curves are shifted significantly to higher deceleration potentials, as compared to the experimental data. Setting the *turbo pump 2 (in)* pressure to 0.019 mbar (dashed lines), which is the actual value measured at the instrument in this region, increases the pressure throughout octopole 2. This shifts the curves towards lower

offset potentials and slightly broadens the interval in which the intensity decreases. The latter corresponds to a broadening of the underlying KED. None of the simulated DPR curves align completely with the experimentally obtained curve. However, the best agreement is obtained when the experimentally determined pressures are applied (*inlet* 0.36 mbar, *turbo pump 2 (in)* 0.019 mbar), which clearly supports the validity of the DSMC results. It is noticeable that the simulated DPR curves all decrease significantly faster than the experimental curve. There are four rationales for the deviation between the simulation and experimental data, which are discussed in the following:

1) The pressure and gas velocity profiles in the ion trajectory simulations are derived from DSMC simulations. The accuracy of the DSMC simulations depends on the quality of the geometry model, which is to some extent limited by the available computing power. Even though the model is based on the real 3D geometry it contains certain simplifications, as a result of the 2D axisymmetric approximation. Whenever possible the boundary conditions of the simulation box are adapted from experimentally determined properties, e.g. gauged pressures. Especially the gas influx into the simulation box is strongly simplified due to the geometry model restrictions. This results in a potentially large uncertainty concerning the pressures and gas velocities of the particle emission regions and, thus, the pressure and gas velocity profiles in the simulations. The slower descending profile of the experimental DPR, compared to the simulation results, corresponds to a broader kinetic energy distribution. The gas inflow into the second vacuum stage is resembling a supersonic gas jet<sup>13</sup> and therefore particularly the gas velocity in this region may be underestimated in the simulations. The DSMC results cannot be validated directly, due to lack of independent data regarding the actual pressure profile and gas velocity. The good agreement of the simulation, which uses experimentally determined pressures as input, with the experiment indicate that the DSMC results yield a reasonable representation of the gas dynamics.

2) The kinetic energy evolution of an ion passing through the ion transfer stage depends strongly on the ion ensemble, i.e., ion  $m/z$  and CCS. The  $m/z$  value also affects the interaction with the electric field and, thus, the ions' transfer properties. As a result, deviations between the ion ensembles in the experiments and simulations lead to different DPR curves. This is the case in the results discussed above, since the ion ensemble in the simulations does only incorporate the ions which

---

<sup>13</sup> Assuming a pressure of 3.6 mbar in the first and 0.36 mbar in the second vacuum stage, the gas flow through the skimmer with a nozzle diameter of 1 mm is choked. This leads to formation of a supersonic expansion into the second vacuum stage [131].

were identified in the experiments. In response, a second set of simulations with a more comprehensive ion ensemble is executed. All ions that are detected with at least 5% relative intensity in the mass spectrum in Figure 15 are added to the simulations. The  $m/z$ -dependent CCS are again estimated from the linear fit of the reference data (fit1 in Figure 28). However, using this comprehensive ion ensemble with 42 different ion species in the simulations does not change the results significantly (trace b) in Figure 30). Simulated CCS-dependent DPR curves for individual ion types (i.e., only one  $m/z$ ) show the expected shift to higher deceleration potentials at smaller CCS values (data not shown). This corresponds to a higher average kinetic energy of the ions upon exiting the transfer stage, caused by the lower collision number. The intensity decrease occurs over a larger  $U_d$  range for smaller CCS, indicating a broader KED for smaller ions. This is in agreement with the results shown in Figure 27, where a higher collision number (higher pressure) results in a narrower KED. Smaller widths of simulated KEDs compared to the experimental KED can be a result of overestimated CCS values in the simulations. The reference data contain values above  $250 \text{ \AA}^2$  between  $m/z$  300 and 550, which is significantly higher than the average values in this range. An alternative linear model of the CCS reference data without the values above  $250 \text{ \AA}^2$  (fit2 in Figure 28) is used to create an ion ensemble for another DPS simulation. The new CCS values deviate from the previously used model by up to -7%. The resulting DPR differs only slightly from the preceding simulations and does not improve the match with the experimental data (trace c) in Figure 30). It is concluded that an error in the CCS values alone cannot explain the deviations between the simulations and experiments. However, the utilized collision model HS1 does only consider purely elastic collisions with constant CCS values. In reality, collision cross sections depend on the relative velocity of the colliding particles and the scattering angle distribution may differ from the isotropic hard sphere scattering law [132]. This potentially introduces errors especially when ions are strongly accelerated, as is the case in the region between octopole 1 and octopole 2. Kinetic energy can also be converted into internal energy during collisions. The detection of fragments of BP ions is the direct proof of inelastic energy conversion in the present experiments. Therefore, it is likely that the hard sphere collision model introduces a significant error into the simulations and contributes to the deviation from experimental results.

3) In the trajectory simulations, only bare gas phase ions are considered. In the experiments, ions are produced via ESI and it is unclear, in which state the ions exist within the starting region in the simulations, i.e., inside the first octopole. It is reasonable to assume that ions are still partly solvated in the second vacuum stage. This would lead to an increase of their collision cross sections. The impact

of desolvation is investigated in simulations, by applying a variable collision cross section that scales with the axial ion position. Ions are started with CCS values that are larger than that of the corresponding bare ions, and then decrease linearly (trace d) in Figure 30) as the ions travels further downstream, until the respective actual CCS values (cf. Table 10) are reached. Due to the larger initial CCS, the resulting DPR is shifted towards lower deceleration potentials and the match with the experimental data between 0 and 2 V is improved. Above 2 V, the curves drop too fast in the simulations, indicating missing high energy ions. The corresponding KED is asymmetric and exhibits a low energy tail. In the simulations, the initial CCS is increased for all ions, which is unrealistic. It is again reasonable to assume that there exist different levels of solvation at the end of octopole 1. Therefore, in another simulation the initial CCS is scaled with a random factor between one and two, weighted with an arbitrarily chosen exponential distribution  $f(x) = \exp(-10x)$ . The result of this simulation (trace e) in Figure 30) shows a trend in the right direction, i.e., a slower decrease of the curve above 2 V. The experimental data are still not matched completely, but it appears that different levels of ion solvation in the transition region between octopole 1 and octopole 2 are contributing to the mismatch between simulation and experimental results.

4) It is an ongoing discussion to what extent charged droplets penetrate into vacuum systems of mass spectrometers. Experimental studies have shown that such droplets do not only enter the vacuum systems but can even penetrate into the analyzer region [133, 134]. These droplets may have  $m/z$  values in the typical operation range of API mass spectrometers, e.g.,  $m/z < 3000$  for the Bruker ion traps<sup>14</sup>. Therefore, they interact with the electric fields inside the transfer stage similarly to ions in that  $m/z$  range. However, the collision cross section of such a droplet is significantly larger than of singly charged ions with comparable  $m/z$ . Therefore, the mobility of the droplets is comparably low. It is conceivable that a non-uniform ion release from droplets in a downstream section of the transfer stage results in a broadening of the KED, similar to the effect of partial solvation of ions. If ions are randomly ejected from the droplets and gain some excess kinetic energy during this process, ions with both lower and higher kinetic energies will be added to the ion ensemble, resulting in a broadening of the KED, as observed in the experiment. This is comparable to the kinetic energy release observed in unimolecular fragmentation experiments (cf. section 3.1.4).

---

<sup>14</sup> A spherical water droplet at the Rayleigh limit with a radius of 1 nm carries four elementary charges and has an  $m/z$  of approx. 600 [135] and an estimated CCS in N<sub>2</sub> of  $3.1 \cdot 10^{-18} \text{ m}^2$ .

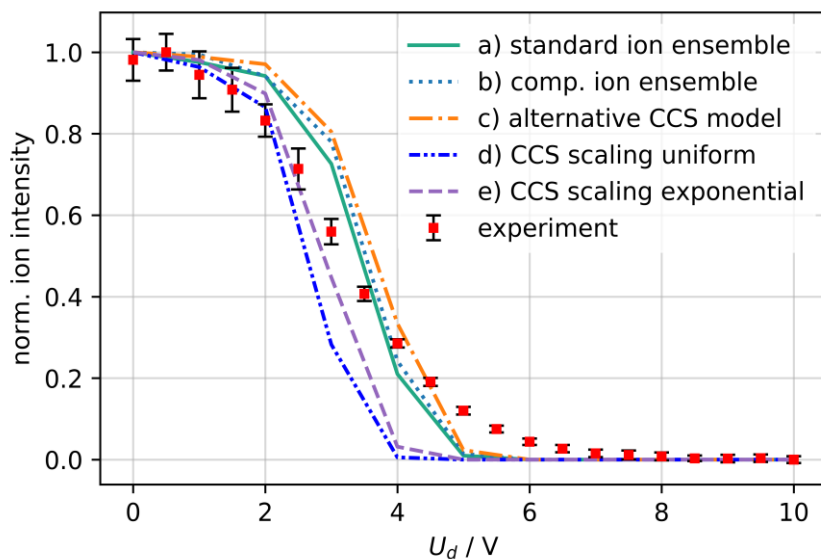


**Figure 30:** DPR from the experiment and simulations with different ion ensembles (a) – e)). The pressure and gas velocity data are taken from the DSMC simulation with 0.36 and 0.019 mbar at the *inlet* and *turbo pump 2 (in)* region, respectively; a) standard ion ensemble (cf. Table 10); b) comprehensive ion ensemble (all ions detected with  $\geq 5\%$  rel. intensity in the experiment); c) comprehensive ion ensemble and alternative CCS model (fit2); d) standard ion ensemble, ions are started with doubled CCS and subsequent linear decrease to the actual value; e) standard ion ensemble, the initial CCS is scaled with an exponentially distributed factor and subsequently reduced according to a sigmoid function to the actual value.

The desolvation and droplet hypotheses are in agreement with the assumption that differences between the HCTplus and amaZon Speed ETD are caused by the different desolvation means of both instruments (cf. section 3.6.2). The dual funnel stage in the amaZon instrument achieves much better desolvation. As a result, bare ions and smaller clusters are injected into the third vacuum stage, where the collision number is sufficiently low for the ions to partly retain the gained kinetic energy. The KED is mainly determined by the acceleration voltages and collisions. In the HCTplus, the desolvation process is spread spatially, possibly up into the third vacuum stage, leading to a broader KED due to the superimposed, blurred desolvation/ion release process. Considering all effects described above, it is concluded that the simulations yield a reasonable representation of the experimental observations.

### 3.7.3 Ion focusing and the observed KED

The experimental determination of KEDs is based on the interaction of the ion ensemble with a potential barrier. The barrier is applied in a region where ions are focused within an electrostatic lens. During a DPS, the focusing properties of the

lens may change in a way that ions are not only deflected due to their kinetic energy but also their incident trajectory. This effect is evaluated in the trajectory simulations by comparing the simulated *observed* KEDs obtained from DPR curves with the ions' *actual* KEDs when they hit the cup electrode. The simulated observed KED is the derivative of the normalized DPR curve fit. The actual KED is the area-normalized fit of the kinetic energy histogram of ions that terminate at the cup electrode. The overlap of the two functions is determined to compare the divergence between the kinetic energy distributions. The overlap integral  $S_{AB}$  of two functions  $f_A(x)$  and  $f_B(x)$ , in the considered range from  $x_1$  to  $x_2$ , is calculated as follows:

$$S_{AB} = \int_{x_1}^{x_2} f_A(x) \cdot f_B(x) dx. \quad (3-7)$$

The functions are normalized such that

$$S_{\Lambda\Lambda} = \int_{x_1}^{x_2} f_{\Lambda}(x) \cdot f_{\Lambda}(x) dx = 1. \quad (3-8)$$

$S_{AB} = 1$  indicates that the two considered functions are identical, while  $S_{AB} = 0$  indicates no overlap. Figure 31 shows as examples the actual and observed KEDs for three different simulations. The overlap integrals for all simulations presented in the preceding sections (different pressure scenarios and ion ensembles) are greater than 0.98. It is concluded that the observed KED generally equals the actual KED.

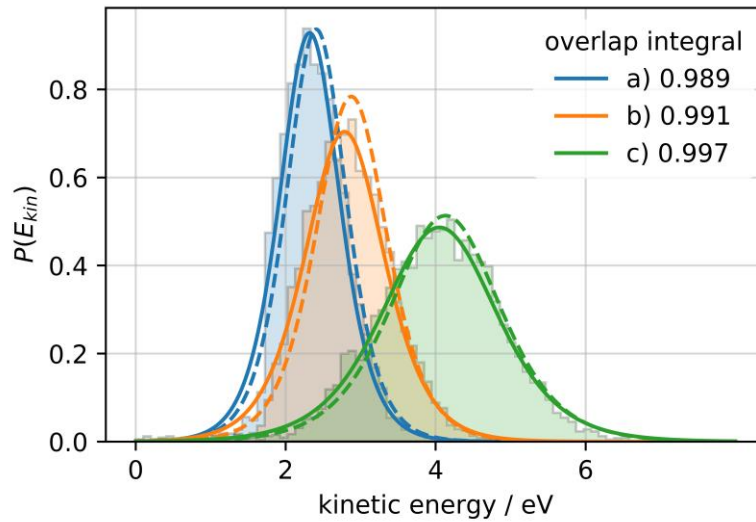


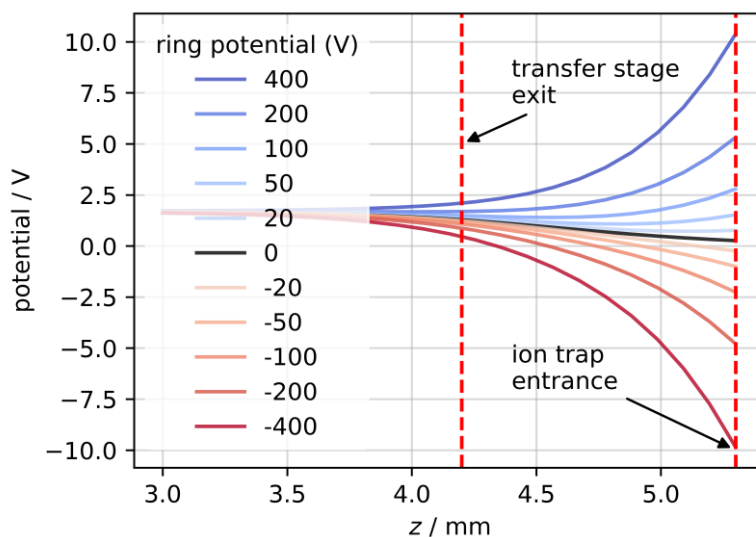
**Figure 31:** Comparison of actual (solid lines) and observed (dashed lines) KEDs and overlap integrals for simulations with different *inlet* pressures: a) 0.36 mbar, b) 0.30 mbar, c) 0.20 mbar.

### 3.7.4 KED modulation by fringe fields

An ion trap model, adapted from the SIMION *pseudopotential* example, is used for modeling the intensity distributions obtained with the HCTplus and amaZon ion traps (cf. section 3.4.2, *Quadrupole ion trap model*). The model contains the ion trap electrodes and an injection electrode, which represents the transfer stage exit lens. Ions are injected into the ion trap in the  $z$  direction, i.e., through an orifice in the cap electrode facing the transfer stage. The trap entrance is positioned at  $z = 5.3$  mm in the simulation model. Even though the cap electrodes are held at ground potential, the RF voltage applied to the ring electrode affects the interface region near the inlet orifice. This leads to a temporal modulation of the electric field between the transfer stage exit and the ion trap entrance (cf. Figure 32).

The distance between the ion transfer stage exit and the ion trap entrance is 1.1 mm in the SIMION model. An ion with  $m/z$  100 and a kinetic energy of 2.5 eV travels with a velocity of about 2200 m/s, resulting in a residence time between the transfer stage and the ion trap of 0.5  $\mu$ s. Since the wavelength of the RF voltage applied to the ring electrode of an ion trap is usually in the range of a microsecond, ions passing through this region may experience a significant proportion of one RF oscillation. However, the sign and magnitude of the potential gradient depends on the phase position of the oscillating field. That leads to a modulation of the ion kinetic energy.

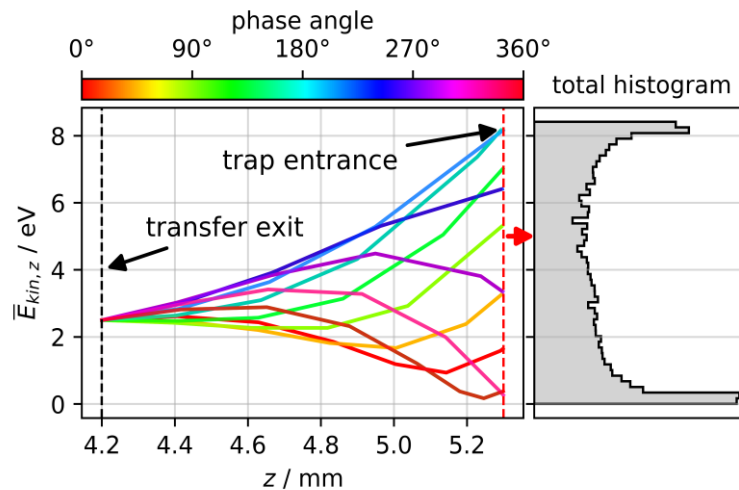
To evaluate the general effect of the variable field in the transition region on the kinetic energy, a trajectory simulation with 100000 ions is executed. The ions



**Figure 32:** Potential along the center axis between the transfer stage exit and ion trap entrance at different ring potentials.

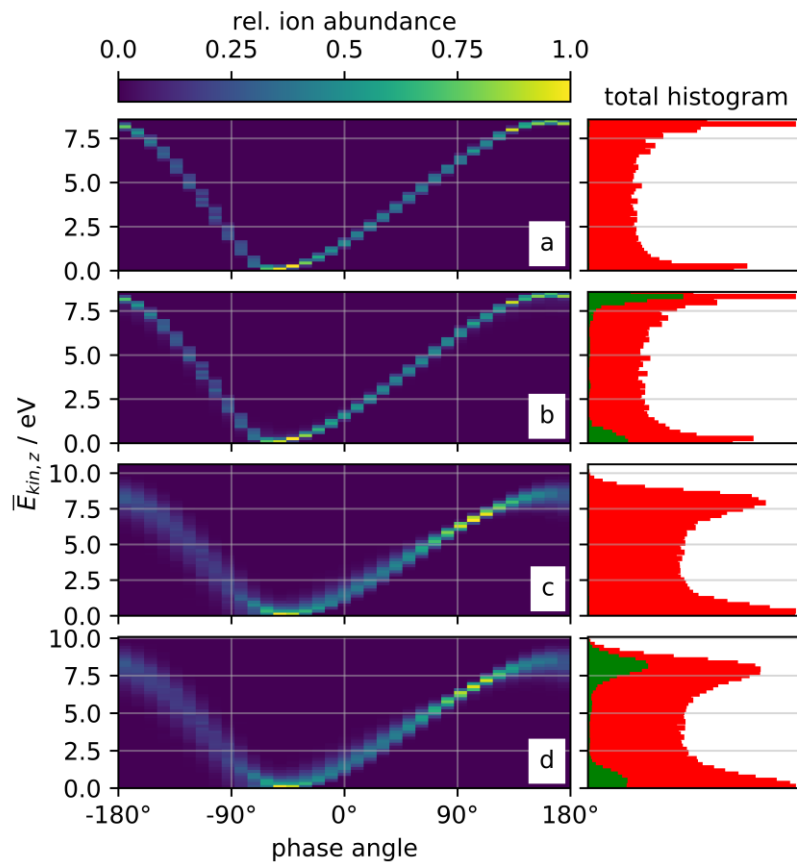
are started in a circular area ( $r = 0.2$  mm) at the transfer exit, i.e., the tip of the injection electrode ( $z = 4.2$  mm), with a kinetic energy of 2.5 eV. The phase position relative to the RF voltage is uniformly distributed over one RF cycle, i.e.,  $1 \mu\text{s}$  in this case. Collisions are not included in the simulations as only interaction with the electric field is evaluated. Subsequent simulations consider collisions and variable ion energies.

Figure 33 shows that the kinetic energy progression strongly depends on the initial phase positions. Ions starting around a phase angle of  $0^\circ$  experience a repulsive potential while traveling through the region between the transfer stage and the trap and have a decreased kinetic energy at the trap entrance, compared to the initial value of 2.5 eV. Ions starting at a different phase angle will experience a net increase of kinetic energy. The kinetic energy histogram of the ions which enter the ion trap shows a broad bimodal distribution. The maxima of the distribution are at the boundaries of the distribution, at minimum and maximum kinetic energies, i.e., around 0 and 8 eV in this case. The phase-angle-dependent kinetic energy at the trap entrance, depicted in Figure 34a, oscillates around the arithmetic mean kinetic energy of roughly 4 eV, with a phase shift of about  $80^\circ$  relative to the RF voltage. Ions starting at a phase angle around  $170^\circ$  and  $300^\circ$  exhibit the narrowest KED at the trap entrance. This explains the small width of the maxima in the total kinetic energy histogram in Figure 33. The KEDs between  $200^\circ$  and  $280^\circ$  are the broadest.



**Figure 33:** Ion kinetic energy progression between the transfer stage exit lens and the ion trap entrance hole (left) and total kinetic energy histogram at the trap entrance (right).  $10^5$  ions are started at different phase angles relative to the RF voltage (200 V, 1 MHz). The initial kinetic energy is 2.5 eV.

Additional simulations were performed with the same model, to investigate the impact of collisions and non-uniform initial ion kinetic energy distributions. Figure 34 shows the results of four different simulations. In the simulations with collisions, a constant pressure is assumed for the whole simulation box. Therefore, collisions are likely overestimated in the regions outside of the ion trap. It becomes apparent that the kinetic energy of ions is not significantly affected at a typical helium pressure of  $3 \cdot 10^{-3}$  mbar inside the ion trap (cf. Figure 34a and b). Changing the initial ion kinetic energy from a single value to a Gaussian distribution with a maximum at 2.5 eV and a FWHM of 1 eV has a large impact on the resulting KED (Figure 34c and d). The general phase angle dependency remains similar, as discussed above. However, the region with the narrowest resulting KED is shifted



**Figure 34:** 2D histograms of the kinetic energy at the trap entrance, after experiencing the oscillating field in the interface region, and the initial phase position for four simulations with different pressures and initial kinetic energies (left): a) 0 mbar/2.5 eV, b)  $3 \cdot 10^{-3}$  mbar/2.5 eV, c) 0 mbar/Gaussian dist. @ 2.5 eV (1 eV FWHM), d)  $3 \cdot 10^{-3}$  mbar/Gaussian dist. @ 2.5 eV (1 eV FWHM). The green sections of the total kinetic energy histograms (right) represent the fraction of ions that are stored in the ion trap after 1 ms.

from  $170^\circ$  to  $100^\circ$ . The phase-angle-dependent KEDs are significantly broadened, especially in the range between  $150^\circ$  and  $300^\circ$ . As a result, the total KED has no sharp boundary on the high energy side, as it was observed with a set initial kinetic energy of 2.5 eV.

For the actual ion trap operation, the phase-angle-dependent kinetic energy distribution of the ions upon entering the ion trap is of interest, because it determines which ions will actually be trapped. Figure 35 depicts the relation between the kinetic energy and phase angle of ions entering the QIT after passing through the fringe field region. During a DPS the kinetic energy is shifted according to the applied deceleration potential. When no ions are deflected from the trap, i.e., the complete initial KED is probed, the resulting KEDs at the trap entrance have comparable shapes. The KEDs are significantly broadened and exhibit maxima at the low and high energy boundaries. The higher the injection voltage, the broader is the resulting KED and the larger is the shift of the KED to higher energies. When a fraction of the ions is deflected from the trap, the resulting KEDs appear to exhibit

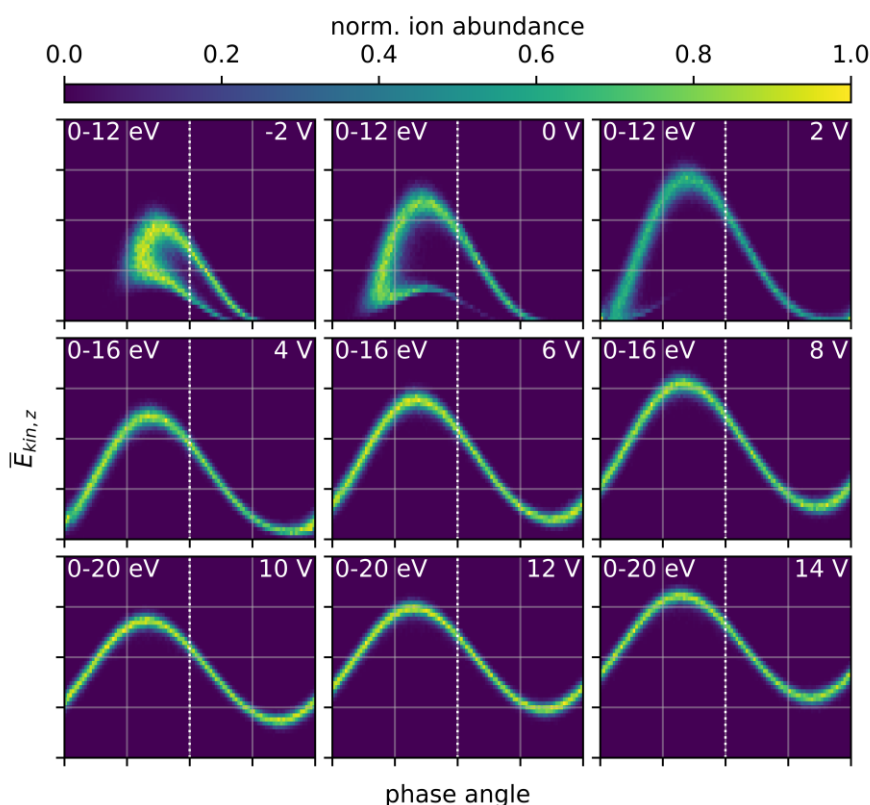


**Figure 35:** Phase-angle-dependent axial ion kinetic energy at the trap entrance for ions with  $m/z$  100 and an initial Gaussian KED with a mean of 2.5 eV and a FWHM of 1 eV, at different injection voltages. The injection voltages are given in the top right corner of each image. The RF voltage amplitude is 200 V. The ranges of the vertical axes are given in the top left corner of each image. The horizontal axes range from  $-180^\circ$  to  $+180^\circ$ .

a substructure (Figure 35, -2 V and 0 V), likely resulting from slow ions which have large residence times in the interface region between the transfer stage and ion trap.

### 3.7.5 Ion acceptance of the QIT

The shape of the observed KED is ultimately formed in the ion trap. The trapping process not only depends on the stability parameter  $q_z$  of the ions in the quadrupolar field but also on the ions' kinetic energy  $\bar{E}_{\text{kin},z}$  which must not exceed the pseudopotential  $\bar{D}_z$  for ions to be stored in a trap of a given size. This is never true for ions entering the quadrupolar field from outside of the trap. Therefore, QITs are usually operated at a helium pressure in the range of  $10^{-3}$  mbar, so that ions are collisionally cooled during injection. Figure 34 clearly indicates the necessity of collisional cooling for trapping ions, as no ions are stored when the pressure in the simulations is set to 0 mbar (Figure 34a and c).

The energy-dependent ion acceptance of the QIT is probed in trajectory simulations.  $10^5$  ions are started evenly distributed in a circular area ( $r = 0.6$  mm) at the trap entrance orifice in the cap electrode facing the injection electrode ( $z = 5.3$  mm), at different phase angles relative to the RF voltage. The initial kinetic energy is uniformly distributed in the required range. Ions are considered trapped when they are still present after 1 ms. The pressure is set to  $3 \cdot 10^{-3}$  mbar. Simulations are run for different ion  $m/z$  and RF voltages.

The normalized ion acceptance distributions for different settings are shown in Figure 36. There is a distinct and systematic correlation of the ion kinetic energy and the phase angle at which the ions enter the QIT. Ions need to enter the ion trap with the kinetic energy matching the present RF phase angle to be trapped. The kinetic energy can not only be too high for the ion to be stored, but also too low. This dependence is not ruled out by collisional cooling at typical ion trap operation pressures. Around  $0^\circ$  the ion kinetic energy has a maximum in all cases. The accepted kinetic energy approaches zero towards  $\pm 180^\circ$ . In total, the ion acceptance distributions exhibit a sinusoidal shape, with a gap at a phase angle of  $180^\circ$ . The energy width and the integral of the ion acceptance are generally larger between  $-180^\circ$  and  $0^\circ$  than between  $0^\circ$  and  $180^\circ$ , which means that ions are more efficiently stored when entering the ion trap during the second half of the RF period. The maximum tolerable kinetic energy scales by the same factor of 3.5 – 4.0 when doubling  $q_z$ , for any ion  $m/z$ . This matches well with the quadratic dependency of the pseudopotential on  $q_z$ . However, the maximum kinetic energy increases with  $m/z$  at constant  $q_z$ . The positions of the ion acceptance distributions are

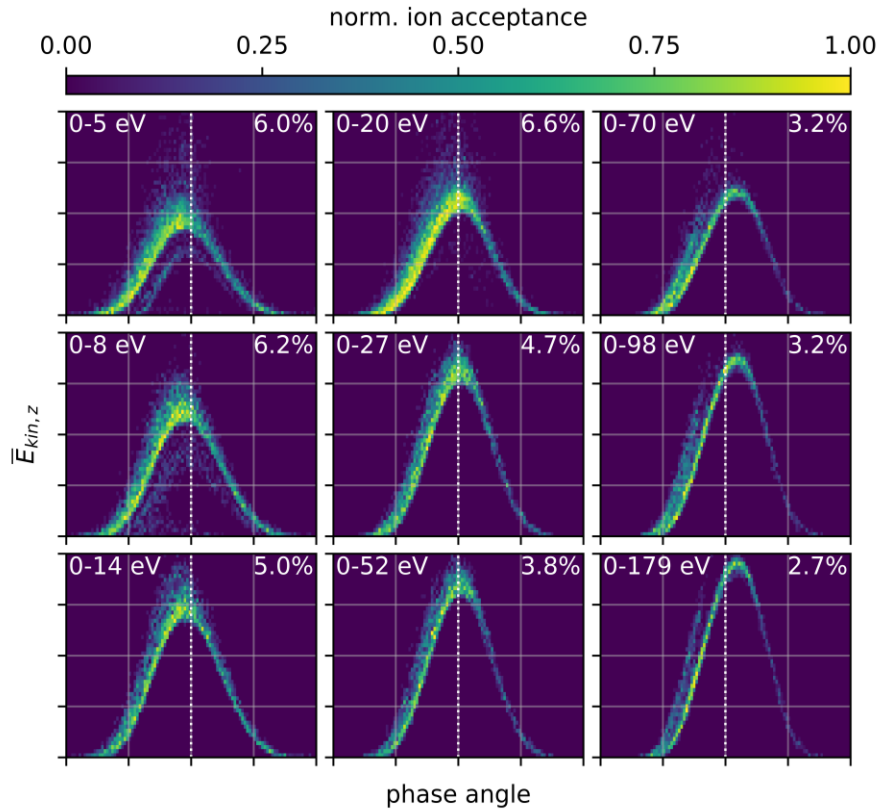


**Figure 36:** Normalized ion acceptance distributions of the QIT in dependence of the kinetic energy and phase angle, for  $q_z = 0.097, 0.195, 0.390$  (from left to right) and  $m/z$  100, 200, 400 (from top to bottom). The ranges of the vertical axes are given in the top left corner in each image; the upper limit is the maximum of the initial energy of trapped ions. All horizontal axes range from  $-180^\circ$  to  $+180^\circ$ . The dotted lines highlight  $0^\circ$ . The relative trapping efficiency with regard to the total ion number is given in the top right corner in each image.

slightly shifted to larger phase angles when  $q_z$  increases. At  $q_z = 0.195$  the distribution is centered at  $0^\circ$ . At  $q_z = 0.097$  and  $0.390$  the distributions move slightly to negative and positive phase angles, respectively. The kinetic energy range in which ions can be stored is much larger than typical kinetic energies of ions entering the trap at standard settings (cf. Figure 34 bottom). For example, with an injection voltage of 1.7 V, RF amplitude of 200 V and  $m/z$  100, the ion kinetic energy at the trap entrance ranges from 0 to 10 eV, while the ion acceptance energy range is between 0 and 20 eV.

The phase-angle- and energy-dependent trapped ion ensemble is the product of the ion acceptance distribution and the phase-angle-dependent KED of ions that enter the trap. Both distributions are calculated as 2D histograms with identical size and resolution in both dimensions. The trapped ion ensemble is obtained by multiplying the histograms. This is depicted in Figure 37. The normalized ion acceptance of the QIT is shown in Figure 37a and the phase-angle-dependent ion KED

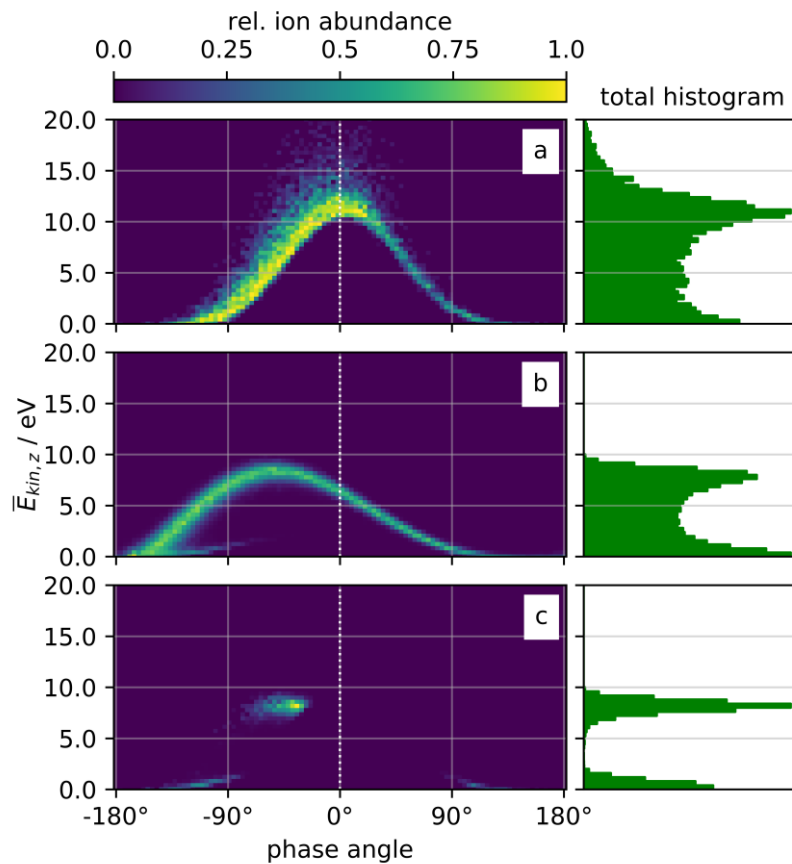


**Figure 37:** a) Kinetic-energy- and phase-angle-dependent ion acceptance of the QIT (left) and total kinetic energy histogram of the trapped ions at the trap entrance (right); b) Phase-angle-dependent ion kinetic energy at the trap entrance after passing through the interface region between the transfer stage exit and the ion trap (left) and total kinetic energy histogram (right); c) Product of the phase-angle-dependent ion acceptance and kinetic energy of ions (left) and total kinetic energy histogram of ultimately trapped ions upon entering the trap (right). All data are for ions with  $m/z$  100 and RF voltage of 200 V. The ion acceptance is normalized to the total number of ions that were started in the simulation in each energy and phase angle bin. The remaining histograms are normalized to the maximum value.

in Figure 37b. Figure 37c depicts the overlap, i.e., the product, of the phase-angle-dependent ion acceptance and the ions' kinetic energy. The stored ion ensemble exhibits irregular and not easily predictable initial kinetic energies, which changes with the injection voltage, i.e., during a DPS experiment. A set of energy- and phase-angle-resolved stored ion ensembles for different injection voltages is shown below (Figure 38). The energy window that leads to efficient storage shifts to higher energies as the injection voltage increases and ions with low kinetic energies are not stored at all, which is very unintuitive in a potential well model.

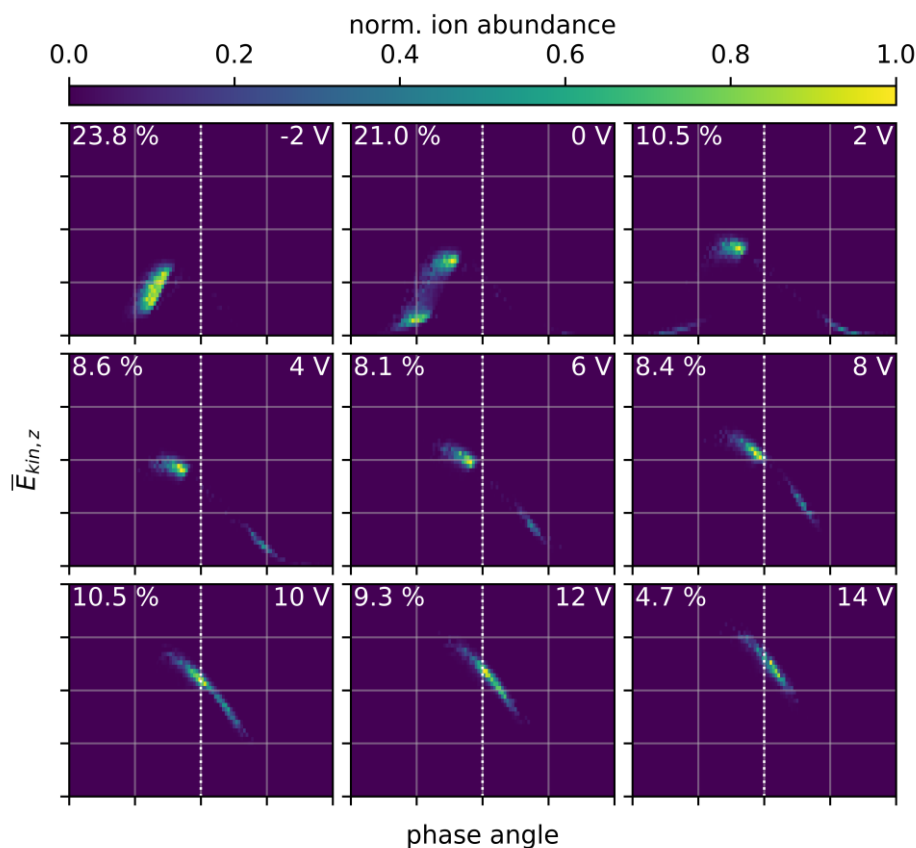


**Figure 38:** Product of the phase-angle-dependent ion acceptance and kinetic energy distributions of ions at the trap entrance, for ions with  $m/z$  100 and an RF voltage of 200 V. The fractions of trapped ions to the total number of ions that enter the ion trap are given in the top left corner of each image. The injection voltages are given in the top right corner of each image. The vertical axes range from 0 eV to 20 eV. The horizontal axes range from  $-180^\circ$  to  $+180^\circ$ .

In conclusion, the shape of the DPR is not only affected by the applied potential barrier, but is always superimposed by the ion acceptance of the ion trap. This explains the deviations between DPR curves obtained from Faraday cup and ion trap measurements. The dependencies of the ion acceptance on the ion  $m/z$ , injection voltage, and RF voltage are reasonably systematic, and this is also reflected in the experimental results. It is emphasized that the DPR is still sensitive to changes of the incident ion KED.

### 3.7.6 DPR data and the actual ion KED

DPR data obtained from ion trap measurements do not necessarily exhibit the expected shape, due to the superimposed ion acceptance of the ion trap (cf. Figure 17). In the range of positive deceleration potentials, i.e., the transfer stage exit po-

tential remains below the reference value, the ion intensity usually exhibits a maximum. When the deceleration potential is decreased the intensity gradually becomes zero. This decrease happens over a deceleration potential range of a few volts to tens of volts, depending on the experimental conditions, i.e., the ion acceptance energy range of the QIT. In some cases, the intensity curve exhibits a second maximum at higher negative deceleration potentials. The FWHM of the DPR curves were found to scale systematically with the respective ions'  $m/z$  or  $q_z$  values. It is of major interest to assess the effects of the actual KED on the observed DPR to obtain information on the actual KED from experimental results. Therefore, two factors are evaluated in DPS simulations:

- 1) The position of the KED (mean kinetic energy)
- 2) The shape, i.e., width and symmetry, of the KED

DPR curves are simulated for three ion species, with  $m/z$  100, 200 and 400, respectively. The ion trap settings are constant for all simulations (RF voltage of 200 V @ 1 MHz). The considered injection voltage ranges from -10 V to +15 V. The deceleration potential  $U_d$  equals the negative injection voltage.

#### *KED position*

As previous results already suggested, the actual KED position, i.e., the mean kinetic energy, cannot be determined from the DPR directly. Figure 39 shows simulated DPR data for different mean ion energies and  $m/z$ . The DPR curves' maximum positions depend on the RF properties. When these properties are fixed, the DPR curves are shifted according to the mean of the initial KED. It is noticeable that the curves run approximately in parallel on the right shoulder of the first maximum. On the left side, their courses partly deviate. At  $q_z = 0.195$  ( $m/z$  100), the intensities decrease slowly and a second maximum occurs. At  $q_z = 0.097$  ( $m/z$  200) and  $q_z = 0.049$  ( $m/z$  400), the curves decrease monotonically. The widths of the DPR curves are larger, the higher the initial mean kinetic energy is, even though the widths of all initial KEDs are the same. This is readily explained by the different fractions of the KED that is probed at each injection voltage and the fringe field modulation of the KED before the ions enter the trap. The ion acceptance of the ion trap is constant for all simulations, but the offered ion ensemble is variable with regard to its KED. At positive injection voltages the complete ion ensemble is entering the ion trap and the ion acceptance is probed with this complete ensemble. The combination of the ion acceptance and the ions KED results in the observed intensity progression. At negative injection voltages (positive  $U_d$ ), a fraction of the ions is deflected from the ion trap and the intensity change is additionally affected

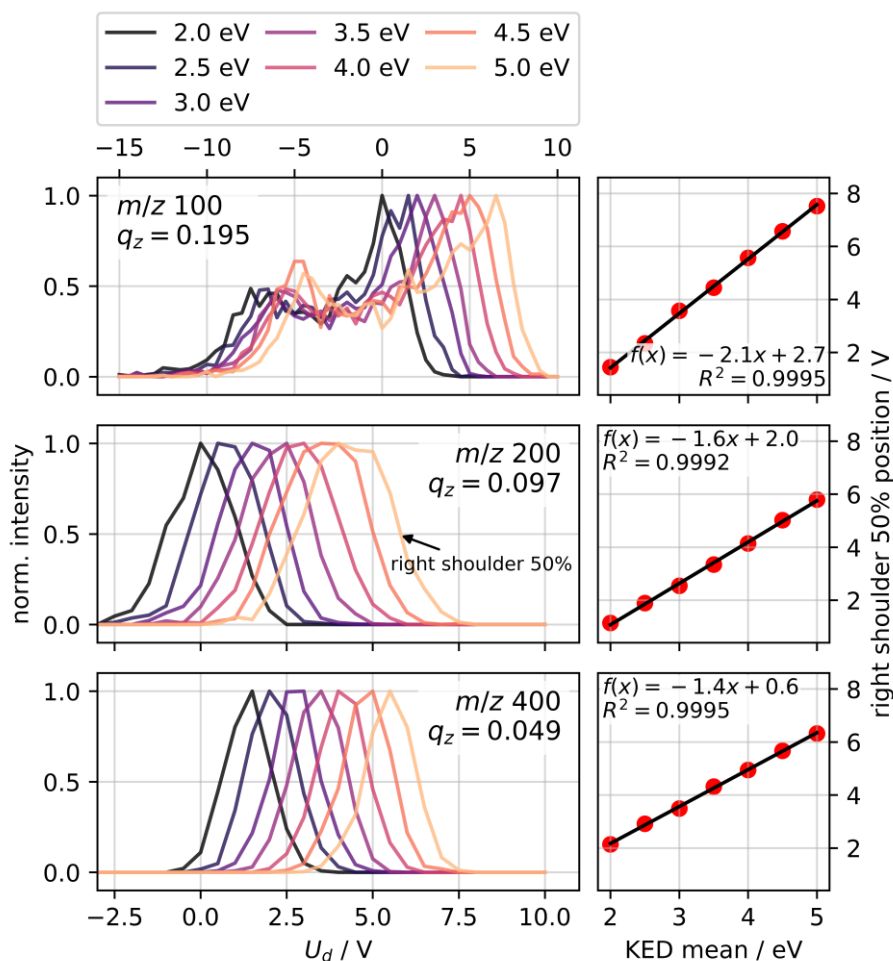


**Figure 39:** Simulated DPR curves for different initial mean kinetic energies of the ion ensemble and  $m/z$  (left) and shift of the DPR curves (right shoulder 50% position) in dependence of the initial mean kinetic energy with linear fits (right). The initial KEDs have Gaussian shapes with a FWHM of 1 eV. The mean energies are given in the legend. Note that the lower and center DPR curves have a different scaling on the  $x$  axis than the upper curve.

by the number of ions that are still detected. This appears to dominate the overall intensity change in the section of the DPR curve to the right of the maximum, which leads to the observed parallel shift of the curves in this region. At lower  $q_z$ , e.g., 0.097 ( $m/z$  200) or 0.049 ( $m/z$  400), the intensities decrease fast after the maximum and do not exhibit a second maximum. For these scenarios, the curves shift also according to the initial mean kinetic energy, but the shape and width is nearly constant. It is concluded that at fixed ion transfer and trap settings, changes of the mean kinetic energy of trapped ions can generally be identified as a parallel shift of the DPR curve in the range of negative injection voltages, i.e., where the actual kinetic energy scan is performed. For a quantitative description the position of the

DPR curves' right shoulders at 50% height are determined. The shift of this position upon changing the initial mean kinetic energy is well described with a linear model (cf. Figure 39, right). The slopes of the resulting fits show quantitatively that the DPR curves are more sensitive to changes of the mean ion energy at higher  $q_z$  values.

### *KED shape*

Changes of the KED's shape, i.e., width and symmetry, are of interest, because that may yield information on the ion formation and desolvation processes. Since the KED is unknown in the experiments, the impact of different KEDs on the corresponding DPR curves is investigated in simulations to support the interpretation of experimental results. DPS simulations with differently shaped initial ion KEDs are executed. The distributions are synthetically created and reflect different conceivable scenarios, e.g., different kinds of asymmetries that may be introduced by non-uniform ion creation. Details on the KEDs are given in Figure 40. The results indicate that it requires careful choice of the ion trap settings and data analysis to distinguish between changes of the KED symmetry and KED broadening. The DPR curves are smoothed with a Savitzki-Golay filter [136] (`scipy.signal.savgol_filter` [26]) with 3<sup>rd</sup> degree polynomials and a window size of 7, to improve clarity. When comparing the three scenarios a), b), and c) in Figure 41, it becomes obvious that  $q_z$  should be as low as possible for this investigation. This leads to the DPR curve with a shape as narrow as possible. At  $q_z = 0.097$  and  $0.049$  the asymmetric broadening of the DPR curve compared to the control (*Gaussian1*) is distin-

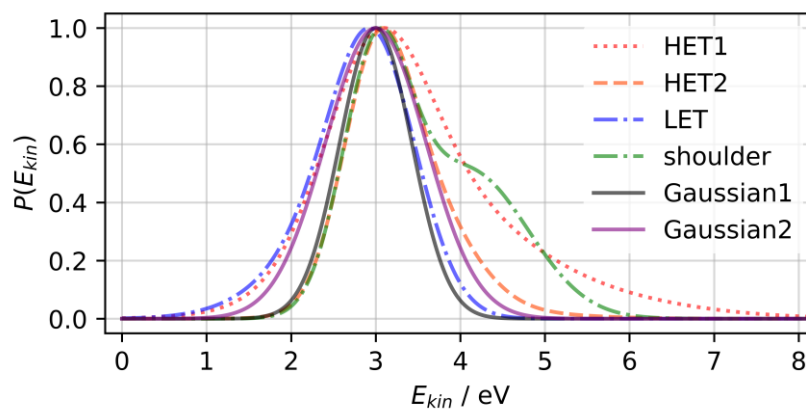


**Figure 40:** Synthetic KEDs with different shapes, created to study the impact of the KED on the DPR in simulations. *HET1* and *HET2* have high energy tails to different extents. *LET* has a low energy tail and *shoulder* exhibits a shoulder on the high energy side. A symmetric Gaussian distribution is shown in black as control. *Gaussian2* is symmetrically broadened compared to *Gaussian1*.

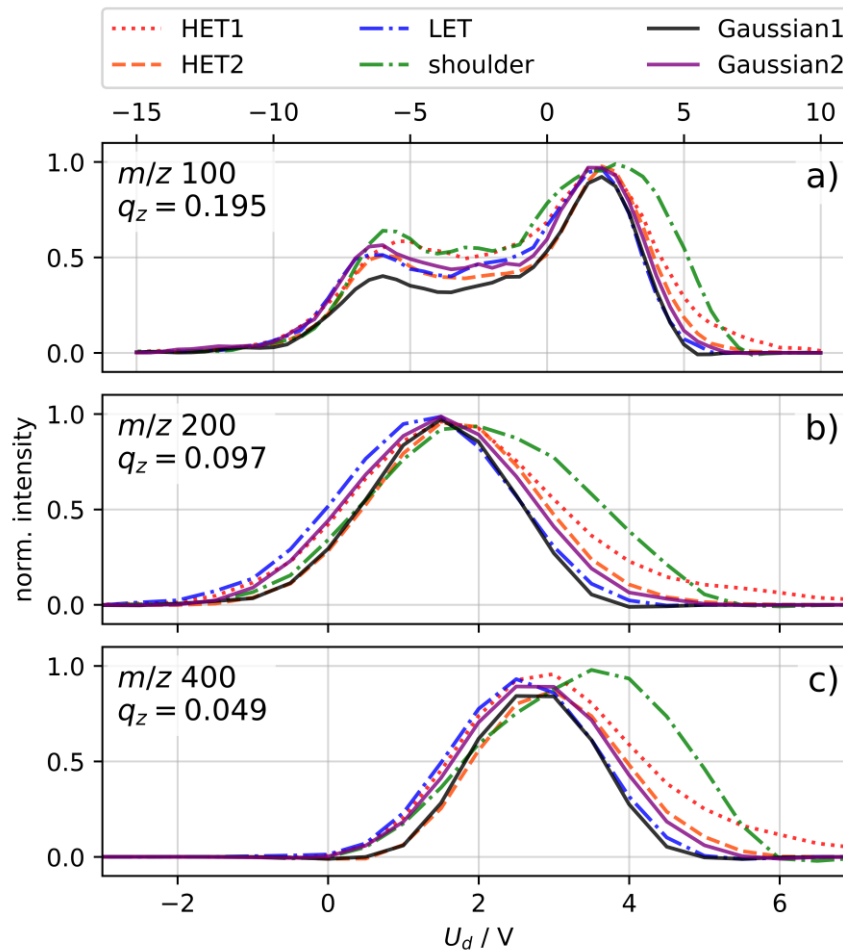


**Figure 41:** Simulated DPR curves with different ion ensembles at different  $q_z$ . The initial KEDs are described above. The control data are shown in black.

guishable from the symmetric broadening. A low energy tail of the initial KED (*LET*) leads to a shift of the left-hand shoulder of the curve to lower  $U_d$ . The right shoulder is not affected. With a high energy tail (*HET1*, *HET2*) the right-hand shoulder shifts to larger deceleration potentials. At  $q_z = 0.195$  the *LET* curve and the symmetrically broadened curve (*Gaussian2*) show little differences. A slight shift of the right shoulder is observable, but this could easily be covered up by noise on the signal. The KED with a shoulder on the high energy side results in significant broadening of the first DPS peak around  $U_d = 2$  V with  $q_z = 0.195$ . At lower  $q_z$ , the peak is significantly broadened ( $q_z = 0.097$ , Figure 41 b)) or the shoulder is directly observable the DPR curve ( $q_z = 0.049$ , Figure 41 c)). This emphasizes again that DPR curves contain the most information on the KED at the lowest possible  $q_z$ . Of course, the accuracy of the DPR curve has a large impact on whether such changes can be detected significantly. In general, the larger the change of the KED the easier

this change can be revealed in a DPS experiment, in comparison to the control experiment (Gaussian1).

In the following, general trends are summarized: A symmetric broadening of the KED results in flattening of the DPR curve on both sides of the first maximum. If a second maximum exists, its intensity increases (compare Gaussian1 and Gaussian2 in Figure 41 a)). A high-energy tail leads to slower increase of the DPR curve's right shoulder. The left shoulder of the first peak is unaffected. If a second maximum exists, an increase of its height is observed (compare Gaussian1 and HET2 in Figure 41 a)). A low-energy tail results in the opposite effect: The right-hand shoulder remains unchanged, but the left flank becomes flatter and the second maximum, if observed, increases in height (compare Gaussian1 and LET in Figure 41 a)).

### **3.8 Application: DPS experiments as a diagnostic tool**

The experimental and numerical results discussed in sections 3.6 and 3.7 show that changes of the KED can be extracted from ion trap DPR data. While the actual KED cannot be determined without knowledge of the energy-dependent ion acceptance of the ion trap, relative changes of the KED can be detected as changes of the intensity progression of a deceleration potential scan. In section 3.6.2 it was already shown that the DPR data from instruments with different ion transfer stages reveal their desolvation capabilities. DPR data measured with the skimmer instrument suggest significantly broader ion KEDs compared to the funnel instrument, owing to their respective means for ion desolvation. In this section, the application of DPS experiments for studying ion dynamics in transfer stages of mass spectrometers is demonstrated.

#### **3.8.1 Combined survival yield and DPS experiments**

The DPS experiments with different acceleration voltages in the ion transfer stage have revealed that complete kinetic re-equilibration takes place in the first and second vacuum stage of the utilized mass spectrometers (section 3.6.1). The Amazon ETD experiments were conducted with a set of thermometer ions (BP ions), which enables estimation of the ions' internal energy distribution  $P(E_{int})$  with the survival yield method, as described in section 3.3.1. The ion properties are given in Table 4 (section 3.3.2). Ion activation was induced by increasing different voltages in the ion transfer stage, namely the RF voltages of funnel 1 and funnel 2, the acceleration voltage between funnel 1 and funnel 2, and the acceleration voltage between funnel 2 and octopole 1. All transfer voltages were set to the values given

in Table 2 (section 3.2.1, *Bruker amaZon ion traps*). For non-RF activation all voltages in the sections of the transfer stage upstream of the activation region were increased by the same value so that only the acceleration voltage in the activation region is changed. For example, the capillary exit and funnel 1 voltages are increased by the same value for activation between funnel 1 and funnel 2 (cf. Figure 6). The standard funnel RF voltages were 196.5 Vpp for funnel 1 and 100 Vpp for funnel 2. These settings resulted in no fragmentation of any of the BP ions.

#### *Survival yield experiments*

The results of the survival yield experiments are shown in Figure 42. At the maximum setpoint for the funnel 1 RF voltage of 400 Vpp, all survival yields are above 80% (purple dots), resulting in an approximated mean internal energy of 1.2 eV. The reduced field strength in funnel 1 is too low for extended fragmentation of the BP ions. The background pressure in funnel 1 is one order of magnitude larger than in funnel 2, with the RF voltages being in the same range. The local pressure in the entrance region of funnel 1 is potentially even higher, due to the supersonic expansion of the capillary effluent.<sup>15</sup> This results in significantly lower reduced field strengths compared to funnel 2. Stronger activation can be achieved by increasing the RF voltage inside funnel 2. At the maximum amplitude of 600 Vpp, the most fragile ion (*p*-CH<sub>3</sub> BP) has a survival yield just above 20%, while the survival yield of the most stable ion (*p*-NO<sub>2</sub> BP) is still at 90%, resulting in a mean internal energy around 2.0 eV (magenta squares). Activation by accelerating ions between funnel 1 and funnel 2 achieves complete fragmentation of the three most fragile BP ions, while the most stable ion has a survival yield below 50% (red diamonds). When the ions are accelerated with 68 V in this region, the mean internal energy is 2.4 eV, which is above the fragmentation energy of *p*-NO<sub>2</sub> BP. The strongest fragmentation is observed when activation is induced between funnel 2 and octopole 1 (orange triangles). In this region, complete fragmentation of all BP ions can be achieved. When the acceleration voltage is set to 26 V the survival yield curve is already underdetermined, as all survival yields are below 20%. From the curve fit a mean internal energy of 2.9 eV can be estimated.

The results are generally as expected: The strongest fragmentation occurs in the experiment in which ions experience the highest reduced field strength, which is when strong activation downstream of funnel 2 takes place (lowest pressure). As

---

<sup>15</sup> The exit pressure of a standard inlet capillary (18 cm length, 0.6 mm i.d.) under choked flow conditions is around 200 mbar [131].

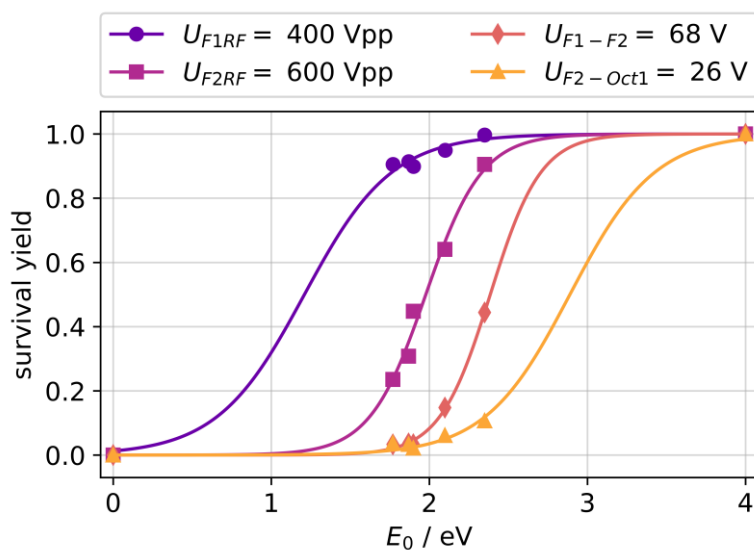


**Figure 42:** Survival yield of benzylpyridinium (BP) ions in dependence of their critical energies  $E_0$  for different activation regions in the amaZon ETD instrument.

the DPS experiments have revealed, the collision number in this region is still sufficiently high for the ions to lose a significant fraction of their kinetic energy gained between funnel 2 and octopole 1, which in turn also enables CID. It is emphasized that the mean internal energies given above are only to be viewed as a qualitative measure. Due to lack of knowledge of the kinetic shift, the absolute position of the kinetic energy distribution is unknown. In fact, the kinetic shift is also variable in the experiments, since activation takes place in different sections of the instrument, which has an impact on the time interval between the activation and detection. Nevertheless, the extent of activation in the different regions is clearly demonstrated in the presented experiments.

The total fragment intensity should be the sum of the intensities of fragments produced in different activation stages, due to the irreversibility of the fragmentation reaction. However, this was not observed in experiments with subsequent RF activation in funnel 1 and funnel 2; the fragmentation response at high funnel 2 RF voltages is unaffected by the funnel 1 RF voltage (data not shown). This can be rationalized in terms of different activation processes prevailing in funnel 1 and 2: It is safe to assume that the capillary effluent contains predominantly solvated ions or even charged droplets when ESI is utilized [133, 134]. Before fragmentation of ions occurs, they must be desolvated. The desolvation process can be promoted by increasing the RF voltage in the first funnel. Collision energies are moderate in funnel 1, due to the comparably high pressure, which promotes cleavage of loosely bound clusters. The reduced field strength inside funnel 2 is potentially higher than in funnel 1, even at low RF voltage settings. When ions are already desolvated

upon entering funnel 2, further activation can lead to fragmentation and the survival yield depends on the RF voltage in funnel 2. At high funnel 2 voltages the reduced field strength is sufficiently high for both desolvation *and* subsequent fragmentation. In both cases, the maximum activation is determined by the collision energy in funnel 2.

Activation induced by the axial acceleration voltage between funnel 1 and 2 achieves stronger fragmentation than RF activation in funnel 2 only. This implies that ions attain higher kinetic energies and therefore collision energies by the axial acceleration than at high RF voltages in funnel 2. The radial focusing force in the funnel depends on the ion distance to the electrodes. A change of the ion beam shape due to the increased acceleration voltage, resulting in an overall larger beam diameter in funnel 2 can also contribute to both declustering and fragmentation.

#### *DPS experiments*

DPR data were recorded for the settings in the survival yield experiments. As already discussed, the BP precursor ions' DPR curves are not affected by changes of acceleration voltages upstream of/within funnel 2. However, the DPR curves of fragment ions of all BP precursor ions, except *p*-NO<sub>2</sub> BP, respond to changes of these activation voltages. Representative DPR curves of the *p*-F BP fragment ion are shown in Figure 43. When fragmentation is induced via the acceleration voltage between funnel 1 and funnel 2 or funnel 2 RF voltage, the second maximum (located at negative  $U_d$ ) of the DPR gains intensity relative to the first maximum. The curve shape at positive  $U_d$  remains constant. The curve shape at low activation settings is interesting by its nature, as the second maximum has a larger intensity than the first maximum. This is in contrast to all previous DPS experiments as well as simulations and suggests the presence of a prominent low energy tail in the KED. A similar effect was reported in section 3.7.2 when a changing CCS was assumed in the region between the second and third vacuum stage. The fragment ions exhibit smaller CCS values than the precursor ions. The change of CCS upon fragmentation is not gradually as in the simulations but occurs instantaneously, which can explain the pronounced effect on the DPR. Therefore, an upstream shift of the fragmentation region of the corresponding ions from the transition region behind funnel 2 is a reasonable explanation for the accompanied behavior of the low energy tail when the activation voltage is increased.

The DPR curves of the precursor ions in dependence of the acceleration voltage between funnel 2 and octopole 1 show the expected shift towards larger  $U_d$  and therefore larger mean kinetic energies, when the acceleration voltage is increased

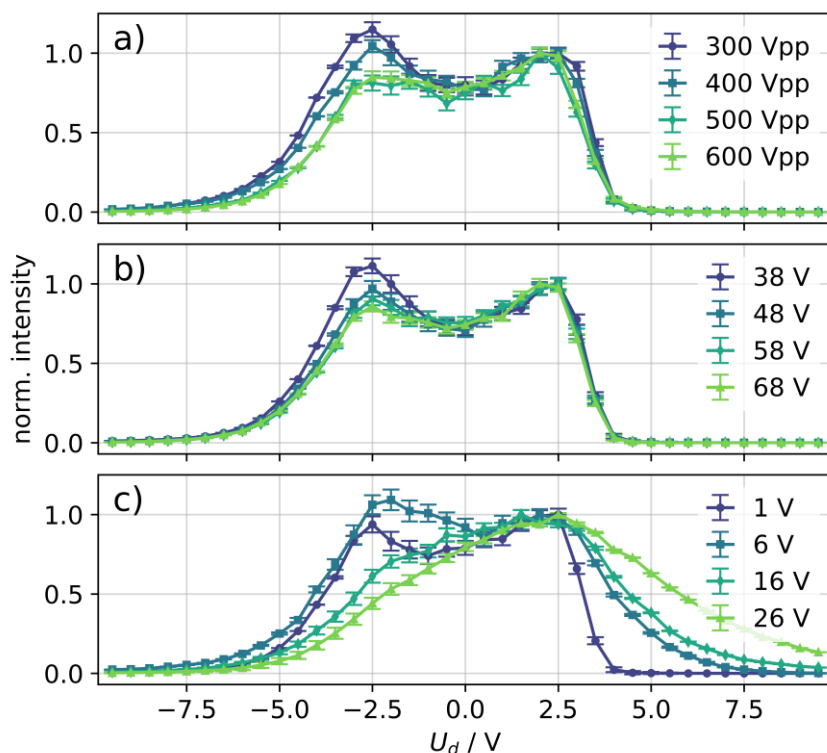


**Figure 43:** DPR curves of the *p*-F BP fragment ion ( $m/z$  109) in different activation experiments: a) Funnel 2 RF voltage, b) acceleration voltage funnel 1-funnel 2, c) acceleration voltage funnel 2-octopole 1. Data are normalized to the maximum at positive  $U_d$ .

from 1 to 16 V. Simultaneously, the curves become significantly skewed towards the right-hand side, which corresponds to a pronounced high energy tail of the KED. Below 16 V acceleration voltage the DPR curves scale with  $m/z$ , as expected from the  $m/z$ -dependent ion acceptance of the QIT. This was also the case in the experiments with activation between funnel 1 and 2 and inside funnel 2. At 16 V and 26 V acceleration voltage this trend changes, and the curves scale with the stability of the precursor ions, i.e., the lower the fragmentation energy, the lower the intensity at high  $U_d$ . For the most fragile BP ions, the KED's high energy tail is strongly depleted. This suggests fragmentation occurring inside the ion trap. Fast ions that would be detected at high deceleration potentials are removed from the mass spectrum due to fragmentation, leading to a depletion of the high energy side of the KED. This effect scales with the fragmentation energy. The scaling according to fragmentation energy is not as pronounced in the DPR curves of the fragment ions, which is a result of the different ion acceptance distributions for the precursor and fragment ions.

The results presented above demonstrate that DPS experiments can reveal effects that are not easily derived from the extent of fragmentation in a survival yield

experiment and, thus, can complement the interpretation thereof. Usually, the survival yield method is applied when information on the internal energy deposition is required, e.g., for characterizing the “harshness” of an ionization technique [65, 67, 119]. DPS experiments provide a means for exposing accompanied changes of ion dynamics in the intermediate part of the ion transfer stage. These effects can be projected onto changes in the upstream region and potentially even in the ion source, if source parameters are varied during the experiments, as will be demonstrated in the following sections.

Finally, it is emphasized that changes of acceleration voltages, especially in the intermediate pressure region of the ion transfer stage, can significantly alter the results of a survival yield experiment. Fragmentation is easily achieved in this region and the impact of acceleration voltages on the fragmentation extent should be carefully evaluated. The energy-dependent ion acceptance needs also to be considered when using trapping devices, which makes it very difficult to evaluate the “true” survival yield of an ion using such instruments.

#### **3.8.2 Sensing changes of the ion evolution during ESI**

The ion formation process in electrospray ionization is still under discussion [74, 75]. It is reasonable to assume that a large fraction of ions is still solvated when they enter the vacuum system of a mass spectrometer, since ions still undergo high numbers of collisions even at intermediate pressure (e.g., in or below the millibar range). Ion-solvent clusters will always be formed under these conditions when polar compounds, e.g., typical solvents used in ESI experiments, are present in the matrix gas [34, 56]. CID of these clusters takes place in the ion transfer stage by applying suitable declustering potentials [35, 137]. Even though the presence of solvent clusters in the vacuum interface is an acknowledged fact in the MS community, they are often left out of discussions regarding the ion formation process. There is also evidence for ESI-generated charged droplets penetrating deeply into vacuum systems of mass spectrometers [133, 134] and their role in the ion formation process is currently under investigation. The abundance of cluster signals in mass spectra is closely related to experimental conditions in the ion source and ion transfer stage. Usually, these conditions are tailored to suppress cluster ions, as they would increase the noise level and complexity in the acquired mass spectra.

##### *Impact of the electrospray voltage*

DPS experiments are performed with the HCTplus and amaZon Speed ETD with ESI voltages set to 1500 V and 4500 V, respectively. Sodium formate is used as analyte. Exemplary DPR curves from EICs are shown in Figure 44. The DPR curves

respond to the change of spray voltage. For all sodium formate ions, the observed change is systematic, i.e., the curves are shifted to lower deceleration potentials as the ESI voltage is decreased, corresponding to a lower average kinetic energy. This is surprising, because changes of acceleration voltages downstream of the ion source, i.e., in the first and second vacuum stages, did not change the DPR at all. Consequently, the ESI voltage cannot directly contribute to the ion kinetic energy at the exit of the transfer stage. In addition to the DPR curve shift, the relative abundance of larger cluster signals in mass spectra is promoted when the ESI voltage is changed to 1500 V. Reducing the ESI voltage has two direct consequences: The potential gradient inside the capillary flattens and the size of primary droplets increases [138]. Note that in Bruker Apollo type API sources (APCI/ESI) the spray needle is grounded and the capillary entrance potential is negatively biased for ESI in positive ion mode.

In the ESI source, ions will either reside in charged droplets or will be solvated by polar solvent molecules [56]. Within the transfer capillary, the clustered ions and droplets are dragged along by the neutral gas. From the capillary entrance

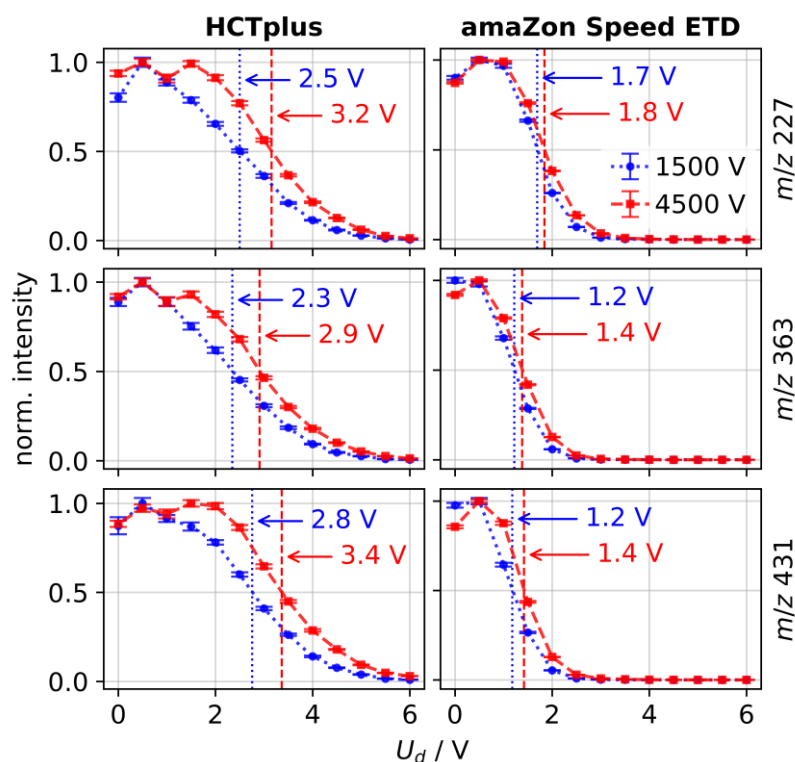


**Figure 44:** DPR curves for  $[(\text{HCO}_2\text{Na})_n\text{Na}]^+$ ,  $n = 3, 5, 6$  ( $m/z$  227, 363, 431), recorded at different ESI voltages (red dots: 4500 V, blue squares: 1500 V) with the HCTplus (left) and amaZon Speed ETD instrument (right). The vertical lines indicate the 50% height positions, which corresponds roughly to the median kinetic energy.

(e.g. -4500 V) to the exit (e.g. +100 V), the potential gradient is repulsive. Decreasing the ESI voltage, which is applied between the *grounded* spray needle and the capillary entrance reduces the repulsive potential barrier. This would lead to an increased ion energy in a collision-free environment. However, this is not the case inside the capillary and adjacent regions. Assuming an electric field of 260 V/cm (ESI voltage of 4500 V) over the entire length of the capillary, the gained kinetic energy between two collisions is in the range of  $1.5 \cdot 10^{-3}$  eV at the capillary entrance (atmospheric pressure, mean free path for  $N_2$ :  $5.9 \cdot 10^{-6}$  cm) and  $7.8 \cdot 10^{-3}$  eV at the capillary exit (200 mbar, mean free path for  $N_2$ :  $3.0 \cdot 10^{-5}$  cm). Both values are far below the mean thermal energy of the background gas (around  $25 \cdot 10^{-3}$  eV for  $N_2$  at 298 K). When the ESI voltage is decreased to 1500 V, the gained energy between two collisions decreases also. Therefore, it is impossible for the ESI voltage to impact on the ion KED at the transfer stage exit and the observation cannot be explained with a direct interaction of ions with the ESI voltage in the ion source region.

It was shown in section 3.6.1 that the acceleration voltages between the capillary exit and octopole 1 (HCTplus) or capillary exit and funnel 2 (amaZon) do not impact on the DPR, which was attributed to the high collision rate in this region, resulting in re-equilibration with the background gas in octopole 1/funnel 2.<sup>16</sup> An effect on the DPR was observed only in the transition region into collision free conditions, between octopole 1 and octopole 2/funnel 2 and octopole 1. Thus, the final ion energy is dominated by the axial acceleration voltage (energy gain) and pressure gradient (energy loss) in this region. The kinetic energy in the upstream part of the transfer stage is thus negligible. In the transition region, the acceleration voltage affected also the cluster signal distribution. A higher acceleration voltage shifted the distribution to smaller clusters. This dependency indicates ion activation (cluster dissociation), and was not observed when the acceleration voltage was increased in the upstream part of the transfer stage.

Additional experiments are carried out with the HCTplus instrument with different pressures in the transfer stage. This is achieved by changing the pumping speed of the roughing pump with a dosing valve. The pressure in the first vacuum stage is varied between 2.8 and 5.2 mbar. As the pressure is increased, the DPR curve is shifted to lower deceleration potentials, indicating a decrease of the aver-

---

<sup>16</sup> The collision number of an ion ( $m/z$  159, CCS  $132 \text{ \AA}^2$ ) traveling through octopole 1 (length 4.5 cm) is estimated to 1600 (pressure 0.36 mbar, temperature 300 K). In reality this number is potentially higher, as it does not include the ion oscillation in the RF field.

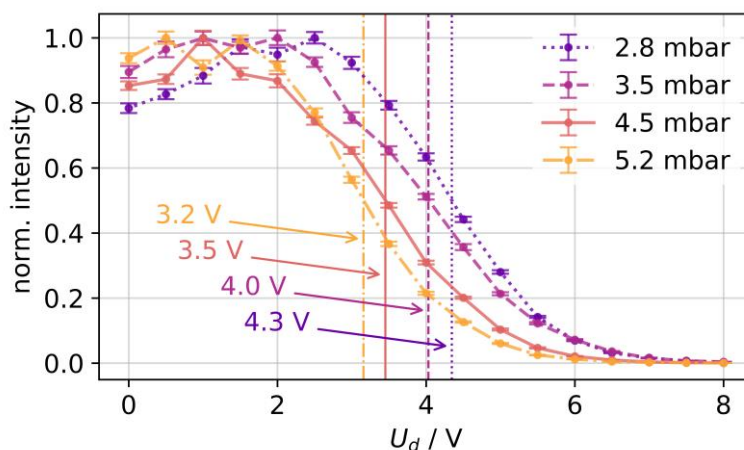


**Figure 45:** DPR curves for  $[(\text{HCO}_2\text{Na})_3+\text{Na}]^+$  ( $m/z$  227) obtained at different pressures in the first vacuum stage of the HCTplus ion trap.

age ion energy (Figure 45). At the same time, the cluster distribution shifts to larger cluster sizes. The pressure change also affects the pressure gradients in the downstream part of the transfer stage, most pronounced in the second vacuum stage and the entrance region of the third stage. Thus, the reduced field strengths in these regions change accordingly, which impacts the degree of CID. The change of the collision number leads to a shift of the average ion energy.

Considering the experimental results described above, the spray-voltage-dependence of the DPR curve is most likely a *mobility* effect. The drift velocity  $v_d$  of an ion is proportional to the electric field strength  $E$  and the ion mobility  $K$  (eq. (3-2)). As discussed before, the field strength between the capillary exit and octopole 1 has no impact on the DPR, due to re-equilibration with the background gas inside octopole 1. Downstream of octopole 1, the field dependency is observed, because of the sufficiently low collision number. When  $E$  is constant, the drift velocity depends only on the ion mobility. The mobility scales inversely with the gas number density  $N$  and the collision cross section  $\Omega$ , according to the Mason-Schamp equation (eq. (3-3)). Therefore, increasing the pressure decreases the drift velocity. This is in agreement with the pressure variation experiments. For the CCS to have an impact on the DPR, it must change in the region downstream of octopole 1. Consequently, ions must not be completely desolvated when exiting octopole 1. An extension of the desolvation process is a logical consequence of an increase of the initial droplet size. This matches the simulation results presented in section 3.7.2 regarding the impact of incomplete desolvation. The different magnitude of the ESI voltage dependency is also in accordance with this rationale. In the HCT-plus data, the observed DPS shift is significantly larger than in the amaZon data. The 50% height position is determined to quantify the shift, which is depicted in

Figure 44. In the HCTplus experiments the curve shifts are in the range of 0.6 V, whereas in the amaZon experiments a shift of about 0.2 V is observed (compare left and right panels in Figure 44). The difference between the two instruments is readily explained by their different vacuum interface designs, which was already discussed in section 3.6.2. The funnel inlet of the amaZon Speed ETD achieves better desolvation than the skimmer inlet of the HCTplus and, thus, minimizes the lifetime of clusters and droplets and related effects. Also, the dry gas flow is lower in the HCTplus experiments than in the amaZon experiments (1.5 vs. 4.0 L/min). A higher dry gas flow promotes desolvation, which agrees with the results. Finally, the off-axis positioning of the transfer capillary in the amaZon instrument also contributes to the desolvation capabilities, as it directs the capillary effluent towards the funnel electrodes, where the field strength is highest.

In summary, all experimental observations agree with the mobility hypothesis. The impact of the ESI voltage on the size of primarily generated droplets is, to the best of the present knowledge, the only reasonable explanation for the experimental observations. The present results strongly suggest that ion desolvation is not necessarily completed in the first vacuum stage, but may only be achieved in deeper parts of the mass spectrometer. At the moment it is unclear, to what extent charged droplets contribute to ion signals observed in mass spectra. This matter is the subject of current research.

#### *Impact of chemical modifiers*

In a recent publication [59] the impact of solvent vapor (chemical modifiers) added to the background gas of a nano-electrospray ionization (nESI) source on the detected ion population, especially on the ratio of different charge states, of Substance P (SP) was evaluated. A charge retention/depletion model was proposed based on the experimental observations and is briefly summarized in the following. Polar protic and polar aprotic modifiers show opposing effects on the recorded mass spectra, i.e., a decrease or an increase of the average charge state of SP, respectively. This is attributed to the different bonding properties of the modifier groups. Protic modifiers (e.g., water, methanol, ammonia) form large hydrogen-bonded clusters, whose proton affinities (PA) scale with the cluster size [139]. These clusters can deprotonate analyte ions (charge depletion). Aprotic modifiers (e.g., acetonitrile, acetone) can only form one hydrogen bond, which limits the size, and thus PA, of pure modifier clusters [140]. These modifiers also readily interact with protonated analyte ions and protect the charge from loss processes (charge retention). In addition, adding a modifier abundantly to the matrix gas of the nESI

source extends the droplet evaporation process and changes the final droplet composition in favor of the modifier. Thus, the chemical environment that ions experience inside the mass spectrometer is heavily dominated by the modifier.

DPS experiments are performed with the same experimental setup and conditions as described in [59], i.e., with the nESI source and Bruker micrOTOF instrument. The deceleration potential is applied between the second skimmer and the second hexapole. The standard acceleration voltage is 1.7 V. The potentials of all transfer elements upstream of the second hexapole are gradually changed by the same value, within the range from 0 to -5 V relative to the standard settings given in Table 3 (section 3.2.1, *Bruker micrOTOF*), which corresponds to a deceleration potential of 0 to 5 V.

A solution of SP (1  $\mu\text{mol/L}$ ) in acetonitrile/water (1/1) and 0.1% formic acid is used as analyte. Chemical modifiers are added to the background gas of the nESI source. Triply ( $\text{SP}^{3+}$ ) and doubly protonated SP ions ( $\text{SP}^{2+}$ ) are detected in the experiments. In general,  $\text{SP}^{3+}$ -modifier clusters appear in mass spectra when aprotic modifiers are used. With protic modifiers, no clusters are detected.

Without any modifier, the DPR of  $\text{SP}^{2+}$  and  $\text{SP}^{3+}$  differ slightly (cf. yellow traces in Figure 46). For  $\text{SP}^{2+}$ , the intensity increases strongly between 3.5 V and 3.0 V, and saturates at  $\leq 2.0$  V. This implies, that ions exhibit a KED between zero and 3.5 eV, with a low energy tail and narrow peak around 3.0 - 3.5 eV before entering

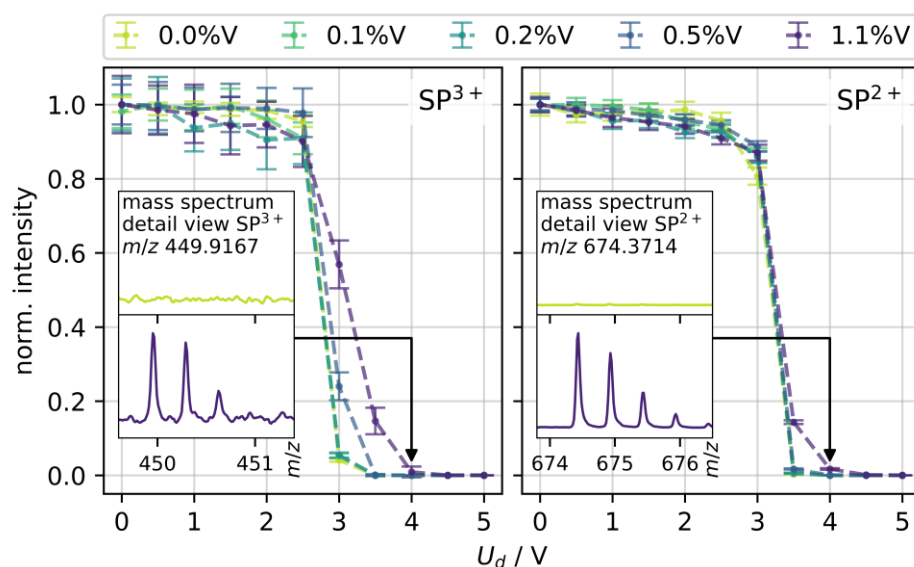


**Figure 46:** DPR data of  $\text{SP}^{3+}$  (left) and  $\text{SP}^{2+}$  ions (right), obtained with the micrOTOF instrument. Methanol is added to the ion source as chemical modifier. Selected excerpts of the mass spectra are embedded in the plots. The methanol mixing ratios are given in the legend.

the hexapole. The  $SP^{3+}$  trace is slightly shifted to smaller deceleration potentials. The curve increases from zero to maximum intensity between 2.5 V and 3.0 V and is more symmetric around the inflection point. The widths of the DPR curves are noticeable when compared with the ion trap experiments (cf. section 3.5). Even though the transfer stages are not entirely identical in the HCTplus and micrOTOF instruments, their principal design is rather similar. Thus, broadening of the KED of ions exiting the transfer stage occurs mainly in the second transfer multipole. The experiments with variable acceleration voltages in the first and second vacuum stage (section 3.6.1) and the DPS simulations (section 3.7.2) further support this conclusion. The differences of the  $SP^{3+}$  and  $SP^{2+}$  data in the present experiments must originate in the upstream part of the DPS region.

The  $SP^{3+}$  signal is depleted when methanol is used as chemical modifier. As seen in Figure 46, the DPS response of the remaining  $SP^{3+}$  ion signal changes significantly. When the methanol mixing ratio is increased, the  $SP^{3+}$  curve's inflection point shifts to larger  $U_d$  and the curve becomes flatter, representing a broadening of the KED on the high energy side. The same is observed for  $SP^{2+}$ , but much less pronounced and only at the highest methanol mixing ratio of 1.1%V. The ions' KED is determined by the electric fields and collisions in the ion transfer stage. When a change of the KED is detected between the second skimmer and hexapole, this change must have taken place upstream of this region. Since the transfer voltages are constant for all experiments, the observed change must be a direct result of the altered ion release and/or desolvation processes. CID experiments have revealed, that the release of bare SP ions is delayed when a modifier is added [59]. It was shown in section 3.7.2 that broadening of the KED in the low-energy part occurs when the desolvation process is non-uniform (cf. Figure 30). The delayed desolvation leading to a spread of the ion release region is a feasible explanation for the observed KED changes in the low energy region (cf. Figure 46,  $U_d < 3$  V). However, the intensity increase in the high-energy regime is the more prominent change of the DPR curve with MeOH addition and this cannot be explained solely with delayed desolvation. It is unlikely that ions will gain or retain higher kinetic energies in the collision-dominated upstream part of the ion transfer stage. Another hypothesis for the increased abundance of high-energy ions when MeOH is used as chemical modifier in the experiments is based on charged droplets generated by ESI that penetrate into the instrument's vacuum system. Such droplets exhibit significantly larger collision cross sections than bare gas phase ions and will therefore more strongly interact with the background gas. The gas is accelerated axially during the transition between the second and third vacuum stage, due to the pressure gradient. It is conceivable that droplets are pushed past the potential barrier by

the gas. Analyte ions that are transported within the droplets to be released downstream of the barrier could explain the increased intensity of high-energy ions observed when MeOH is used as modifier. Additionally, this mechanism would also account for the “survival” of  $SP^{3+}$  ions, because they are released into the gas phase only in a near-collision-free region where charge depletion by the chemical modifier cannot occur anymore. This rationale is supported by a recent study that presents strong evidence for the presence of charged droplets inside the vacuum systems of different commercial mass spectrometers [134]. It is emphasized that the observed high-energy tail is not due to increased noise in the spectra. SP ions are clearly detected, as can be seen in the bottom parts of the inset spectra in Figure 46.

Qualitatively, the same effect is observed for  $SP^{3+}$  and  $[SP^{3+}+ACN]$  when acetonitrile is used as modifier. The results of the corresponding experiments are shown in Figure 47. The DPR curve broadens in the high energy range as the acetonitrile mixing ratio is increased, indicating a high energy tail in the KED. In addition, the slope in the range between 0 V and 2.5 V changes systematically, which suggests a promoted low energy tail at higher acetonitrile mixing ratios. A similar trend is detected for  $SP^{2+}$  in the range between 0 and 3.0 V. At 4.7%V acetonitrile mixing ratio, the curve strongly resembles the curves of  $SP^{3+}$  and  $[SP^{3+}+ACN]$ . This supports the notion of delayed  $SP^{2+}$  ion formation from  $SP^{3+}$  *downstream* of the DPS region from charged droplets.

CID experiments have revealed that ions are heavily solvated when a modifier is added, as it completely suppresses fragmentation in the first vacuum stage. Additional CID experiments are performed with acetonitrile as chemical modifier. When ions are activated between skimmer 2 and hexapole 2, a change of the  $SP^{3+}/[SP^{3+}+ACN]$  signal intensity ratio is observed. Both signals change in the opposite direction, which implies that  $SP^{3+}$  is formed by dissociation of  $[SP^{3+}+ACN]$  clusters. At an acceleration voltage of 6.7 V the  $SP^{3+}$  signal becomes the base peak of the mass spectrum. At higher acceleration voltages, fragmentation of SP ions sets in and both the  $SP^{3+}$  and  $[SP^{3+}+ACN]$  signals decrease, while their ratio remains constant. It is conceivable that both the declustering and fragmentation reactions become collision-controlled due to the high collision energy. The collision probability for bare  $SP^{3+}$  and its first ACN cluster should be similar, because the size of ACN is negligible compared to SP, which results in comparable collision numbers.

Even though the DPS results are not entirely understood, they illustrate that adding a chemical modifier to the nano-electrospray experiments has a strong im-

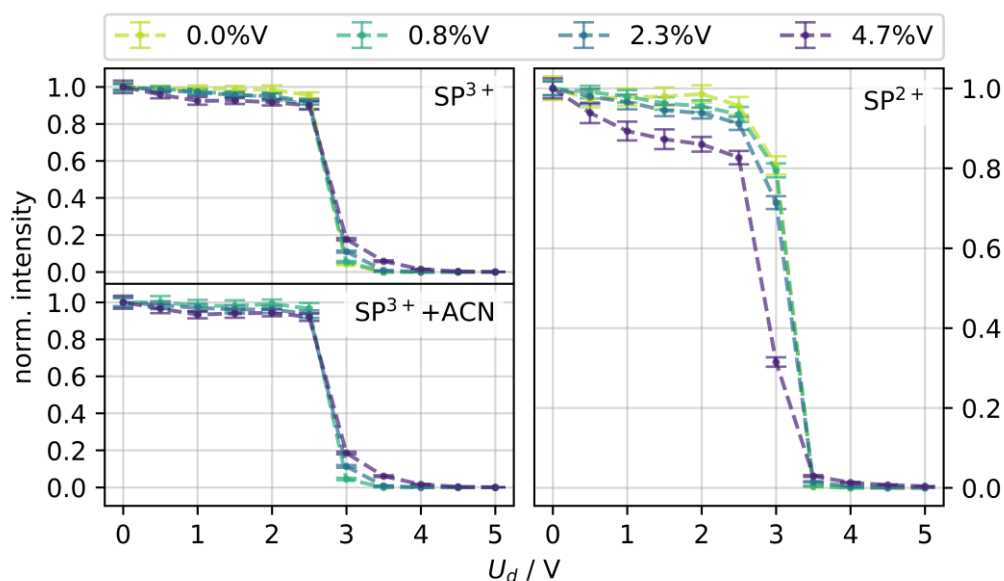


**Figure 47:** DPR curves of SP ions (SP<sup>2+</sup>, SP<sup>3+</sup>, [SP<sup>3+</sup>+ACN]), obtained with the microTOF instrument. Acetonitrile (ACN) is added to the ion source as chemical modifier. The acetonitrile mixing ratios are given in the legend.

impact on the ion dynamics in the transfer stage. The observed shifts of the KED must result from changes of the ion release or desolvation process. The CID experiments reveal that the desolvation process can be significantly delayed at selected experimental conditions. In the discussion on charged droplets being present in mass spectrometer transfer stages, the results from this work emerge in a new context.

### 3.9 Summary and outlook

The implementation, characterization, and application of the DPS method for determining kinetic energy distributions in ESI-MS was presented in this chapter. The occurrence of DPR curves was evaluated under different experimental conditions and interpretation of data was supported by computational modeling of gas and ion dynamics in the ion transfer stage and QIT. This combined approach has revealed the systematic impact of the energy-dependent ion acceptance of the QIT on the DPR curve shape and enabled interpretation thereof with regard to changes of the KED of ions inside the transfer stage. The DPR curves obtained from Faraday cup and QIT measurements exhibit significant differences and only the former allows for determination of actual kinetic energy distributions. However, the QIT DPR curves still contain the kinetic energy information and more importantly are sensitive towards changes of the KED. It follows that the DPS method can be utilized for studying the impact of experimental conditions on ion dynamics that translates into kinetic energy shifts and is not directly discernible in mass spectra,

e.g., the re-equilibration of ions inside the transfer stage. Ion ensembles and single ion species can be analyzed when mass resolved data are available.

The complementary application of the DPS method with survival yield experiments leads to additional information regarding the activation mechanisms in different sections of the ion transfer stage. These results emphasize the complexity of processes inside a mass spectrometer, which are often coupled to multiple parameters. The survival yield is easily shifted significantly by slight changes of the acceleration voltages in the transfer stage and it should be carefully evaluated if such shifts are the result of actual changes of the internal energy, or are caused by the transfer properties and interactions with the mass analyzer.

DPS experiments showed clearly that the skimmer inlet stage of the HCTplus ion trap makes this instrument sensitive even to changes in the ion source or vacuum interface region. It can therefore be utilized to study droplet and ion dynamics in the inlet region in ESI experiments. The dual funnel inlet stage of the amaZon ion trap instruments achieves much better desolvation, which essentially destroys the information on the temporal evolution of droplets and the release of ions. Even though this is the desired performance for analytical applications, it limits the use of such an instrument for studying ion dynamics that occur in the ion source and vacuum interface region. The off-axis alignment of the inlet capillary may very well contribute to this process, as it forces all constituents of the capillary effluent to approach the funnel electrodes, where the electric field strength is highest. These findings highlight the potential superior usability of 'older' MS systems for *fundamental* studies.

The DPS method is easily implemented, provided that complete control over transfer voltages is available. This is probably the biggest limitation, since MS manufacturers often only provide partial control over voltages and modern control software is usually tailored to match requirements for analytical applications. In this case, close collaboration with technical support or development departments of the instrument vendors is essential.

DPS experiments can potentially be of benefit for different fields of fundamental research in mass spectrometry instrumentation and API-related ion dynamics. The results presented in this work were mainly obtained with Bruker ion trap mass spectrometers. There is no restriction of the method regarding other API mass spectrometers, except that energy-dependent interactions of ions with different mass analyzers need to be characterized. It was shown, that the skimmer and funnel inlet stages behaved differently regarding the sensitivity to changes of ion source parameters. The study of desolvation capabilities of different inlet stages can be further expanded, e.g., capillary-skimmer vs. nozzle-skimmer stages.

Also, kinetic energy effects in tandem mass spectrometers with dedicated collision cells (e.g., QTOF, triple quadrupole) or ion mobility devices (e.g., trapped ion mobility [141], travelling wave ion mobility [142], differential mobility spectrometry [143]) can be studied. The role of charged droplets in ESI-MS was briefly addressed in section 3.8.2. It is feasible, that DPS experiments can provide an additional tool for understanding the droplet evolution process. This is especially promising in combination with an instrument with a “soft” sampling stage, such as the Bruker HCTplus device.

## 3.10 Appendix

### 3.10.1 Fitting functions and optimized parameters used in 3.7.1

The functions used for fitting the pressure and velocity data obtained from DSMC simulations, as well as the corresponding optimized parameters are given below:

$$f_1(x) = a \cdot e^{\frac{b}{x^d+c}} \quad (3-9)$$

$$f_2(x) = a \cdot x + b \quad (3-10)$$

$$f_3(x) = a \cdot (x + b)^2 + c \quad (3-11)$$

$$f_4(x) = a \cdot b^{x+c} \quad (3-12)$$

$$f_5(x) = a \cdot e^{\frac{(x-b)^2}{2 \cdot c^2}} + d \quad (3-13)$$

$$f_6(x) = \sum_{i=1}^2 a_i \cdot e^{\frac{(x-b_i)^2}{2 \cdot c_i^2}} \quad (3-14)$$

**Table 11:** Optimized parameters for the pressure data fits

segment	eq.	a	b	c	d
1 (purple)	(3-11)	$-5.13 \cdot 10^{-4}$	$1.51 \cdot 10^1$	$2.89 \cdot 10^{-1}$	-
2 (blue)	(3-9)	$3.66 \cdot 10^{-3}$	$2.98 \cdot 10^1$	1.16	7.81
3 (orange)	(3-9)	$1.08 \cdot 10^{-3}$	$4.52 \cdot 10^4$	3.77	$1.40 \cdot 10^4$
4 (green)	(3-10)	$-7.24 \cdot 10^{-6}$	$1.29 \cdot 10^{-3}$	-	-
5 (red)	(3-12)	$2.21 \cdot 10^1$	$5.21 \cdot 10^{-1}$	$-1.13 \cdot 10^2$	-
6 (dark red)	(3-10)	0	$1.00 \cdot 10^{-5}$	-	-

**Table 12:** Optimized parameters for the velocity data fits

segment	eq.		a	b	c	d
1 (purple)	(3-10)		3.22	$5.44 \cdot 10^1$	-	-
2 (blue)	(3-14)	$i=1$	$1.42 \cdot 10^2$	$-8.39 \cdot 10^1$	-4.80	-
		$i=2$	$1.92 \cdot 10^2$	1.47	2.33	-
3 (orange)	(3-12)		$1.86 \cdot 10^1$	1.03	$5.73 \cdot 10^1$	-
4 (green)	(3-12)		$6.64 \cdot 10^1$	$9.77 \cdot 10^{-1}$	$-5.18 \cdot 10^1$	-
5 (red)	(3-13)		$7.03 \cdot 10^1$	$1.32 \cdot 10^2$	1.26	$-5.29 \cdot 10^{-1}$

## 4 Modeling of an FT ion trap

The Zeiss iTrap<sup>17</sup> is an FT-based quadrupole ion trap mass spectrometer developed for monitoring of semiconductor-related processes. The instrument utilizes a pulsed gas inlet in combination with in-trap electron ionization (EI). This results in a complex interplay of varying parameters during the measurement that are difficult to assess individually in an experimental approach. In this chapter, different stages during the data acquisition cycle are studied with numerical simulations to characterize the fundamental processes that impact the outcome of an experiment. This allows the separate treatment of different aspects, including the transient pressure profile, the interaction of the ionizing electron beam with the quadrupolar field, and ion-neutral and ion-ion interactions. The results can be merged stepwise to obtain a comprehensive model of the entire data acquisition cycle.

The sections in the data acquisition cycle have different requirements regarding the simulations and data analysis. SPARTA (cf. section 2.3) is used for modeling of Knudsen and molecular flow dynamics with the DSMC method. Electron and ion trajectory simulations in electric fields are conducted with SIMION (cf. section 2.2). In addition, IDSimF (cf. section 2.1) enables ion trajectory simulations with consideration of space charge with large particle numbers. An overview of the simulation workflow is given in Figure 48.

### 4.1 Introduction

The foundation for quadrupole ion trap mass spectrometry was laid in 1953 by Wolfgang Paul and coworkers with the first publication on the mass-selective storage of ions in quadrupolar fields [144] and early experimental results with a prototype instrument [145]. While the first commercial quadrupole *mass filters* became available in the 1960s [146, 147], the introduction of commercial quadrupole *ion trap* mass spectrometers was not until the 1980s and was only made possible by the discovery that operating ion traps at an increased gas pressure significantly increases both sensitivity and mass resolution [106, 148, 149]. Nondestructive ion

---

<sup>17</sup> The iTrap technology was acquired by the Atlas Copco Group in 2020 and integrated into its subsidiary Edwards Vacuum.

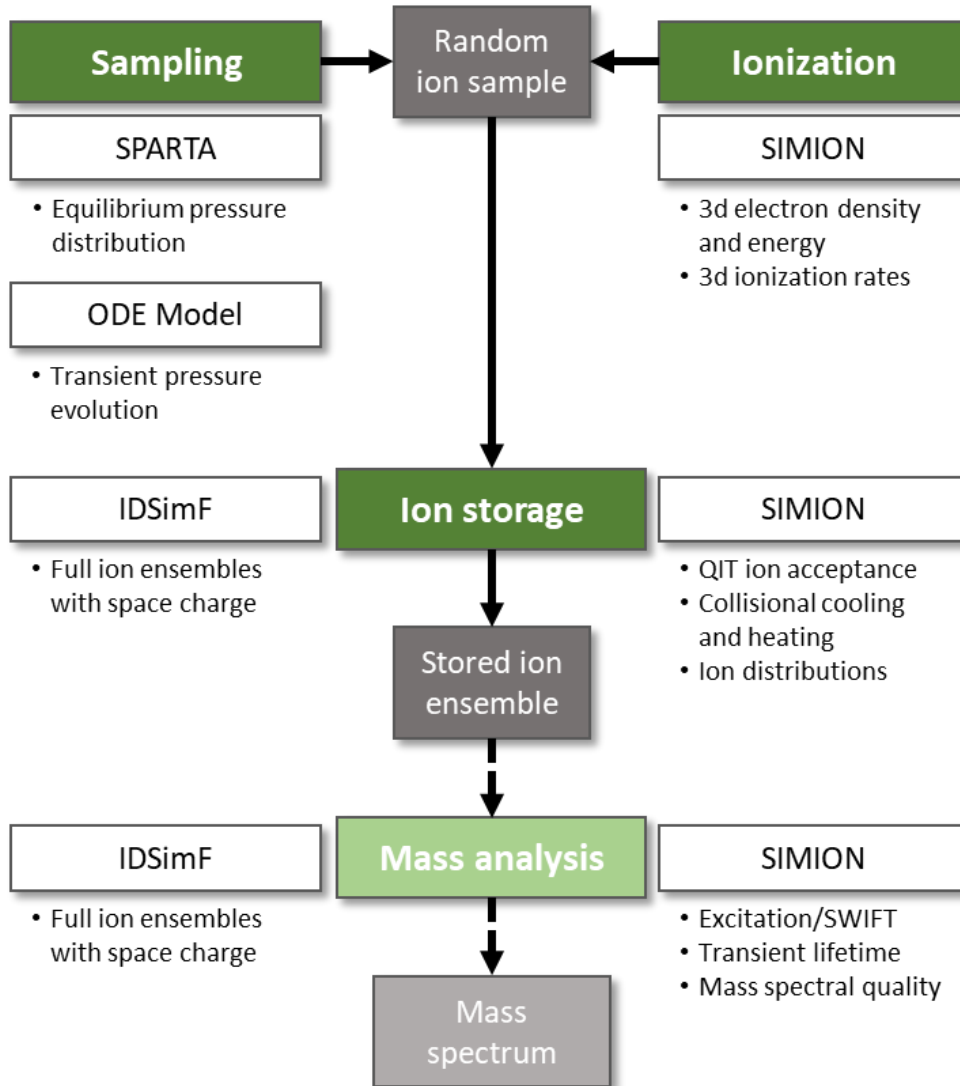


**Figure 48:** FT-QIT simulation workflow diagram. This chapter focuses on the sampling, ionization, and ion storage sections.

detection was utilized in the first quadrupole ion trap instrument developed by Paul and coworkers [145]. The detection was based on the power absorption in an auxiliary oscillating field applied between the cap electrodes, with its frequency matching the axial secular frequency of stored ions. After the commercial success of quadrupole ion trap mass spectrometers operating in mass-selective ejection mode, several research groups studied the capabilities for nondestructive FT-based ion detection in QITs by recording the image current that is induced by oscillating ions inside the ion trap [150–154]. This mode of operations promised further improvement of QIT-MS performance [155]. There are two major challenges that have to be dealt with for successful operation of an FT-QIT and have prevented the *successful* commercial implementation of such instruments up to now:

1) Detecting the ion signal, which is orders of magnitude smaller than the signal produced by crosstalk from the primary RF voltage of the ion trap that establishes the trapping field. Aliman et al. developed a broad-bandwidth detection technique that compensates for the primary RF voltage crosstalk [154, 156], which was eventually implemented in the first commercial FT-QIT mass spectrometer, the Zeiss iTrap [157].

2) Handling of distorted ion motion due to field imperfections and space charge, which results in shifts of ion secular frequencies and which can also lead to fusion of adjacent peaks (peak coalescence). This is a well-known issue occurring in different types of ion trap devices, e.g., Paul, Kingdon and Penning traps, respectively [158, 159].

#### 4.1.1 iTrap: principle of operation

Mass analysis in the iTrap is based on detection of the image current that is induced in the cap electrodes of a quadrupole ion trap and subsequent FT analysis of the recorded transient signal. A brief overview of the principle of operation is given below. For detailed information on the instrument and operational parameters the reader is referred to [160]. A sketch of the iTrap setup is displayed in Figure 49. The ion trap consists of a ring and two cap electrodes. The RF voltage for establishing the trapping field is applied to the ring electrode. The cap electrodes act as sensing electrodes for detection of the image current. Auxiliary voltages for ion excitation are also applied to the cap electrodes. The instrument utilizes in-trap EI for ionizing neutral sample gas. Sample gas is introduced into the ion trap through a hole in the ring electrode. A pneumatically driven atomic layer deposition (ALD) valve (Swagelok, Neuss, Germany) is used for sampling. The electron source (e-gun) is positioned at the ring electrode and consists of an electron-emitting filament with Wehnelt, focus, and anode electrodes (the e-gun is simplified in Figure 49 for clarity).

The electron beam formed by the e-gun enters the ion trap through an orifice in the ring electrode. The electron energy is defined by the anode (typically held at +70 V in regard to the filament) and the ring electrode voltages. The electron energy is non-uniform due to the RF voltage applied to the ring electrode. Sample gas is introduced directly into the ion trap via a ceramic tube connected to the ALD valve port. The pressure inside the ion trap is transiently increased by the expanding gas pulse. The electron beam is gated, so that ionization inside the trap occurs only in a short time interval during the gas pulse application and does not interfere with the mass analysis. For mass analysis, undisturbed ion oscillations are re-

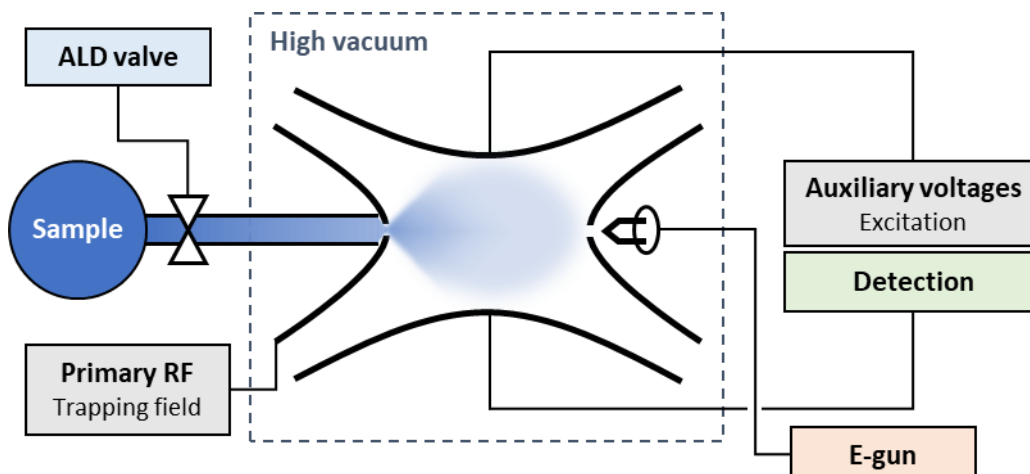


**Figure 49:** Sketch of the iTrap system. The inlet tube and e-gun are displayed across from each other for clarity but are actually aligned orthogonally. The e-gun is simplified for clarity.

quired. Therefore, a post-ionization delay is implemented to allow the pressure to settle to a tolerable level ( $<10^{-6}$  mbar). Subsequently, the ions' axial secular oscillations are excited by application of a DC voltage pulse to the cap electrodes.

An extended introduction to ion dynamics in a quadrupolar field is given in section 3.1.5. The coherent ion oscillation is required for detecting an image current, since opposing motions of randomly oscillating ions would eventually cancel out the signal. FT analysis of the recorded transient signal yields the frequency spectrum of the ions' secular oscillations. From eq. (3-10) the relationship between the secular frequency  $\omega_z$  and the mass-to-charge ratio  $m/e$  can be obtained:

$$\frac{m}{e} = \frac{2\sqrt{2}q_z V}{\omega_z(r_0^2 + 2z_0^2)\Omega} \quad (4-15)$$

where  $q_z$  is the axial stability parameter,  $V$  is the RF voltage,  $r_0$  and  $z_0$  are the ion trap dimensions in radial and axial direction, respectively, and  $\Omega$  is the radial frequency of the RF voltage. It is noted that the mass-to-charge ratio in atomic units  $m/z$  is typically used in the context of mass spectrometry. Exemplary operation parameters for the iTrap are given in Table 13.

These parameters may change depending on the measurement scenario. The sampling pressure and time directly impact the trap pressure during ionization and therefore the number of created ions. The ion number also scales with the ionization current and time. The pre- and post-ionization delays are implemented to adjust the ionization window to the gas pulse. A longer delay is usually applied after the ionization step, to let the pressure settle below  $10^{-6}$  mbar before mass analysis.

**Table 13:** Exemplary iTrap operation parameters

Sampling pressure	1 mbar
Sampling time	20 ms
Pre-ionization delay	5 ms
Ionization current	10 $\mu$ A
Ionization time	1 ms
Post-ionization delay	50-300 ms
Stimulus pulse height	10 V
Stimulus pulse length	2 $\mu$ s
Analysis delay	1 ms
Transient length	16 ms

The stimulus parameters determine the excitation level of the stored ions. The transient length ultimately limits the attainable mass resolution and can be adjusted for different resolution requirements.

#### 4.1.2 Perturbations in ion trap mass spectrometry

The operation of trapping devices, i.e., ion traps and transfer multipoles, is based on the characteristic interactions of ions with electric and magnetic fields. These interactions can be adversely affected by mainly (among others, cf. [161]) three effects: field imperfections, ion-neutral interactions (collisions) and ion-ion interactions (space charge).

##### *Field imperfections*

The motion of ions in a pure quadrupolar field is described by solutions to the Mathieu equation and is independent of the ion position [100]. Deviations from an ideal geometry due to, e.g., truncated electrodes, non-hyperbolic electrode shape, and electrode misalignment, lead to introduction of higher-order multipole fields (e.g., hexapole, octopole), which are superimposed on the quadrupolar field. As a result, the ion secular frequencies become dependent on the axial and radial position [162]. Higher-order multipoles cause nonlinear resonances inside the stability region, resulting in energy absorption and, thus, a fast increase of the ion oscillation amplitude. This can lead to undesired ion loss, when ions exhibit specific stability conditions [163, 164]. If the magnitude of higher-order multipoles is significantly smaller than that of the quadrupolar field the ion motion in the center of the trap is still dominated by the latter. In this case, nonlinear resonances mainly affect ions with large oscillation amplitudes [165]. In scanning QITs, the ion motion is

cooled by collisions with a low-mass buffer gas, typically helium, resulting in focusing of the ion cloud at the trap center. Large oscillation amplitudes are induced during mass-selective ejection and the occurrence of a nonlinear resonance can be utilized to shorten the ejection process, effectively improving mass resolution, peak shape, signal-to-noise ratio, and space charge tolerance of a QIT mass spectrometer [166–168]. In case of an FT-QIT, large oscillation amplitudes over long time intervals are required for ion detection without ejecting ions from the trap. During the detection period, nonlinear resonances can have a strong impact on the oscillation frequencies and therefore adversely affect the spectral quality [169–171].

### *Collisions*

Collisions play a pivotal role in conventional QIT mass spectrometry, as they are *necessary* to confine ions that were generated in an external ion source [101, 107, 145]. Ions that are injected into the ion trap lose a fraction of their kinetic energy due to collisions with the buffer gas and can therefore be stored. In a QIT with FT-based detection, collisions *adversely* affect the mass analysis. The loss of kinetic energy due to collisions leads to a fast decay of the coherent ion oscillation, which is the basis for image current detection. The detected signal intensity is proportional to the oscillation amplitude, and mass resolution scales with the length of the transient signal. Therefore, collisions adversely impact both sensitivity and mass resolution in an FT-based QIT [154]. Consequently, combining an FT-QIT with an external ion source introduces contradicting prerequisites. Increasing and decreasing the pressure inside the ion trap during different sections of an acquisition cycle may be the most obvious workaround for meeting these requirements. However, this negatively impacts on the duty cycle of such an instrument due to the required pumping time between the gas pulse and the mass analysis.

The effect of purely elastic collisions on the ion motion in a quadrupolar field is in general dependent on the ratio of the masses of the ion  $m_{\text{ion}}$  and the neutral gas particle  $m_{\text{gas}}$  [101]. When  $m_{\text{ion}} \gg m_{\text{gas}}$ , collisions result in damping of the ions' secular motion [172]. The micromotion is mainly unaffected by the collisions so that ions stay in phase with the RF field. This effect is utilized for storing externally generated ions in a QIT with helium as a low-mass buffer gas and is called *collisional cooling*. The opposite is the case for  $m_{\text{ion}} \ll m_{\text{gas}}$ . Ions are strongly scattered when a collision takes place, leading to dephasing of the micromotion caused by the RF field. As a result, ions are accelerated in the field and take up energy. This

process is known as *RF heating*. For a mass ratio of one, Major and Dehmelt reported a constant average ion kinetic energy for the special case of head-on collisions. Of course, this is not the case in a real system. [101]

When in-trap ionization is utilized, collisions are not required for ion trapping because ions are generated within the quadrupolar field. However, sample gas needs to be introduced into the ion trap, which results in an increase in pressure. Both collisional cooling and RF heating of ions may occur, depending on the sample gas composition. The duty cycle of an in-trap ionization FT trap is limited by the pumping time between sampling and analysis.

### *Space charge*

The theoretical description of the ion motion in a quadrupolar field summarized in section 3.1.5 is only valid for single ions. The presence of additional charges adds additional forces, which increase in magnitude, the more ions are stored inside an ion trap at the same time. In general, space charge leads to a distortion of ion trajectories, which is detectable as shifts of the secular frequency. This effect was experimentally quantified in Bruker esquire 3000 plus and HCT mass spectrometers. The maximum ion numbers that are tolerable for a mass spectrometric analysis (*spectral capacity limit*)<sup>18</sup> are  $6 \cdot 10^4$  and  $6 \cdot 10^5$  for the two instruments, respectively. The HCT incorporates an optimized geometry and phase-correlation between the applied RF voltages, which increases the space charge tolerance [168]. This effect can be accounted for as long as a systematic dependency of the mass shift on the ion number is given. When the ion number is significantly increased, ions will be lost from the trap due to the strong defocusing force introduced by space charge. Fischer determined this *storage capacity limit* to be a few million ions per cubic centimeter in one of the first QIT instruments [145].

In FT-based high-resolution mass spectrometry, e.g., FTICR and Orbitrap MS, space-charge-induced fusion of peaks (coalescence) [173], that are separated only by a fraction of a nominal mass, needs to be addressed, to retain the high-resolution capabilities. This requires precise control of the trapped ion number and calibration procedures to compensate for space charge induced mass shifts [174, 175]. Typical ion numbers are in the range of  $10^5$  to  $10^6$  in both FTICR cells (Penning trap) [176] and Orbitrap analyzers (Kingdon trap) [177]. It should be noted, that the space charge limit depends on the utilized instrument and experimental parameters [175], e.g., the magnetic field strength in FTICR [178].

---

<sup>18</sup> An observed mass shift of 0.25 Da was chosen as the limit in the referred work.

The reported space charge effects in QIT experiments with non-destructive detection are much more severe, e.g., complete merging of  $\text{Ho}^+$  ( $m/z$  165) and  $\text{Er}^+$  ( $m/z$  162) peaks to a single peak at the average mass of both ion species [159] or merging of the  $^{13}\text{C}$  isotope peak into the larger all- $^{12}\text{C}$  peak [179]. Loss of mass resolution due to distortion of the coherent ion motion was also attributed to ion-ion interactions [171]. It appears that space charge is the main reason that – up to now – prevented the commercial success of FT-QIT-MS. The only effective means to prevent space-charge-related effects in a given experimental setup is to reduce the number of stored ions in the trap. Space charge effects can also be observed in scanning QIT-MS experiments (cf. section 13 in [168]). Corresponding mass spectra show distortion of peaks, e.g., position shifts and broadening [180]. The charge density can be varied in commercial scanning QIT instruments via the accumulation time of ions from an external ion source. The total signal of the charged particle detector (e.g. SEV) gives a confident value for the total ion number in one mass spectrum, since space charge in the ion trap distorts the ion ejection process, but not the ion detection. However, if the ion ejection is distorted by space charge the number of ejected ions may not reflect the number of stored ions in the ion trap anymore. Ions that are outside of the observed mass range in an experiment can also lead to unexpected overloading of the trap when these ions are not detected by the charge control mechanism, but contribute to the space charge in the ion trap. In an FT ion trap, the signal intensity is directly related to the characteristic ion motion. If this motion is disturbed by space charge, the change of intensity may become a function or even independent of the total number of stored ions and, therefore, determination of the ion number becomes challenging if not impossible. The ion trap loading cannot be controlled without a reliable means of charge control.

### 4.1.3 Electron ionization

The ionization process in electron ionization (EI) is based on the interactions of neutrals in the gas phase with accelerated electrons. The electrons are emitted from a heated filament (thermionic emission [181]) and are accelerated in an electric field into the ionization volume. The typical acceleration voltage in EI sources in mass spectrometry is 70 V, which ideally results in an electron energy of 70 eV. EI cross sections of most molecules exhibit a maximum at an electron energy of 70 eV and this value is well above the ionization energy of any molecule or atom.<sup>19</sup>

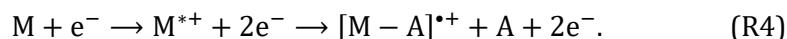
---

<sup>19</sup> Ionization energies of organic molecules are typically in the range of 9 eV [182].

EI produces predominantly singly charged radical cations  $M^{\bullet+}$  by removing an electron from the target molecule or atom  $M$  (R1). Multiply (R2) and negatively charged ions (R3) are only observed with EI in special cases [183].



Typically, an excess of energy is transferred to the ionized molecules during the ionization process, which makes EI a *hard* ionization method. 70 eV mass spectra of molecules are usually characterized by abundant fragment signals, resulting from internal energy deposition during ionization followed by rapid unimolecular decay (R4). The molecular ion ( $M^{\bullet+}$ ) peak is not necessarily the base peak and may not be observed at all [184]. In general, the fragmentation process is based on the formation of a *metastable* radical cation  $M^{\bullet+}$  that undergoes unimolecular dissociation into a fragment radical cation and a neutral fragment A:



The ionization rate  $R_i$  [ $s^{-1}$ ] (eq. (4-16)) with EI is determined by the incident electron current  $I_e$  [ $s^{-1}$ ], the neutral analyte density  $N_A$  [ $cm^{-3}$ ], the ionization cross section for a given electron energy  $\sigma_i(\text{KE})$  [ $cm^2$ ], and the length of the ionization volume  $\Delta x$  [ $cm$ ]:

$$R_i = I_e \cdot N_A \cdot \sigma_i(\text{KE}) \cdot \Delta x. \quad (4-16)$$

For the typical iTrap operation parameters (Table 13) the number of generated ions is approximately  $7 \cdot 10^{11}$ , assuming an electron energy of 70 eV and that the ionization pressure equals the sampling pressure (1 mbar). The actual pressure inside the ion trap however is significantly lower [160]. When in-trap EI is utilized while the RF voltage is active, the electron energy becomes time- and space-dependent, due to interaction of the electrons with the oscillating trap field. This impacts on the ionization rate and is thus further assessed in sections 4.3.2 and 4.3.3.

## 4.2 Gas sampling

Sample gas is introduced into the ion trap with a pneumatically driven atomic layer deposition (ALD) valve (Swagelok, Neuss, Germany). The gas is directed through a ceramic tube and through an orifice in the ring electrode. The trap pressure is evaluated with two approaches: DSMC simulations are performed for modeling the equilibrium pressure in the ion trap that is attained when gas is continuously introduced. This scenario is decoupled from the complex transient gas dynamics during the gas pulse. The transient pressure profile is estimated with an ordinary

differential equation (ODE) model. The boundary conditions for the model are obtained by matching with experimental pressure data for the inlet tube and vacuum recipient.

#### 4.2.1 SPARTA DSMC model

The gas flows during the gas pulse are at least partly in the Knudsen flow regime [131], where the continuum assumption of fluid dynamics become invalid. This requires modeling with statistical methods. The SPARTA program is used for DSMC simulations. A 2D-axisymmetric approximation of the ion trap geometry is used for the DSMC simulations, owing to the very high computational demand for 3D simulations. The model describes the approximated ion trap electrodes and a gas inlet tube. The gas inlet tube is relocated from the ring to one of the cap electrodes due to symmetry restrictions. The pressure inside the ion trap (area A in Figure 50) is of particular interest in the simulations performed with this model.

The gas inlet is located at the lower section of the  $xhi$  boundary. The boundary type is adapted to the simulation scenario, with either an opened or closed valve. For the opened valve the *vanish* surface collision model is used and the properties (inflow coordinates, temperature and pressure) of the inflowing gas are defined via the `emit/face/file fix`. The section of  $xhi$  outside of the gas inlet tube is covered by an additional surface, parallel to the boundary. The  $xlo$  boundary mimics the surface of the turbo pump. A base pressure of  $10^{-9}$  mbar is a realistic assumption for the ion trap recipient. This is realized in the model with a subsonic boundary condition. The pump surface transmission of 36% is mimicked with a reaction model at the boundary, which removes 36% of the incoming particles and reflects the rest. The  $yhi$  boundary is a reflective boundary and  $ylo$  is the axis of symmetry.

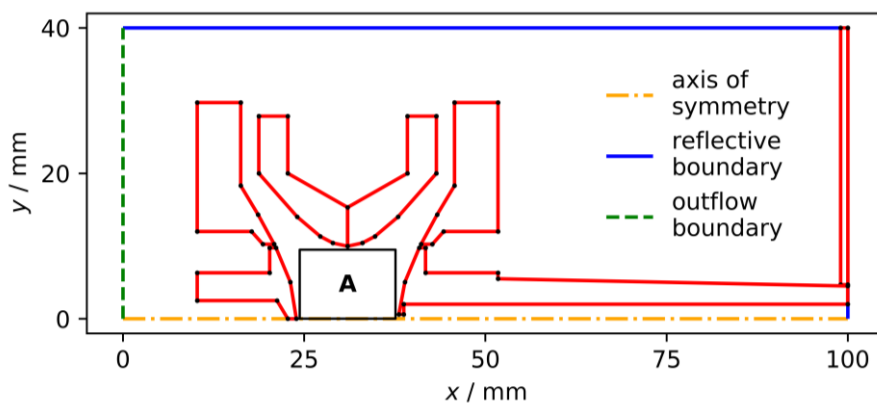


**Figure 50:** SPARTA simulation box with the ion trap and gas inlet. The area marked with A is used for calculating the average trap pressure.

**Table 14:** Boundary parameters for the gas inlet model

xlo	“pump”, surface collision model: diffuse (298.0 K, accommodation coefficient = 0.0), surface reaction model: particle deletion probability 0.36, particle emission: emit/face subsonic ( $10^{-7}$ Pa, 298.0 K)
xhi	“valve”, open (gas pulse): surface collision model: vanish, particle emission: emit/face/file; closed: surface collision model: specular
ylo	axis of symmetry
yhi	surface collision model: specular

**Table 15:** Sampling simulation parameters for different gases and sample pressures

Gas	Sample pressure (mbar)	Grid cell length (mm)	Timestep length (s)
N <sub>2</sub>	0.001	0.67	$10^{-7}$
	0.01	0.83	$10^{-7}$
	0.1	0.56	$10^{-7}$
	1	0.05	$10^{-8}$
He	0.001	0.67	$10^{-7}$
	0.01	0.83	$10^{-7}$
	0.1	0.67	$10^{-7}$
	1	0.17	$2 \cdot 10^{-8}$

All boundary parameters are summarized in Table 14. Simulations with different sample pressures are performed for N<sub>2</sub> and He as matrix gas. The grid cell size is adapted to the pressure and gas properties. Table 15 summarizes the simulation parameters.

Preliminary simulations have shown that the surface collision model has no significant impact on the obtained results inside the volume between the trap electrodes and, thus, the specular reflection model is used for all surfaces. Also, the impact of the simulation box size is negligible for calculating the pressure within the trap. Accordingly, the simulation box dimensions are minimized to reduce computation time.

#### 4.2.2 Equilibrium pressure distribution

The actual sampling process is highly dynamic and depends on several factors that are difficult to assess and to incorporate into a simulation. This includes, for example, the exact sampling valve geometry and variations of the sample pressure. For

verification of the simulation results, a scenario is selected that allows comparison with experimental data. When the inlet valve is not pulsed but kept open for a sufficiently long timeframe, eventually an equilibrated static pressure distribution is reached. The experimentally determined static pressures can thus be compared with the equilibrium pressures in the simulations.

Experimental pressure data are provided by Zeiss. The pressure is measured upstream of the ALD valve (sample), inside the inlet tube (tube), and in the vacuum recipient of the ion trap (recipient). Pfeiffer TPR281 Pirani (sample) and PKR261 compact full range gauges (tube and recipient, all gauges from Pfeiffer Vacuum GmbH, Asslar, Germany) were used for the pressure measurements. Data are available for helium and air as sample gas. Sample pressures are in the range of 0.01 – 1 mbar. In the simulations, the equilibrium pressures are evaluated at representative positions, i.e., the center of the inlet tube and the volume outside of the trap. In addition, the pressure inside the ion trap is determined. Helium and nitrogen are used as gas species and the sample pressures are chosen according to the experimental conditions.

At the beginning of each simulation, the simulation box is filled homogeneously with particles according to a pressure of  $10^{-9}$  mbar. This is also the base pressure at the turbo pump, which is realized with the subsonic boundary condition at the *pump* boundary (*xlo*) in the simulation. The boundary condition at the *inlet* region (*xhi*) defines the inlet pressure of 1, 0.1, 0.01 or 0.001 mbar. The simulations converge towards equilibrium states with static pressure distributions. 200 timesteps of the equilibrium state are averaged for evaluation of the simulation results. An exemplary pressure distribution is shown in Figure 51.

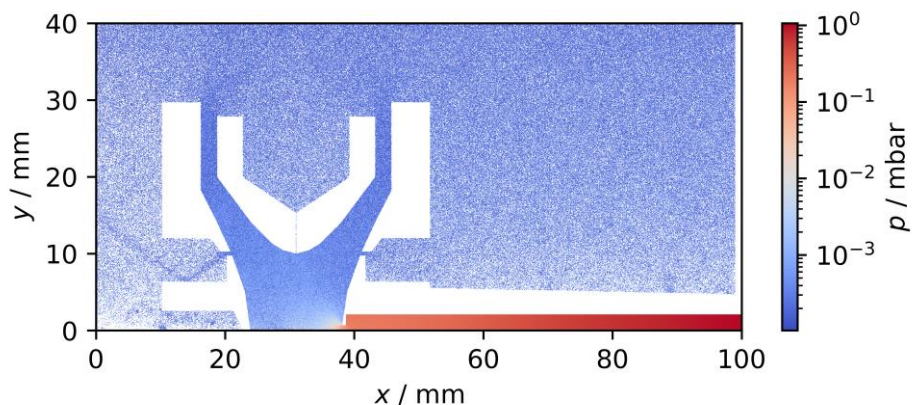


**Figure 51:** Equilibrium pressure distribution for  $N_2$  with a sample pressure of 1 mbar. White areas represent the ion trap and inlet geometry.

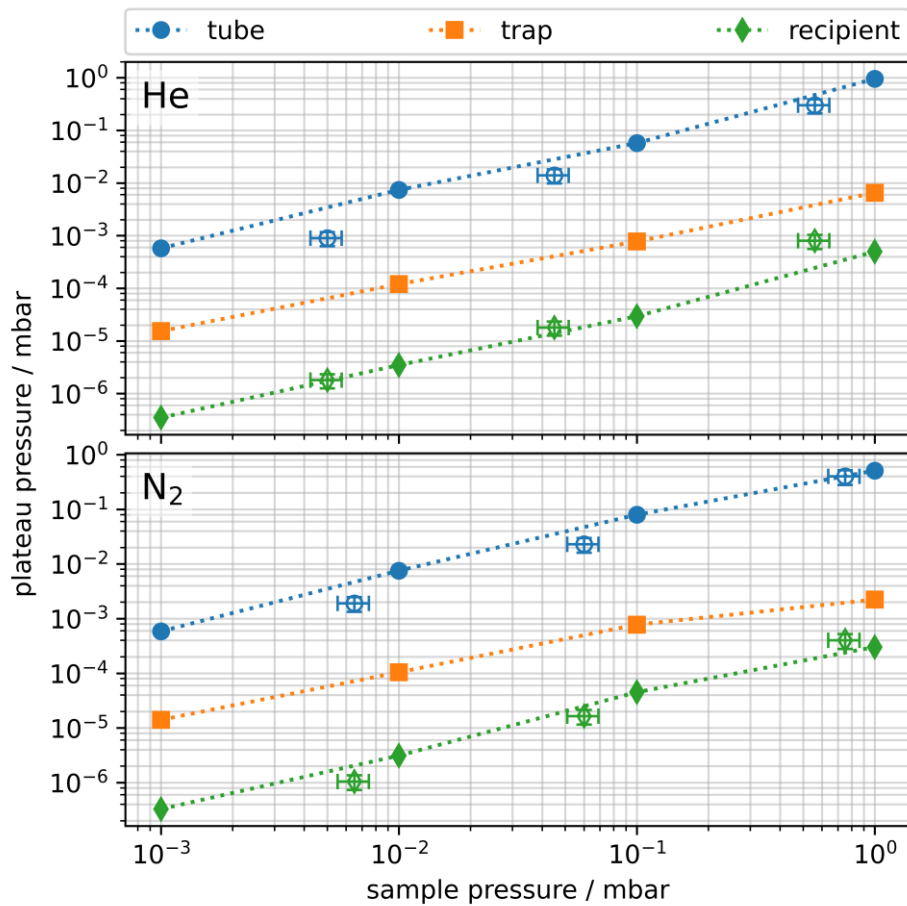


**Figure 52:** Equilibrium pressures at different locations in dependence of the sample pressure for helium (top) and nitrogen (bottom), obtained from DSMC simulations. Open markers represent experimental data.

The simulation results are summarized in Figure 52. The equilibrium pressures inside the inlet tube, ion trap, and recipient are proportional to the sample pressure for both helium and nitrogen. The accordance with experimental data is acceptable, given the strongly simplified simulation geometry compared to the real setup. The positions of the vacuum gauges in the experiments can also impact the measured pressures. A critical parameter for DSMC simulations is the ratio of actual and simulated particles ( $f_{num}$ ). For statistically representative results, there should be at least 20 simulated particles in a volume of the cubic mean free path. This is important for reliable inter-particle collision statistics and, thus, is critical in collision-dominated regimes. In the present simulations, the majority of collisions take place inside the inlet tube, where the pressure is highest. Furthermore, the high-pressure regions in the simulations are in the Knudsen or free molecular flow regime and, thus, a strong impact of collisions is only expected in a comparably small section of the simulation box. Inside the ion trap and the outer volume,

the inter-particle interactions become negligible, particularly at lower sampling pressures. The impact of the  $fnum$  value on the simulation results was evaluated in a test simulation model (data not shown). These simulations show that a significant increase of  $fnum$ , which results in a lower number of simulated particles and diminishes the simulation accuracy, still yields the same results as when a lower  $fnum$  value (higher number of simulated particles) is used. The main difference between simulations with different  $fnum$  is simply the noise level of the data. It is thus concluded, that the  $fnum$  values used in the present simulations do not distort the obtained results and that the simulations give a reasonable representation of the ion trap pressure. In the studied range, the ion trap pressure is about two orders of magnitude smaller than the sample pressure. It is noted that for short gas pulses, which are usually applied in real ion trap measurements, the trap pressure may be lower than the equilibrium pressure, when the equilibration time is exceeding the gas pulse length. However, for a gas pulse with a length of 20 ms and a sample pressure of 2.5 mbar the trap pressure was estimated to be  $1.4 \cdot 10^{-3}$  mbar from experiments [160], which is only slightly lower than the equilibrium pressure obtained with a sample pressure of 1 mbar for  $N_2$  in the simulations. This suggests that the equilibrium pressure may be nearly reached inside the trap during the gas pulse. With a mean gas velocity of 475 m/s for  $N_2$  at 298 K and a trap diameter of 20 mm, gas molecules will collide 475 times with the trap electrodes during a 20 ms gas pulse, which appears to be sufficient for equilibration of the gas flow.

### 4.2.3 Transient pressure evolution

The temporal evolution of the pressure during the gas pulse and the pumping process is difficult to model with DSMC due to the large difference of particle density between the inlet and the ion trap and vacuum recipient. For meaningful modeling of the inlet region, very large particle numbers are required, which increases computation time to an impractical degree. Therefore, the temporal pressure evolution is evaluated with an ordinary differential equation (ODE) model that represents three regions of the iTrap setup and the particle flows between these regions. The model is visualized in Figure 53. The regions of interest are the Inlet, Trap and Recipient, which represent the corresponding sections of the iTrap instrument. Pressures were experimentally determined inside the inlet tube and the vacuum recipient. Thus, the model parameters can be adapted to match with the experimental data and then be used to interpolate the pressure in the trap.

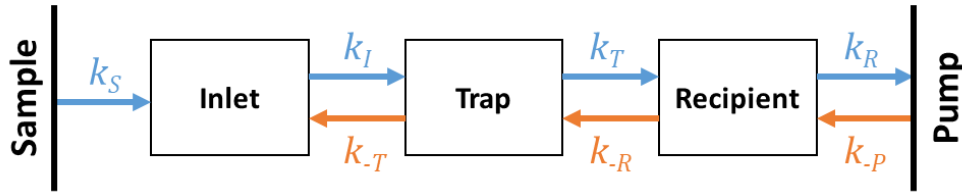


**Figure 53:** ODE model with the different regions and the rate constants that determine the particle flows between the regions.

Three differential equations are used to describe the particle transport:

$$\frac{dN_{Inlet}}{dt} = k_S + k_{-T} - k_I \quad (4-17)$$

$$\frac{dN_{Trap}}{dt} = k_I + k_{-R} - k_T - k_{-T} \quad (4-18)$$

$$\frac{dN_{Recipient}}{dt} = k_T + k_{-P} - k_R - k_{-R} \quad (4-19)$$

The particle transport rates are determined by the inflow from the upstream region, the outflow into and the backflow from the downstream region. It is assumed that gas is transported linearly through the system, i.e., only neighboring sections of the model are connected. Gas is introduced from a reservoir (Sample region) into the Inlet and is removed at the Pump region. The backflow from the Pump region ( $k_{-P}$ ) establishes the base pressure in the system. The particle influx from the Sample region is governed by the rate constant  $k_S$ , which is approximated by the flow rate through a nozzle (eqs. (4-24) and (4-25)). These equations are valid in the viscous flow regime for frictionless flow and are used as an approximation for the model to avoid modeling of the actual flow in the complex geometry with e.g. DSMC. The flow in this region is in the Knudsen regime, with a Knudsen number  $K_n = 0.016$ . The Knudsen number is the quotient of the mean free path  $\lambda$  and the characteristic length  $l$  of the geometry [131], in this case the nozzle diameter:

$$K_n = \frac{\lambda}{l} = \frac{k_b T}{\sqrt{2} \pi \sigma^2 p l}, \quad (4-20)$$

where  $k_b$  is the Boltzmann constant,  $T$  is the temperature,  $\sigma$  is the gas diameter,  $p$  is the pressure and  $l$  is the characteristic length of the geometry. The Knudsen number represents a measure of the probability that inter-particle interactions take place while a gas transitions through the respective geometry. Continuous flow prevails for  $K_n < 0.01$ , Knudsen flow in the range  $0.01 < K_n < 0.5$ , and molecular flow for  $K_n > 0.5$  [131]. The mass flow rate  $q_m$  through a nozzle is given by [131]:

$$q_m = A_{min} \cdot p_0 \cdot \sqrt{\frac{2M}{RT}} \cdot \left(\frac{p_k}{p_0}\right)^{\frac{1}{\kappa}} \cdot \sqrt{\frac{\kappa}{\kappa-1} \left\{1 - \left(\frac{p_k}{p_0}\right)^{\frac{\kappa-1}{\kappa}}\right\}}, \quad (4-21)$$

where  $A_{min}$  is the area of the nozzle,  $p_0$  is the inlet pressure,  $M$  is the molar mass of the gas,  $R$  is the universal gas constant,  $T$  is the temperature,  $p_k$  is the outflow pressure and  $\kappa$  is the heat capacity ratio of the gas. At a sufficiently large pressure difference the flow becomes choked, i.e., the mass flow rate  $q_m^*$  is independent of the outflow region pressure  $p_k$  [131]:

$$q_m^* = A_{min} \cdot p_0 \cdot \left(\frac{2}{\kappa+1}\right)^{\frac{1}{\kappa-1}} \cdot \sqrt{\frac{2\kappa}{\kappa+1} \cdot \frac{M}{RT}}. \quad (4-22)$$

The particle flow rate is calculated by dividing the mass flow rate by  $M$  and multiplying with the Avogadro constant  $N_A$ . All other rate constants are set to the respective effusion rates, because  $K_n$  is usually larger than 0.5 in the other regions. The effusion rate  $z_W$  is given by [185]:

$$z_W = \frac{p_0 N_A A}{\sqrt{2\pi M R T}}, \quad (4-23)$$

where  $A$  is the opening area of the region. The model is numerically integrated with `scipy.integrate.solve_ivp` from the SciPy package [26], with the default Runge-Kutta method *RK45* [186].

The Inlet, Trap and Recipient regions are characterized by their volumes and connecting areas through which gas is traversing the regions. The volumes and areas are taken from the 3D CAD model of the iTrap. Sample and Pump are characterized by constant pressures. The parameters are summarized in Table 16.

**Table 16:** ODE model parameters

Region	Parameter	Value
Sample	pressure $p_S$	1 mbar $\cdot f_{p0} \cdot f_{pS}$
	outflow area $A_S$	$1.32 \cdot 10^{-5} \text{ m}^2$
Inlet	outflow area $A_I$	$1.83 \cdot 10^{-6} \text{ m}^2$
	volume $V_I$	$4.34 \cdot 10^{-6} \text{ m}^3$
Trap	outflow area $A_T$	$9.00 \cdot 10^{-4} \text{ m}^2$
	volume $V_T$	$1.47 \cdot 10^{-5} \text{ m}^3$
Recipient	outflow area $A_R$	$2.74 \cdot 10^{-3} \text{ m}^2$
	volume $V_R$	$6.71 \cdot 10^{-4} \text{ m}^3$
Pump	pressure $p_P$	$10^{-7} \text{ mbar}$

Experimental data are available for pressure measurements with air at a sample pressure of 1 mbar with different gas pulse lengths between 10 ms and 5 s. The model solution is matched with the experimental data by scaling the inflow from the Inlet region. This is accomplished upon scaling the inlet pressure and the mass flow rate with different factors, which account for the gas-pulse-length-dependent decrease of the sample pressure ( $f_{ps}$ ) and the deviation of the actual gas flow conditions from the base assumptions of the applied equations for calculating the flow rate ( $f_{p0}, f_{q\_scale}$ ). In the Knudsen flow regime, the flow rate does not scale with pressure in the same way as it does in the continuous flow regime, and is typically lower than calculated with the corresponding formulas. As a consequence, the gas flow is significantly overestimated in the model when the abovementioned formulas are applied. This is empirically corrected with the scaling factors. The value of  $f_{ps}$  is between 0.75 and 0.95, depending on the gas pulse length. The other factors are constant,  $f_{p0} = 0.62$  and  $f_{q\_scale} = 0.006$ . The required decrease of the inflow is due to the real inlet geometry, which consists of a tube with an orifice at the entrance (valve) and the exit (orifice in the ring electrode), which both have smaller diameters than the tube. The tube restricts the gas flow by its conductance, which decreases the flow rate through the upstream valve. The conductance is not only determined by the tube dimensions, but is also decreased by the small exit aperture.

The model solutions are depicted in Figure 54. The transient pressure profiles in the Inlet and Recipient regions are well reproduced, especially for longer gas pulses. With pulse lengths  $< 100$  ms, the calculated Inlet pressures increase faster in the beginning than the corresponding experimental values. This is explained with a delayed response in the experiments. The vacuum gauge is connected to the inlet line via a short 6 mm tube which limits the gas transport into the gauge. The system is in the Knudsen flow regime during the gas pulse and transits into molecular flow conditions when the pressure decreases below 0.02 mbar. Therefore, the equilibration time in the vacuum gauge is long compared to the total gas pulse length, which leads to a delayed observed pressure increase and thus systematically lower inlet pressures at short pulse lengths. When the pulse length is increased the vacuum gauge and inlet tube pressures equilibrate during the gas pulse. The experimentally observed pressure profiles with gas pulse lengths exceeding 100 ms are well reproduced, which in turn yields an estimate of the required equilibration time for the inlet vacuum gauge under the given conditions between 100 and 250 ms. The vacuum gauge in the recipient is directly connected via a CF40 flange, therefore it is assumed that the data at this location are not affected by the geometry.

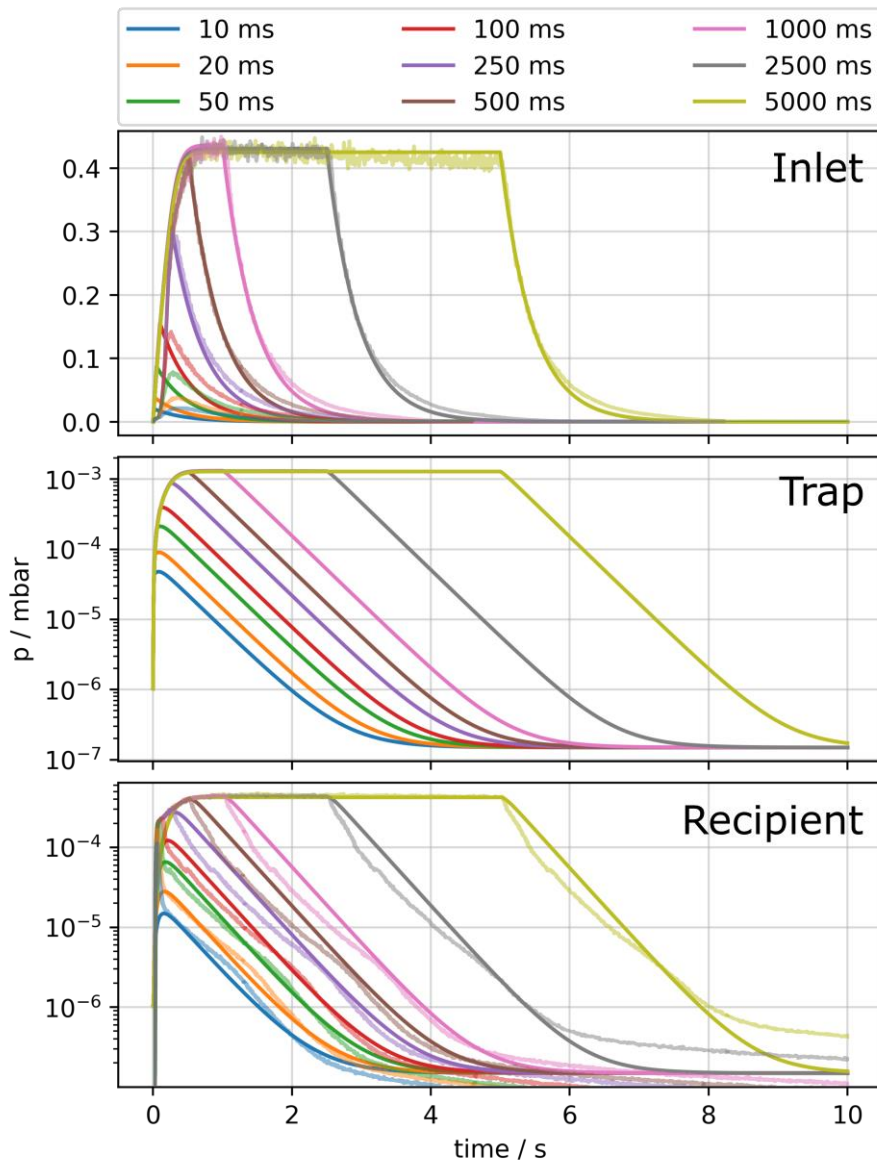


**Figure 54:** Pressure profiles for air from the ODE model solutions for different gas pulse lengths. The sample pressure in the experimental data is 1 mbar. Top: Inlet region with experimental data (transparent lines); center: Trap region; bottom: Recipient region with experimental data (transparent lines).

The pressures gauged in the recipient exhibit different temporal profiles over the course of the experiments. Initially, the pressures increase sharply during the opening time of the valve. For gas pulse lengths up to 100 ms the maxima in the corresponding model solutions are lower and the peaks are broader. The narrower peak in the experiments could be qualitatively reproduced with the model by adding another particle flow from the Inlet directly into the Recipient during the gas-pulse. It is feasible that gas leaks out of the inlet tube, as there is only a loosely

plugged connection between the inlet socket, the tube, and the ring electrode. It is therefore assumed that the larger pressure peak during the gas pulse is only observed in the recipient and not in the ion trap. For gas pulse lengths above 100 ms the pressure in the recipient increases faster in the experiment than in the model. Again, adding a flow from the Inlet to the Recipient region does alleviate this discrepancy. Changes of the flow dynamics, e.g., occurrence of shockwaves in the inlet tube due to a large pressure gradient, are feasible to occur when the valve is opened, which can also account for the different pressure pulse profile. Although there are some differences between the experimental and modeled pressure decrease curves, the general trend and temporal scale of the process is in good accordance for all gas pulse lengths. It is thus assumed that the model solution for the Trap pressure also represents a reasonable approximation of the trap pressure. The equilibrium trap pressure of  $1.3 \cdot 10^{-3}$  mbar attained with gas pulse lengths of  $< 500$  ms is in good agreement with the corresponding DSMC simulation as presented in section 4.2.2. The maximum trap pressure increases systematically with the pulse length and saturates at gas pulse lengths above 250 ms. The results suggest that the pressure inside the ion trap exhibits the same temporal profile as the pressure in the vacuum recipient, but is slightly higher. As a result, the time necessary for the pressure within the trap to decrease below  $10^{-6}$  mbar is in the range of seconds, even for the shortest gas pulse. This is unfavorably long for efficient operation when pressures below  $10^{-6}$  mbar are required for proper mass analysis, as is the case for the iTrap system.

### 4.3 Electron beam simulations

In a conventional EI source electrons are accelerated with an applied voltage (typically 70 V) into the ionization chamber, to accomplish a defined electron energy. This is important to obtain reproducible spectra for comparison with spectra databases, as fragmentation patterns depend heavily on the ionization energy. When using in-trap ionization, the electrons interact with the oscillating field inside the trap. As a result, the electron energy is modulated both temporally, in dependence of the RF phase, and spatially, in dependence of the position in the quadrupolar field. Hence, for calculating ionization rates in such a setup, knowledge of the ion density and energy distribution, as well as energy-dependent ionization cross sections are required. The latter are available from literature, e.g., the NIST database [187]. The electron density and energy distributions are calculated from electron trajectory simulation results. The SIMION result files contain the electron trajectories and kinetic energies. A data processing library is developed in Python for ex-

traction of data and analysis based on the result files to calculate the electron density and average electron energy. The library uses the SciPy [26] and NumPy [25] packages for data processing. The 3D density and energy distributions are calculated and displayed as 3D histograms. The PyEVTK [188] package is used for exporting the 3D distributions as *vtr* files [189], which are readable by visualization software, e.g. Paraview [29].

### 4.3.1 SIMION model

Electron trajectory simulations are performed with SIMION using a full ion trap model, covering the e-gun electrodes (filament, anode, Wehnelt, and focus) as well as the trap electrodes. The grid resolution of 0.1 mm in the ion trap model that is usually used for ion trajectory simulations is not sufficient for an accurate field representation inside the e-gun region, where the critical sizes of electrodes are below 1 mm. This leads to large field inaccuracies, especially in close proximity to curved electrode surfaces. Therefore, a high-resolution model (grid cell length 0.01 mm) of the e-gun is used for accurate modeling of the electron beam. Due to small differences between the model geometries the focus electrode potential in the high-resolution model is changed from -55 V to -50 V. This leads to a satisfactory agreement of the potential distributions of both models in the region between the e-gun anode and the ring electrode (cf. Figure 55, green line), which in turn allows the transfer of particles between the two models with a negligible potential jump.

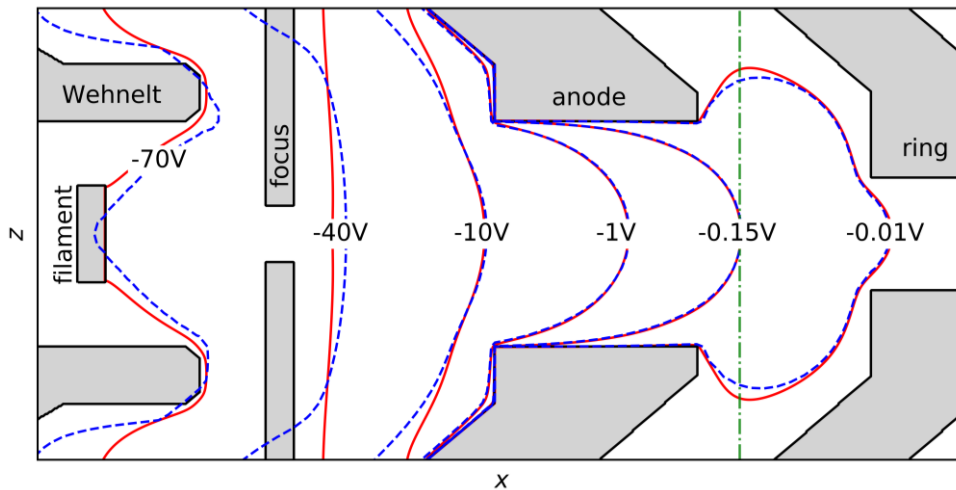


**Figure 55:** Potential contour lines of the e-gun models in the  $xz$  plane; dashed blue lines: low resolution model, solid red lines: high resolution model. The electrodes of the high-resolution model are displayed in grey. The green vertical line indicates the position at which particles are transferred between the models.

**Table 17:** EI source and trap voltages for electron beam simulations

Filament	-70 V
Anode	0 V
Wehnelt	-73 V
Focus	-55 V
Ring electrode	-70 – 500 V
Cap electrodes	0 V

The residence time of electrons inside the ion trap (approx. 4 ns @ 70 eV) is considerably smaller than one RF period (1  $\mu$ s @ 1MHz RF frequency), therefore the electrons experience a nearly constant electric field while traveling through the ion trap. This allows the ring to be set to a fixed voltage in the simulations. This decreases the computation time significantly, as the electric field scaling needs to be performed only once instead of in every timestep. The electrode potentials are given in Table 17.

Since the electron acceleration voltage is -70 V, electrons are deflected from the ring electrode when the ring potential is  $\leq -70$  V. The lowest ring potential in the simulations is thus -70 V. In each simulation,  $10^5$  electrons are initialized evenly distributed over the filament surface. The initial electron kinetic energy is set according to an MBD at 1400 K (filament temperature), which is a reasonable approximation [93]. This was done by implementing the distribution function and a rejection sampling method in the ion definition file. The initial direction of movement is set orthogonally to the filament surface.

### 4.3.2 Electron beam density and energy

The electron beam widens as it propagates through the ion trap, yielding a conical shape. The electron density is highest at the center axis and decreases towards the trap boundaries. With increasing ring potential, the beam is focused on the center axis, resulting in a narrower shape. The electron energy upon entering the ion trap is  $-e \cdot (U_{\text{filament}} - U_{\text{ring}})$ , e.g., 170 eV for a ring potential of 100 V and a filament potential of -70 V. At a ring potential of -70 V, electrons entering the ion trap are comparably slow, as they retain only their initial thermal energy inside the trap. Nevertheless, the residence time of these “thermal” electrons inside the ion trap is still smaller than one RF period. When the ring potential is below -70 V, electrons are deflected from the ring electrode and cannot enter the ion trap. This essentially leads to a

## Modeling of an FT ion trap

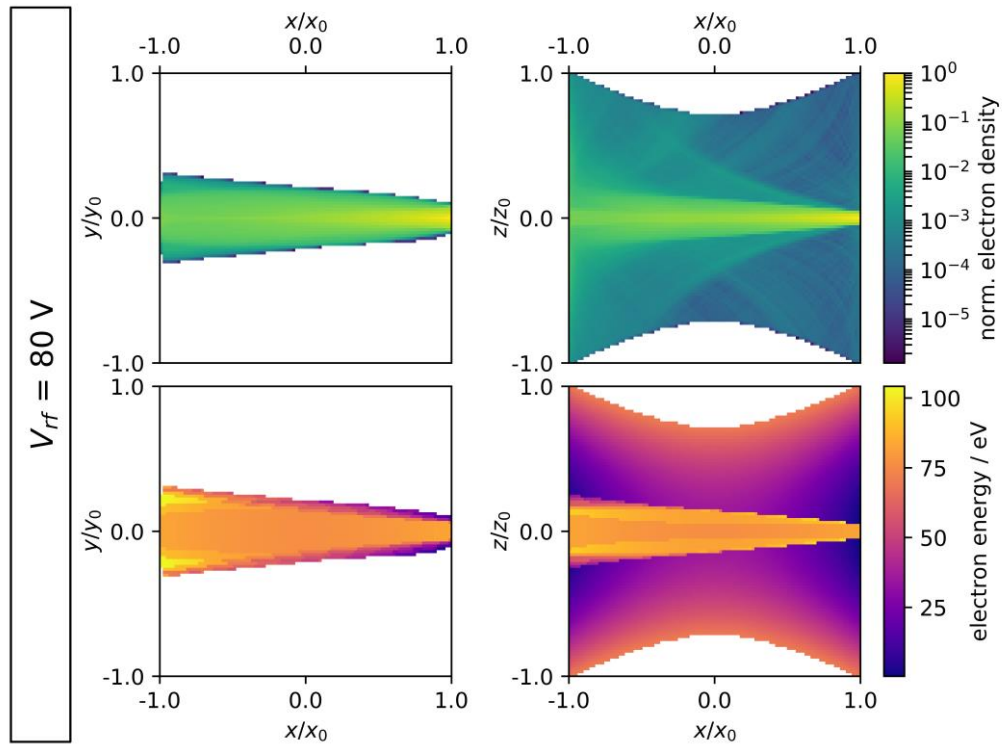


**Figure 56:** Half-sections of the normalized electron density (top) and energy (bottom) in the xy (left) and xz plane (right) for an RF voltage of 80 V, averaged over one RF cycle.

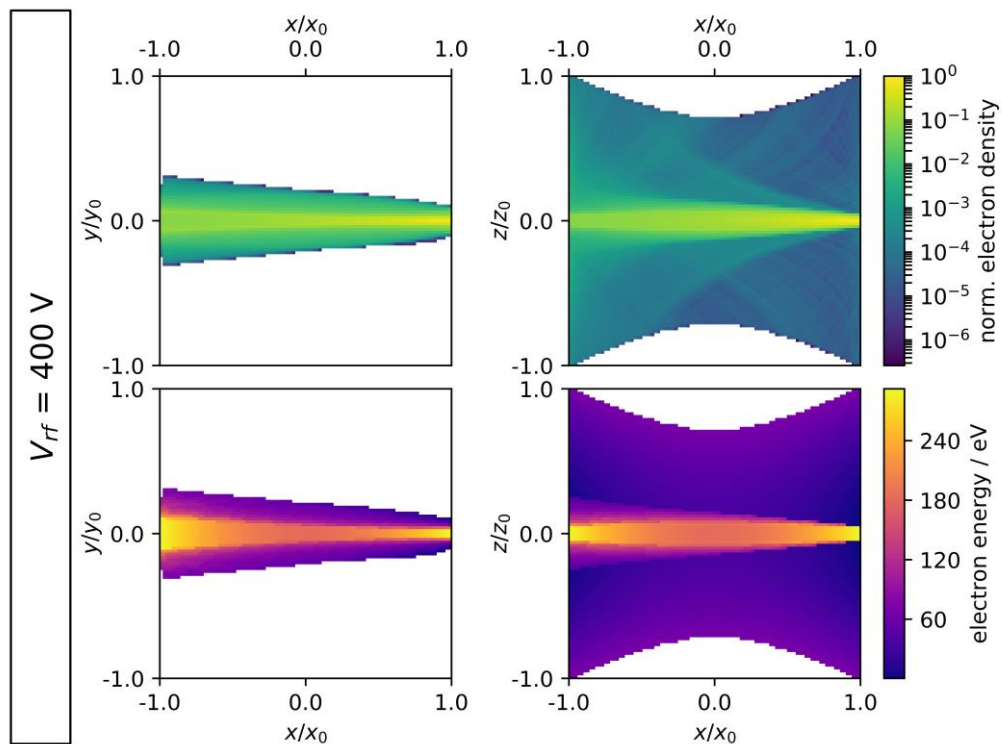


**Figure 57:** Half-sections of the normalized electron density (top) and energy (bottom) in the xy (left) and xz plane (right) for an RF voltage of 400 V, averaged over one RF cycle.

gating of the electron beam at RF voltages above 70 V. With a ring potential of 0 V the electron energy is solely defined by the filament voltage and is constant inside the trap. At all other potentials the quadrupolar field leads to spatially variable electron energies. As seen in Figure 56 and Figure 57, the RF-averaged electron energy varies significantly inside the ion trap. The potential distribution has a minimum or maximum in the trap center, depending on the polarity of the applied potential. Accordingly, the electron energy decreases or increases, respectively, towards the center. The average electron density is the highest along the central axis of the electron beam. The electron density diminishes very fast towards the beam boundaries. The electron energy has its maxima near the entry and exit holes in the ring electrode.

### 4.3.3 In-trap ionization rates

Spatially resolved ionization rates, averaged over a full RF cycle, are calculated from the 3D electron density and energy distributions. The ionization rates for nonuniform electron energy are calculated for each grid cell of a 3D electron density distribution, according to eq. (4-16). The ionization volume length is replaced by the grid cell length  $\Delta x_{\text{cell}}$ . The corresponding ionization cross sections for the mean electron kinetic energy in each cell  $\sigma_{i,\text{cell}}(\text{KE})$  are determined by linear interpolation of literature data (H<sub>2</sub>O, N<sub>2</sub> and O<sub>2</sub>: [190], Ar: [191]). The electron current is weighted with the relative electron density per cell, which is calculated as the ratio of the electron number per cell  $N_{e,\text{cell}}$  and the total number of electrons in the simulation  $N_{e,\text{sim}}$ . The resulting, spatially resolved ionization rate distribution  $R_{i,3D,v}$  is calculated for a defined ring potential:

$$R_{i,3D,v} = \frac{N_{e,\text{cell}}}{N_{e,\text{sim}}} \cdot I_e \cdot N_A \cdot \sigma_{i,\text{cell}}(\text{KE}) \cdot \Delta x_{\text{cell}} . \quad (4-24)$$

Due to the dynamic trapping field inside the ion trap, the ionization rate depends on the phase of the RF oscillation. The electron beam simulations were performed with static ring potentials to reduce computation time. The dynamic field is then approximated stepwise by a set of static fields, each with a given ring potential  $v$ . The total ionization rate for one RF cycle  $R_{i,3D,\text{RF}}$  is calculated as the weighted sum of  $R_{i,3D,v}$ :

$$R_{i,3D,\text{RF}} = \sum_v R_{i,3D,v} \cdot w_{\text{RF},v} . \quad (4-25)$$

The weighing factor  $w_{\text{RF},v}$  is the relative temporal contribution of a static field to the approximated dynamic field. The segmentation of the RF cycle is illustrated in Figure 58.

## Modeling of an FT ion trap

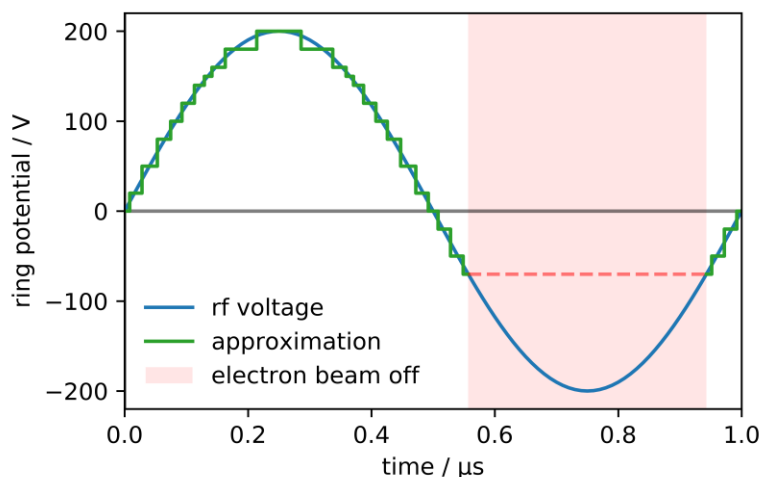


**Figure 58:** Step-wise approximation of the RF voltage by intervals of static ring potentials.

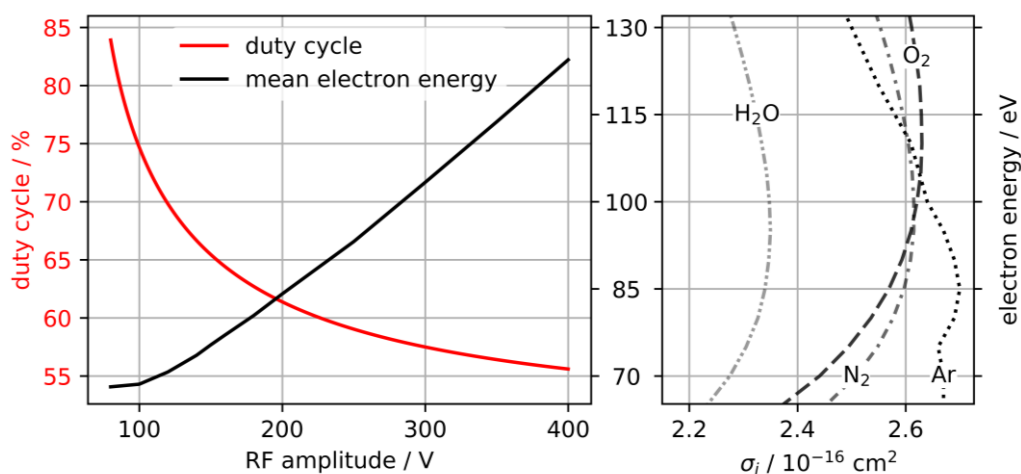


**Figure 59:** Electron beam duty cycle and mean electron energy inside the ion trap (left) and energy-dependent EI cross sections of selected compounds (right).

When the negative ring potential exceeds the electron acceleration voltage in the e-gun, electrons are repelled from the ring electrode and do not enter the ion trap, leading to a gating effect. As a result, increasing the RF amplitude decreases the ionization duty cycle (Figure 59, left). Since EI cross sections depend on the electron energy (Figure 59, right) the mean electron energy inside the ion trap impacts on the total ionization rate.

Figure 60 shows ionization rates for common matrix and background gases. For all these compounds the ionization rate decreases monotonically as the RF amplitude increases. The number of produced ions per millisecond is in the range of one million at typical ionization conditions and a trap pressure of  $10^{-6}$  mbar. This

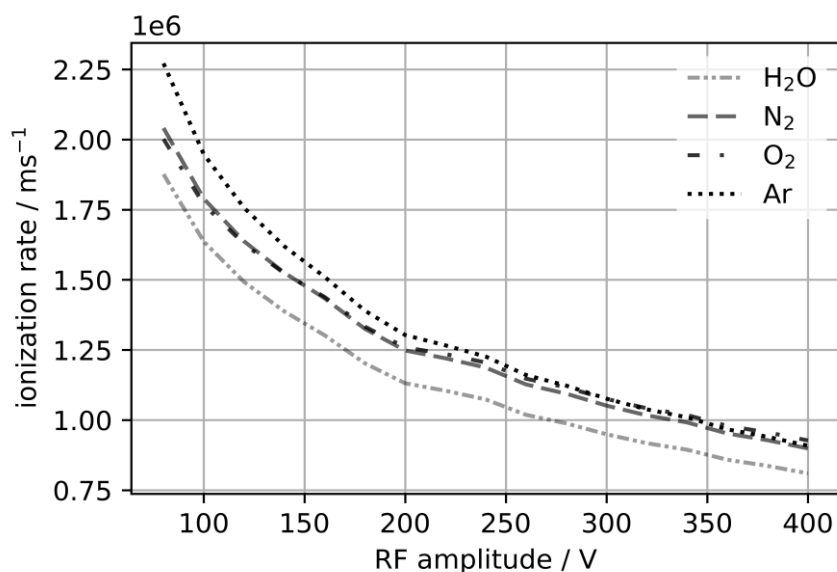


**Figure 60:** RF-voltage-dependent ionization rates of selected compounds at an ionization pressure of  $10^{-6}$  mbar and an electron current of  $10 \mu\text{A}$ .

implies that the ion trap is easily overloaded with ions, especially when the analyte compound of interest is present at trace mixing ratios and thus prolonged ionization times, gas pulse lengths, and increased sample pressures are necessary to achieve the required sensitivity. In comparison to typical scanning QIT mass spectrometers, this value is already above the spectral capacity limit. This holds even true for the Bruker High Capacity Trap (HCT), which has an optimized geometry for improved space charge capacity. The gas experiments and simulations discussed in section 4.2 suggest that the pressure inside the FT QIT may well increase up to  $10^{-3}$  mbar. With the same ionization parameters as for the simulations discussed in the present section, the number of generated ions would rise to the order of one billion. In this context, it is obvious – and this was shown experimentally [160] – that application of SWIFT for selective ejection of matrix ions is a *prerequisite* for the operation of the FT-QIT.

Figure 61 shows the spatial distributions of ions generated by in-trap EI, which resemble the shape of the electron beam. The highest ionization rate is in the center of the beam, along the axis of propagation. Since the electron density decreases steeply in the  $y$  and  $z$  directions, the ionization volume is basically shaped like a truncated cone with a small opening angle. Gaps in the ionization rate distribution near the ring electrode in the  $xz$  plane are due to low electron energies in these regions.

## Modeling of an FT ion trap

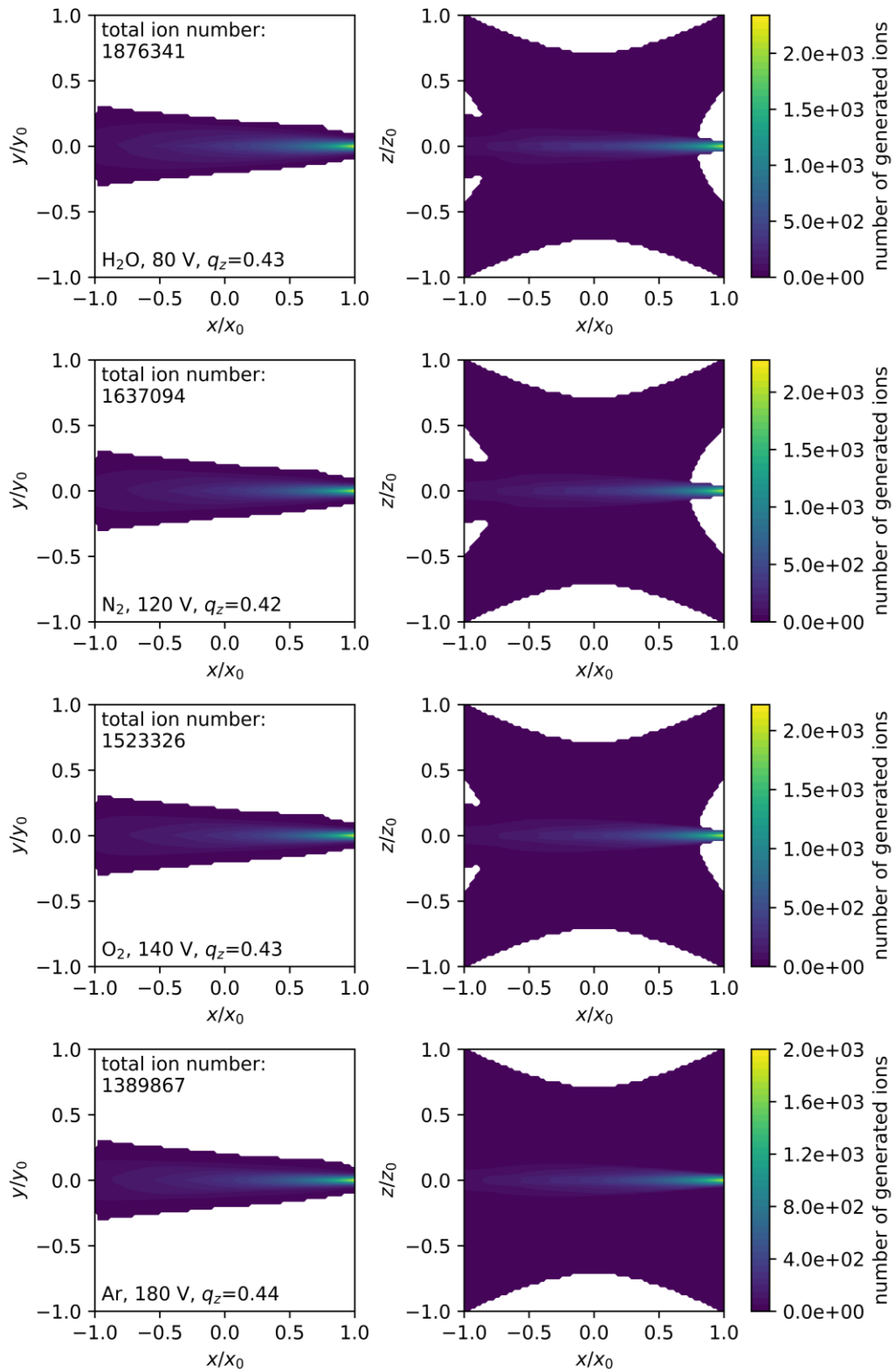


**Figure 61:** Projections of the ion densities obtained for different analytes with constant ionization parameters:  $p_i = 10^{-6}$  mbar,  $I_e = 6.2 \cdot 10^{13} \text{ s}^{-1} \triangleq 10 \text{ } \mu\text{A}$ ,  $t_i = 1$  ms.

#### 4.3.4 Ion definition files for trajectory simulations

The ion definition files required for subsequent ion trajectory simulations are created with a Python script, which arranges the ion parameters to the appropriate format. The parameters are: ion mass, charge, time of birth (TOB), initial kinetic energy or velocity, direction, and position. The TOB is distributed uniformly over the selected ionization time. The initial ion kinetic energy is set according to an MBD ( $T = 298$  K). A random sample of this distribution is generated with a rejection sampling function and is arbitrarily assigned to the ions. For small ion numbers (e.g.  $10^4$  ions), the ion positions are sampled from the ionization rate distribution with a 3D rejection sampling function implemented in Python. The method scales poorly with sample size, due to the large fraction of the distribution that has very small or zero probability. Since the electron density and therefore the ionization rate varies by orders of magnitude inside the ion trap, ions will mainly be created in a comparatively small region. A fraction of the 3D ionization rate distribution, containing only values above a threshold (e.g., 0.1% of the maximum density), is selected prior to sampling, to effectively decrease computation time, without changing the distribution of the resulting samples. However, the method remains comparably slow. Therefore, it is only used for small sample numbers ( $n \leq 10^4$ ). For larger ion ensembles ( $n > 10^4$ ), mandatory for space charge simulations in IDSimF, the ionization rate distribution is resampled with a Gaussian kernel density estimator (`scipy.stats.gaussian_kde` [26]). This allows very fast generation of large random samples from this distribution. An exemplary ion ensemble is depicted in Figure 62. SIMION ion definition files are stored in the native *fly2* file format. For IDSimF, the ion parameters are stored in a *csv* file.

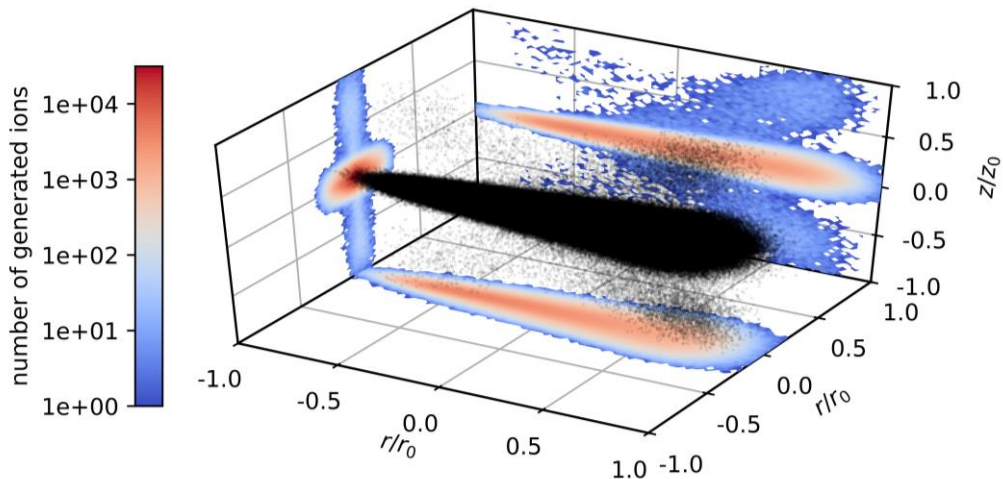


**Figure 62:** Ion ensemble ( $n = 1.4 \cdot 10^6$ , black dots) and color-coded projections of the ion density.

## 4.4 Ion storage

As discussed earlier, ions are generated during the ionization time at different positions within the quadrupolar field. The stability parameter  $q_z$  determines whether an ion is stably oscillating in the field. Loss of stable ions can occur in a real QIT due to three processes:

- 1) In a QIT with finite dimensions, ions can be created on terminal trajectories, i.e., they eventually collide with an electrode, even though they are theoretically stable.
- 2) Deviations of the electrode geometry from the purely hyperbolic shape, e.g., misalignments or holes in the electrodes, can lead to field errors that promote ion loss.
- 3) Ions can experience defocusing forces due to collisions with the background gas or space charge.

The previously calculated ion samples (section 4.3.4) are used to initialize ion trajectory simulations to investigate the trapping efficiency in dependence of the ionization parameters as well as ion loss processes during a measurement cycle.

### 4.4.1 SIMION and IDSimF model

Ion trajectory simulations with SIMION and IDSimF are performed with the complete ion trap model, including the cap and ring electrodes as well as the e-gun. The SIMION potential arrays are also used in IDSimF. Ion definition files are created according to the calculated ionization rates (cf. section 4.3.4). The RF voltage with a frequency of 1 MHz is applied to the ring electrode. The RF amplitude is adjusted to the respective ion  $m/z$ . Collisions are calculated with the hard-sphere collision models available in SIMION and IDSimF. Ion-ion interactions are only considered in IDSimF.

### 4.4.2 Ion acceptance of the QIT

The stability of an ion in a 3D quadrupolar field is determined by its stability parameter  $q_z$ . However, since the quadrupolar field inside an ion trap is spatially limited by the trap electrodes, ion trajectories may be terminal even if the ion is theoretically stable, according to its stability parameter. An obvious example is an ion that enters the ion trap from the outside. This ion's kinetic energy exceeds the pseudopotential by its incident kinetic energy and will thus eventually collide with one of the electrodes. Ions that are created inside the trap by electron ionization retain the thermal kinetic energies of the neutral precursors, which is significantly

lower than typical ion injection energies. Ions can still be lost, e.g., due to field errors, resulting from non-ideally shaped electrodes or unfavorable starting conditions within the RF field.

The spatial ion acceptance of the iTrap is investigated with SIMION and IDSimF simulations. Both simulation programs are used with an identical ion trap geometry and ion definitions.  $10^5$  ions are started uniformly distributed in a cylindrical volume with a radius of  $r_0 = 10$  mm and a length of  $2z_0 = 14$  mm. The initial kinetic energy is zero. Collisions and space charge are not considered. The stored ion distribution is evaluated after 1 ms. Since the ion trap is approximately rotationally symmetrical<sup>20</sup>, the ion acceptance can be expressed in terms of the ions' axial and radial positions,  $z$  and  $r$ . The ion acceptance is the spatially resolved proportion of trapped ions in relation to the total number of ions in the simulation. It is calculated from the initial spatial distribution of ions that are trapped and the initial spatial distribution of all ions, which both are the 2D histograms of the respective ions'  $r$  and  $z$  positions. Figure 63 shows the ion acceptance for  $N_2^+$  ions for two different  $q_z$  values. SIMION and IDSimF results are shown side by side for comparison. Generally, ions generated in the center of the ion trap are stored efficiently; the ion acceptance decreases with increasing  $r$  and  $z$  position. With increasing RF voltage or  $q_z$  (the results for ions with different  $m/z$  but the same  $q_z$  are identical), the ion acceptance decreases faster in both  $z$  and  $r$  direction. The effect is more pronounced along the  $z$  axis. This is reflected in the distribution of ion termination positions in the simulations. A large number of ions is lost at the cap electrodes and this number increases when the RF voltage is increased. With an RF voltage of 50 V ( $q_z = 0.174$ ) 25% of the ions that are lost terminate on one of the cap electrodes. At 200 V ( $q_z = 0.696$ ) the fraction of ions that are lost at one of the cap electrodes increases to 41%. In the SIMION results, the maximum ion acceptance in the trap center increases when the RF voltage is increased. In IDSimF, the maximum ion acceptance in the trap center does not depend on the RF voltage and is slightly higher as compared to the SIMION results. Field errors caused by holes in the ion trap electrodes do not lead to a decreased acceptance of ions that are created near these regions. The ion loss at the ring electrode is constant over the entire circumference of the electrode. The slits in the cap electrodes are far away from the volume in which ions usually dwell when they are stored in the ion trap and there is no increased ion loss detectable near these slits. In general, the ion loss is largest in the regions with the smallest inner dimensions, i.e., the electrode vertices.

---

<sup>20</sup> This is not entirely true due to holes in the ring electrode, which break symmetry.

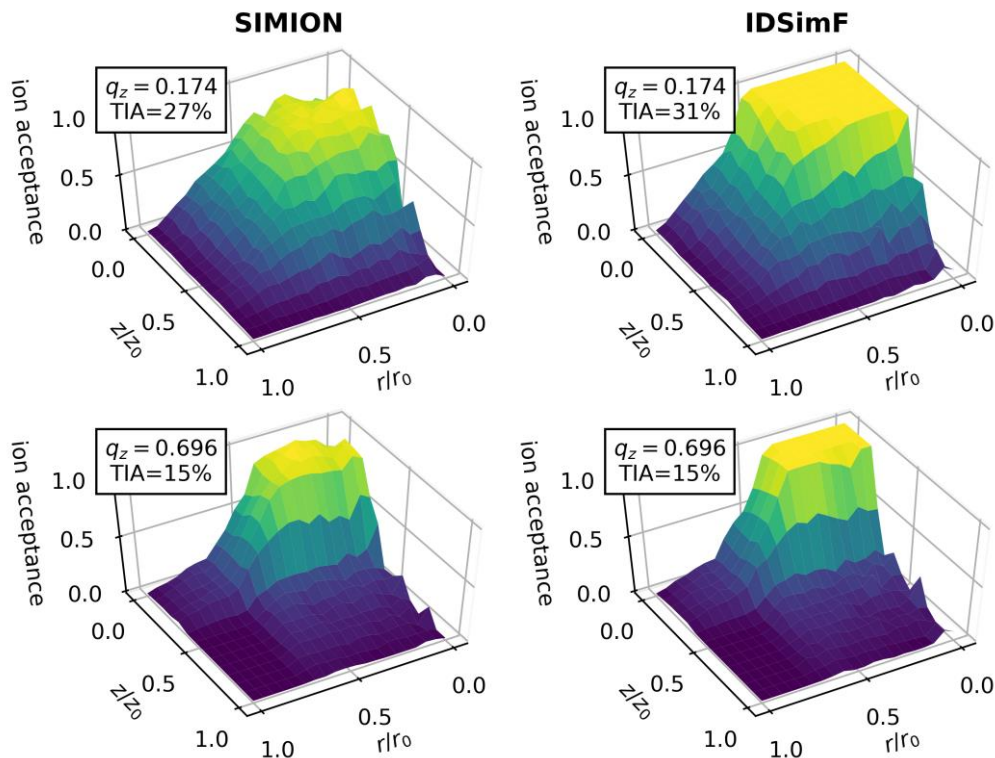


**Figure 63:** Comparison of the spatial ion acceptance distributions of the FT-QIT in dependence of the ions' initial  $r$  and  $z$  position for two different  $q_z$  values. Results from SIMION (left) and IDSimF simulations (right) are shown. The relative total ion acceptance TIA represents the percentage of ions that is active in the simulations after 1 ms.

The ion acceptance is a spatial and temporal function of ion creation relative to the sinusoidal RF voltage, i.e., the RF phase angle. Ions that terminate at the cap electrodes exhibit a significantly different phase angle distribution than ions that are lost at the ring electrode. Exemplary initial spatial and phase angle distributions of ions that terminate at the cap and ring electrodes, respectively, are shown in Figure 64. The spatial distribution of ions that are lost at the cap electrodes shows that ions from the center region ( $z = -4 - 4$  mm) do not terminate at the cap electrodes. The width of this gap in  $z$  direction becomes smaller when the RF voltage is increased. The same behavior is observed for ion loss at the ring electrode, but in the  $r$  direction. The discontinuity around  $r = 7$  mm (Figure 64, left) and  $z = 4$  mm (Figure 64, right) is due to the overlap of the cap and ring electrode loss distributions in this region. The ion loss is a result of the interaction of the ions with the dynamic field: Ions that are created close to one of the electrodes while the electric force acts towards this electrode are easily lost when they reach the electrode surface before the direction of the electric force changes. When ions are created when the electric force acts away from the electrode, it may occur that the

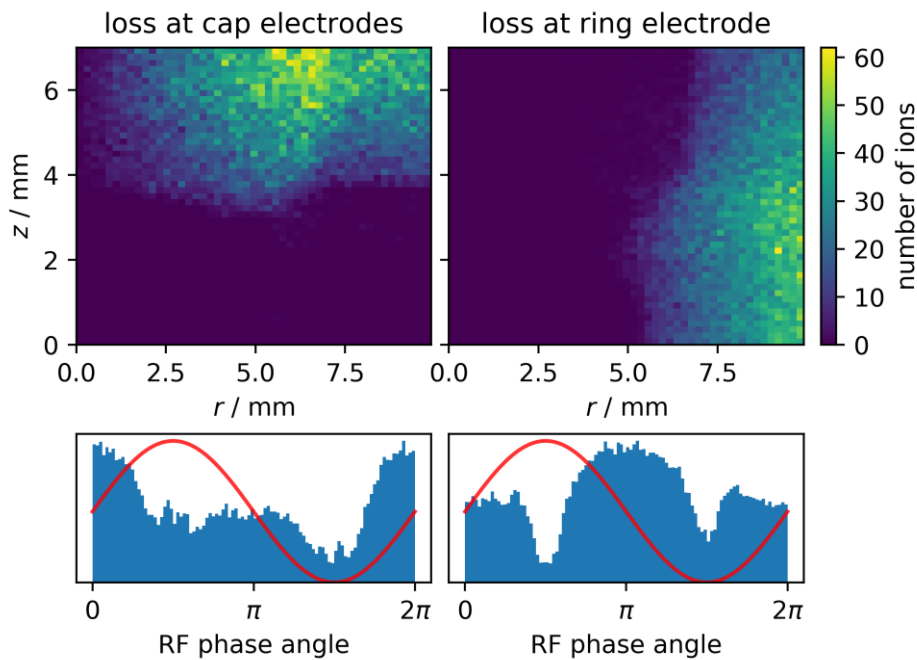


**Figure 64:** Initial spatial (top) and RF phase angle distributions (bottom) of  $N_2^+$  ions in a QIT that are lost at the cap electrodes (left) and ring electrode (right). The RF voltage is 50 V ( $q_z = 0.174$ ). The red lines illustrate the RF voltage. The results are obtained with IDSimF.

ions arrive at the ion trap center at a time when the electric field has inverted. Then the ions are accelerated further in the same direction towards the opposing electrode. These ions will gain sufficiently large kinetic energies within one RF cycle and terminate at the opposing electrode. Of course, there are infinite combinations of points of creation in space and time, which results in the complex shape of the phase angle distributions (Figure 64, bottom). Ions that are created close to the center of the ion trap mostly remain stable. These ions do not gain enough kinetic energy in the first half of the RF oscillation to “outrun” the field and thus remain trapped. The different shapes of the RF phase angle distributions for ion loss at the cap and ring electrodes result from the different  $r$  and  $z$  dimensions of the ion trap. This introduces a shift in the temporal relationship between ion creation and ion loss in both directions.

#### *SIMION vs. IDSimF*

There are minor differences between the SIMION and IDSimF results without consideration of space charge: The spatial ion acceptance is slightly higher in the trap center in the IDSimF simulations. In the phase-dependent ion loss distribution for the ring electrode obtained from SIMION simulations, a local minimum appears at a phase angle of  $180^\circ$  when the RF voltage is above 120 V. This minimum is not

present in the IDSimF results. These differences are attributed to the different trajectory integration methods that are utilized in both programs: SIMION uses a Runge-Kutta method [13]. The timestep length in SIMION is determined by the trajectory quality factor  $T.Qual$ , which was set to 3 in the present simulations. When  $T.Qual$  is positive, the timestep length is dynamically adjusted to increase the accuracy for certain cases (e.g., large field gradients, velocity reversal, near electrode surfaces). IDSimF builds on a Verlet method [1] with constant timestep length. When compared directly, the trajectories of individual ions obtained with both programs show deviations. The magnitude of the difference scales with the timestep length in IDSimF. The timestep length in the present IDSimF simulations was  $10^{-8}$  s, which was found to be a reasonable trade-off between accuracy and simulation time. For a timestep length of  $10^{-8}$  s in IDSimF, the maximum deviation is in the range of 1‰ for the  $z$  and 2‰ in the  $r$  position and the mean deviations are -0.3‰ ( $r$ ) and 0.002‰ ( $z$ ). In general, the difference between the integration methods becomes negligible when randomizing events such as collisions or ion-ion interactions are considered because these processes distort the pure interaction of the ions with the electric field. Since IDSimF was primarily developed to provide a tool for ion trajectory simulations with consideration of space charge, collisions, and chemical reactions, the lower trajectory accuracy at moderate timestep sizes can be tolerated. The IDSimF results were carefully assessed in benchmark simulations. Even though the Verlet integrator can introduce small errors, the bulk properties resulting from interactions with the electric field (e.g., secular oscillation and micromotion frequencies) are correctly displayed.

### *Space charge*

At high charge densities, space charge creates a defocusing force on the ions. The effect of Coulombic repulsion on the ion storage capacity of the ion trap is evaluated with IDSimF. Identical simulation parameters are used as in the previously discussed simulations without space charge. Collisions are not considered. The initial number of ions is  $10^5$  in all simulations and the number of charges is determined by the space charge factor ( $scf$ ), e.g., a space charge factor of 50 results in  $50 \cdot 10^5$  charges. Figure 65 shows the spatial ion acceptance for different  $q_z$  and space charge factors.

With a space charge factor of 1 ( $\triangleq 10^5$  charges, Figure 65, second row) the ion acceptance distribution is comparable to the distribution without space charge (Figure 63, top row). An increase in total charge number does decrease the extent of the plateau region in the trap center (in which the ion acceptance has its maximum) in  $r$  direction. The decrease of ion acceptance in the trap center with  $r$  is

steeper the higher the charge number. This appears to be counterintuitive, because an ion in the trap center experiences space charge from all directions so that the additional forces should cancel out, while ions at the boundary of the ion cloud experience a net outward force from the ion cloud. However, ions with a large initial  $r$  or  $z$  position are swiftly lost due to their point of creation (as discussed above) and, thus, their loss rate is nearly unaffected by space charge. This is the case in the ion acceptance distributions with consideration of space charge, cf. Figure 65 for  $r/r_0 = z/z_0 \geq 0.5$ .

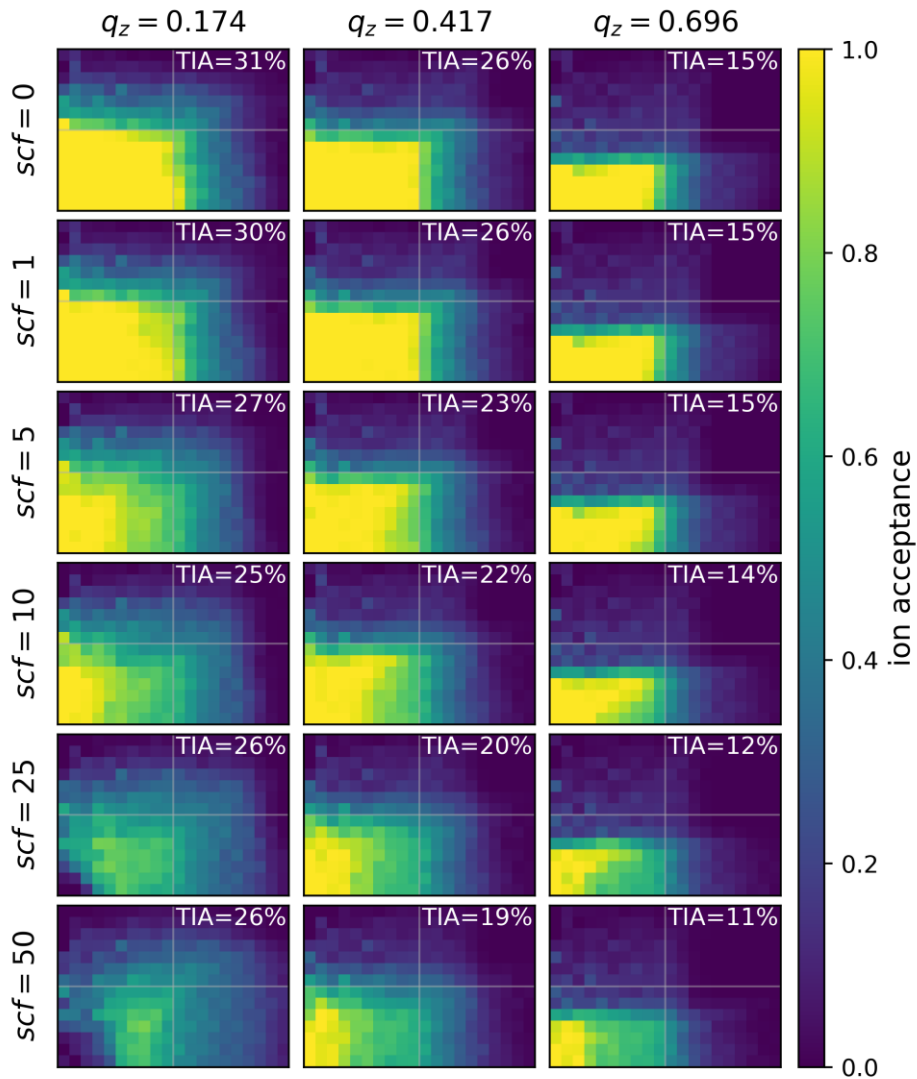


**Figure 65:** Spatial ion acceptance distributions of the FT-QIT for different  $q_z$  (from left to right) and  $scf$  (from top to bottom). The relative total ion acceptance TIA represents the percentage of ions in the simulations that are active after 1 ms has elapsed. The horizontal and vertical axes are the  $r$  and  $z$  axis of the ion trap, respectively.

The relative total ion acceptance (TIA) is the fraction of the number of stored ions after 1 ms and the initial ion number in the simulation. The TIA differs between SIMION and IDSimF results without space charge at lower  $q_z$  (Figure 63, top) which is attributed to the different trajectory integration methods used in both programs, as discussed before (section 4.4.2, *SIMION vs. IDSimF*). Generally, the TIA decreases with increasing  $q_z$  (Figure 65, from left to right). This trend is also observed in the simulations with consideration of space charge, but the magnitude of TIA values is lower than without space charge. This was already inferred from the spatial ion acceptance distributions, where parts of the distribution diminished with increasing charge number (cf. Figure 65, from top to bottom). In the considered  $scf$  range (1 - 50), the change of the TIA in dependence of the  $scf$  is in the single digit percent range. With  $q_z = 0.696$  and  $q_z = 0.417$  the TIA decreases monotonically; the magnitude is smaller at higher  $q_z$ . This is due to the fact that the TIA without space charge depends heavily on  $q_z$ . At higher  $q_z$ , the number of ions that are lost due to their initial position is significantly larger than at low  $q_z$ , e.g., 31% at  $q_z = 0.174$  vs. 15% at  $q_z = 0.696$  (Figure 65, top row). This causes a) different total charge numbers in the trap and b) different ion cloud dimensions, especially along the  $z$  axis (cf. Figure 65, from left to right). High  $q_z$  values favor smaller ion numbers and smaller  $z$  extensions of the ion cloud, resulting in a lower impact of space charge, and *vice versa*. Surprisingly, the TIA does not decrease significantly at  $q_z = 0.174$  for  $scf > 10$  (Figure 65, left column). The corresponding spatial ion acceptance distributions reveal that the maximum around  $r = z = 0$  becomes a minimum in these cases, resulting in a new maximum in the range of  $r = 0.3$  and  $z = 0$ . At the same time the distribution becomes broader in both  $r$  and  $z$  direction, which overcompensates the elevated ion loss at the trap center. This explains the increase of TIA with  $scf > 10$ . The steep decrease of ion acceptance in the trap center with increasing  $scf$  is a result of the ion motion in the quadrupolar field. The initial direction of movement of ions that are created in the center is towards the electrodes. Due to the high charge density in the simulations, these ions are additionally pushed further outwards by the ion cloud potential, resulting in loss of these ions at the cap and ring electrodes. This is prevented at higher  $q_z$  by the larger focusing force of the quadrupolar field.

Increasing space charge in the simulations does not only impact the spatial ion acceptance distribution and total number of stored ions, but also the dynamic motion of the ions in the quadrupolar field. The undisturbed ion motion is characterized by a fixed phase angle relative to the RF voltage (micromotion) and a constant secular frequency. When the ion trajectory is displayed in  $(u, v_u)$  phase space

(where  $u$  is the spatial coordinate and  $v_u$  is the corresponding velocity), this representation yields the typical elliptic relationship between the ion position and velocity in a quadrupolar field [192–194], which is also obtained in the simulations without space charge (Figure 66, left). The ion motion results in an oscillation of the ion cloud’s volume and thus density. Space charge disturbs the field-defined ion motion, leading to a randomization of the trajectories in phase space and loss of the initial phase correlation with the RF field. This is clearly seen in the phase space plot as blurring of the elliptical relationship between the ion position and velocity (Figure 66, right). This is in principle comparable to the impact of collisions on the ion trajectories (cf. section 4.4.4). However, collisions are individual events that disturb the ion motion erratically, while space charge does apply a permanent force that changes in magnitude over time. When the collision frequency is small compared to the ion secular frequency, the phase space trajectory is shifted but retains the elliptic shape. This is seen in Figure 68 (section 4.4.4). The ensemble effect of space charge does shift the trajectory continuously, leading to the blurring of the elliptic shape. Both processes lead to a dampening of the defined oscillation of the ion cloud and an essentially static mean ion distribution after an initial equilibration time. At higher RF voltages, or  $q_z$ , this equilibration time increases in the simulations. Note however that the total ion number decreases faster at higher  $q_z$  and the different equilibration times can also be a result of the different total charge density.

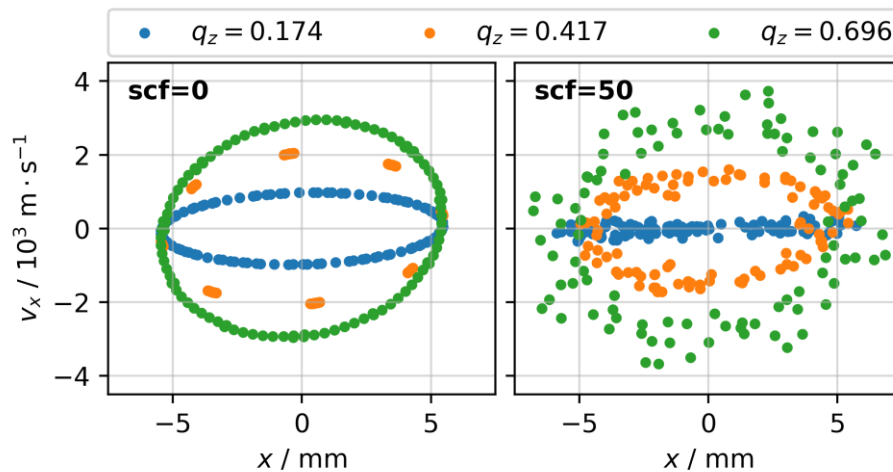


**Figure 66:** Trajectory of an  $\text{N}_2^+$  ion in  $(x, v_x)$  phase space at different  $q_z$  values with  $scf = 0$  (left) and  $scf = 50$  (right).

### 4.4.3 Stored ion ensemble and storage capacity

When the shape of the ion acceptance is put into context with the previously described spatially resolved ionization rates in the iTrap (cf. section 4.3.3), there is actually a beneficial overlap of both these distributions: The ion beam created with the electron beam has its main density along the ion trap's  $r$  direction with only little radial width (with regard to the ion beam). The actual stored ion ensemble is evaluated in a simulation with an ensemble of  $\text{Ar}^+$  ions according to the spatial ionization rates described in section 4.3.3. The ion sample is created for an ionization pressure of  $10^{-6}$  mbar, filament emission current of  $10 \mu\text{A}$ , ionization time of  $1 \text{ ms}$  and RF voltage of  $140 \text{ V}$  ( $q_z = 0.487$ ). These settings yield about  $1.5 \cdot 10^6$  ions. The size of the ion sample is set to  $10^5$  with  $scf = 15$ , to reduce computation time while retaining the actual total charge number. Another simulation with  $scf = 50$  ( $\cong 5 \cdot 10^6$  charges) is performed for comparison. The stored ion ensembles after  $1.1 \text{ ms}$  (i.e.,  $0.1 \text{ ms}$  after the ionization time) and after  $5.0 \text{ ms}$  are shown in Figure 67, along with 2D projections of the ion density.

The spatial distribution of the ionization rate can be approximated by a truncated cone with the axis of symmetry in  $r$  direction of the ion trap. The randomizing space charge interaction leads to a symmetric shape of the stored ion cloud, which is independent of the initial distribution. The shape of the stored ion cloud can be

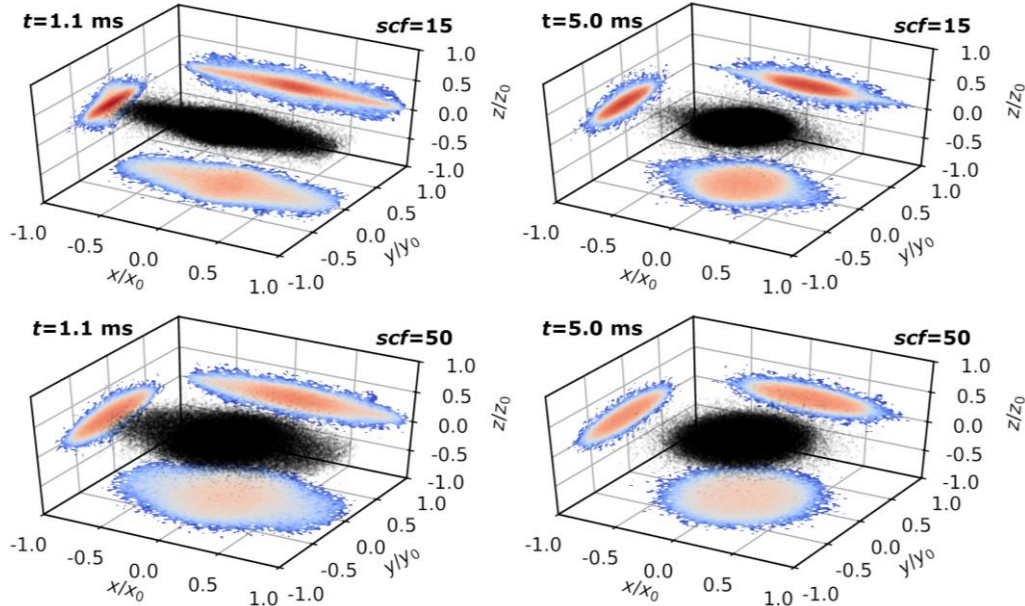


**Figure 67:** Stored  $\text{Ar}^+$  ion ensembles and 2D projections of the ion density after  $1.1 \text{ ms}$  (left) and  $5 \text{ ms}$  (right) with  $scf = 15$  (top) and  $scf = 50$  (bottom). The color scaling is the same for all four images.  $10^5$  ions are started in the simulations. The RF voltage is  $140 \text{ V}$  ( $q_z = 0.487$ ).

approximated by an oblate spheroid in the ion trap center. The shape of the spheroid is characterized by two semi-axes  $a$  and  $c$ , which are parallel to the ion trap's  $r$  and  $z$  axes, respectively. The lengths of the semi-axes are approximated by the triple standard deviation of the respective ion positions.

$$a = 3 \cdot \sqrt{\frac{\sum_{i=1}^n (x_i - \bar{x})^2}{n-1}} = 3 \cdot \sqrt{\frac{\sum_{i=1}^n (y_i - \bar{y})^2}{n-1}} \quad (4-26)$$

$$c = 3 \cdot \sqrt{\frac{\sum_{i=1}^n (z_i - \bar{z})^2}{n-1}} \quad (4-27)$$

After the ionization time, the ion number and the dimensions of the ion cloud change over time, converging against an equilibrium state with a constant ion density, i.e., volume and ion number. The ion cloud volume is approximated by the oblate spheroid volume  $V_{os}$ , which is given by [195]:

$$V_{os} = \frac{4}{3} \pi a^2 c. \quad (4-28)$$

The equilibrium charge densities for the simulations with  $scf = 15$  and  $scf = 50$  are  $4.20 \cdot 10^6 \text{ cm}^{-3}$  and  $3.77 \cdot 10^6 \text{ cm}^{-3}$ , respectively (cf. Table 18). The difference between the two simulation results are readily explained by the impact of the  $scf$  on the spatial ion acceptance discussed in section 4.4.2, *Space charge*.

**Table 18:** Equilibrium ion cloud parameters from IDSimF simulations with different  $scf$

scf	Ion number	$V_{os}$ (cm <sup>3</sup> )	Charge density (cm <sup>-3</sup> )
15	$5.38 \cdot 10^4$	$1.92 \cdot 10^{-1}$	$4.20 \cdot 10^6$
50	$3.66 \cdot 10^4$	$4.85 \cdot 10^{-1}$	$3.77 \cdot 10^6$

These charge densities represent the storage capacity limit of the iTrap and are in very good agreement with experimental values of  $2 \cdot 10^6 \text{ cm}^{-3}$  and  $4 \cdot 10^6 \text{ cm}^{-3}$  for  $\text{N}_2^+$  and  $\text{Kr}^+$  ions, respectively, that were determined by Fischer in one of the first QIT instruments [145]. There are slight differences between the simulation and the conditions of the experiments performed by Fischer. The QIT used in the experiments had twice the size ( $r_0 = 20 \text{ mm}$ ) of the iTrap, however, both ion traps satisfy the condition  $r_0^2 = 2z_0^2$ . The  $q_z$  value in the experiments can be estimated from the given experimental parameters: ion trap dimensions:  $r_0 = 20 \text{ mm}$ ,  $z_0 \approx 14.2 \text{ mm}$ ; RF frequency: 500 kHz; resonance frequency of  $\text{N}_2^+$  ions: 150 kHz. With these values, eq. (3-10) yields  $q_z = 0.845$ . In the simulations presented above  $q_z$  is lower ( $q_z = 0.487$ ) and the difference between the experiments and simulations matches well with the trend of the  $q_z$ -dependence of the ion acceptance (cf.

section 4.4.2, *Space charge*). The TIA for the conditions in the simulations is 20% for  $scf = 15$  and 17% for  $scf = 50$  (extrapolated from the data in Figure 65). For the higher  $q_z$  value in the experiments ( $q_z = 0.845$ ), the TIA is estimated to 8% and 7%, respectively. With these TIA values, the charge densities obtained in the simulations ( $q_z = 0.487$ ) are extrapolated to  $1.68 \cdot 10^6 \text{ cm}^{-3}$  for  $scf = 15$  and  $1.55 \cdot 10^6 \text{ cm}^{-3}$  for  $scf = 50$ , which is in very good agreement with the experimental literature data.

### 4.4.4 Collisions and ion loss

Collisions of ions with the background gas (*buffer gas*) are essential for scanning quadrupole ion traps with an external ion source. Due to collisions with a low molecular weight background gas ions experience during the injection into the trap, the ions' kinetic energies decrease (*collisional cooling*), which in turn improves the trapping efficiency. This is one of the reasons why the pressure inside scanning ion traps is held in the range of  $10^{-3}$  mbar [106]. Helium is commonly used as background gas. Using a heavier background gas can lead to a net increase of the mean ion energy, which is expressed by the term *RF heating* (cf. section 4.1.1, *Collisions*). When in-trap ionization is utilized (i.e., ions are created within the quadrupolar field), there is no necessity for a buffer gas promoting ion trapping. In fact, every collision an ion undergoes during the subsequent mass analysis damps its oscillation and reduces the measured signal intensity. Hence, the FT operation requires the trap pressure to be as low as possible. Collisions can also adversely affect the ion storage process, as scattering of ion trajectories potentially leads to ion loss. The extent of collisional cooling and heating of the ion motion depends on the ratio of the molecular ion and neutral mass. In general, the average ion energy increases, when the gas mass is larger than the ion mass and *vice versa* [101] (cf. section 4.1.1, *Collisions*).

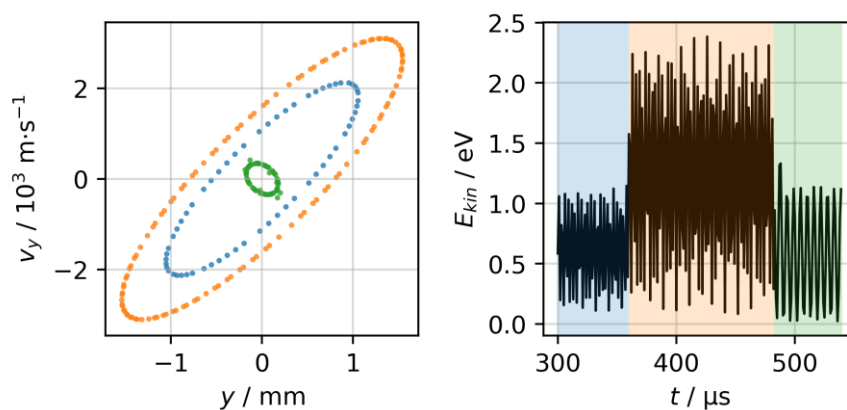
#### *Ion loss rates*

Collision-induced ion loss rates and lifetimes are evaluated with ion trajectory simulations in SIMION, utilizing the HS1 collision model. The temporal evolution of an ensemble of  $\text{Ar}^+$  ions ( $m/z$  40) is analyzed at different pressures. In each simulation, 5000 ions are started uniformly distributed in a spherical volume in the trap center with a radius of 2.5 mm. The initial kinetic energy is set to zero. Different background gas masses are used to investigate the impact of the neutral-ion mass ratio. The RF amplitude is 200 V ( $q_z = 0.486$ ) in all simulations. Table 19 summarizes the background gas parameters.

**Table 19:** Background gas information for collision-induced ion loss simulations with Ar<sup>+</sup> ions ( $m/z$  40)

Gas mass (Da)	Represented gas	Neutral-ion mass ratio	Collision cross section ( $10^{-19}$ m <sup>2</sup> ) [185]
4	He	0.1	2.8
20	Ne	0.5	3.0
28	N <sub>2</sub>	0.7	3.9
40	Ar	1.0	3.6
84	Kr	2.1	3.9

Figure 68 depicts an exemplary  $(y, v_y)$  phase space plot of a single Ar<sup>+</sup> ion inside the ion trap with argon as background gas (left), as well as the temporal evolution of the ion's total kinetic energy (right). The phase space trajectory shows the typical elliptic relationship between the ion position and velocity in a quadrupolar field [192–194]. There are three sections in the trajectory that can be easily distinguished due to their different spread in phase space. These sections are also clearly discernible as changes in the temporal evolution of the total kinetic energy. The oscillation of the total kinetic energy is uniform as long as the ion motion is undisturbed. The abrupt change in amplitude is induced by a collision event, which scatters the ion trajectory and results in a different phase relationship between ion motion and RF field. This is in contrast to the effect of space charge, which results in a continuous distortion of the RF phase relation (cf. Figure 66, right). When comparing the phase space and kinetic energy plot in Figure 68, it becomes obvious that energy can be transferred between the different coordinates: while the maxi-

**Figure 68:** Trajectory of an Ar<sup>+</sup> ion in an argon gas matrix in  $(y, v_y)$  phase space at  $10^{-3}$  mbar (left) and the ion's total kinetic energy over time (right). The colors in the left plot correspond to the colored areas in the right plot.

mum total kinetic energy is comparable in the first (blue) and third section of the trajectory (green), the maximum energy in the  $y$  direction (represented by the maximum velocity and position) is significantly different in these sections. This is due to energy transfer from the  $y$  coordinate to the  $x$  and  $z$  coordinates. In the shown example the total kinetic energy increases after the first collision and decreases again after the second collision, even though the gas mass equals the ion mass ( $m_{\text{gas}}/m_{\text{ion}} = 1.0$ ). This is because the collisions are generally not ideal head-on collisions but occur at different angles and relative velocities (cf. 4.1.1, *Collisions*). Ultimately, a single collision can trigger ion loss by scattering the ion so that its trajectory becomes terminal, i.e., the maximum oscillation amplitude exceeds the ion trap dimensions. The loss of individual ions is not caused by a step-wise increase of their kinetic energy but by single collision events. Thus, the term *collisional excitation* is more suitable in this context and will be used accordingly hereinafter, rather than *RF heating*, which is more of a bulk effect and carries the connotation of a continuous energy increase. The ions' pre-collision parameters, i.e., position, velocity and RF phase correlation, impact on the probability of ion loss after such a collision but these parameters are random, i.e., independent of experimental conditions. The frequency of strongly dephasing collisions that lead to ion loss scales with the neutral-ion mass ratio. Therefore, low mass background gases are usually used in RF trapping devices. This is also reflected in the simulation results: no strong scattering is observed at a mass ratio of 0.1 ( $\text{Ar}^+$  ions in helium), but collision-induced ion loss occurs already with a mass ratio of 0.5 ( $\text{Ar}^+$  ions in neon) and becomes more pronounced when the background gas mass is further increased.

The kinetics of the collision-induced ion loss is bimolecular and can be described with a second order rate equation:

$$\frac{dN}{dt} = -k_{\text{loss}} \cdot N \cdot N_g, \quad (4-29)$$

with the second-order rate coefficient  $k_{\text{loss}}$  and the number densities of the ion  $N$  and the gas  $N_g$ . The gas density is constant over time at constant pressure and the process can therefore be reduced to a pseudo-first-order process. The ion loss rate then depends only on the ion density  $N$ . The ion density over time  $N_t$  is determined by the pseudo-first-order rate coefficient  $k'_{\text{loss}} = k_{\text{loss}} \cdot N_g$ , with the second-order rate coefficient  $k_{\text{loss}}$  and  $N_g$  for a given pressure:

$$\ln\left(\frac{N_t}{N_0}\right) = -k'_{\text{loss}} \cdot t = -\frac{1}{\tau'_{\text{loss}}} \cdot t, \quad (4-30)$$

where  $N_0$  is the initial ion number and  $t$  is the time. The lifetime  $\tau'_{\text{loss}}$  for the first-order loss process is defined as the inverse rate coefficient [196].

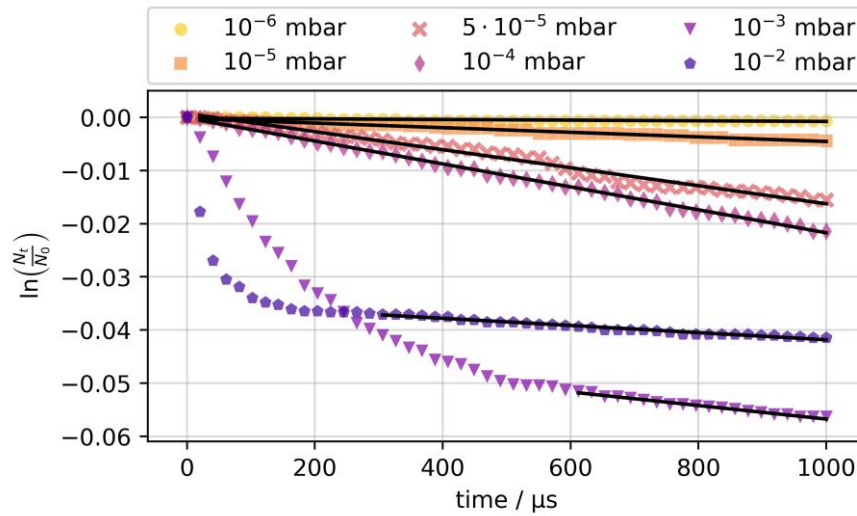


**Figure 69:** Exemplary kinetic analysis of the loss of  $\text{Ar}^+$  ions in a neon gas matrix at different pressures. The black lines are linear fits of the data.

According to (4-30), the logarithm of the ion loss rate is constant over time and this is confirmed in the simulations. The kinetic analysis of the loss of  $\text{Ar}^+$  ions in a neon gas matrix at different pressures is shown as an example in Figure 69.

A linear behavior of the logarithm of the normalized ion number is observed at pressures  $\leq 10^{-4}$  mbar, which is expected for a first-order process. At higher pressures, the order of the ion loss rate coefficient changes over time. This is a result of collisional cooling of the ion motion, which directly correlates to the number of collisions. The mean ion energy as well as the mean ion cloud radius both exhibit the same temporal profile as the ion loss curve (compare Figure 69 and Figure 71). When the mean ion cloud size and ion energy has equilibrated, the individual ion loss probability becomes constant and is lower than expected: Ions with a small radial position and kinetic energy are less likely to be deflected on a terminal trajectory because they have to experience strong scattering. It is of course debatable, which ion loss rate describes these scenarios best. The initial loss matches the expected pressure dependency, i.e., the ion loss rate changes monotonically with pressure. However, when looking at the timescale of the equilibration process (tens to hundreds of *microseconds* at  $\geq 10^{-3}$  mbar) compared to the typical lifetime of ions during an ion trap measurement (tens to hundreds of *milliseconds*), the equilibrium loss constant is the more appropriate quantity in this context. Therefore, the equilibrium ion loss constants are evaluated whenever the ion loss rate changes over time. At lower pressures, the change of the mean ion cloud size and ion energy is negligible in the considered time frame and thus the impact on the ion loss rate is not showing in the data.

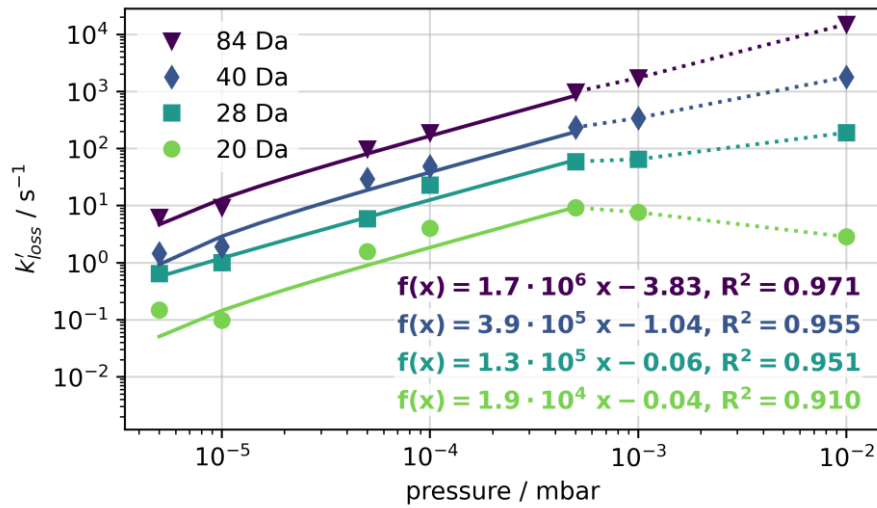


**Figure 70:** Pseudo-first-order rate coefficient  $k'_{\text{loss}}$  of the collision-induced ion loss of  $\text{Ar}^+$  ions in dependence of the background pressure for different gas masses. The solid lines are linear fits and the corresponding functions with optimized parameters and  $R^2$  values are given in the lower right part of the plot.

The pseudo-first-order rate coefficients are evaluated for all background gases listed in Table 19 except for helium, where no significant ion loss occurs. The second-order rate coefficients are obtained from the pressure dependency of the pseudo-first-order coefficients (cf. Figure 70). The linear scaling of  $k'_{\text{loss}}$  with pressure below  $10^{-3}$  mbar confirms the first-order dependency on the gas density in this range and therefore the assumption that the collision-induced ion loss is a second-order process. The rate coefficients are summarized in Table 20.

The ion lifetime strongly depends on both pressure and gas mass and varies between  $10^{-4}$  s for  $10^{-2}$  mbar with krypton as background gas, and 10 s for  $5 \cdot 10^{-6}$  mbar with neon as background gas. The mass dependency of the second-order rate coefficient can be expressed with an exponential function:

$$k_{\text{loss}} = 7 \cdot 10^6 \cdot \exp\left(-2.924 \cdot \left(\frac{m_{\text{ion}}}{m_{\text{gas}}}\right)\right). \quad (4-31)$$

The lifetimes for all gases exhibit a negative correlation below  $10^{-3}$  mbar and are shifted in along the y axis in dependence of the gas mass. Above  $5 \cdot 10^{-4}$  mbar, the trend changes, depending on the gas mass. With Ne as background gas ( $m_{\text{gas}}/m_{\text{ion}} = 0.5$ ), the lifetime increases again above  $5 \cdot 10^{-4}$  mbar and deviates from the trend at lower pressures. The deviation is more pronounced when the gas

**Table 20:** Pseudo-first-order coefficients  $k'_{\text{loss}}$  and second-order rate coefficients  $k_{\text{loss}}$  for the collision-induced ion loss with different gases

	Ne	N <sub>2</sub>	Ar	Kr
$p$ (mbar)				
			$k'_{\text{loss}}$ (s <sup>-1</sup> )	
$5 \cdot 10^{-6}$	$1.5 \cdot 10^{-1}$	$6.4 \cdot 10^{-1}$	1.5	6.3
$1 \cdot 10^{-5}$	$9.9 \cdot 10^{-2}$	1.0	1.9	9.4
$5 \cdot 10^{-5}$	1.6	6.0	$2.9 \cdot 10^1$	$9.9 \cdot 10^1$
$1 \cdot 10^{-4}$	4.1	$2.3 \cdot 10^1$	$4.9 \cdot 10^1$	$1.9 \cdot 10^2$
$5 \cdot 10^{-4}$	9.3	$5.9 \cdot 10^1$	$2.4 \cdot 10^2$	$9.8 \cdot 10^2$
$1 \cdot 10^{-3}$	7.6	$6.5 \cdot 10^1$	$3.4 \cdot 10^2$	$1.7 \cdot 10^3$
$1 \cdot 10^{-2}$	2.8	$1.9 \cdot 10^2$	$1.8 \cdot 10^3$	$1.5 \cdot 10^4$
			$k_{\text{loss}}$ (mbar <sup>-1</sup> s <sup>-1</sup> )	
	$1.9 \cdot 10^4$	$1.3 \cdot 10^5$	$3.9 \cdot 10^5$	$1.7 \cdot 10^6$

mass decreases. In the higher pressure range the collision number increases to an extent, where collisional cooling starts to occur within the time frame of the simulations. This changes the ion cloud properties, i.e., mean dimensions and kinetic energy, over time. Figure 71 shows the mean Ar<sup>+</sup> ion cloud radius evolution over time, which is a measure for the extent of collisional cooling. The ion cloud properties remain basically constant at and below  $10^{-4}$  mbar. The probability of ion loss scales with the ions' initial radial position, i.e., ions that are created closer to the electrodes are more prone to loss. When collisional cooling decreases the ion cloud size and kinetic energy, the ion loss decreases accordingly. In the case of neon as background gas, the probability of strong collisional excitation is comparably low, due to the low neutral-ion mass ratio, and is overcompensated by collisional cooling above  $10^{-4}$  mbar. At  $10^{-2}$  mbar the ion cloud size has equilibrated after ca. 300  $\mu\text{s}$ , independent of the background gas mass. At  $10^{-3}$  mbar the equilibrium is not reached during the simulation, i.e., the equilibration time is  $>1000 \mu\text{s}$ . In contrast to the equilibration time, the mean equilibrium ion cloud radius scales with  $m_{\text{gas}}$  (Ne: 0.9 mm, N<sub>2</sub>: 1.2 mm, Ar: 1.5 mm). The extent of collisional excitation is *mass-dependent* while the equilibration time is *pressure-dependent*. The extent of collisional cooling (reduction of ion cloud radius) decreases with increasing gas mass and this is reflected in the different flattening of the lifetime curves above  $5 \cdot 10^{-4}$  mbar. For krypton, the effect of collisional cooling is barely observed because the collision-induced ion loss rate is significantly larger than the collisional cooling rate. The mean ion cloud size in the simulation with krypton as background

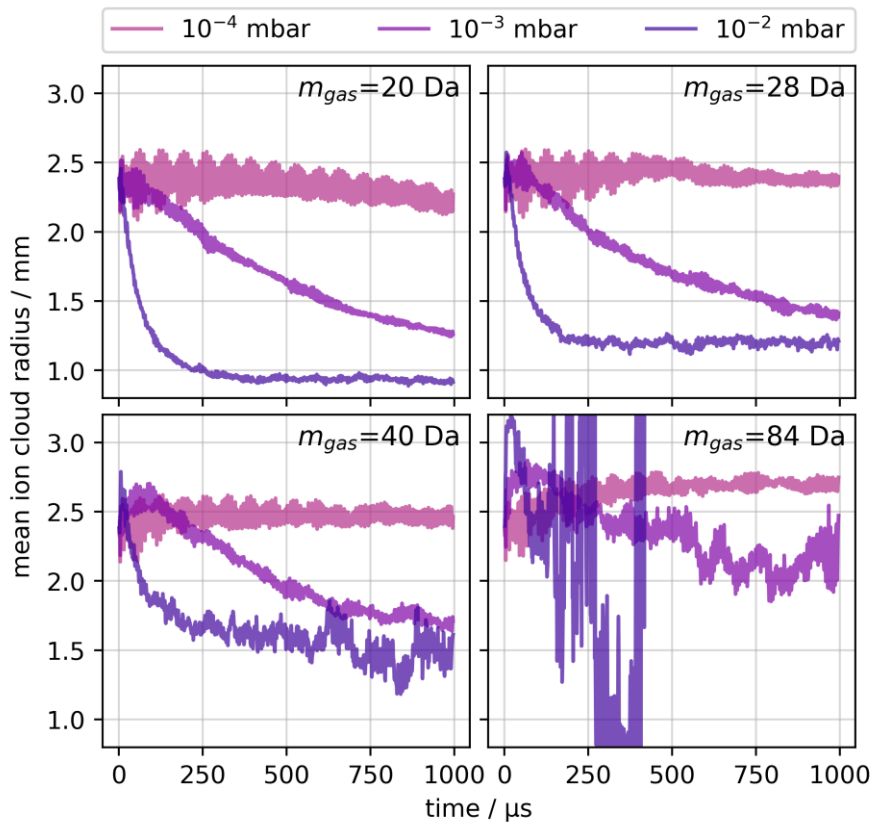


**Figure 71:** Temporal evolution of the mean  $\text{Ar}^+$  ion cloud radius in simulations with different background gases: top left: Ne, top right,  $\text{N}_2$ , bottom left: Ar, bottom right: Kr. The decrease of the mean ion cloud radius is due to collisional cooling. With krypton ( $m_{\text{gas}}=84$  Da) as background gas, all ions are lost after  $420 \mu\text{s}$ .

gas decreases between 0 and  $400 \mu\text{s}$  (Figure 71, bottom right), but this is due to the favored loss of ions with large initial radial positions. This effectively reduces the mean ion cloud radius and could wrongly be interpreted as collisional cooling.

#### *Comparison with experimental data*

Ion lifetimes were experimentally determined by Fischer in one of the first QIT instruments [145]. In the experiments, ions were continuously created by in-trap EI over the course of 30 ms and the ion intensity was repeatedly measured. The intensity increased linearly at first and saturated after a certain time, due to equilibration of the ionization and loss rates. The experimental results are depicted in Fig. 15 in [145]. The data are recreated and shown in Figure 72.

Fischer defined the lifetime in the experiment as the fraction of the saturation intensity  $h_\infty$  and the initial slope of the temporal ion intensity  $h_0$ , which is equal to the inverse rate coefficient of the pseudo-first-order ion loss. The average lifetime

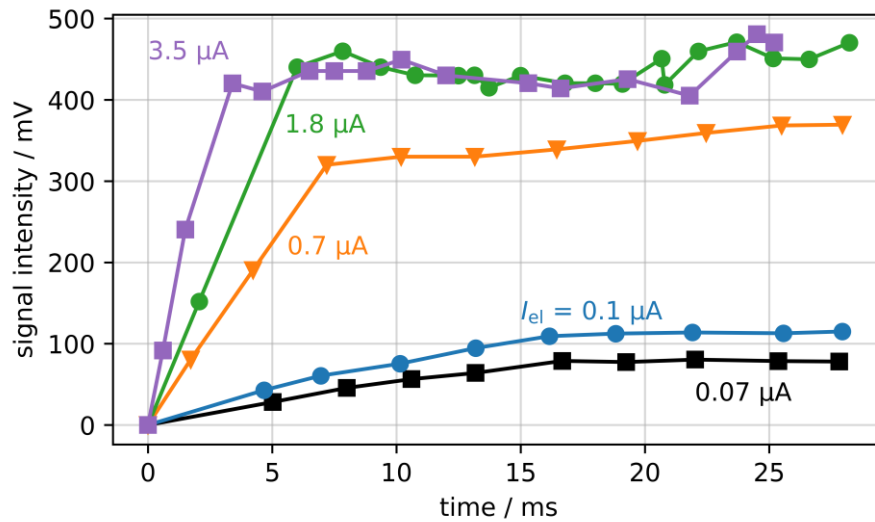


**Figure 72:** Signal intensity of  $\text{N}_2^+$  ions over time for different filament emission currents  $I_{el}$  at a trap pressure of  $6 \cdot 10^{-6}$  Torr, measured by Fischer. The data are recreated from Fig. 15 in [145].

was 15 ms for  $\text{N}_2^+$  at a pressure of  $8 \cdot 10^{-6}$  mbar [145]. This value is considerably lower than the value obtained in the present work for a comparable scenario, i.e.,  $\text{Ar}^+$  ions in Ar background gas ( $\tau_{\text{loss}} \approx 500$  ms, section *Ion loss rates*). This is not surprising, since the conditions in the experiment and the simulations are rather different, e.g., different ion trap size and trapping field parameters.

The impact of different factors contributing to this discrepancy is thus investigated: The experiment is recreated in an IDSimF simulation with the iTrap geometry and consideration of collisions and space charge, to identify factors that contribute to the significantly shorter lifetime in the experiment. The IDSimF simulation parameters are selected to match the conditions of the experiment depicted in Fig. 14 in [145] as close as possible. An  $\text{N}_2^+$  ion ensemble is created from the ionization rate distribution for an electron current of  $0.1 \mu\text{A}$ , RF voltage of 240 V ( $q_z = 0.835$ ), and a trap pressure of  $8 \cdot 10^{-6}$  mbar. The space charge factor is set to 15, which reduces the total particle number in the simulation by this factor to save computation time. Ions are continuously started over the total simulation time of 30 ms. Figure 73 depicts the temporal evolution of the trapped ion number (simulation, red line) and measured ion intensity (values recreated from Fig. 15 in [145], black data). Both datasets are normalized to the saturation value that is attained towards the end of the simulation and experiment. The result of the simulation is in excellent agreement with the experimental data. The lifetime of 15 ms stated by Fischer is reproduced from the experimental data when the first four points

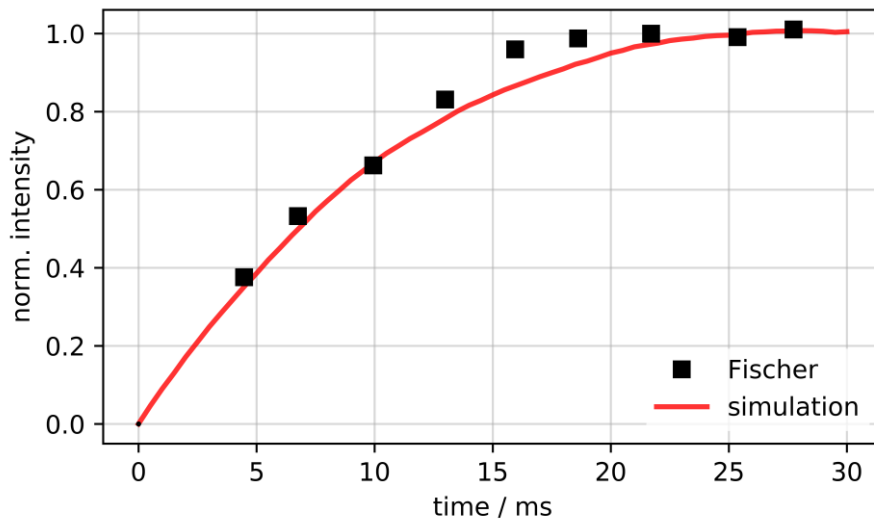


**Figure 73:** Comparison of experimental data of the normalized ion intensity evolution over time from [145] (black data) and results from a corresponding IDSimF simulation (red line).

(including zero) are used for calculating  $h_0$ .  $h_\infty$  is calculated as the arithmetic mean of the last four values. Using the same time intervals for calculating the lifetime from the simulation results, the same value of 15 ms is obtained. This accordance gives confidence that there are no significant systematic errors in the simulations and that the deviation of the SIMION results presented earlier in this section (*Ion loss rates*) are due to differences between the experiment and simulation boundary conditions. These differences are discussed in the following:

1) The information on the gas composition in the experiment is incomplete. It is stated that the total pressure was  $6 \cdot 10^{-6}$  torr ( $8 \cdot 10^{-6}$  mbar) and the  $N_2$  partial pressure was  $3 \cdot 10^{-6}$  torr ( $4 \cdot 10^{-6}$  mbar). If the remaining gas components have a larger mass than  $N_2$ , the lifetime would decrease due to the promotion of stronger scattering collisions. This is feasible because heavier compounds, namely krypton ( $m/z$  84) and propane ( $m/z$  38 - 43), were studied in this work. However, the lifetime for krypton as background gas obtained in the present work is still considerably larger than 15 ms. The impact of a heavier gas present in the experiments is therefore unlikely to explain the deviation.

2) Another reason for the lower lifetime in the experiment could be the method for ion detection. The primary RF voltage was superimposed with a sawtooth voltage, which results in a periodic shift of the operation point of the QIT. An auxiliary RF voltage was applied between the cap electrodes for detection. The stability parameters of ions inside the trap are shifted due to the sawtooth voltage and the auxiliary RF voltage is attenuated when ions oscillate at the resonance frequency.

This effect is proportional to the number of ions in resonance. When ions are in resonance they absorb energy from the electric field and this could lead to additional ion losses. However, auxiliary voltages were not yet implemented in the IDSimF simulation, which matches the experiment very well. It is therefore concluded that the means of detection has no significant impact on the ion lifetime.

3) In the SIMION simulations, ions are created in a confined volume in the center of the ion trap, where the ion acceptance has a maximum (cf. Figure 65, center column). In the experiment however, ions were generated with in-trap EI. The electron beam enters the ion trap through one of the cap electrodes, therefore ions are created along the  $z$  axis of the QIT and the ion acceptance decreases with increasing  $z$  position, as discussed in section 4.4.2. The ion acceptance in  $z$  direction is particularly low at large  $q_z$  values, as it is the case in the experiment. As a result, the fraction of ions that is created at unfavorable positions with regard to the ion acceptance is smaller in the simulations than it was in the experiment, which in turn leads to overestimated lifetimes in the simulations. In addition, ions are more likely to be scattered onto a terminal trajectory when they are in close vicinity to an electrode. However, the ion loss due to the spatial ion acceptance occurs typically during a few secular oscillations, which is significantly faster than the collision-induced ion loss at low pressures.

4) The  $q_z$  value was higher in the experiment ( $q_z = 0.845$ ) than in the SIMION simulations for determining the collision-induced ion loss rates (section *Ion loss rates*,  $q_z = 0.486$ ). The lower value in the simulations was chosen to match better the typical trapping field settings of the iTrap. It is feasible to assume that the trapping field properties impact the ion lifetime, as it does significantly alter the ion acceptance distribution (cf. section 4.4.2). This hypothesis is investigated with another IDSimF simulation to model the experiment with a different RF voltage of 120 V ( $q_z = 0.417$ ). This simulation yields an ion lifetime of approximately 38 ms, which supports the conclusion that a lower  $q_z$  results in longer ion lifetimes. The different  $q_z$  does therefore at least partly contribute to the deviation of the lifetimes determined with the SIMION model from the experimental value determined by Fischer.

5) According to Fisher, the ion loss is a result of collisional scattering of ions onto trajectories that terminate in one of the trap electrodes as well as superimposed defocusing by space charge. The latter is in agreement with his experiments with variable electron currents (cf. Figure 72). Higher currents yield more ions and, thus, larger space charge, which leads to a decrease of the average ion lifetime. The lifetimes for all experiments are calculated from the data presented in Fig. 15 in [145], the results are given in Table 21.

**Table 21:** Average lifetimes for different electron currents, calculated from the ion intensities over time in Fig. 15 in [145]

Electron current ( $\mu\text{A}$ )	$h_\infty$ (mV)	$h_0$ (mV $\cdot\text{ms}^{-1}$ )	Average lifetime (ms)
0.07	78.6	5.40	15
0.1	113	7.57	15
0.7	349	44.4	8
1.8	439	73.3	6
3.5	438	123	4

Above 0.1  $\mu\text{A}$ , the electron current has a strong impact on the lifetime. The values for 0.07 and 0.1  $\mu\text{A}$  are however identical, suggesting that the impact of space charge is negligible at the lower ion densities and that the value of 15 ms is the space-charge-free ion lifetime. This is in agreement with the previously presented results regarding the ion acceptance of the iTrap (cf. section 4.4.2, *Space charge*), which showed only a small impact of space charge on the total ion acceptance. Also, the equilibrium ion number that is obtained in the IDSimF simulation is around  $6 \cdot 10^5$ , which is well below the storage capacity of both the ion traps (cf. section 4.4.3). Therefore, space charge cannot explain the significantly shorter lifetimes in the experiment as compared to results of the SIMION simulations.

The abovementioned discussion suggests that the SIMION simulations presented in this section (*Ion loss rates*) reflect the pure collision-induced ion loss process decoupled from other factors. Space charge is not considered and the selected initial ion distribution, which is limited to a small volume in the ion trap center, diminishes the impact of the spatial ion acceptance of the trap. The latter appears to contribute significantly to the total ion lifetime. The experimental lifetime determined by Fischer is reproduced with IDSimF when the simulation parameters are matched with the experimental conditions. The major difference between the experiment and the IDSimF simulation as compared to the SIMION simulations is the initial ion distribution and the ion loss caused by the spatial ion acceptance remains as the only feasible explanation for the observed discrepancy. Therefore, it is emphasized that the total ion lifetimes are considerably smaller than the pure collision-induced ion loss lifetimes.

#### 4.4.5 Ion suppression

Ion suppression caused by space charge is a widely known issue for the operation of ion traps [160, 179, 197]. The pulsed gas inlet and resulting high ionization pressures applied in the iTrap do not only yield large ion numbers, which can promote

adverse space-charge-effects, but lead also to varying ion lifetimes due to collision-induced ion loss. The loss rates scale with the neutral-ion mass ratio and low mass ions are therefore more prone to loss at high trap pressures than heavier ions. EI typically results in fragmentation of molecular ions due to substantial internal energy deposition during the ionization process. As a result, EI spectra of molecules usually contain ion signals distributed over a wide mass range. This distribution can be deteriorated by collision-induced ion loss, which compromises the capability of identifying substances by their characteristic fragmentation pattern.

The effect of different ionization pressures on ion suppression is evaluated with an ODE model. The model describes the ion formation with the pressure-dependent ionization rate  $R_i(p)$  and the ion loss with the pressure- and mass-dependent collision-induced ion loss rate coefficient  $k_{\text{loss}}(p, m)$ . The ionization rate is proportional to the pressure. The loss rate is interpolated from the pressure dependency described in section 4.4.4. Loss rate coefficients for ions with different  $m/z$  are derived from the mass dependency expressed by eq. (4-31). The rate equation for the ion number change is

$$\frac{dN}{dt} = R_i(p) - k_{\text{loss}}(p, m) \quad (4-32)$$

during ionization and

$$\frac{dN}{dt} = -k_{\text{loss}}(p, m) \quad (4-33)$$

outside of the ionization window.

Benzene is used as a model compound. Loss rate constants are determined for all ions present in the reference EI spectrum from NIST [187]. The temporal pressure profiles are obtained with the ODE model for the 20 ms gas pulse from section 4.2.3, with inlet pressures between 0.1 and 10.0 mbar. Ionization occurs 5 ms after the gas pulse. The ionization time is 5 ms. The model is numerically integrated with `scipy.integrate.solve_ivp` from the SciPy package [26], with the default Runge-Kutta method *RK45* [186].

The ion number over time increases swiftly during the ionization time and decreases exponentially afterwards. The number of each ion species after 1 s is evaluated and used as scaling factor for the corresponding peak in the reference spectrum to generate simulated spectra for the respective inlet pressure. The peaks are displayed as Gaussians with a FWHM of  $m/z$  0.1. The resulting spectra for 0.1, 1.0 and 10.0 mbar sample pressure are shown in Figure 74, along with the NIST spectrum.

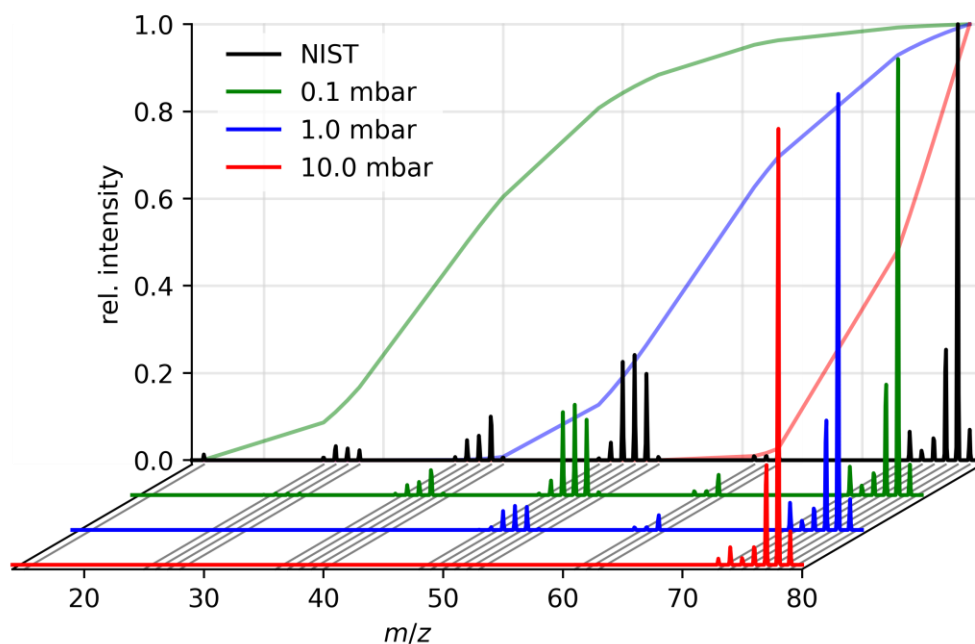


**Figure 74:** Reference EI mass spectrum of benzene from NIST [187] (black) and simulated spectra at different sample pressures (green, blue and red). The grey lines indicate the positions of all peaks in the NIST spectrum. The green, blue and red lines in the background depict the  $m/z$ -dependent relative intensity due to collision-induced ion loss.

The reference spectrum contains the molecular ion peak ( $m/z$  78) and series of characteristic fragment peaks that are formed with 70 eV-EI. At a sample pressure of 0.1 mbar, the peaks at  $m/z$  15 and around  $m/z$  27 are already completely suppressed. The corresponding ions have a neutral-ion mass ratio around or larger than 1 and therefore exhibit lifetimes that are significantly shorter than the time scale of a measurement cycle (cf. section 4.4.4, *Ion loss rates*). When the sample pressure and therefore the trap pressure is further increased, the maximum pressure and pumping time increases, which leads to loss of ions with mass ratios even below 1. The fragment spectrum is almost completely lost at 10.0 mbar. The green, blue and red curves in Figure 74 show the  $m/z$ -dependent relative intensities for 0.1, 1.0 and 10.0 mbar sample pressure, respectively. These curves show a cut-off that shifts towards higher  $m/z$  when the pressure is increased.

These results demonstrate that mass spectra obtained with the pulsed gas mode exhibit strong low-mass discrimination due to collision-induced ion loss. This effect is more pronounced, the higher the ionization pressure is. This potentially removes information from the spectra regarding the identity of a compound (characteristic fragments) and the composition of the sample (compounds with a high neutral-ion mass ratio). This counteracts the increase of intensity that is usually achieved with higher sample pressure.

#### 4.5 Implications for operation of an FT-QIT with in-trap ionization – summary and conclusion

Brachthäuser reported complete loss of the observed toluene signal ( $m/z$  91) at high sample pressures (Fig. 62 in [160]) and explained this observation with space-charge-induced ion loss, and other adverse effects occurring during operation of the iTrap, e.g., mass shifts and peak fusion, are known to be attributed to space charge. In the experiment, a mixture of 500 ppbv toluene in  $N_2$  was analyzed with constant ionization conditions (20 ms gas pulse length, 5 ms ionization delay, 5 ms ionization time) and only the sample pressure was gradually increased from 0.8 to 9.2 mbar. The RF voltage was 350 V, which sets the LMCO to  $m/z$  37.5. Matrix ions formed from  $N_2$  ( $N^+$  at  $m/z$  14,  $N_2^+$  at  $m/z$  28) are therefore unstable and ejected from the ion trap. After the applied delay time of 900 ms between the gas pulse and mass analysis, all ions below the LMCO are confidently removed from the trap. The ejection of unstable ions does usually occur on the timescale of the secular oscillation period, which is 4.6  $\mu$ s for  $N_2^+$  ions at 350 V. Therefore, accumulation of large numbers of matrix ions does not occur and toluene ions are predominantly stored during the experiment. Other common background ions, e.g.,  $H_2O^+$  ( $m/z$  18) or  $O_2^+$  ( $m/z$  32) from residual air are also below the LMCO. This should prevent the build-up of high charge densities in the trap. As shown in this section, collision-induced ion loss is a feasible explanation for the observed signal loss at increased sample pressure, as it can result in *complete* loss of ions from the trap when  $N_2$  or Ar are used as background gas in iTrap experiments.

An effective means alleviating this adverse effect is the use of light matrix gases, e.g., helium or hydrogen. With these, ions will experience collisional cooling which can even benefit the mass analysis due to a smaller size of the trapped ion cloud. In residual-gas mode or generally low ionization pressures, collision-induced ion loss eventually becomes negligible.

#### 4.5 Implications for operation of an FT-QIT with in-trap ionization – summary and conclusion

The sampling, ionization, and ion storage in an FT-QIT employing in-trap ionization was studied in this work. The presented results are put into context with the ion trap measurement cycle. The gas simulations (section 4.2) suggest that the trap pressure increases to  $>10^{-4}$  mbar for typical sampling conditions (1 mbar sample pressure, 20 ms gas pulse length). This is in the pressure range of chemical ionization (CI) sources and considerably higher than in conventional EI sources, where the standard operating pressure is usually in the range of  $10^{-6}$  mbar [183]. Chemical transformations can thus occur under these conditions and must be included in the interpretation of mass spectra. This was already observed in mass spectra

of toluene (T), which contained the signal of protonated toluene  $[T+H]^+$  at  $m/z$  93 (Fig. 82 in [160]). This ion can be formed in the reaction of the toluene radical cation  $T^{+\bullet}$  ( $m/z$  92) with neutral toluene [198] and is absent in standard 70 eV EI spectra. In another experiment, the formation of  $[T-H+CH_2]^+$  ( $m/z$  105) from the reaction of  $[T-H]^+$  and neutral toluene was observed during the repeated analysis of the same ion population (Fig. 89 in [160]). The analyte usually represents only a small fraction of the gas inside the ion trap during ionization. Thus, the majority of ions that are formed are matrix ions which can lead to secondary ionization reactions of the analyte. Hydrogen, which is often used as matrix gas in semiconductor-related processes, is a common reagent gas in conventional CI and generates protonated molecules with  $H_3^+$  as the reactant ion. EI of  $N_2$  creates  $N_2^{+\bullet}$  which can act as a charge-transfer reactant ion [183]. CI mass spectra are usually not at all comparable to 70 eV EI spectra. Therefore, good knowledge of the trap pressure during and after ionization aids to interpret mass spectra, which potentially represent ion ensembles that resemble a result of a mixture of CI and EI.

In-trap EI rates depend on the applied RF voltage, due to the dependency of the mean electron energy on the RF voltage, and are therefore not easily calculated from eq. (4-16). The electron energy also impacts on the fragmentation pattern, which is why library EI spectra are determined under precisely controlled conditions. Ill-defined ionization conditions reduce the validity of a database search and thus compromise the capability of identifying compounds by their characteristic fragmentation pattern. Vacher and coworkers reported a shift of the relative intensities of observed toluene fragments by several percent with an electron energy of 78 eV compared to the 70 eV reference spectrum [199], which emphasizes the severe necessity of well-controlled ionization conditions for compound identification via databases.

The results presented in section 4.3.3 have shown that the average electron energy varies significantly with typical trap RF voltages, e.g., around 70 eV at 100 V and 125 eV at 400 V. Since the EI cross sections of most molecules and atoms exhibit maxima in the range of 70 eV, a shift of the average electron energy does not result in a corresponding shift of relative ion intensities in one particular spectrum. For example, a mixture of 78%  $N_2$ , 20%  $O_2$ , 1% Ar and 1% benzene yields only slightly different relative ion intensities with constant electron energy of 70 eV and in-trap EI at different RF voltages. A comparison of the relative intensities for this scenario is given in Table 22. It can however not be excluded that the relative intensities in a spectrum may differ extensively compared to a database 70 eV spectrum, when compounds with significantly different EI responses are present.

## 4.5 Implications for operation of an FT-QIT with in-trap ionization – summary and conclusion

**Table 22:** 70 eV EI cross sections  $\sigma_i$  and relative ion intensities  $I_{rel}$  of an exemplary gas mixture with 70 eV EI and in-trap EI with RF voltages of 100 V and 200 V

Analyte	Mixing ratio (%)	$\sigma_i(70 \text{ eV})$ ( $10^{-16} \text{ cm}^2$ )	$I_{rel}(70 \text{ eV})$ (%)	$I_{rel}(100 \text{ V})$ (%)	$I_{rel}(200 \text{ V})$ (%)
Ar	1.0	2.441 <sup>a)</sup>	1.3	1.4	1.3
Benzene	1.0	2.67 <sup>b)</sup>	7.9	7.7	7.3
N <sub>2</sub>	78.0	2.508 <sup>b)</sup>	100.0	100.0	100.0
O <sub>2</sub>	21.0	15.025 <sup>b)</sup>	28.0	25.3	25.9

a) Taken from ref. [191].

b) Taken from ref. [190].

The ion ensemble created with in-trap EI has its main density around the propagation axis of the electron beam, i.e., the  $r$  axis of the ion trap. In combination with the spatial ion acceptance of the QIT, stored ion ensembles occupy an approximately oblate spheroidal volume (cf. Figure 67). The storage capacity is estimated to be  $10^6 - 10^7 \text{ cm}^{-3}$ , depending on the RF voltage. The trap volume that can reasonably be filled with ions (oblate spheroid volume with  $a = r_0$  and  $c = z_0$ ) is  $3 \text{ cm}^3$ . That results in an absolute storage capacity of  $(3 - 30) \cdot 10^6 \text{ cm}^{-3}$ . The ionization rate for typical ionization conditions at a pressure of  $10^{-6} \text{ mbar}$  is in the range of  $10^9 \text{ s}^{-1}$ . With realistic trap pressures of  $10^{-4} \text{ mbar}$  during ionization, the storage capacity is exceeded by at least one order of magnitude. For the analysis of an analyte present at a mixing ratio of 1 ppmv only 1 – 10 ions are stored under these conditions, assuming equal storage efficiencies for the analyte and matrix ions. This boldly emphasizes the necessity for selective removal of matrix ions, when ions are non-selectively generated. The collision-induced ion loss discussed in section 4.4.4 does work in favor of ions that have a larger mass than the matrix gas, as it predominantly removes ions with a large neutral-ion mass ratio. This process may become negligible for very small mass ratios; thus, H<sub>2</sub> and He are the preferred matrix gases for the iTrap. Helium and hydrogen ions are in almost all cases below the LMCO of the ion trap and are thus efficiently removed. The same behavior can be achieved for high mass matrix gases by increasing the RF voltage, provided that the ions of interest have a larger  $m/z$  than the matrix. If this is not the case, matrix ions can be selectively removed by SWIFT excitation. Only the selective removal of excess matrix ions allows accumulation of detectable numbers of analyte ions. The urgent necessity for SWIFT for removing matrix ions was already clearly voiced by Brachthäuser [160] and is quantified in terms of modeling approaches in the present work.

One pivotal figure of merit of an analytical method is its sensitivity and the related necessity of maximizing the measured signal intensity. In the iTrap, the detected signal, i.e., the image current, is proportional to the number of *coherently* oscillating ions. The total ion number can be controlled with the electron current of the e-gun, the ionization time, and the ionization pressure. It was shown in section 4.4.4 that the pressure does have a significant impact on the ion lifetime, which can become smaller than the timescale of a measurement cycle. Collision-induced ion loss introduces a mass-dependent suppression of ions and was identified as a significant disturbance in the iTrap acquisition procedure, which potentially leads to loss of spectral information – to the extent of complete signal loss.

The time between the gas pulse and the mass analysis cycle is limited by the pressure reduction rate within the trap, which ultimately limits the duty cycle of the instrument. This can be improved by increasing the gas conductance of the trap. With improved conductance, the maximum trap pressure decreases, which reduces the extent of collision-induced ion loss and therefore aids to retain spectral information. However, this does naturally decrease sensitivity. As repeatedly stated before, the use of low mass matrix gases is highly recommended.

Careful control of the ion number present in the trap volume is pivotal, as it allows operation in a range where space charge effects are predictable and manageable, e.g., correction of space-charge-induced mass shifts with a charge-dependent calibration. Without a reliable means of charge control, the interpretation of the acquired mass spectra is rendered difficult, if not impossible. It is at least debatable if the measured ion signal in the FT-QIT is generally proportional to the ion number and, thus, a reliable means for evaluating the number of ions in a spectrum. When the ion motion is significantly distorted by space charge, the measured ion current is severely manipulated to the extent of virtually meaningless system response. A charge control method based on the measured image current signal should be validated with an independent determination of the present ion number, e.g., with a secondary electron multiplier.

### **4.5.1 Comment on mass resolution and space charge**

The impact of space charge on the performance of ion traps is described in the literature and well understood (cf. section 4.1.1, *Space charge*) – and was identified as the main cause of several challenges during the operation of the iTrap: mass shifts, ion suppression, and peak fusion are observed when high ion numbers are present in the trap. These effects are not the focus of this work, but have emerged as a field of interest at the department of Physical and Theoretical Chemistry at the University of Wuppertal for a number of years [1, 6–11], and were thoroughly

## 4.5 Implications for operation of an FT-QIT with in-trap ionization – summary and conclusion

studied as benchmark scenarios during the development of the simulation program IDSimF.

The development of new mass analyzer concepts should generally advance compared to established methods. In case of the FT-QIT, one proposed advantage over quadrupole-filter-based residual gas analyzers (RGAs), which are commonly used for monitoring in semiconductor processes, is the capability of acquiring high-resolution mass spectra [157]. The mass signals observed in iTrap spectra are generally narrow and reported mass resolutions are often in the range of several thousand and even up to 20000 [157, 160]. However, the mass resolution, i.e., the fraction of the peak position  $m$  and the peak width  $\Delta m$ , does not necessarily resemble the resolving power of the method, i.e., its actual capability of separating two adjacent peaks. There is strong evidence that peak coalescence severely reduces the resolving power of the iTrap. As an example, the spectrum of diborane (Fig. 73 in [160]) does not contain the isotopic peaks of the diborane ions, e.g.,  $^{11}\text{B}_2\text{H}_3$  ( $m/z$  25.0415),  $^{10}\text{B}^{11}\text{BH}_4$  ( $m/z$  25.0530) and  $^{10}\text{B}_2\text{H}_5$  ( $m/z$  25.0645). In contrast, only single (“fused”) peaks are visible at the nominal masses of the diborane species, even though the mass resolution determined *from* these peaks is sufficiently large for fully resolving the isotopic pattern. This example demonstrates that the maximum attainable mass resolving power is severely compromised by space charge. The mass resolving power of an iTrap is thus not necessarily represented by the mass resolution of individual peaks.

### 4.5.2 Space charge simulations with IDSimF

IDSimF has proven to be a valuable tool for studying ion dynamics in scenarios, where space charge is to be considered. The lack of a graphical user interface in IDSimF may be deterrent for some potential users, but the comparably low effort of learning basic usage of a command line program gives access to a very powerful open-source tool for space charge simulations in various settings, e.g., trapping devices or ion mobility spectrometry (IMS). IDSimF is continuously further developed and will hopefully soon be recognized as a valuable tool in the MS and IMS community.

The ionization rates calculated in this work can be used to create realistic ion ensembles for future simulations focusing on ion excitation and mass analysis. IDSimF enables space charge simulations with large particle counts, which in turn give valuable insights into the dynamics of stored ions under different conditions, e.g., different excitation schemes. The implementation of the Shockley-Ramo theorem [4, 5] for image current detection in electrodes provides a means for simulating actual transients and mass spectra in IDSimF. With realistic ion numbers for

## Modeling of an FT ion trap

ion trap experiments in the range of  $\leq 10^5$ , a true particle count based simulation of ion ensembles is currently within reach of IDSimF, especially when considering today's availability of affordable cloud computing power.

## List of abbreviations

ALD	atomic layer deposition
API	atmospheric pressure ionization
CAD	computer-aided design
CCS	collision cross section
CI	chemical ionization
DC	direct current
DPR	deceleration potential response
DPS	deceleration potential scan
EI	electron ionization
EIC	extracted ion chromatogram
ESI	electrospray ionization
fft	fast Fourier transform
FI	field ionization
FT	Fourier transform
FWHM	full width at half maximum
GC	gas chromatography
GC-MS	gas chromatography-mass spectrometry
HCT	high capacity trap
ICP	inductively coupled plasma
ipaMS	Institute for Pure and Applied Mass Spectrometry
KED	kinetic energy distribution
KER	kinetic energy release
LMCO	low mass cut off
LOD	limit of detection
MBD	Maxwell-Boltzmann distribution
MCP	microchannel plate
MS	mass spectrometry
nESI	nano-electrospray ionization
PA	proton affinity
PTC	physical and theoretical chemistry
QIT	quadrupole ion trap
RF	radio frequency

## List of Abbreviations

RGA	residual gas analyzer
RPA	retarding potential analyzer
scf	space charge factor
SP	Substance P
SSR	sum of squared residuals
TIA	total ion acceptance
TIC	total ion chromatogram
TOB	time of birth

## List of tables

Table 1: HCTplus standard ion source and transfer stage settings .....	21
Table 2: amaZon ETD/amazon speed ETD standard ion source and transfer stage settings .....	23
Table 3: micrOTOF standard ion source and transfer stage settings .....	24
Table 4: Precursor and fragment $m/z$ and critical energies of benzylpyridinium ions.....	29
Table 5: Boundary parameters for the octopole DSMC simulations.....	30
Table 6: Electrode potentials in the transfer stage ion trajectory simulations .....	33
Table 7: Standard values for entrance voltages in the first three vacuum stages.....	38
Table 8: Overview of analytes used in the experiments .....	43
Table 9: SPARTA simulations, <i>inlet</i> and <i>turbo pump 2 (in)</i> pressures.....	50
Table 10: Ion species in SIMION simulations for modeling of the DPR, adapted from experiments in section 3.5. CCS values are estimated from reference data.....	54
Table 11: Optimized parameters for the pressure data fits.....	87
Table 12: Optimized parameters for the velocity data fits.....	88
Table 13: Exemplary iTrap operation parameters.....	93
Table 14: Boundary parameters for the gas inlet model .....	99
Table 15: Sampling simulation parameters for different gases and sample pressures .....	99
Table 16: ODE model parameters.....	104
Table 17: EI source and trap voltages for electron beam simulations .....	109
Table 18: Equilibrium ion cloud parameters from IDSimF simulations with different <i>scf</i> .....	125
Table 19: Background gas information for collision-induced ion loss simulations with $\text{Ar}^+$ ions ( $m/z$ 40) .....	127
Table 20: Pseudo-first-order coefficients $k_{\text{loss}}'$ and second-order rate coefficients $k_{\text{loss}}$ for the collision-induced ion loss with different gases .....	131
Table 21: Average lifetimes for different electron currents, calculated from the ion intensities over time in Fig. 15 in [145] .....	136

## List of Tables

Table 22: 70 eV EI cross sections $\sigma_i$ and relative ion intensities $I_{rel}$ of an exemplary gas mixture with 70 eV EI and in-trap EI with RF voltages of 100 V and 200 V.....	141
---	-----

## List of figures

Figure 1: Comprehensive API cluster chemistry mechanism. Reprinted with permission from [36]. Copyright 2014 John Wiley & Sons, Ltd.....	10
Figure 2: Charge retention/charge depletion mechanism scheme .....	13
Figure 3: Excerpt of the stability diagram in $(a_z, q_z)$ phase space .....	17
Figure 4: Schematic of the Bruker HCTplus instrument with attached Apollo ESI source.....	21
Figure 5: Exemplary excerpt of a temporal evolution of the ion current $I$ during a DPS experiment (top left) and the differential ion current $\Delta I$ used for segment recognition (bottom left).....	22
Figure 6: Schematic of the Bruker amaZon instrument with attached Apollo ESI source.....	24
Figure 7: Schematic of the Bruker micrOTOF instrument with attached custom nESI source. ....	25
Figure 8: Workflow for obtaining KEDs from experimental data. ....	26
Figure 9: Survival yield analysis example .....	28
Figure 10: Fragmentation scheme for benzylpyridinium ions.....	29
Figure 11: Half section views of the real octopole 3D model (top) and the 3D representation of the axisymmetric geometry used for SPARTA simulations (bottom).....	31
Figure 12: Octopole SPARTA model .....	31
Figure 13: Three-quarter section view of the transfer-stage model used for SIMION simulations .....	32
Figure 14: Half section view of the ion trap geometry used for modeling of the DPS experiments in SIMION. ....	34
Figure 15: Ion trap mass spectrum of the sodium formate solution showing $[(\text{HCOONa})_n + \text{Na}]^+$ clusters ( $n = 2, 3, 5, 6$ ) and background ions .....	35
Figure 16: Acceleration-voltage-dependent ion current from a DPS experiment with two fitting models (top) and the resulting energy distributions (bottom).....	35
Figure 17: Normalized DPS results from the TIC, EICs of sodium formate clusters and phthalate ions, and the ion current measured with the cup electrode. Error bars are not shown for clarity.....	37

## List of Figures

Figure 18: Exemplary DPR traces from the EIC of $[(\text{HCOONa})_3+\text{Na}]^+$ (left) and the TIC (right) recorded with the HCTplus instrument (cf. Figure 4) for different acceleration voltages .....	39
Figure 19: DPR traces from EICs of <i>p</i> -CN BP ( $m/z$ 195) and its fragment ion ( $m/z$ 116) and the TIC, recorded with the amaZon ETD instrument (cf. Figure 6) for different acceleration voltages .....	39
Figure 20: DPR with Gompertz fit (dotted lines) from ion current measurements with different acceleration voltages between octopole 1 and octopole 2 (left) and corresponding KEDs (right).....	40
Figure 21: DPR of sodium formate clusters and the TIC obtained with the HCTplus (dashed lines) and amaZon Speed ETD ion trap (solid lines). .....	41
Figure 22: Normalized DPR from experiments with extended $U_d$ range with multiple (left) and single ion signals (right) .....	44
Figure 23: Width of the extended DPR peaks for different substance classes in dependence of the stability parameter $q_z$ .....	46
Figure 24: Frames from a DSMC simulation showing the pressure distribution inside the simulation box. A steady state is reached after 3 ms. ....	48
Figure 25: Results from simulation 1. Steady state pressure profile in the octopole chamber, averaged over 7 ms (top), pressure curve (center) and axial gas velocity curve along the center of octopole 2 from a SPARTA simulation (bottom).....	49
Figure 26: Pressure (top) and velocity curves (bottom) from SPARTA simulations (cf. Table 9); the data are smoothed with a moving average for clarity. ....	50
Figure 27: Ion energy histograms after passage through a plate capacitor at different pressures. ....	52
Figure 28: CCS reference data [123] were fitted with a linear model for estimating mass-dependent CCS values. Fit1 considers all values, fit2 ignores values above $250 \text{ \AA}^2$ . ....	53
Figure 29: DPR curves from simulations with different <i>inlet</i> and <i>turbo pump 2 (in)</i> pressures and experimental data .....	54
Figure 30: DPR from the experiment and simulations with different ion ensembles.....	58
Figure 31: Comparison of actual (solid lines) and observed (dashed lines) KEDs and overlap integrals for simulations with different <i>inlet</i> pressures..	59
Figure 32: Potential along the center axis between the transfer stage exit and ion trap entrance at different ring potentials. ....	60

Figure 33: Ion kinetic energy progression between the transfer stage exit lens and the ion trap entrance hole (left) and total kinetic energy histogram at the trap entrance (right).....	61
Figure 34: 2D histograms of the kinetic energy at the trap entrance, after experiencing the oscillating field in the interface region, and the initial phase position .....	62
Figure 35: Phase-angle-dependent axial ion kinetic energy at the trap entrance.	63
Figure 36: Normalized ion acceptance distributions of the QIT in dependence of the kinetic energy and phase angle .....	65
Figure 37: a) Kinetic-energy- and phase-angle-dependent ion acceptance of the QIT .....	66
Figure 38: Product of the phase-angle-dependent ion acceptance and kinetic energy distributions of ions at the trap entrance .....	67
Figure 39: Simulated DPR curves for different initial mean kinetic energies of the ion ensemble and $m/z$ .....	69
Figure 40: Synthetic KEDs with different shapes, created to study the impact of the KED on the DPR in simulations .....	70
Figure 41: Simulated DPR curves with different ion ensembles at different $q_z$ .....	71
Figure 42: Survival yield of benzylpyridinium (BP) ions in dependence of their critical energies $E_0$ for different activation regions in the amaZon ETD instrument. ....	74
Figure 43: DPR curves of the $p$ -F BP fragment ion ( $m/z$ 109) in different activation experiments .....	76
Figure 44: DPR curves for $[(\text{HCO}_2\text{Na})_n+\text{Na}]^+$ , $n = 3, 5, 6$ ( $m/z$ 227, 363, 431), recorded at different ESI voltages.....	78
Figure 45: DPR curves for $[(\text{HCO}_2\text{Na})_3+\text{Na}]^+$ ( $m/z$ 227) obtained at different pressures in the first vacuum stage of the HCTplus ion trap.....	80
Figure 46: DPR data of $\text{SP}^{3+}$ (left) and $\text{SP}^{2+}$ ions (right), obtained with the micrOTOF instrument. Methanol is added to the ion source as chemical modifier .....	82
Figure 47: DPR curves of SP ions ( $\text{SP}^{2+}$ , $\text{SP}^{3+}$ , $[\text{SP}^{3+}+\text{ACN}]$ ), obtained with the micrOTOF instrument. Acetonitrile (ACN) is added to the ion source as chemical modifier .....	85
Figure 48: FT-QIT simulation workflow diagram. This chapter focuses on the sampling, ionization, and ion storage sections.....	90
Figure 49: Sketch of the iTrap system. The inlet tube and e-gun are displayed across from each other for clarity but are actually aligned orthogonally. The e-gun is simplified for clarity.....	92

## List of Figures

Figure 50: SPARTA simulation box with the ion trap and gas inlet.....	98
Figure 51: Equilibrium pressure distribution for N <sub>2</sub> with a sample pressure of 1 mbar .....	100
Figure 52: Equilibrium pressures at different locations in dependence of the sample pressure for helium (top) and nitrogen (bottom), obtained from DSMC simulations .....	101
Figure 53: ODE model with the different regions and the rate constants that determine the particle flows between the regions. ....	103
Figure 54: Pressure profiles for air from the ODE model solutions for different gas pulse lengths. The sample pressure in the experimental data is 1 mbar. Top: Inlet region with experimental data (transparent lines); center: Trap region; bottom: Recipient region with experimental data (transparent lines).....	106
Figure 55: Potential contour lines of the e-gun models in the xz plane.....	108
Figure 56: Half-sections of the normalized electron density (top) and energy (bottom) in the xy (left) and xz plane (right) for an RF voltage of 80 V, averaged over one RF cycle.....	110
Figure 57: Half-sections of the normalized electron density (top) and energy (bottom) in the xy (left) and xz plane (right) for an RF voltage of 400 V, averaged over one RF cycle.....	110
Figure 58: Step-wise approximation of the RF voltage by intervals of static ring potentials.....	112
Figure 59: Electron beam duty cycle and mean electron energy inside the ion trap (left) and energy-dependent EI cross sections of selected compounds (right).....	112
Figure 60: RF-voltage-dependent ionization rates of selected compounds.....	113
Figure 61: Projections of the ion densities obtained for different analytes with constant ionization parameters .....	114
Figure 62: Ion ensemble ( $n = 1.4 \cdot 10^6$ , black dots) and color-coded projections of the ion density.....	115
Figure 63: Comparison of the spatial ion acceptance distributions of the FT-QIT in dependence of the ions' initial $r$ and $z$ position for two different $q_z$ values. Results from SIMION (left) and IDSimF simulations (right) are shown.....	118
Figure 64: Initial spatial (top) and RF phase angle distributions (bottom) of N <sub>2</sub> <sup>+</sup> ions in a QIT that are lost at the cap electrodes (left) and ring electrode (right).....	119

Figure 65: Spatial ion acceptance distributions of the FT-QIT for different $q_z$ (from left to right) and $scf$ (from top to bottom) .....	121
Figure 66: Trajectory of an $N_2^+$ ion in $(x, v_x)$ phase space at different $q_z$ values with $scf = 0$ (left) and $scf = 50$ (right).....	123
Figure 67: Stored $Ar^+$ ion ensembles and 2D projections of the ion density after 1.1 ms (left) and 5 ms (right) with $scf = 15$ (top) and $scf = 50$ (bottom) .....	124
Figure 68: Trajectory of an $Ar^+$ ion in an argon gas matrix in $(y, v_y)$ phase space at $10^{-3}$ mbar (left) and the ion's total kinetic energy over time (right).127	
Figure 69: Exemplary kinetic analysis of the loss of $Ar^+$ ions in a neon gas matrix at different pressures .....	129
Figure 70: Pseudo-first-order rate coefficient $k'_{loss}$ of the collision-induced ion loss of $Ar^+$ ions in dependence of the background pressure for different gas masses.....	130
Figure 71: Temporal evolution of the mean $Ar^+$ ion cloud radius in simulations with different background gases:.....	132
Figure 72: Signal intensity of $N_2^+$ ions over time for different filament emission currents $I_{el}$ at a trap pressure of $6 \cdot 10^{-6}$ Torr, measured by Fischer. The data are recreated from Fig. 15 in [145]. .....	133
Figure 73: Comparison of experimental data of the normalized ion intensity evolution over time from [145] (black data) and results from a corresponding IDSimF simulation (red line).....	134
Figure 74: Reference EI mass spectrum of benzene from NIST [187] (black) and simulated spectra at different sample pressures (green, blue and red) .....	138

## List of Figures

## References

- [1] W. Wissdorf, D. Erdogdu, M. Thinius, T. Benter. Ion Dynamics Simulation Framework (IDSIMF): An Open Source Trajectory Simulation Framework. *Proceedings of the 68th ASMS Conference on Mass Spectrometry and Allied Topics, Online Meeting, 2020*.
- [2] L. Verlet. Computer "Experiments" on Classical Fluids. I. Thermodynamical Properties of Lennard-Jones Molecules. *Phys. Rev.*, 159, 98–103, **1967**, <https://doi.org/10.1103/PhysRev.159.98>.
- [3] J. Barnes, P. Hut. A hierarchical  $O(N \log N)$  force-calculation algorithm. *Nature*, 324, 446–449, **1986**, <https://doi.org/10.1038/324446a0>.
- [4] W. Shockley. Currents to Conductors Induced by a Moving Point Charge. *J. Appl. Phys.*, 9, 635–636, **1938**, <https://doi.org/10.1063/1.1710367>.
- [5] S. Ramo. Currents Induced by Electron Motion. *Proc. IRE*, 27, 584–585, **1939**, <https://doi.org/10.1109/JRPROC.1939.228757>.
- [6] D. Erdogdu, W. Wissdorf, C. Polaczek, F. Stappert, H. Kersten, T. Benter, M. Allers, A. T. Kirk, S. Zimmermann. Simulation of Cluster Dynamics in High Kinetic Energy IMS (HiKE-IMS). *Proceedings of the 67th ASMS Conference on Mass Spectrometry and Allied Topics, Atlanta, GA, 2019*.
- [7] D. Erdogdu, M. Allers, W. Wissdorf, C. Markert, H. Kersten, S. Zimmermann, T. Benter. Chemical Reaction and Transport Simulations of Positive Reactant Ions in High Kinetic Energy Ion Mobility Spectrometry (HiKE-IMS). *Proceedings of the 68th ASMS Conference on Mass Spectrometry and Allied Topics, Online Meeting, 2020*.
- [8] D. Erdogdu, W. Wissdorf, F. Stappert, H. Kersten, T. Benter. Chemical Kinetics and Ion Transport Simulations: Cluster Dynamics in Differential Ion Mobility Spectrometry. *Proceedings of the 67th ASMS Conference on Mass Spectrometry and Allied Topics, Atlanta, GA, 2019*.

## References

- [9] W. Wißdorf, H. Kersten, B. Schneider, T. Covey, J. Hager, T. Benter. Fast space charge simulations: Simulation of ion-ion and background gas interaction in a linear quadrupole. *Proceedings of the 65th ASMS Conference on Mass Spectrometry and Allied Topics, Indianapolis, IN, 2017*.
- [10] W. Wißdorf, C. Polaczek, Y. Brachthäuser, H. Kersten, A. Brockhaus, M. Ali-man, V. Derpmann, A. Laue, T. Benter. Ion dynamics simulation: Space charge effects in a fourier transform 3D-ion trap (FT-ion trap). *Proceedings of the 65th ASMS Conference on Mass Spectrometry and Allied Topics, Indianapolis, IN, 2017*.
- [11] W. Wißdorf, Y. Brachthäuser, A. Brekenfeld, H. Kersten, T. Benter. Evaluation of Space Charge Effects in Scanning- vs. Fourier Transform (FT)-Quadrupole Ion Traps (QITs). *Proceedings of the 66th ASMS Conference on Mass Spectrometry and Allied Topics, San Diego, CA, 2018*.
- [12] G. van Rossum, F. L. Drake. *Python 3 Reference Manual*, CreateSpace, Scotts Valley, CA, **2009**.
- [13] D. J. Manura, D. A. Dahl. *SIMION Version 8.0 User Manual. 4th revised edition, 2008*.
- [14] R. Ierusalimsky. *Programming in Lua*, 4th edition, Lua.org, Rio de Janeiro, **2016**.
- [15] W. Wissdorf, L. Seifert, V. Derpmann, S. Klee, W. Vautz, T. Benter. Monte Carlo simulation of ion trajectories of reacting chemical systems: mobility of small water clusters in ion mobility spectrometry. *Journal of the American Society for Mass Spectrometry*, 24, 632–641, **2013**, <https://doi.org/10.1007/s13361-012-0553-1>.
- [16] SPARTA Direct Simulation Monte Carlo (DSMC) Simulator, <http://sparta.sandia.gov>.
- [17] M. A. Gallis, J. R. Torczynski, S. J. Plimpton, D. J. Rader, T. Koehler. Direct simulation Monte Carlo: The quest for speed. *AIP Conf. Proc.*, 1628, 27–36, **2014**, <https://doi.org/10.1063/1.4902571>.
- [18] G. A. Bird. Approach to Translational Equilibrium in a Rigid Sphere Gas. *Phys. Fluids*, 6, 1518–1519, **1963**, <https://doi.org/10.1063/1.1710976>.
- [19] M. Fang, Z.-H. Li, Z.-H. Li, J. Liang, Y.-H. Zhang. DSMC modeling of rarefied ionization reactions and applications to hypervelocity spacecraft reentry

- flows. *Adv. Aerodyn.*, 2, **2020**, <https://doi.org/10.1186/s42774-020-00030-1>.
- [20] A. Ebrahimi, E. Roohi. DSMC investigation of rarefied gas flow through diverging micro- and nanochannels. *Microfluid. Nanofluidics*, 21, **2017**, <https://doi.org/10.1007/s10404-017-1855-1>.
- [21] G. A. Bird. Definition of mean free path for real gases. *Phys. Fluids*, 26, 3222–3223, **1983**, <https://doi.org/10.1063/1.864095>.
- [22] K. Koura, H. Matsumoto. Variable soft sphere molecular model for inverse-power-law or Lennard-Jones potential. *Phys. Fluids A*, 3, 2459–2465, **1991**, <https://doi.org/10.1063/1.858184>.
- [23] W. J. Morokoff, A. Kersch. A comparison of scattering angle models. *Comput. Math. with Appl.*, 35, 155–164, **1998**, [https://doi.org/10.1016/S0898-1221\(97\)00265-4](https://doi.org/10.1016/S0898-1221(97)00265-4).
- [24] Sandia National Laboratories. SPARTA Users Manual, <https://sparta.sandia.gov/doc/Manual.pdf>, **2021**.
- [25] C. R. Harris, K. J. Millman, S. J. van der Walt, R. Gommers, P. Virtanen, D. Cournapeau, E. Wieser, J. Taylor, S. Berg, N. J. Smith, R. Kern, M. Picus, S. Hoyer, M. H. van Kerkwijk, M. Brett, A. Haldane, J. F. Del Río, M. Wiebe, P. Peterson, P. Gérard-Marchant, K. Sheppard, T. Reddy, W. Weckesser, H. Abbasi, C. Gohlke, T. E. Oliphant. Array programming with NumPy. *Nature*, 585, 357–362, **2020**, <https://doi.org/10.1038/s41586-020-2649-2>.
- [26] P. Virtanen, R. Gommers, T. E. Oliphant, M. Haberland, T. Reddy, D. Cournapeau, E. Burovski, P. Peterson, W. Weckesser, J. Bright, S. J. van der Walt, M. Brett, J. Wilson, K. J. Millman, N. Mayorov, A. R. J. Nelson, E. Jones, R. Kern, E. Larson, C. J. Carey, Í. Polat, Y. Feng, E. W. Moore, J. VanderPlas, D. Laxalde, J. Perktold, R. Cimrman, I. Henriksen, E. A. Quintero, C. R. Harris, A. M. Archibald, A. H. Ribeiro, F. Pedregosa, P. van Mulbregt. SciPy 1.0: fundamental algorithms for scientific computing in Python. *Nat. Methods*, 17, 261–272, **2020**, <https://doi.org/10.1038/s41592-019-0686-2>.
- [27] J. D. Hunter. Matplotlib: A 2D Graphics Environment, Zenodo, **2007**, <https://doi.org/10.1109/MCSE.2007.55>.

## References

- [28] Q. Koziol, D. Robinson. HDF5, Lawrence Berkeley National Laboratory (LBNL), Berkeley, CA (United States), **2018**, <https://doi.org/10.11578/DC.20180330.1>.
- [29] U. Ayachit. *The ParaView guide. Updated for ParaView version 4.3*, Full color version, Kitware, Los Alamos, **2015**.
- [30] C. Sullivan, A. Kaszynski. PyVista: 3D plotting and mesh analysis through a streamlined interface for the Visualization Toolkit (VTK). *J. Open Source Softw.*, 4, 1450, **2019**, <https://doi.org/10.21105/joss.01450>.
- [31] J. J. Thomson. Bakerian Lecture: Rays of Positive Electricity. *Proceedings of the Royal Society of London. Series A, Containing Papers of a Mathematical and Physical Character*, 89, 1–20, **1913**.
- [32] S. Klee, M. Thinius, K. J. Brockmann, T. Benter. Capillary atmospheric pressure chemical ionization using liquid point electrodes. *Rapid Commun. Mass Spectrom.*, 28, 1591–1600, **2014**, <https://doi.org/10.1002/rcm.6944>.
- [33] B. L. Boys, M. C. Kuprowski, J. J. Noël, L. Konermann. Protein oxidative modifications during electrospray ionization: solution phase electrochemistry or corona discharge-induced radical attack? *Anal. Chem.*, 81, 4027–4034, **2009**, <https://doi.org/10.1021/ac900243p>.
- [34] S. Klee, V. Derpmann, W. Wißdorf, S. Klopotoski, H. Kersten, K. J. Brockmann, T. Benter, S. Albrecht, A. P. Bruins, F. Dousty, T. J. Kauppila, R. Kostiainen, R. O'Brien, D. B. Robb, J. A. Syage. Are clusters important in understanding the mechanisms in atmospheric pressure ionization? Part 1: Reagent ion generation and chemical control of ion populations. *J. Am. Soc. Mass Spectrom.*, 25, 1310–1321, **2014**, <https://doi.org/10.1007/s13361-014-0891-2>.
- [35] A. P. Bruins. Mass spectrometry with ion sources operating at atmospheric pressure. *Mass Spectrom. Rev.*, 10, 53–77, **1991**, <https://doi.org/10.1002/mas.1280100104>.
- [36] S. Klee, A. Brockhaus, W. Wißdorf, M. Thinius, N. Hartmann, T. Benter. Development of an ion activation stage for atmospheric pressure ionization sources. *Rapid Commun. Mass Spectrom.*, 29, 143–154, **2015**, <https://doi.org/10.1002/rcm.7082>.

- [37] Z. Du, D. J. Douglas, N. Konenkov. Elemental analysis with quadrupole mass filters operated in higher stability regions. *J. Anal. At. Spectrom.*, 14, 1111–1119, **1999**, <https://doi.org/10.1039/a804022b>.
- [38] P. H. Dawson (Ed.). *Quadrupole mass spectrometry and its applications*, American Institute of Physics, Woodbury, **1995**.
- [39] P. H. Dawson. Fringing fields in the quadrupole mass filter. *Int. J. Mass Spectrom. Ion Phys.*, 6, 33–44, **1971**, [https://doi.org/10.1016/0020-7381\(71\)83002-4](https://doi.org/10.1016/0020-7381(71)83002-4).
- [40] H.W. Brubaker, "An improved quadrupole mass analyser" in *Advances in Mass Spectrometry, Vol. 4* (Ed.: E. Kendrick), Institute of Petroleum: London, **1968**.
- [41] W. C. Wiley, I. H. McLaren. Time-of-Flight Mass Spectrometer with Improved Resolution. *Rev. Sci. Instrum.*, 26, 1150–1157, **1955**, <https://doi.org/10.1063/1.1715212>.
- [42] B. A. Mamyrin. Time-of-flight mass spectrometry (concepts, achievements, and prospects). *Int. J. Mass Spectrom.*, 206, 251–266, **2001**, [https://doi.org/10.1016/S1387-3806\(00\)00392-4](https://doi.org/10.1016/S1387-3806(00)00392-4).
- [43] D. Meschede, H. Vogel, C. Gerthsen. *Gerthsen Physik*, 24., überarbeitete Auflage, Springer, Berlin, **2010**, <https://doi.org/10.1007/978-3-642-12894-3>.
- [44] E. A. Mason, E. W. McDaniel. *Transport properties of ions in gases*, Wiley, New York, **1988**, <https://doi.org/10.1002/3527602852>.
- [45] W. Hang, C. Lewis, V. Majidi. Practical considerations when using radio frequency-only quadrupole ion guide for atmospheric pressure ionization sources with time-of-flight mass spectrometry. *Analyst*, 128, 273–280, **2003**, <https://doi.org/10.1039/b209109g>.
- [46] M. M. Shahin. Mass-Spectrometric Studies of Corona Discharges in Air at Atmospheric Pressures. *The Journal of Chemical Physics*, 45, 2600–2605, **1966**, <https://doi.org/10.1063/1.1727980>.
- [47] K. Vékey. Internal Energy Effects in Mass Spectrometry. *J. Mass Spectrom.*, 31, 445–463, **1996**, [https://doi.org/10.1002/\(SICI\)1096-9888\(199605\)31:5<445::AID-JMS354>3.0.CO;2-G](https://doi.org/10.1002/(SICI)1096-9888(199605)31:5<445::AID-JMS354>3.0.CO;2-G).

## References

- [48] C. Lifshitz. Time-dependent mass spectra and breakdown graphs. 2. The kinetic shift in pyridine. *J. Phys. Chem.*, 86, 606–612, **1982**, <https://doi.org/10.1021/j100394a006>.
- [49] W. A. Chupka. Effect of Unimolecular Decay Kinetics on the Interpretation of Appearance Potentials. *The Journal of Chemical Physics*, 30, 191–211, **1959**, <https://doi.org/10.1063/1.1729875>.
- [50] S. Klee, S. Albrecht, V. Derpmann, H. Kersten, T. Benter. Generation of ion-bound solvent clusters as reactant ions in dopant-assisted APPI and APLI. *Anal. Bioanal. Chem.*, 405, 6933–6951, **2013**, <https://doi.org/10.1007/s00216-013-7114-8>.
- [51] A. Yousef, S. Shrestha, L. A. Viehland, E. P. F. Lee, B. R. Gray, V. L. Ayles, T. G. Wright, W. H. Breckenridge. Interaction potentials and transport properties of coinage metal cations in rare gases. *The Journal of Chemical Physics*, 127, 154309, **2007**, <https://doi.org/10.1063/1.2774977>.
- [52] A. Good, D. A. Durden, P. Kebarle. Ion–Molecule Reactions in Pure Nitrogen and Nitrogen Containing Traces of Water at Total Pressures 0.5–4 torr. Kinetics of Clustering Reactions Forming  $H^+(H_2O)_n$ . *The Journal of Chemical Physics*, 52, 212–221, **1970**, <https://doi.org/10.1063/1.1672667>.
- [53] E. P. Grimsrud, P. Kebarle. Gas phase ion equilibria studies of the hydrogen ion by methanol, dimethyl ether, and water. Effect of hydrogen bonding. *J. Am. Chem. Soc.*, 95, 7939–7943, **1973**, <https://doi.org/10.1021/ja00805a002>.
- [54] A. Hansel, A. Jordan, R. Holzinger, P. Prazeller, W. Vogel, W. Lindinger. Proton transfer reaction mass spectrometry: on-line trace gas analysis at the ppb level. *Int. J. Mass Spectrom. Ion Proc.*, 149-150, 609–619, **1995**, [https://doi.org/10.1016/0168-1176\(95\)04294-U](https://doi.org/10.1016/0168-1176(95)04294-U).
- [55] R. B. Cody. Observation of molecular ions and analysis of nonpolar compounds with the direct analysis in real time ion source. *Anal. Chem.*, 81, 1101–1107, **2009**, <https://doi.org/10.1021/ac8022108>.
- [56] R. B. Cole (Ed.). *Electrospray ionization mass spectrometry*, Wiley, New York, NY, **1997**.

- [57] J. C. DeMuth, J. Bu, S. A. McLuckey. Electrospray droplet exposure to polar vapors: delayed desolvation of protein complexes. *Rapid Commun. Mass Spectrom.*, 29, 973–981, **2015**, <https://doi.org/10.1002/rcm.7188>.
- [58] R. R. Ogorzalek Loo, R. Lakshmanan, J. A. Loo. What protein charging (and supercharging) reveal about the mechanism of electrospray ionization. *J. Am. Soc. Mass Spectrom.*, 25, 1675–1693, **2014**, <https://doi.org/10.1007/s13361-014-0965-1>.
- [59] M. Thinius, C. Polaczek, M. Langner, S. Bräkling, A. Haack, H. Kersten, T. Benter. Charge Retention/Charge Depletion in ESI-MS: Experimental Evidence. *J. Am. Soc. Mass Spectrom.*, 31, 773–784, **2020**, <https://doi.org/10.1021/jasms.9b00044>.
- [60] A. T. Iavarone, J. C. Jurchen, E. R. Williams. Effects of solvent on the maximum charge state and charge state distribution of protein ions produced by electrospray ionization. *J. Am. Soc. Mass Spectrom.*, 11, 976–985, **2000**, [https://doi.org/10.1016/S1044-0305\(00\)00169-0](https://doi.org/10.1016/S1044-0305(00)00169-0).
- [61] B. E. Winger, K. J. Light-Wahl, R. D. Smith. Gas-phase proton transfer reactions involving multiply charged cytochrome c ions and water under thermal conditions. *J. Am. Soc. Mass Spectrom.*, 3, 624–630, **1992**, [https://doi.org/10.1016/1044-0305\(92\)85003-3](https://doi.org/10.1016/1044-0305(92)85003-3).
- [62] S. A. McLuckey. Collision energy effects in tandem mass spectrometry as revealed by a proton-bound dimer ion. *J. Mass Spectrom.*, 19, 545–550, **1984**, <https://doi.org/10.1002/oms.1210191104>.
- [63] H. I. Kenttämaa, R. Cooks. Internal energy distributions acquired through collisional activation at low and high energies. *Int. J. Mass Spectrom. Ion Proc.*, 64, 79–83, **1985**, [https://doi.org/10.1016/0168-1176\(85\)85038-2](https://doi.org/10.1016/0168-1176(85)85038-2).
- [64] V. Gabelica, E. de Pauw, M. Karas. Influence of the capillary temperature and the source pressure on the internal energy distribution of electrosprayed ions. *Int. J. Mass Spectrom.*, 231, 189–195, **2004**, <https://doi.org/10.1016/j.ijms.2003.10.010>.
- [65] M. A. Fenner, C. N. McEwen. Survival yield comparison between ESI and SAI: Mechanistic implications. *Int. J. Mass Spectrom.*, 378, 107–112, **2015**, <https://doi.org/10.1016/j.ijms.2014.07.023>.

## References

- [66] K. M. Hines, D. H. Ross, K. L. Davidson, M. F. Bush, L. Xu. Large-Scale Structural Characterization of Drug and Drug-Like Compounds by High-Throughput Ion Mobility-Mass Spectrometry. *Anal. Chem.*, 89, 9023–9030, **2017**, <https://doi.org/10.1021/acs.analchem.7b01709>.
- [67] E. R. Stephens, M. Dumlao, D. Xiao, D. Zhang, W. A. Donald. Benzylammonium Thermometer Ions: Internal Energies of Ions Formed by Low Temperature Plasma and Atmospheric Pressure Chemical Ionization. *J. Am. Soc. Mass Spectrom.*, 26, 2081–2084, **2015**, <https://doi.org/10.1007/s13361-015-1272-1>.
- [68] J. F. Cahill, V. Kertesz, O. S. Ovchinnikova, G. J. van Berkel. Comparison of Internal Energy Distributions of Ions Created by Electrospray Ionization and Laser Ablation-Liquid Vortex Capture/Electrospray Ionization. *J. Am. Soc. Mass Spectrom.*, 26, 1462–1468, **2015**, <https://doi.org/10.1007/s13361-015-1195-x>.
- [69] C. Collette, L. Drahos, E. de Pauw, K. Vékey. Comparison of the internal energy distributions of ions produced by different electrospray sources. *Rapid Commun. Mass Spectrom.*, 12, 1673–1678, **1998**, [https://doi.org/10.1002/\(SICI\)1097-0231\(19981130\)12:22<1673::AID-RCM385>3.0.CO;2-A](https://doi.org/10.1002/(SICI)1097-0231(19981130)12:22<1673::AID-RCM385>3.0.CO;2-A).
- [70] C. Collette, E. de Pauw. Calibration of the internal energy distribution of ions produced by electrospray. *Rapid Commun. Mass Spectrom.*, 12, 165–170, **1998**, [https://doi.org/10.1002/\(SICI\)1097-0231\(19980227\)12:4<165::AID-RCM140>3.0.CO;2-1](https://doi.org/10.1002/(SICI)1097-0231(19980227)12:4<165::AID-RCM140>3.0.CO;2-1).
- [71] L. Drahos, R. M. A. Heeren, C. Collette, E. de Pauw, K. Vékey. Thermal energy distribution observed in electrospray ionization. *J. Mass Spectrom.*, 34, 1373–1379, **1999**, [https://doi.org/10.1002/\(SICI\)1096-9888\(199912\)34:12%3C1373::AID-JMS907%3E3.0.CO;2-%23](https://doi.org/10.1002/(SICI)1096-9888(199912)34:12%3C1373::AID-JMS907%3E3.0.CO;2-%23).
- [72] D. Touboul, M. C. Jecklin, R. Zenobi. Ion internal energy distributions validate the charge residue model for small molecule ion formation by spray methods. *Rapid Commun. Mass Spectrom.*, 22, 1062–1068, **2008**, <https://doi.org/10.1002/rcm.3469>.

- [73] M. Nefliu, J. N. Smith, A. Venter, R. G. Cooks. Internal energy distributions in desorption electrospray ionization (DESI). *J. Am. Soc. Mass Spectrom.*, 19, 420–427, **2008**, <https://doi.org/10.1016/j.jasms.2007.11.019>.
- [74] M. Mann. The ever expanding scope of electrospray mass spectrometry—a 30 year journey. *Nat. Commun.*, 10, 3744, **2019**, <https://doi.org/10.1038/s41467-019-11747-z>.
- [75] L. Konermann, E. Ahadi, A. D. Rodriguez, S. Vahidi. Unraveling the mechanism of electrospray ionization. *Anal. Chem.*, 85, 2–9, **2013**, <https://doi.org/10.1021/ac302789c>.
- [76] E. U. Condon, H. D. Smyth. The Critical Potentials of Molecular Hydrogen. *Proc. Natl. Acad. Sci. U.S.A.*, 14, 871–875, **1928**, <https://doi.org/10.1073/pnas.14.11.871>.
- [77] J. Laskin, C. Lifshitz. Kinetic energy release distributions in mass spectrometry. *J. Mass Spectrom.*, 36, 459–478, **2001**, <https://doi.org/10.1002/jms.164>.
- [78] W. Bleakney. The Ionization of Hydrogen by Single Electron Impact. *Phys. Rev.*, 35, 1180–1186, **1930**, <https://doi.org/10.1103/PhysRev.35.1180>.
- [79] W. W. Lozier. A Study of the Velocities of H<sup>+</sup> Ions Formed in Hydrogen by Dissociation Following Electron Impact. *Phys. Rev.*, 36, 1285–1292, **1930**, <https://doi.org/10.1103/PhysRev.36.1285>.
- [80] J. T. Tate, W. W. Lozier. The Dissociation of Nitrogen and Carbon Monoxide by Electron Impact. *Phys. Rev.*, 39, 254–269, **1932**, <https://doi.org/10.1103/PhysRev.39.254>.
- [81] W. W. Lozier. The Heats of Dissociation of Hydrogen and Nitrogen. *Phys. Rev.*, 44, 575–581, **1933**, <https://doi.org/10.1103/PhysRev.44.575>.
- [82] H. D. Hagstrum, J. T. Tate. Ionization and Dissociation of Diatomic Molecules by Electron Impact. *Phys. Rev.*, 59, 354–370, **1941**, <https://doi.org/10.1103/PhysRev.59.354>.
- [83] J. A. Hipple, E. U. Condon. Detection of Metastable Ions with the Mass Spectrometer. *Phys. Rev.*, 68, 54–55, **1945**, <https://doi.org/10.1103/PhysRev.68.54>.

## References

- [84] J. H. Beynon, R. M. Caprioli, W. E. Baitinger, J. W. Amy. The ion kinetic energy spectrum and the mass spectrum of argon. *Int. J. Mass Spectrom. Ion Phys.*, 3, 313–321, **1969**, [https://doi.org/10.1016/0020-7381\(69\)80077-X](https://doi.org/10.1016/0020-7381(69)80077-X).
- [85] J. H. Beynon, R. G. Cooks, J. W. Amy, W. E. Baitinger, T. Y. Ridley. Design and Performance of a Mass-analyzed Ion Kinetic Energy (MIKE) Spectrometer. *Anal. Chem.*, 45, 1023A-1031A, **1973**, <https://doi.org/10.1021/ac60334a763>.
- [86] F. W. McLafferty, T. A. Bryce. Metastable-ion characteristics: characterization of isomeric molecules. *Chem. Commun. (London)*, 1215–1217, **1967**, <https://doi.org/10.1039/C19670001215>.
- [87] R. G. Cooks, R. W. Kondrat, M. Youssefi, J. L. McLaughlin. Mass-analyzed ion kinetic energy (MIKE) spectrometry and the direct analysis of coca. *J. Ethnopharmacol.*, 3, 299–312, **1981**, [https://doi.org/10.1016/0378-8741\(81\)90060-X](https://doi.org/10.1016/0378-8741(81)90060-X).
- [88] M. A. Grayson. Origins of Tandem Mass Spectrometry. *ASMS History Posters, History of the Science of MS*, **2012**.
- [89] I. A. Kaltashov, C. C. Fenselau. A Direct Comparison of "First" and "Second" Gas Phase Basicities of the Octapeptide RPPGFSPF. *J. Am. Chem. Soc.*, 117, 9906–9910, **1995**, <https://doi.org/10.1021/ja00144a017>.
- [90] S. A. McLuckey, D. Cameron, R. G. Cooks. Proton affinities from dissociations of proton-bound dimers. *J. Am. Chem. Soc.*, 103, 1313–1317, **1981**, <https://doi.org/10.1021/ja00396a001>.
- [91] P. Scheier, B. Dünser, T. D. Märk. Supersymmetric Fission of Multiply Charged Fullerene Ions. *Phys. Rev. Lett.*, 74, 3368–3371, **1995**, <https://doi.org/10.1103/PhysRevLett.74.3368>.
- [92] P. A. M. van Koppen, J. Brodbelt-Lustig, M. T. Bowers, D. V. Dearden, J. L. Beauchamp, E. R. Fisher, P. B. Armentrout. Carbon-hydrogen bond activation as the initial step in the Co<sup>+</sup>-mediated demethanation of propane: the critical role of angular momentum at the rate-limiting transition state. *J. Am. Chem. Soc.*, 112, 5663–5665, **1990**, <https://doi.org/10.1021/ja00170a054>.

- [93] H. Boersch. Experimentelle Bestimmung der Energieverteilung in thermisch ausgelsten Elektronenstrahlen. *Z. Physik*, 139, 115–146, **1954**, <https://doi.org/10.1007/BF01375256>.
- [94] W. B. Hanson, S. Sanatani, D. Zuccaro, T. W. Flowerday. Plasma measurements with the retarding potential analyzer on Ogo 6. *J. Geophys. Res.*, 75, 5483–5501, **1970**, <https://doi.org/10.1029/JA075i028p05483>.
- [95] L. B. King, A. D. Gallimore, C. M. Marrese. Transport-Property Measurements in the Plume of an SPT-100 Hall Thruster. *J. Propuls. Power*, 14, 327–335, **1998**, <https://doi.org/10.2514/2.5301>.
- [96] N. Jiang, N. Zhao, H. Liu, T. Fang. Mass-resolved retarding field energy analyzer and its measurement of ion energy distribution in helicon plasma. *Nucl. Instr. and Meth. in Phys. Res. B*, 229, 508–518, **2005**, <https://doi.org/10.1016/j.nimb.2004.12.121>.
- [97] M. A. Dexter, H. J. Reid, B. L. Sharp. The effect of ion energy on reactivity and species selectivity in hexapole collision/reaction cell ICP-MS. *J. Anal. At. Spectrom.*, 17, 676–681, **2002**, <https://doi.org/10.1039/b205674g>.
- [98] I. Feldmann, N. Jakubowski, D. Stuewer. Application of a hexapole collision and reaction cell in ICP-MS Part I: Instrumental aspects and operational optimization. *Fresenius J. Anal. Chem.*, 365, 415–421, **1999**, <https://doi.org/10.1007/s002160051633>.
- [99] Mathieu, Émile. Mémoire sur le mouvement vibratoire d'une membrane de forme elliptique. *J. Math. Pures Appl.*, 137–203, **1868**.
- [100] R. E. March, J. F. J. Todd. *Quadrupole ion trap mass spectrometry*, 2nd edition, J. Wiley, Hoboken, N.J., **2005**, <https://doi.org/10.1002/0471717983>.
- [101] F. G. Major, H. G. Dehmelt. Exchange-Collision Technique for the rf Spectroscopy of Stored Ions. *Phys. Rev.*, 170, 91–107, **1968**, <https://doi.org/10.1103/PhysRev.170.91>.
- [102] H. G. Dehmelt, "Radiofrequency Spectroscopy of Stored Ions I: Storage" in *Advances in Atomic and Molecular Physics* (Eds.: D. R. Bates, I. Esterman). Academic Press, New York, NY, London, **1967**.
- [103] M. Nand Kishore, P. K. Ghosh. Trapping of ion injected from an external source into a three-dimensional r.f. quadrupole field. *Int. J. Mass Spectrom.*

## References

- Ion Phys.*, 29, 345–350, **1979**, [https://doi.org/10.1016/0020-7381\(79\)80004-2](https://doi.org/10.1016/0020-7381(79)80004-2).
- [104] J. Todd, D. A. Freer, R. M. Waldren. The quadrupole ion store (QUISTOR). Part xii. The trapping of ions injected from an external source: A description in terms of phase-space dynamics. *Int. J. Mass Spectrom. Ion Phys.*, 36, 371–386, **1980**, [https://doi.org/10.1016/0020-7381\(80\)85070-4](https://doi.org/10.1016/0020-7381(80)85070-4).
- [105] Chun-Sing O, Hans A. Schuessler. Confinement of ions created externally in a radio-frequency ion trap. *J. Appl. Phys.*, 52, 1157–1166, **1981**, <https://doi.org/10.1063/1.329731>.
- [106] G. C. Stafford, P. E. Kelley, J. Syka, W. E. Reynolds, J. Todd. Recent improvements in and analytical applications of advanced ion trap technology. *Int. J. Mass Spectrom. Ion Proc.*, 60, 85–98, **1984**, [https://doi.org/10.1016/0168-1176\(84\)80077-4](https://doi.org/10.1016/0168-1176(84)80077-4).
- [107] J. N. Louris, J. W. Amy, T. Y. Ridley, R. G. Cooks. Injection of ions into a quadrupole ion trap mass spectrometer. *Int. J. Mass Spectrom. Ion Proc.*, 88, 97–111, **1989**, [https://doi.org/10.1016/0168-1176\(89\)85010-4](https://doi.org/10.1016/0168-1176(89)85010-4).
- [108] R. E. Kaiser, R. G. Cooks, J. Moss, P. H. Hemberger. Mass range extension in a quadrupole ion-trap mass spectrometer. *Rapid Commun. Mass Spectrom.*, 3, 50–53, **1989**, <https://doi.org/10.1002/rcm.1290030213>.
- [109] R. K. Julian, R. G. Cooks. Broad-band excitation in the quadrupole ion trap mass spectrometer using shaped pulses created with the inverse Fourier transform. *Anal. Chem.*, 65, 1827–1833, **1993**, <https://doi.org/10.1021/ac00062a006>.
- [110] M. Laušević, M. Splendore, R. E. March. Modulated Resonant Excitation of Selected Polychlorobiphenyl Molecular Ions in an Ion Trap Mass Spectrometer. *J. Mass Spectrom.*, 31, 1244–1252, **1996**, [https://doi.org/10.1002/\(SICI\)1096-9888\(199611\)31:11<1244::AID-JMS417>3.0.CO;2-U](https://doi.org/10.1002/(SICI)1096-9888(199611)31:11<1244::AID-JMS417>3.0.CO;2-U).
- [111] S. Guan, A. G. Marshall. Stored waveform inverse Fourier transform (SWIFT) ion excitation in trapped-ion mass spectrometry: Theory and applications. *Int. J. Mass Spectrom. Ion Proc.*, 157–158, 5–37, **1996**, [https://doi.org/10.1016/S0168-1176\(96\)04461-8](https://doi.org/10.1016/S0168-1176(96)04461-8).

- [112] A. G. Marshall, T.-C. L. Wang, L. Chen, T. L. Ricca, "New Excitation and Detection Techniques in Fourier Transform Ion Cyclotron Resonance Mass Spectrometry" in *ACS Symposium Series* (Ed.: M. V. Buchanan). American Chemical Society, Washington, DC, **1987**.
- [113] R. E. March. Quadrupole ion trap mass spectrometry: theory, simulation, recent developments and applications. *Rapid Commun. Mass Spectrom.*, 12, 1543–1554, **1998**, [https://doi.org/10.1002/\(SICI\)1097-0231\(19981030\)12:20<1543::AID-RCM343>3.0.CO;2-T](https://doi.org/10.1002/(SICI)1097-0231(19981030)12:20<1543::AID-RCM343>3.0.CO;2-T).
- [114] H. Wang. US 6,797,948, "Multipole Ion Guide", **2004**.
- [115] B. Gompertz. On the nature of the function expressive of the law of human mortality, and on a new mode of determining the value of life contingencies. *Phil. Trans. R. Soc. B*, 513–583, **1825**, <https://doi.org/10.1098/rstl.1825.0026>.
- [116] V. Gabelica, E. de Pauw. Internal energy and fragmentation of ions produced in electrospray sources. *Mass Spectrom. Rev.*, 24, 566–587, **2005**, <https://doi.org/10.1002/mas.20027>.
- [117] K. V. Barylyuk, K. Chingin, R. M. Balabin, R. Zenobi. Fragmentation of benzylpyridinium "thermometer" ions and its effect on the accuracy of internal energy calibration. *J. Am. Soc. Mass Spectrom.*, 21, 172–177, **2010**, <https://doi.org/10.1016/j.jasms.2009.09.023>.
- [118] D. Gatineau, A. Memboeuf, A. Milet, R. B. Cole, H. Dossmann, Y. Gimbert, D. Lesage. Experimental bond dissociation energies of benzylpyridinium thermometer ions determined by threshold-CID and RRKM modeling. *Int. J. Mass Spectrom.*, 417, 69–75, **2017**, <https://doi.org/10.1016/j.ijms.2017.03.002>.
- [119] G. A. Harris, D. M. Hostetler, C. Y. Hampton, F. M. Fernández. Comparison of the internal energy deposition of direct analysis in real time and electrospray ionization time-of-flight mass spectrometry. *J. Am. Soc. Mass Spectrom.*, 21, 855–863, **2010**, <https://doi.org/10.1016/j.jasms.2010.01.019>.
- [120] E.-L. Zins, C. Pepe, D. Schröder. Energy-dependent dissociation of benzylpyridinium ions in an ion-trap mass spectrometer. *J. Mass Spectrom.*, 45, 1253–1260, **2010**, <https://doi.org/10.1002/jms.1847>.

## References

- [121] T. Neugebauer, "Dynamics of the Collision-Induced Dissociation Process in Quadrupole Ion Traps and its Application", *Dissertation*, Friedrich-Alexander-Universität Erlangen-Nürnberg, **2019**, <https://opus4.kobv.de/opus4-fau/frontdoor/index/index/docId/12556>.
- [122] D. V. C. Awang, B. A. Dawson, M. Girard, A. Vincent, I. Ekiel. The product of reserpine autoxidation. *J. Org. Chem.*, 55, 4443–4448, **1990**, <https://doi.org/10.1021/jo00301a043>.
- [123] J. A. Picache, B. S. Rose, A. Balinski, K. L. Leaptrot, S. D. Sherrod, J. C. May, J. A. McLean. Collision cross section compendium to annotate and predict multi-omic compound identities. *Chem. Sci.*, 10, 983–993, **2019**, <https://doi.org/10.1039/c8sc04396e>.
- [124] Unified CCS Compendium, <https://mcleanresearchgroup.shinyapps.io/CCS-Compendium/>, **2021**.
- [125] S. M. Stow, T. J. Causon, X. Zheng, R. T. Kurulugama, T. Mairinger, J. C. May, E. E. Rennie, E. S. Baker, R. D. Smith, J. A. McLean, S. Hann, J. C. Fjeldsted. An Interlaboratory Evaluation of Drift Tube Ion Mobility-Mass Spectrometry Collision Cross Section Measurements. *Anal. Chem.*, 89, 9048–9055, **2017**, <https://doi.org/10.1021/acs.analchem.7b01729>.
- [126] C. Ieritano, J. Featherstone, A. Haack, M. Guna, J. L. Campbell, W. S. Hopkins. How Hot are Your Ions in Differential Mobility Spectrometry? *J. Am. Soc. Mass Spectrom.*, **2020**, <https://doi.org/10.1021/jasms.9b00043>.
- [127] J. V. Iribarne. On the evaporation of small ions from charged droplets. *J. Chem. Phys.*, 64, 2287–2294, **1976**, <https://doi.org/10.1063/1.432536>.
- [128] B. A. Thomson, J. V. Iribarne. Field induced ion evaporation from liquid surfaces at atmospheric pressure. *The Journal of Chemical Physics*, 71, 4451–4463, **1979**, <https://doi.org/10.1063/1.438198>.
- [129] M. Dole, L. L. Mack, R. L. Hines, R. C. Mobley, L. D. Ferguson, M. B. Alice. Molecular Beams of Macroions. *The Journal of Chemical Physics*, 49, 2240–2249, **1968**, <https://doi.org/10.1063/1.1670391>.
- [130] J. B. Fenn. Ion formation from charged droplets: roles of geometry, energy, and time. *J. Am. Soc. Mass Spectrom.*, 4, 524–535, **1993**, [https://doi.org/10.1016/1044-0305\(93\)85014-0](https://doi.org/10.1016/1044-0305(93)85014-0).

- [131] M. Wutz, H. Adam, W. Walcher. *Handbuch Vakuumtechnik. Theorie und Praxis*, 6., durchgesehene und verbesserte Auflage, Vieweg+Teubner Verlag, Wiesbaden, s.l., **1997**, <https://doi.org/10.1007/978-3-322-99421-9>.
- [132] P. S. Prasanth, J. K. Kakkassery. Molecular models for simulation of rarefied gas flows using direct simulation Monte Carlo method. *Fluid Dyn. Res.*, **40**, 233–252, **2008**, <https://doi.org/10.1016/j.fluidyn.2007.10.001>.
- [133] Y. Kang, B. B. Schneider, T. R. Covey. On the Nature of Mass Spectrometer Analyzer Contamination. *J. Am. Soc. Mass Spectrom.*, **28**, 2384–2392, **2017**, <https://doi.org/10.1007/s13361-017-1747-3>.
- [134] C. Markert, M. Thinius, L. Lehmann, C. Heintz, F. Stappert, W. Wissdorf, H. Kersten, T. Benter, B. B. Schneider, T. R. Covey. Observation of charged droplets from electrospray ionization (ESI) plumes in API mass spectrometers. *Anal. Bioanal. Chem.*, **2021**, <https://doi.org/10.1007/s00216-021-03452-y>.
- [135] P. Kebarle, M. Peschke. On the mechanisms by which the charged droplets produced by electrospray lead to gas phase ions. *Anal. Chim. Acta*, **406**, 11–35, **2000**, [https://doi.org/10.1016/S0003-2670\(99\)00598-X](https://doi.org/10.1016/S0003-2670(99)00598-X).
- [136] A. Savitzky, M. J. E. Golay. Smoothing and Differentiation of Data by Simplified Least Squares Procedures. *Anal. Chem.*, **36**, 1627–1639, **1964**, <https://doi.org/10.1021/ac60214a047>.
- [137] T. R. Covey, B. A. Thomson, B. B. Schneider. Atmospheric pressure ion sources. *Mass Spectrom. Rev.*, **28**, 870–897, **2009**, <https://doi.org/10.1002/mas.20246>.
- [138] K. Tang, A. Gomez. Monodisperse Electrosprays of Low Electric Conductivity Liquids in the Cone-Jet Mode. *J. Colloid Interface Sci.*, **184**, 500–511, **1996**, <https://doi.org/10.1006/jcis.1996.0645>.
- [139] R. Knochenmuss, O. Cheshnovsky, S. Leutwyler. Proton transfer reactions in neutral gas-phase clusters: 1-Naphthol with H<sub>2</sub>O, D<sub>2</sub>O, CH<sub>3</sub>OH, NH<sub>3</sub> and piperidine. *Chem. Phys. Lett.*, **144**, 317–323, **1988**, [https://doi.org/10.1016/0009-2614\(88\)87121-5](https://doi.org/10.1016/0009-2614(88)87121-5).
- [140] C. A. Deakyne, M. Meot-Ner, C. L. Campbell, M. G. Hughes, S. P. Murphy. Multicomponent cluster ions. I. The proton solvated by CH<sub>3</sub>CN/H<sub>2</sub>O. *The Journal*

## References

- of Chemical Physics*, 84, 4958–4969, **1986**,  
<https://doi.org/10.1063/1.449982>.
- [141] F. Fernandez-Lima, D. A. Kaplan, J. Suetering, M. A. Park. Gas-phase separation using a trapped ion mobility spectrometer. *Int. J. Ion Mobil. Spectrom.*, 14, 93–98, **2011**, <https://doi.org/10.1007/s12127-011-0067-8>.
- [142] K. Giles, S. D. Pringle, K. R. Worthington, D. Little, J. L. Wildgoose, R. H. Bateman. Applications of a travelling wave-based radio-frequency-only stacked ring ion guide. *Rapid Commun. Mass Spectrom.*, 18, 2401–2414, **2004**,  
<https://doi.org/10.1002/rcm.1641>.
- [143] J. F. de La Mora, S. Ude, B. A. Thomson. The potential of differential mobility analysis coupled to MS for the study of very large singly and multiply charged proteins and protein complexes in the gas phase. *Biotechnol. J.*, 1, 988–997, **2006**, <https://doi.org/10.1002/biot.200600070>.
- [144] W. Paul, H. Steinwedel. Notizen: Ein neues Massenspektrometer ohne Magnetfeld. *Z. Naturforsch. A*, 8, 448–450, **1953**, <https://doi.org/10.1515/zna-1953-0710>.
- [145] E. Fischer. Die dreidimensionale Stabilisierung von Ladungsträgern in einem Vierpolfeld. *Z. Physik*, 156, 1–26, **1959**,  
<https://doi.org/10.1007/BF01332512>.
- [146] P. H. Dawson, N. R. Whetten, "Mass Spectroscopy Using RF Quadrupole Fields" in *Advances in Electronics and Electron Physics*. Elsevier, **1970**.
- [147] Electronic Associates, Inc. *Anal. Chem.*, 39, 133A, **1967**,  
<https://doi.org/10.1021/ac60255a834>.
- [148] G. C. Stafford, P. E. Kelley, D. R. Stephens. US 4,540,884, "Method of mass analyzing a sample by use of a quadrupole ion trap", **1985**.
- [149] A. V. Mordehai, J. D. Henion. A novel differentially pumped design for atmospheric pressure ionization-ion trap mass spectrometry. *Rapid Commun. Mass Spectrom.*, 7, 205–209, **1993**,  
<https://doi.org/10.1002/rcm.1290070308>.
- [150] D. E. Goeringer, R. I. Crutcher, S. A. McLuckey. Ion Remeasurement in the Radio Frequency Quadrupole Ion Trap. *Anal. Chem.*, 67, 4164–4169, **1995**,  
<https://doi.org/10.1021/ac00118a020>.

- [151] M. Soni, V. Frankevich, M. Nappi, R. E. Santini, J. W. Amy, R. G. Cooks. Broadband fourier transform quadrupole ion trap mass spectrometry. *Anal. Chem.*, 68, 3314–3320, **1996**, <https://doi.org/10.1021/ac960577s>.
- [152] J. H. Parks, S. Pollack, W. Hill. Cluster experiments in radio frequency Paul traps: Collisional relaxation and dissociation. *The Journal of Chemical Physics*, 101, 6666–6685, **1994**, <https://doi.org/10.1063/1.468361>.
- [153] Y. Zerega, P. Perrier, M. Carette. Performance enhancement of a Fourier transform ion trap mass spectrometer using indirect ion-motion frequency measurement. *Meas. Sci. Technol.*, 14, 323–328, **2003**, <https://doi.org/10.1088/0957-0233/14/3/311>.
- [154] M. Aliman, A. Glasmachers. A novel electric ion resonance cell design with high signal-to-noise ratio and low distortion for Fourier transform mass spectrometry. *J. Am. Soc. Mass Spectrom.*, 10, 1000–1007, **1999**, [https://doi.org/10.1016/S1044-0305\(99\)00078-1](https://doi.org/10.1016/S1044-0305(99)00078-1).
- [155] R. G. Cooks, C. D. Cleven, L. A. Horn, M. Nappi, C. Well, M. H. Soni, R. K. Julian. Non-destructive detection of ions in a quadrupole ion trap using a d.c. pulse to force coherent ion motion: a simulation study. *Int. J. Mass Spectrom. Ion Proc.*, 146/147, 147–163, **1995**, [https://doi.org/10.1016/0168-1176\(95\)04209-4](https://doi.org/10.1016/0168-1176(95)04209-4).
- [156] M. A. Aliman, "Ein Beitrag zur breitbandigen Massenspektrometrie mit elektrischen Ionenresonanzzellen (EIRZ)", *Dissertation*, Bergische Universität Wuppertal, **1998**.
- [157] H. Y. Chung, M. Aliman, G. Fedosenko, A. Laue, R. Reuter, V. Derpmann, L. Gorkhover, M. Antoni, "Very sensitive real-time inline process mass spectrometer based on FFT Ion Trap technique" in *2016 27th Annual SEMI Advanced 2016*.
- [158] L. Paša-Tolić, Y. Huang, S. Guan, H. S. Kim, A. G. Marshall. Ultrahigh-resolution matrix-assisted laser desorption/ionization Fourier transform ion cyclotron resonance mass spectra of peptides. *J. Mass Spectrom.*, 30, 825–833, **1995**, <https://doi.org/10.1002/jms.1190300607>.
- [159] K. Jungmann, J. Hoffnagle, R. G. DeVoe, R. G. Brewer. Collective oscillations of stored ions. *Phys. Rev. A (Coll Park)*, 36, 3451–3454, **1987**, <https://doi.org/10.1103/PhysRevA.36.3451>.

## References

- [160] Y. Brachthäuser, "Development and characterization of a Fourier Transform based Quadrupole Ion Trap (FT-QIT) technique for process and residual gas analysis", *Dissertation*, Bergische Universität Wuppertal, **2017**, <https://portal.dnb.de/opac.htm?method=simpleSearch&cqlMode=true&query=idn%3D1192844327>.
- [161] K. Cox, C. Cleven, R. Cooks. Mass shifts and local space charge effects observed in the quadrupole ion trap at higher resolution. *Int. J. Mass Spectrom. Ion Proc.*, 144, 47–65, **1995**, [https://doi.org/10.1016/0168-1176\(95\)04152-B](https://doi.org/10.1016/0168-1176(95)04152-B).
- [162] Y. Wang. Non-linear resonance conditions and their relationships to higher multipole fields in ion traps and quadrupole mass filters. *Rapid Commun. Mass Spectrom.*, 7, 920–928, **1993**, <https://doi.org/10.1002/rcm.1290071013>.
- [163] K. L. Morand, S. A. Lammerts, R. G. Cooks. Letter to the editor. *Rapid Commun. Mass Spectrom.*, 5, 491, **1991**, <https://doi.org/10.1002/rcm.1290051014>.
- [164] F. Guidugli, P. Traldi. A phenomenological description of a black hole for collisionally induced decomposition products in ion-trap mass spectrometry. *Rapid Commun. Mass Spectrom.*, 5, 343–348, **1991**, <https://doi.org/10.1002/rcm.1290050802>.
- [165] D. M. Eades, J. V. Johnson, R. A. Yost. Nonlinear resonance effects during ion storage in a quadrupole ion trap. *J. Am. Soc. Mass Spectrom.*, 4, 917–929, **1993**, [https://doi.org/10.1016/1044-0305\(93\)80017-S](https://doi.org/10.1016/1044-0305(93)80017-S).
- [166] J. Franzen. Simulation study of an ion cage with superimposed multipole fields. *Int. J. Mass Spectrom. Ion Proc.*, 106, 63–78, **1991**, [https://doi.org/10.1016/0168-1176\(91\)85012-B](https://doi.org/10.1016/0168-1176(91)85012-B).
- [167] J. Franzen, R.-H. Gabling, G. Heinen, G. Weiss. US 5,028,777, "Method for mass-spectroscopic examination of a gas mixture and mass spectrometer intended for carrying out this method", **1991**.
- [168] R. E. March, J. F. J. Todd. *Practical Aspects of Trapped Ion Mass Spectrometry Volume 4. Theory and Instrumentation*, CRC Press, Hoboken, **2010**, <https://doi.org/10.1201/9781420083729>.

- [169] M. Carette, Y. Zerega. Non-linearity influences on the axial secular-motion spectrum of ions confined in a Fourier transform ion trap mass spectrometer. Experimental studies. *J. Mass Spectrom.*, 41, 71–76, **2006**, <https://doi.org/10.1002/jms.947>.
- [170] A. Janulyte, Y. Zerega, M. Carette. Harmful influences of confinement field non-linearities in mass identifying for a Fourier transform quadrupole ion trap mass spectrometer. *Int. J. Mass Spectrom.*, 263, 243–259, **2007**, <https://doi.org/10.1016/j.ijms.2007.02.048>.
- [171] M. Nappi, V. Frankevich, M. Soni, R. Cooks. Characteristics of a broad-band Fourier transform ion trap mass spectrometer. *Int. J. Mass Spectrom.*, 177, 91–104, **1998**, [https://doi.org/10.1016/S1387-3806\(98\)14038-1](https://doi.org/10.1016/S1387-3806(98)14038-1).
- [172] R. F. Wuerker, H. Shelton, R. V. Langmuir. Electrodynamic Containment of Charged Particles. *J. Appl. Phys.*, 30, 342–349, **1959**, <https://doi.org/10.1063/1.1735165>.
- [173] Y. Naito, M. Inoue. Peak Confluence Phenomenon in Fourier Transform Ion Cyclotron Resonance Mass Spectrometry. *J. Mass Spectrom. Soc. Jpn.*, 42, 1–9, **1994**, <https://doi.org/10.5702/massspec.42.1>.
- [174] P. M. Remes, J. D. Canterbury, M. W. Senko. Improved Control of Ion Populations for Orbitrap Mass Analysis. *Proceedings of the 62th ASMS Conference on Mass Spectrometry and Allied Topics, Baltimore, MD*, **2014**.
- [175] U. M. Hohenester, P. Barbier Saint-Hilaire, F. Fenaille, R. B. Cole. Investigation of space charge effects and ion trapping capacity on direct introduction ultra-high-resolution mass spectrometry workflows for metabolomics. *J. Mass Spectrom.*, 55, **2020**, <https://doi.org/10.1002/jms.4613>.
- [176] E. N. Nikolaev, Y. I. Kostyukevich, G. N. Vladimirov. Fourier transform ion cyclotron resonance (FT ICR) mass spectrometry: Theory and simulations. *Mass Spectrom. Rev.*, 35, 219–258, **2016**, <https://doi.org/10.1002/mas.21422>.
- [177] R. H. Perry, R. G. Cooks, R. J. Noll. Orbitrap mass spectrometry: instrumentation, ion motion and applications. *Mass Spectrom. Rev.*, 27, 661–699, **2008**, <https://doi.org/10.1002/mas.20186>.

## References

- [178] I. A. Boldin, E. N. Nikolaev. Theory of peak coalescence in Fourier transform ion cyclotron resonance mass spectrometry. *Rapid Commun. Mass Spectrom.*, 23, 3213–3219, **2009**, <https://doi.org/10.1002/rcm.4231>.
- [179] E. R. Badman, G. E. Patterson, J. M. Wells, R. E. Santini, R. G. Cooks. Differential non-destructive image current detection in a fourier transform quadrupole ion trap. *J. Mass Spectrom.*, 34, 889–894, **1999**, [https://doi.org/10.1002/\(SICI\)1096-9888\(199908\)34:8<889::AID-JMS848>3.0.CO;2-C](https://doi.org/10.1002/(SICI)1096-9888(199908)34:8<889::AID-JMS848>3.0.CO;2-C).
- [180] H. Qiao, C. Gao, D. Mao, N. Konenkov, D. J. Douglas. Space-charge effects with mass-selective axial ejection from a linear quadrupole ion trap. *Rapid Commun. Mass Spectrom.*, 25, 3509–3520, **2011**, <https://doi.org/10.1002/rcm.5255>.
- [181] F. Guthrie. XXXI. On a relation between heat and static electricity. *The London, Edinburgh, and Dublin Philosophical Magazine and Journal of Science*, 46, 257–266, **1873**, <https://doi.org/10.1080/14786447308640935>.
- [182] S. G. Lias, P. Ausloos. Ionization energies of organic compounds by equilibrium measurements. *J. Am. Chem. Soc.*, 100, 6027–6034, **1978**, <https://doi.org/10.1021/ja00487a009>.
- [183] J. H. Gross. *Mass Spectrometry. A Textbook*, 2nd edition, Springer-Verlag Berlin Heidelberg, Berlin, Heidelberg, **2011**, <https://doi.org/10.1007/978-3-642-10711-5>.
- [184] C. J. W. Brooks. Some aspects of mass spectrometry in research on steroids. *Phil. Trans. R. Soc. A*, 293, 53–67, **1979**, <https://doi.org/10.1098/rsta.1979.0079>.
- [185] P. W. Atkins, J. de Paula. *Atkins' physical chemistry*, 8th edition, Oxford Univ. Press, Oxford, **2006**.
- [186] J. R. Dormand, P. J. Prince. A family of embedded Runge-Kutta formulae. *J. Comput. Appl. Math.*, 6, 19–26, **1980**, [https://doi.org/10.1016/0771-050X\(80\)90013-3](https://doi.org/10.1016/0771-050X(80)90013-3).
- [187] P. Linstrom. *NIST Chemistry WebBook, NIST Standard Reference Database 69*, National Institute of Standards and Technology, **1997**, <https://doi.org/10.18434/T4D303>.
- [188] P. Herrera. PyEVTk, <https://github.com/paulo-herrera/PyEVTk>, **2021**.

- [189] L. S. Avila. *The VTK user's guide. Install, use and extend the visualization toolkit ; covers installation on PC, Unix, and Mac OSX, includes example scripts, C++ source code, images and data, shows how to extend VTK for your own applications*, 11th edition, Kitware, Clifton Park, NY, **2010**.
- [190] K. Irikura. *Electron-Impact Cross Section for Ionization and Excitation, NIST Standard Reference Database 107*, National Institute of Standards and Technology, **1997**, <https://doi.org/10.18434/T4KK5C>.
- [191] H. C. Straub, P. Renault, Lindsay B. G., K. A. Smith, R. F. Stebbings. Absolute partial and total cross sections for electron-impact ionization of argon from threshold to 1000 eV. *Phys. Rev. A (Coll Park)*, 52, 1115–1124, **1995**, <https://doi.org/10.1103/PhysRevA.52.1115>.
- [192] P. H. Dawson. A detailed study of the quadrupole mass filter. *Int. J. Mass Spectrom. Ion Phys.*, 14, 317–337, **1974**, [https://doi.org/10.1016/0020-7381\(74\)80067-7](https://doi.org/10.1016/0020-7381(74)80067-7).
- [193] P. H. Dawson. Energetics of ions in quadrupole fields. *Int. J. Mass Spectrom. Ion Phys.*, 20, 237–245, **1976**, [https://doi.org/10.1016/0020-7381\(76\)80152-0](https://doi.org/10.1016/0020-7381(76)80152-0).
- [194] M. Baril, A. Septier. Piégeage des ions dans un champ quadrupolaire tridimensionnel à haute fréquence. *Rev. Phys. Appl. (Paris)*, 9, 525–531, **1974**, <https://doi.org/10.1051/rphysap:0197400903052500>.
- [195] I. N. Bronstein, K. A. Semendjajew. *Taschenbuch der Mathematik*, 12. Auflage, Harri Deutsch, Frankfurt/Main und Zürich, **1972**.
- [196] P. L. Houston. *Chemical Kinetics and Reaction Dynamics*, Dover Publications, Newburyport, **2012**.
- [197] A. Kharchenko, G. Vladimirov, R. M. A. Heeren, E. N. Nikolaev. Performance of Orbitrap mass analyzer at various space charge and non-ideal field conditions: simulation approach. *J. Am. Soc. Mass Spectrom.*, 23, 977–987, **2012**, <https://doi.org/10.1007/s13361-011-0325-3>.
- [198] J. E. Bartmess. Gas-phase ion chemistry of 5-methylene-1,3-cyclohexadiene (o-isotoluene) and 3-methylene-1,4-cyclohexadiene (p-isotoluene). *J. Am. Chem. Soc.*, 104, 335–337, **1982**, <https://doi.org/10.1021/ja00365a082>.

## References

- [199] J. R. Vacher, F. Jorand, N. Blin-Simiand, S. Pasquiers. Electron impact ionization cross-sections of toluene. *Chem. Phys. Lett.*, 434, 188–193, **2007**, <https://doi.org/10.1016/j.cplett.2006.12.014>.